A Discontinuous Transport Methodology for Solidification Modelling

A thesis submitted to the University of Manchester for the degree of Doctor of Philosophy in the Faculty of Engineering and Physical Sciences

2014

Xiaozhu Ju

School of Mechanical, Aerospace and Civil Engineering

Table of Contents

List of Tables

List of Figures

Abstract

Phase change in solidification and melting can be described with the aid of discontinuous functions. The aim of this project is to establish effective methodologies for the solution of discontinuous phase-change problems. The classic capacitance method, which distributes the effect of any discontinuity present over a finite region (typically an element), can suffer from inaccurate energy transport. Improvement is possible with the application of the classic non-physical enthalpy method. However, this approach is known to suffer with the imposition of material velocity, which gives rise to negative thermal capacitance providing a source of error and instability. In order to improve on the performance of the capacitance method and the classic non-physical enthalpy method, this research introduces a series of new non-physical variables. Firstly, a new non-physical enthalpy is defined via the weak form of the energy transport equation. The classical non-physical enthalpy was defined using a temporal integral term. In the new definition, the non-physical enthalpy involves both a temporal and an advection term, which is shown to avoid the generation of negative capacitance and improve the stability of advection heat transfer in numerical methods. Secondly, control volume analysis is performed on weighted and unweighted forms of the governing energy equation involving non-physical enthalpy. The analysis is shown to reveal non-physical source terms that facilitate the removal of phase-change discontinuities. Thirdly, it is demonstrated in the thesis how a non-physical heat source must be introduced into the governing non-physical transport equation to remove discontinuities arising from non-physical terms related to advection. To demonstrate the accuracy and stability of the new method, it is implemented in the finite element method for both one-dimensional linear rod elements and two dimensional triangular elements. Update techniques and root finding methods, such as the predictor-corrector method, the secant method and the homotopy method, are applied to solve the non-linear system of equations, which are constructed with the new theory. Results returned from the one-dimensional numerical experiments are compared with exact solutions, which show reasonable accuracy. Numerical experiments for isothermal solidification with advection-diffusion in both one and two dimensions demonstrate the feasibility of the new methodology.

Declaration

I declare that no portion of the work referred to in the thesis has been submitted in support of an application for another degree or qualification of this or any other university or other institute of learning.

Copyright Statement

Acknowledgement

I am truly indebted and thankful to my supervisor, Dr. Keith Davey, for his invaluable help and guidance to this project, and for his wisdom and knowledge that inspires me and helps me to understand the subject. I would like to show my gratitude to my advisor, Prof. Hector Iacovides for his helpful advice in end-of-year examinations. I also would like to thank my parents and my girlfriend for their love, support and patience. At last, I would like to give my regards to all people who helped me during this study.

Nomenclature

Latin alphabet:

a	= parameter for the MMS	T_m	= melting temperature
a_Θ	= additional unknown degree freedom	$\hat{h}'$	= non-physical jump term
		h_c	= force convective coefficient
A_e	= cross-sectional area of element	h_l	= specific enthalpy of liquid
b	= parameter for the MMS	h_s	= specific enthalpy of solid
$\hat{c}$	= non-physical capacitance	h_{sol}	= enthalpy of solidification
$[\hat{C}]$	= capacitance matrix	H	= enthalpy
c_{app}	= apparent capacitance	$[J]$	= Jacobian matrix
c_{eff}	= effective capacitance	k_l	= thermal conductivity of liquid
c_l	= specific capacitance of liquid	k_s	= thermal conductivity of solid
c_s	= specific capacitance of solid	$[K]$	= conductivity matrix
C	= Concentration	$\left[\widetilde{\overline{K}}\right]$	= enriched conductivity matrix
C_j	= unknown constant for trail solution	L	= latent heat of fusion
		L_e	= length of element
D	= coefficient of diffusion	M_e	= total mass
f_l	= volume liquid fraction	M_l	= mass in the liquid phase
f_s	= volume solid fraction	$\underline{n}$	= outward unit normal
f_j	= trial solutions	N_j	= element shape functions

g_l = volume ratio of liquid

g_m = volume ratio of mushy zone

g_s = volume ratio of solid

G = Gibbs free energy

G_V = volumetric Gibbs free energy

h = specific enthalpy

$\hat{h}$ = non-physical enthalpy

$\{Q\}$ = loading vector of external heat

Q_m = manufactured source

$\hat{Q}$ = non-physical source

r = radius of nuclei

r^* = critical radius of nuclei

R = residual

$\underline{s}$ = general flux term

St = Stefan Number

S = entropy

t = time

Δt = time interval

$\underline{tn}$ = tangent outward unit normal

T = temperature

T' = 1st order derivative of

NE = total number of enriched nodes

NN = total number of nodes

P_e = elemental Pecl ̀et number

$\underline{q}$ = heat flux of conduction

$\{q\}$ = loading vector of flux

$\{\tilde{Q}\}$ = loading vector of non-physical source

Q = external heat source

$\{T_p\}$ = predicted temperature field

T_s = temperature of solid

T_{sol} = solidus temperature

δT = artificial temperature range

$\underline{v}$ = material velocity field

$\underline{v}^*$ = CV velocity field

$\underline{v}^+$ = discontinuity velocity field

$\underline{v}^\times$ = elemental discontinuity velocity field

$\underline{v_i}$ = velocity of the phase interface

$\underline{v_s}$ = velocity of solid material

$\underline{v_l}$ = velocity of liquid material

V_e = volume of element

temperature

T_o = fixed boundary temperature

T_{amb} = ambient temperature

T_e = trial solution of temperature

T_{init} = initial temperature

T_l = temperature of liquid

T_{liq} = liquidus temperature

T_{ref} = reference temperature

V_l = volume of liquid

V_m = volume of mushy zone

V_s = volume of solid

W = weighting functions

x, y, z = space coordinates

x = co-ordinate in the spatial reference system

X_i = the phase interface position

Greek alphabet:

α = thermal diffusivity

α_l = thermal diffusivity of liquid

α_s = thermal diffusivity of solid

β = parameter for liquid fraction

δT = artificial temperature range

Γ = control surface

Γ_D = boundary for Dirichlet's BC

Γ_i = boundary of phase interface

Γ_N = boundary for Neumann's BC

ε = emissivity

ϵ = relative error

θ = weighting term of θ-method

ϑ = number of simultaneous

ρ = density

ρ_s = the density of solid

ρ_l = the density of liquid

Σ_i = boundary of Γ_i

Υ = element based volume fraction

ς = node number

φ = general unknown field variable function

ψ_Θ = enrichment shape function

χ^* = co-ordinate in the computational reference system

Ω = control volume

Ω^+ = CV encloses to the phase

algebraic equations

κ = parameter for the MMS

λ = transcendental parameter

ν = viscosity

H = enthalpy per unit volume

ξ, η = natural space coordinates

interface

Ω_e = elemental control volume

Ω_f = swept CV by the discontinuity front

Ω_l = control volume of liquid

Ω_s = control volume of solid

$\Omega \backslash \Gamma_i$ = CV without discontinuity

Subscripts:

e = element

f = swept control volume by the discontinuity

i = phase interface

l = liquid

N = normal component

s = solid

T = tangential component

xx = component in x direction

yy = component in y direction

Superscripts:

$*$ = related to the computational reference system

$+$ = related to the discontinuity in a moving CV

$\times$ = related to a discontinuity in a moving element

Operators:

$\nabla \cdot \blacksquare$ = the divergence operator

$\nabla \blacksquare$ = gradient operator

∇_{Γ_i} = gradient operator on the

$\boldsymbol{sign}(\blacksquare)$ = signed function

$\|\blacksquare\|$ = norm

$]\blacksquare[$ = jump

	tangential plane of the phase interface	$\lfloor\blacksquare\rfloor$	= row vector
$\underline{\blacksquare}$	= vector	$\{\blacksquare\}$	= column vector
$\overline{\blacksquare}$	= Laplace transform	$\boldsymbol{min}(\blacksquare)$	= minimum value
$\hat{\blacksquare}$	= non-physical	$\boldsymbol{erf}(\blacksquare)$	= error function
$\tilde{\blacksquare}$	= enriched	$\blacksquare:\blacksquare$	= Frobenius inner product
$\tilde{\blacksquare}$	= non-physical variables in system of equations		

Abbreviations

1D	one dimension
2D	two dimension
CS	control surface
CV	control volume
CVCM	control volume capacitance method
FDM	finite difference method
FEM	finite element method
FVM	finite volume method
MES	method of exact solutions
MMS	method of manufactured solutions
NN	number of node
NELS	total number of elements
PDE	partial differential equation

XFEM extended finite element method

Chapter 1 Introduction

Solidification is the phase transformation in which the liquid turns into the solid when its temperature is lowered below its freezing point. Solidification involves two stages, which are nucleation and crystallization. The molecules gather into clusters during nucleation, and a nuclei is formed when the cluster reaches a critical radius. In the second stage, crystal growth originates from the nuclei and proceeds until the material is completely solid. During the solidification process, latent heat is released because no energy is required to overcome the intermolecular attractive force to keep the molecules apart. This phenomenon is reflected in a strong discontinuity in enthalpy (there is a jump in the change of enthalpy) and a weak discontinuity (there is a jump in the gradient) in temperature. Solidification is of industrial importance because it is a feature of welding and casting processes [1]. Casting of metals has a very long history, and it is still one of the most important processes for the manufacturing industry. It is claimed that 90% of manufactured goods make use of the casting process [2-3]. Foundry reports indicate that solidification modelling is not only a cost-effective investment but also a major technical asset [4]. Thus, both academic researchers and industrial technicians are interested in studying and understanding the solidification process. A good understanding of such phenomena leads to better control and improvement in the quality of products. In recent years, mathematical models and numerical methods have developed greatly, which has helped the research community to understand the physical behaviour of solidification.

The mathematical modelling of solidification involves the conservation equations of mass, momentum, energy and concentration. The conservation equations can be formulated in a strong form involving partial differential equations, or in a weak form which involves integrals and typically Lagrangian or Eulerian descriptions of the governing physics. This project particularly focuses on the conservation of energy in its weak form. As regards solidification problems, the sensible heat is the heat exchange of a thermodynamic system, which can be evaluated from the mass of the system, the specific capacity and the temperature change of the system. Solidification is also a moving boundary problem, where the latent heat energy is associated with the movement of the boundary/phase interface. In the mathematical modelling and analysis, the latent heat of fusion makes the solidification problem highly nonlinear. Such problems were first established by Stefan in 1889. The

relationship between the phase interface/moving boundary and the latent heat of fusion is termed a Stefan condition. Consequently the mathematical modelling of solidification is often categorized as a Stefan problem.

The transport equation that governs the conservation of energy can be solved by numerical methods. The numerical methods for solidification can be divided into moving mesh methods and fixed grid methods. Early research on the moving mesh methods involved the placement of extra nodes on the phase interface [5-7]. The position of phase boundary is approximated by the Stefan Condition. This strategy was only applied effectively to two-dimensional problems with time being one of the dimensions accounted for in the computational grid [5-7]. Recently, studies on the front tracking method have become more active. Well-known approaches include the extended finite element method (XFEM) [8-14] and the level-set method [8,11,13-22]. In references [8, 12, 16, 19], the research focuses particularly on solidification problems. An essential component of the front tracking method is believed to be the evaluation of the position of the phase front or the velocity of the phase front. The fixed grid method can be further classified into capacitance methods [23-41] and the source-based methods [42-55]. Their difference is that the latent heat effect is captured by the capacitance or by the source term. These methods do not need to track the phase front. Consequently, the fixed grid method can be easily implemented into any existing finite element program. In the earlier works on the capacitance method, it was usually incorporated into the FDM [23-28]. Several critics indicated that capacitance methods suffer inaccuracy, wrong phase transformation time and oscillations of temperature after phase change [7, 25, 28]. However, the method has been improved by scientists and engineers in many ways, such as the approximation of liquid fraction/ratio of liquid phase, the weak formulation and the evaluation of thermal capacitance [28-41]. The source-based method is the “twin brother” of the capacitance method. It is known that latent heat is essential to Stefan problems [28]. The difference between the various approaches is how they deal with the latent heat. If latent heat is evaluated with capacitance, then it is a capacitance method. If the latent heat is treated as a source, then it is the source based method. To the author’s knowledge, the source based method is less popular than the enthalpy method (a particular type of capacitance method), and it seems that the source based method is only used in conjunction with the FDM and FVM. In the recent years, thanks to the significantly advanced performance of computers, the front tracking methods have been developed for multi-dimensional problems with complex geometry. The simulation of dendrite growth is of particular interest to researchers

[56-57]. For the capacitance and the source-based methods, they are preferred by engineers because they are more physically understandable. The methods are modified more or less to satisfy specific cases [57-61].

Two studies highlighted in this field are the non-physical enthalpy method provided by Davey and Mondragon [62-63], and an enrichment scheme provided by Cosimo *et al.*[64]. The non-physical enthalpy method can be classified as a fixed grid method. In this method, a non-physical enthalpy is defined through the transport equation in weak form. With this definition, the rate change of physical enthalpy and the change of advection/convection are reflected by the rate change of non-physical enthalpy alone. The non-physical enthalpy is made continuous at a discontinuity and it gives rise to the possibility that a physical discontinuity can be represented by a continuous non-physical field on which a non-physical source is superimposed. The non-physical enthalpy method can be a fixed grid method, which means that, it can be easily implemented with existing finite-element programmes. Also it is able to provide excellent accuracy with great computational time-efficiency. The enrichment scheme provided by Cosimo *et al.* can be classified as a front tracking method. It is founded on XFEM, in which, the enrichment shape function is used to discretize the element with discontinuity. The formulation of enrichment shape function requires the position of phase interface and it is approximated by the temperature profile from current time step. It is accurate, and its major advantage is that it avoids the complex meshing and re-meshing technique of front tracking method by the application of XFEM.

However, the non-physical enthalpy method has its limitations. First of all, when considering the numerical aspect, the non-physical source is accounted for with a capacitance term, which more or less returns the method back to the CVCM. Secondly, the non-physical enthalpy method does not consider the possibility that the weighting functions may vary with movement of the control volume. Control volumes (used in the analysis) track the movement of the discontinuity and care must be taken to properly describe the behaviour of the weighting functions, which are typically considered invariant with respect to mesh movement. Thirdly, the solution method for the non-physical enthalpy method is a bisection method. This method requires that the solution should be between the present value and predicted value. This criteria is not always guarantied in the solution procedure and the programme may fail to converge. Lastly, the non-physical enthalpy method is only able to deal with advection-diffusion problems where the material velocity is relatively small. The enrichment scheme has only been applied to one-dimensional conduction-diffusion

problems so far, and advection is not considered. Hence, the non-physical enthalpy method has room for improvement.

The main objective of this project is to establish an effective methodology for discontinuous phase change problems. Isothermal solidification is of particular interest, which has a distinct phase interface between solid and liquid. The concept underpinning this project is to introduce non-physical variables through transport equations, which helps to remove the discontinuity from these equations, but it generates non-physical source-like term that captures the discontinuity. This non-physical variable method can be categorized as a fixed grid method. The benefit of this concept may be the improvement of stability and accuracy when advection terms are present in the transport equations. Furthermore, the finite element method (FEM) has its advantages when modelling problems with complex geometry and boundaries, and it is also a well-developed technique. Thus, this project prefers to do investigations with the FEM.

This project firstly tries to enhance the non-physical enthalpy method provided by references [62-63]. A new analysis of discontinuity embodied in the weighted non-physical transport equation is given by considering the variable weighting function in a moving control volume. Then, new system of finite element equations is established with the consideration of a non-physical source which captures the latent heat energy. And at last, three alterative solution methods are implemented to the non-physical enthalpy method, which are the predictor corrector method, the secant method and the homotopy method. The actions mentioned above helps to better understand the non-physical concept. Then, a new definition of non-physical enthalpy is provided which includes a non-physical advective term and a non-physical source term, and the introduction of these new non-physical terms enables the non-physical method to deal with the phase change problem with advection.

The contribution of this subject involves:

(1) Alternative solution methods such as the predictor-corrector method, the secant method and the homotopy method are now available for the classical non-physical enthalpy method;
(2) The effects of liquid fraction and the update procedure on the non-physical variable are studied, which can serve as a guide for the development of this method;
(3) The applications of both non-physical capacitance method and non-physical source method can provide accurate results for isothermal solidification;

(4) The application of non-physical capacitance and non-physical source through a new definition can accurately simulate isothermal solidification with advection-diffusion. This can be applied to the industrial processes such as continuous casting, squeezing casting, etc.;
(5) The new definition of non-physical variable method is applied to two-dimensional simulation, which makes it more practical.

The layout of this thesis is as follow:

Chapter 2: A literature review is presented in this chapter, which includes the basic knowledge of non-physical methods such as the transport equation, the Lagrangian and Eulerian descriptions etc..

Chapter 3: This chapter is the theoretical study on the non-physical enthalpy method introduced by [62-63], which shows the mathematical procedure involved in the definition of the non-physical variables from transport equations. A new analysis of a discontinuity embodied in the weighted non-physical transport equation is given by considering the variable weighting function in a moving control volume. A new system of finite element equations is established with the consideration of a non-physical source which captures the latent heat energy. Moreover, the importance of volume fraction to the non-physical method is highlighted.

Chapter 4: This chapter is the numerical study on the non-physical enthalpy method with reconstructed system of finite element equations, which illustrates how non-physical variables such as the non-physical capacitance and the non-physical source are implemented into one-dimensional solidification cases.

Chapter 5: This chapter shows the mathematical procedure involved in a new definition of the non-physical variables from the transport equations. This new definition involves advection in the governing equation. The advection means that both solid and liquid are transporting energy by the movement of material. Such phenomenon can be seen in industrial processes such as continuous casting and squeezing casting.

Chapter 6: The new non-physical variable method is applied to one-dimensional finite element method, which examines the feasibility of the method.

Chapter 7: Two dimensional models are made in this chapter, in order to further examine the feasibility of applying the non-physical variable methods in commercial-like practical higher dimensional models.

Chapter 8 This chapter is about conclusions which include the achievements made, the limitations of the work and some possible future works.

Chapter 2 Literature Review

2.1 General

The solidification problem is a coupled problem of heat transfer and fluid dynamics. The physics behind the solidification process includes the conservation of mass, the conservation of concentration, the conservation of momentum and the conservation of energy. This project focuses on the conservation of energy, which is governed by the first law of thermodynamics. The governing equation can be written in a strong from as

$$\frac{\partial}{\partial t}\rho h + \nabla \cdot \left(\rho h \underline{v}\right) = \nabla \cdot (k \nabla T) + Q \qquad (2—1)$$

where ρ is the density, h is the specific enthalpy, $\underline{v}$ is the velocity field, k is the conductivity, T is the temperature and Q is the heat source. The operator $\nabla \cdot = \partial/\partial x + \partial/\partial y + \partial/\partial z$ is the divergence operator.

Solidification is not only a problem of heat transfer but also a problem of phase change. In a phase change problem, the system generates one or more moving boundary interfaces. Certain jump conditions are associated with these boundary interfaces. How to evaluate the jump conditions as well as the boundary interface position is a particular difficulty for the solution of the phase change problem. With solidification, the phase change involves differences in material properties, such as

$$\rho = g_s \rho_s + g_l \rho_l \qquad (2—2a)$$

$$k = g_s k_s + g_l k_l \qquad (2—2b)$$

where g denotes the volume fraction of solid/liquid [28, 32-60] or the ratio of solid/liquid within a control volume (CV) [24], and the subscript s and l refer to the solid and liquid respectively. The evaluation of g can be achieved in various schemes, and they are essential to the enthalpy method and the source based method [29, 65, 44].

The boundary conditions of the phase interface is governed by

$$k_s \nabla T_s - k_l \nabla T_l = \rho L \frac{dX_i}{dt} \qquad (2—2c)$$

where ∇ is the gradient operator defined in a Cartesian system by $\nabla = \{\partial/\partial x \quad \partial/\partial y \quad \partial/\partial z\}$.

Equation (2—2c) is the well-known Stefan condition, where L is the latent heat and $\underline{X_i}$ denotes the interface position.

The partial differential equation (2—1) cannot be directly applied at the phase interface. Thus, the Stefan condition is used to describe the behaviour at the phase interface. It shows that the difference in temperature gradients at both side of the phase interface is related to the phase interface velocity. The relationship between enthalpy and the temperature is sketched in Figure 2.1, where T_m denotes the melting temperature and T_v denotes the vaporization temperature. In the enthalpy method, latent heat is accounted for through the definition of enthalpy. This diagram gives rise to the following relationships:

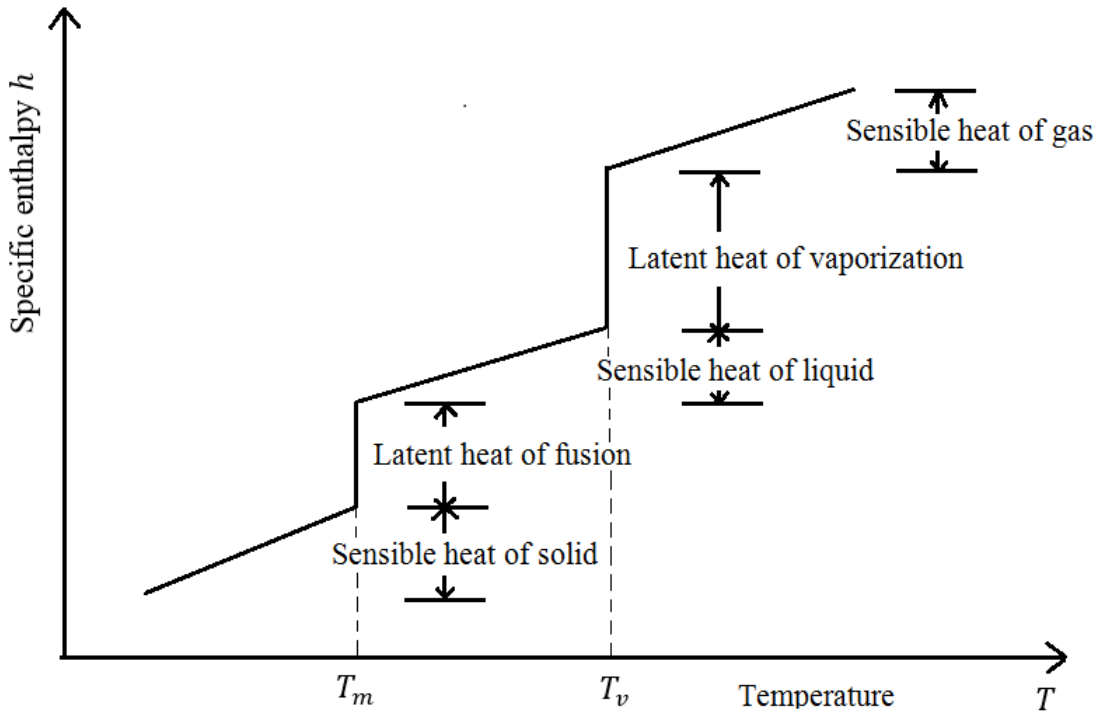

Figure 2.1: The relationship between enthalpy and temperature in the change of phase

$$h_s = h_{sol} + \int_{T_{sol}}^{T} c_s(T')d\,T' \qquad (2—3a)$$

$$h_l = h_{sol} + L + \int_{T_{liq}}^{T} c_l(T')\,dT' \qquad (2—3b)$$

where h represents the specific enthalpy, T_{sol} is the solidus temperature and h_{sol} is the reference specific enthalpy, i.e. $h_{sol} = c_s T_{sol}$. The subscripts s and l denote the solid phase and liquid phase respectively [65, 39, 41, 62-53].

The problem is transient, so it requires an initial condition (IC) along with boundary conditions (BC), i.e.

$$T(\underline{x}, t) = T_{init}(\underline{x}) \quad if \quad t = 0, \forall \underline{x} \in \Omega \tag{2—4d}$$

$$T(\underline{x}, t) = T_o \quad if \quad \underline{x} \in \Gamma_N \tag{2—4e}$$

$$-k\nabla T(\underline{x}, t) = \underline{q} \cdot \underline{n} \quad if \ \underline{x} \in \Gamma_D \tag{2—4f}$$

Equation (2—4d) is the prescribed value for field unknowns to initialise and start the solution of the problem. For example, the temperature T_{init} refers to the initial temperature of the material. Equation (2—4e) is the Robin boundary condition. Equation (2—4f) is the Dirichlet boundary condition, where the flux $\underline{q}$ can be the boundary fluxes due to conduction, convection or radiation. A sketch of the thermal system is depicted in Figure 2.2. Equations (2—4a) to (2—4f) are the complete mathematical model, which requires to be solved for solidification problems.

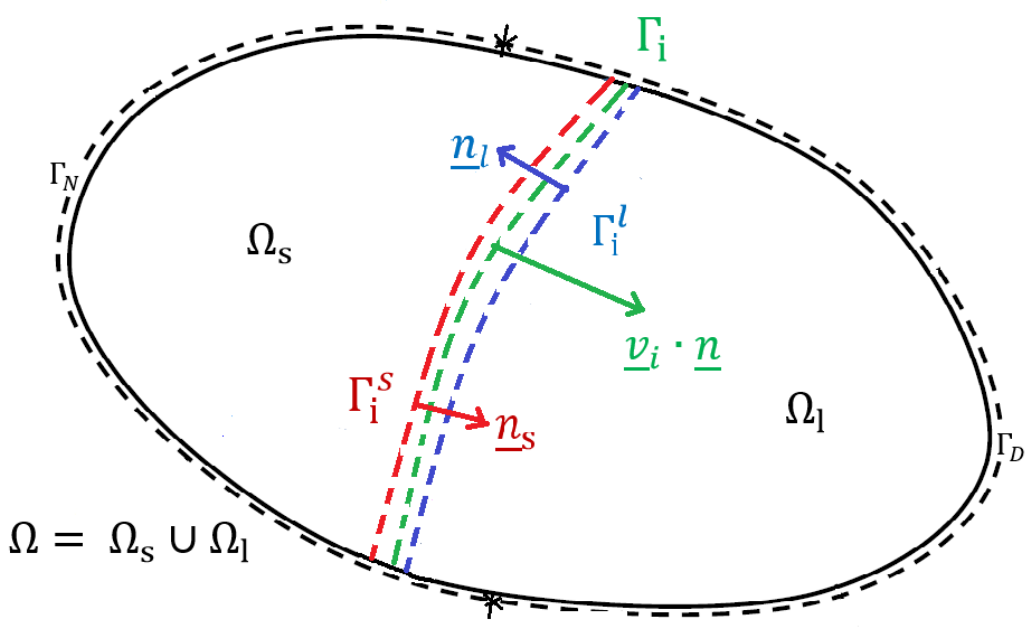

Figure 2.2: Thermal system for solidification problems

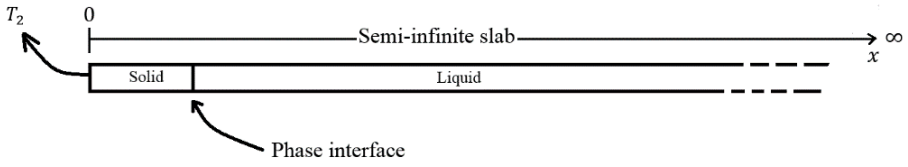

Figure 2.3: Semi-infinite Stefan problem

The exact solution of a classic Stefan problem can be found in references [67-68]. As seen in these references, the exact solution is obtained by the consideration of a one-dimensional semi-infinite slab, which is originally liquid and is solidifying. A sketch of the problem is shown in Figure 2.3. The boundary condition is the Dirichlet boundary condition. Application of the Neumann's method gives the exact solution as

$$T(x,t) = \begin{cases} T_2 + (T_{sol} - T_2)\dfrac{\boldsymbol{erf}\left(\frac{x}{2\sqrt{\alpha_s t}}\right)}{\boldsymbol{erf}(\lambda)} & if \;\; x < X_i \\ T_1 + (T_{sol} - T_1)\dfrac{\boldsymbol{erfc}\left(\frac{x}{2\sqrt{\alpha_l t}}\right)}{\boldsymbol{erfc}(\nu\lambda)} & if \;\; X_i \leq x \end{cases} \tag{2—5}$$

where T_1 is the initial temperature, T_2 is the fixed boundary temperature, and thermal diffusivity of material $\alpha = k/\rho c$, $\nu = \sqrt{\alpha_s/\alpha_l}$. The position of phase interface $X_i = 2\lambda\sqrt{\alpha_s t}$. The operator $\boldsymbol{erf}(\blacksquare)$ is the error function and $\boldsymbol{erfc}(\blacksquare)$ is the complementary error function. The parameter λ can be calculated through

$$\frac{St_s}{\lambda\sqrt{\pi}e^{\lambda^2}\,\boldsymbol{erf}(\lambda)} + \frac{St_l}{(\nu\lambda)\sqrt{\pi}e^{(\nu\lambda)^2}\,\boldsymbol{erfc}(\nu\lambda)} = 1 \tag{2—6}$$

where $St_s = c_p(T_{sol} - T_1)/L$ and $St_l = c_p(T_{sol} - T_2)/L$, are the Stefan numbers.

The exact solution can be used as a criterion to determine how accurate the numerical method is. Therefore, this project also uses another exact solution as benchmark, which is obtained by replacing the Dirichlet boundary to the Robin boundary condition, i.e. $k_s \partial T/\partial x = h_c(T - T_{amb})$. The exact solution with this type of boundary condition can be written as

$$T(x,t)=\begin{cases}\left(\frac{T_{sol}-T_{amb}}{\frac{1}{h_c\sqrt{\pi\alpha_s t}}+\mathrm{erf}(\frac{X_i(t)}{2\sqrt{\alpha_s t}})}\right)\boldsymbol{erf}\left(\frac{x}{2\sqrt{\alpha_s t}}\right)+\frac{T_{sol}+T_{amb}h_c\sqrt{\pi\alpha_s t}\boldsymbol{erf}(\frac{X_i(t)}{2\sqrt{\alpha_s t}})}{1+h_c\sqrt{\pi\alpha_s t}\boldsymbol{erf}(\frac{X_i(t)}{2\sqrt{\alpha_s t}})} & (0\le x<X_i(t))\\ T_{init}+(T_{sol}-T_{init})\frac{\boldsymbol{erfc}\left(\frac{x}{2\sqrt{\alpha_l t}}\right)}{\boldsymbol{erfc}(\lambda\sqrt{\frac{\alpha_s}{\alpha_l}})} & (x>X_i(t))\end{cases} \quad (2—7)$$

where T_{init} is the initial temperature and T_{amb} is the ambient temperature. Its detailed derivation can be seen in Appendix I—(a).

The value of λ can be computed via a transcendental equation, which is established by substituting equation (2—7) into the Stefan condition. After simplification, the equation is written as

$$\sqrt{\pi}\lambda=-\frac{St_s}{e^{\lambda^2}\left(\frac{1}{h_c\sqrt{\pi\alpha_s t}}+\mathrm{erf}(\lambda)\right)}+\frac{St_l}{ve^{(v\lambda)^2}erfc(v\lambda)} \quad (2—8)$$

where $St_s=c_s(T_{sol}-T_2)/L$ and $St_l=c_l(T_1-T_{sol}/L$ are the Stefan numbers, and $v=\sqrt{\alpha_s/\alpha_l}$.

A direct solution of equation (2—8) can be conducted through a good root finding method, such as the Newton's method, which is used in this project.

2.2 The front tracking method

The extended finite element method (XFEM) has become a hot topic for front tracking methods recently. It is developed from the Galerkin finite element method (GFEM), so they have many features in common. The XFEM is aimed at solving the discontinuous problems. In place of the normal shape functions which are utilised in the GFEM, the shape functions established for the XFEM are called the enrichment functions. An example of one-dimensional shape functions is provided in Figure 2.4. In the XFEM, the enrichment functions are applied to the element which contains the discontinuity front; this element is called an enriched element. The nodes of the enriched element are called the enriched nodes. The adjacent elements, which share the node with the enriched element, are the partially enriched elements. The unknown field variables, such as temperature, are usually approximated as

$$T_e = \sum_{\varsigma=1}^{NN} N_\varsigma T_\varsigma + \sum_{\Theta=1}^{NE} E_\Theta a_\Theta \quad (2—9)$$

where T_e is the trial solution of temperature, N_ς is the classical FEM shape function, T_ς is the nodal temperature, E_Θ is the enriched shape function and a_Θ are additional unknown degrees of freedom. Here, NN is the total number of nodes of an element and NE is the total number of the enriched functions.

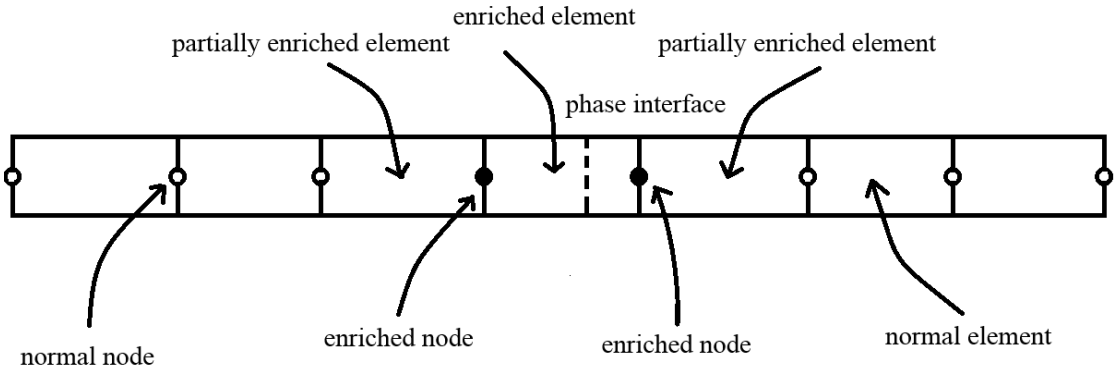

Figure 2.4: The one-dimensional XFEM

An enrichment scheme provided by Cosimo *et al* is a typical application of XFEM [64]. This scheme starts from the application of weighed residual method to equation (2—1). The weighted governing equation is expressed as

$$\int_\Omega W\left(\rho\dot{h} - \nabla\cdot(k\nabla T) - Q\right)dV = 0 \quad (2—10)$$

where $\dot{h}$ is the rate change of specific enthalpy, and W is the shape function.

The latent heat energy influences the thermodynamic system by the identity

$$h(T) = \int_{T_{ref}}^{T} c(T')dT' + Lf_l(T) \quad (2—11)$$

which is identical to the relationships described in equations (2—3a) and (2—3b). The liquid fraction is evaluated as a Heaviside step function, i.e. $f_l(T) = H_{eav}(T - T_m)$ [64].

The enrichment scheme uses the enrichment function provided by Coppola-Owen and Codina in reference [69]. In order to construct the enrichment shape function, the enrichment scheme firstly consider a simple level set function φ as

$$\varphi = x - x_a \quad (2—12)$$

where the position of phase interface is evaluated as $x_a = x_1 + s(x_2 - x_1)$.

The enrichment scheme contains one enriched node, i.e. $\Theta = 1$ in equation (2—9). So the enrichment shape function is given as

$$E(x) = \begin{cases} \frac{x-x_1}{x_a-x_1} = \frac{\varphi_1-\varphi}{\varphi_1} & x \le x_a \\ \frac{x_2-x}{x_2-x_a} = \frac{\varphi_2-\varphi}{\varphi_2} & x > x_a \end{cases} \quad (2—13)$$

Thus, equation (2—9) reduces to

$$T_e = \sum_{\varsigma=1}^{NN} N_\varsigma T_\varsigma + E(x)a \quad (2—14)$$

where a is the only enriched nodal value for one-dimensional problem.

It can be seen from equation (2—12) to equation (2—14) that, the construction of enrichment shape functions requires the evaluation of phase interface position x_a. Classic front tracking methods prefer to construct a hyperbolic-type partial differential equation to evaluate the interface position [8, 70]. Rao *et al*. [70] and Chessa *et al.* [8] considered that the phase interface position is moving with a velocity $\underline{v_i}$, thus the level set field $\varphi(\underline{x}, t)$ is governed by a hyperbolic-type PDE which is

$$\frac{\partial \varphi}{\partial t} + \underline{v_i} \cdot \nabla \varphi = 0 \quad (2—15)$$

when $\varphi = 0$, the $\underline{x} \in \Gamma_i$ is called the 0 level set. In order to solve equation (2—15), the velocity field $\underline{v_i}$ is a vector i.e. $\underline{v_i} = V_i \underline{n_i}$, and the scalar V_i is required to be found. Since equation (2—15) is hyperbolic, a least-squared method is typically required for numerical stabilization [71-76]. As a matter of fact, in order to solve Stefan problems by the XFEM and level set method, two extra systems of equations (equation (2—15) and equation (2—2c)) are required to be solved. On top of that, the velocity of phase interface must be evaluated. Unfortunately, studies so far on the front tracking method, such as in reference [8, 14, 106-107], do not provide much detail on how the Stefan Condition is evaluated. Sethian *et. al.* [77] determine the phase front velocity through the Stefan equation. However the application of Green function, Fourier series and Taylor series to the Stefan equation makes it rather complicated. The enrichment scheme uses a simple strategy to avoid constructing and evaluating a level-set function such as equation (2—15). The strategy is to evaluate the parameter s in equation (2—12) through temperature as

$$s = \frac{T_m - T_1 - a}{T_2 - T_1} \tag{2—16}$$

Then, the enrichment function can be constructed. It is only applied to the element in which, the discontinuity is contained. For the continuous elements, normal shape functions are applied. The system of equations is solved by the Newton-Raphson method and the line-search method [64].

To author's knowledge, several difficulties of XFEM are listed as below:

(1) The enrichment shape functions and the extra nodal degree of freedom generates a larger matrix than the GFEM, which will obviously cost extra computational time and storage space;
(2) Special attention must be taken when assembling the system because three kinds of matrices are involved. These matrices are the standard matrix, the partial enriched matrix and the fully enriched matrix;

The XFEM requires the accurate position of the interface. Therefore, the high accuracy achieved by XFEM is related to the accuracy of the prescribed interface position. However, for Stefan-like problems, the evaluation of interface position itself is a great challenge for multi-dimensional problems.

2.3 The non-physical enthalpy method

This project is based on the recent non-physical enthalpy method provided by Davey and Mondragon [63]. In references [63], the definition of non-physical enthalpy is defined via the weak form of energy transport equation as

$$\frac{D^*}{D^*t}\int_\Omega \hat{h}\, dV = \frac{D^*}{D^*t}\int_\Omega \rho h\, dV + \int_\Gamma \rho h \left(\underline{v} - \underline{v}^*\right)\cdot \underline{n} d\Gamma = -\int_\Gamma \underline{q}\cdot \underline{n} d\Gamma + \int_\Omega \rho Q\, dV \tag{2—17}$$

where $\hat{h}$ is the non-physical enthalpy, $\underline{v}^*$ is the control volume velocity, Ω is a control volume transported with $\underline{v}^*$ and Γ is the boundary of Ω. The derivative $D^*/D^*t = \partial/\partial t + \underline{v}^* \cdot \nabla$.

It can be seen in equation (2—17) that, the rate change of physical enthalpy and the change of enthalpy due to advection are now all reflected by the change of non-physical enthalpy

alone. The non-physical enthalpy is forced to be continuous in the control volume, i.e. $]\hat{h}\underline{n}[= 0$, where the bracket]■[signifies a jump. Then, discontinuity can be isolated in a non-physical source $\widehat{h'}$ through mathematical analysis. A schematic sketch of the relationship between the non-physical enthalpy $\hat{h}$ and the non-physical source $\widehat{h'}$ can be seen in Figure 2.5.

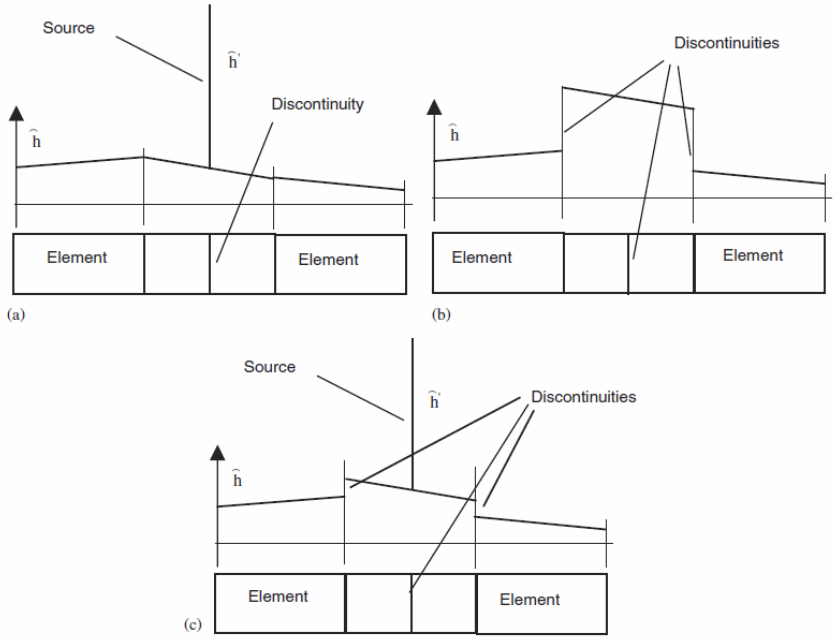

Figure 2.5: Non-physical behaviour on 1D elements: (a) moving source; (b) edge discontinuities; and (c) moving source and edge discontinuities [63].

Both Figure 2.5 (a) and Figure 2.5 (c) depict possible relationships of $\hat{h}$ and $\widehat{h'}$ depending on how the two terms are evaluated. If the non-physical source $\widehat{h'}$ is able to completely remove the discontinuity in $\hat{h}$, then their relationship is depicted in Figure 2.5 (a). If the non-physical source $\widehat{h'}$ only removes part of the discontinuity in $\hat{h}$, but the magnitude of discontinuity is much lowered in $\hat{h}$, then their relationship is depicted in Figure 2.5 (c). It has to be mentioned that, the non-physical enthalpy $\hat{h}$ is still continuous within the element which contains the phase interface. The Figure 2.5 (b) is a sketch of control volume capacitance method which was developed by Davey *et al* [66].

In the definition of non-physical enthalpy, the control volume velocity $\underline{v}^*$ governs the shape and position of the control volume. It is defined for the convenience of analysis and solution. For example, on setting $\underline{v}^* = \underline{v}$, where $\underline{v}$ is the material velocity, equation (2—17) becomes

the Lagrangian descripted transport equation. This is not always permitted because the material velocity is discontinuous on the phase interface. So, one simple setting is $\underline{v}^* = \underline{0}$, and equation (2—17) returns the Eulerian descripted transport equation. It is always permitted because $\underline{0}$ is continuous.

The transport equation (2—17) is not ideally suited for analysing a phase interface, and it can be seen that no information about discontinuity is provided in this equation. Therefore, it is necessary to consider another control volume Ω^+ which movement is controlled by velocity $\underline{v}^+$. The transport equation with in this control volume is

$$\frac{D^+}{D^+t}\int_{\Omega^+}\hat{h}\,dV = \frac{D^+}{D^+t}\int_{\Omega^+}\rho h\,dV + \int_{\Gamma^+}\rho h\left(\underline{v}-\underline{v}^+\right)\cdot\underline{n}d\Gamma = -\int_{\Gamma^+}\underline{q}\cdot\underline{n}d\Gamma + \int_{\Omega^+}\rho Q\,dV \tag{2—18}$$

Application of equation (2—18) to a control volume Ω_i which encloses to the phase interface, it gives

$$\frac{D^+}{D^+t}\int_{\Omega_i}\hat{h}\,dV + \int_{\Gamma-\Gamma_i^s-\Gamma_i^l}\hat{h}\left(\underline{v}^*-\underline{v}^+\right)\cdot\underline{n}dA + \int_{\Gamma_i^s}\hat{h}\left(\underline{v}^*-\underline{v}^+\right)\cdot\left(-\underline{n}\right)d\Gamma + \int_{\Gamma_i^l}\hat{h}\left(\underline{v}^*-\underline{v}^+\right)\cdot\left(-\underline{n}\right)d\Gamma = \frac{D^+}{D^+t}\int_{\Omega_i}\rho h\,dV + \int_{\Gamma-\Gamma_i^s-\Gamma_i^l}\rho h\left(\underline{v}-\underline{v}^+\right)\cdot\underline{n}d\Gamma + \int_{\Gamma_i^s}\rho h\left(\underline{v}-\underline{v}^+\right)\cdot\left(-\underline{n}\right)d\Gamma + \int_{\Gamma_i^l}\rho h\left(\underline{v}-\underline{v}^+\right)\cdot\left(-\underline{n}\right)d\Gamma = -\int_{\Gamma-\Gamma_i^s-\Gamma_i^l}\underline{q}\cdot\underline{n}d\Gamma - \int_{\Gamma_i^s}\underline{q}\cdot\left(-\underline{n}\right)d\Gamma - \int_{\Gamma_i^l}\underline{q}\cdot\left(-\underline{n}\right)d\Gamma + \int_{\Omega_i}\rho Q\,dV \tag{2—19}$$

where $\Gamma-\Gamma_i^s-\Gamma_i^l$, Γ_i^s and Γ_i^l are the boundary of Ω_i.

When the control volume Ω_i is shrunk down until its volume is zero, i.e. $vol(\Omega_i)\to 0$ with $\Gamma_i \subset \Omega_i$. A source equation can be derived as

$$\frac{D^+}{D^+t}\int_{\Gamma_i}\hat{h}'\,d\Gamma + \int_{\Sigma_i}\hat{h}'\left(\underline{v}^*-\underline{v}^+\right)\cdot\underline{tn}d\Sigma + \int_{\Gamma_i}\left]\hat{h}\left(\underline{v}^*-\underline{v}^+\right)\cdot\left(-\underline{n}\right)\right[d\Gamma = \int_{\Gamma_i}\left]\rho h\left(\underline{v}-\underline{v}^+\right)\cdot\left(-\underline{n}\right)\right[d\Gamma = -\int_{\Gamma_i}\left]\underline{q}\cdot\left(-\underline{n}\right)\right[d\Gamma \tag{2—20}$$

where the bracket]■[signifies a jump term, Σ_i is the boundary of Γ_i, and $\underline{tn}$ is the outward pointing unit normal in the tangent plane of the Γ_i on the curve Σ_i. Equation (2—20) provides the definition for non-physical source $\hat{h}'$ in Figure 2.5 (a) and (c). It also facilitates the isolation of discontinuity from the non-physical enthalpy $\hat{h}$.

The non-physical enthalpy method can be a fixed grid method, which means that, it can be easily implemented into the existing finite element method and programmes. The semi-discretized equation can be obtained by the application of weighed residual method. The weighed transport equation is

$$\frac{D^*}{D^*t}\int_\Omega W\hat{h}\,dV = \frac{D^*}{D^*t}\int_\Omega W\rho h\,dV - \int_\Omega \rho h(\underline{v}-\underline{v}^*)\cdot\nabla W\,dV + \int_\Gamma W\rho h\,(\underline{v}-\underline{v}^*)\cdot\underline{n}d\Gamma = \int_\Omega \underline{q}\cdot\nabla W\,dV - \int_\Gamma W\underline{q}\cdot\underline{n}d\Gamma + \int_\Omega \rho Q\,dV \quad (2—21)$$

where W is the weighting function, and it is assumed transport invariantly with the control volume Ω [63]. Analysis shows that some sources are contained in the terms $\int_\Omega \rho h(\underline{v}-\underline{v}^*)\cdot\nabla W\,dV$ and $\int_\Omega \underline{q}\cdot\nabla W\,dV$. The annihilation of these sources are achieved by the application of α-time integration to the term $\int_\Omega \underline{q}\cdot\nabla W\,dV$ and the strong form of source equation (2—20).

The discontinuity can be isolated by the subtraction of the weighted source equation off from the weighted transport equation. The weighted transport equation without discontinuity can be written as

$$\frac{D^*}{D^*t}\int_{\Omega\backslash\Gamma_i}\hat{h}\,dV = \frac{D^*}{D^*t}\int_\Omega \rho h\,dV + \int_\Gamma \rho h(\underline{v}-\underline{v}^*)\cdot\underline{n}d\Gamma - \left(\int_{\Gamma_i}\right]\rho h(\underline{v}-\underline{v}^+)\cdot(-\underline{n})\Big[d\Gamma\Big) = -\int_\Gamma \underline{q}\cdot\underline{n}dA + \int_\Omega \rho Q\,dV - \left(-\int_{\Gamma_i}\right]\underline{q}\cdot(-\underline{n})\Big[\,dA\Big) \quad (2—22)$$

where $\Omega\backslash\Gamma_i$ signifies the control volume without discontinuity.

With the discontinuity isolated, the element continuous approximation for the weighting function W and the non-physical enthalpy $\hat{h}$ can be applied. In order to calculate the temperature field through equation (2—22), the non-physical capacitance $\hat{c}$ is introduced, i.e. $\hat{h}=\hat{c}T$ for $T\neq 0$. The evaluation of $\hat{c}$ can be conducted by the application of mean-value approach to the integration. Then, equation (2—22) can be solved by the application of bisection method and the successive over-relaxation method [63].

Review of reference [63] generates some considerations about the non-physical enthalpy method. Firstly, reference [63] considers the weighting function transport invariantly with the control volume Ω. However, further consideration needs to be taken for the weighting function transporting with the control volume Ω^+, where the derivative D^+W/D^+t is not

necessarily zero. Secondly, the mathematical derivation of non-physical enthalpy method is very clear. The equation required to be solved by finite element method is well established as equation (2—21). However, when considering the numerical aspect, the source $\left(-\int_{\Gamma_i} \right]\underline{q}\cdot(-\underline{n})\left[d\Gamma\right)$ is accounted for with a capacitance term, which more or less returns the method back to the CVCM. Thirdly, the bisection method is a simple and robust root finding method. However, this method requires that the root should be between the present value and predicted value. This criterion is not always guarantied in the solution procedure and the programme may fail to converge. Fourthly, the non-physical enthalpy method ignores the movement of material, i.e. the material velocity $\underline{v}=0$. For advection dominated problem, it will give rise to negative capacitance, and the influence of negative capacitance requires further study.

2.4 Advection/convection in solidification

Much research neglects the term of advection/convection. Advection is defined as the transport of property, such as enthalpy, by the motion of material. The motion can exist in both solid and liquid. Convection is defined as the transport of property by the fluid flow or the diffusion. Therefore, convection only exists in the liquid and not in the solid. However, the process of solidification does not only involve thermal conduction through solid phase and liquid phase, it also involves heat transfer due to the motion of material [78]. Advection is related to the velocity of material, which is present in the second term $\nabla\cdot\left(\rho h\underline{v}\right)$ in equation (2—1). This term may also relate to natural convection, which has both advection and diffusion. It is driven by the buoyancy forces [79-81]. Many solidification phenomena can be affected by the natural convection, such as macrosegregation, phase-interface stability, dendrite growth, etc. [82]. The solid phase has no natural convection, so only conductive heat transfer is considered in solid. But liquid material can flow, so the heat transfer of liquid is controlled by both diffusion and advection [83]. In other studies, such as ice in a stream, the solid is also moving with flowing water. In industry, squeeze casting and continuous casting, solid material is forced to move through a mould by the incoming liquid material, so, advection exists in both phases.

Advection brings the issue of instability to the numerical methods. Numerical oscillations [71-74] arise as a consequence of unstable modes associated with complex eigenvalue from large elemental Pecl ̀t numbers [84-86]. In order to resolve this problem, Courant *et al.*

introduced the upwind method to the hyperbolic PDEs [87]. This technique has been applied to numerical methods, such as in references [88-89]. The upwind method is popular for the FDM and FVM. With the FEM gaining popularity for fluid applications, the Petrov-Galerkin method and the least-squares methods have developed for enhancing the stability of the general Galerkin method. The Petrov-Galerkin is also an upwind method, which has been applied to the solidification [90-94]. Applications of the least-squared method can be found in references [95-100].

In the Petrov-Galerkin method, the weighting functions adopted in the Galerkin method are modified to weight the node from upwind element heavier than the node from the current element. The idea of least-squares method came from the field of probability and statistics, due to an interest in the establishment of a linear relationship between variables. In the normal weighted residual method, for an equation such as

$$v\frac{\partial T}{\partial x} = q \tag{2—23}$$

The residual $R(T,x) = v(\partial T/\partial x) - q$ goes to 0, which is identically zero for an exact solution but non-zero otherwise. The finite element equation is obtained by weighting equation over the domain of interest, i.e.

$$\int_{\Omega_e} WR(T,x)\, dV = 0 \tag{2—24}$$

where Ω_e is the domain of an element.

The difference between the least-squares method and the normal weighted residual method is that the weighting function is the derivative of residual instead of the shape functions, such as

$$W = \frac{\partial R(T,x)}{\partial T} \tag{2—25}$$

Assuming that T is the unknown field variable, the equation $\int_{\Omega_e}(\partial R(T,x)/\partial T)R(T,x)\, dV = 0$ tries to find the best T that minimizes the error.

Comparing the upwind method, the Petrov-Galerkin method and the least-squares method from the literature, it can be seen that, the classical upwind method suffers the problem of under-diffusion [101], though it is the simplest method to stabilise the numerical methods, and it can be easily applied to the FDM, FVM and FEM. The Petrov-Galerkin method is

applied to the FEM, where the weighting function is changed, which gives rise to assembled system matrices, which are slightly more complex than that involved in the standard Galerkin method. Once the matrices are created, however they can be used widely to solve a great many of problems. The approach overcomes the under-diffusion problem encounted in the classical finite element method. The least-squared method is less popular than the other two methods. The main drawback of this method is that, it gives rise to relatively complex system matrices. For first-order PDE [102], such as reduced wave equation [103], it is relatively easy to apply the least-squared method. However, for second order PDEs, such as steady state convection-diffusion heat transfer [104], the difficulty is significantly increased.

2.5 Summary

This chapter aimed to review previous research related to the study of the numerical methods for solidification. Solidification is a phase change problem, and the evaluation of latent heat of fusion is needed prior to the problem. If the method focuses on the condition of the phase interface through Stefan condition, such as the interface position and the interface velocity, then the method is categorized into the front tracking method. If the method attempts to deal with the latent heat of fusion, then it is categorized as an enthalpy method. In this chapter, deep review of two recent studies are provided, one is for the front tracking method and the other is for the enthalpy method. Voller [105] in 1990 listed some requirements for the methods. Over the last twenty years, the classical methods have been improved, while some new methods are developed. The front tracking methods are now able to deal with the multi-dimensional problems with complex geometry. This advance has been achieved with the dramatically advanced performance of computers. However, they are still difficult to be implemented into the existing computer codes because extra systems of equations are generated to track and update the condition of the phase front. It also makes the front tracking method not very computationally effective, although it is considered more accurate than enthalpy methods. Enthalpy methods have also been improved greatly, such as the control volume capacitance method. The modern enthalpy method inherits many advantages of the classical enthalpy method. It can be easily applied to the existing finite element method to deal with the multidimensional problems. Also, the simplicity of the enthalpy methods makes them more efficient than the front tracking method, and nowadays, they are able to provide results with desired accuracy.

Both methods however have some drawbacks. For example, the front tracking methods have to evaluate the Stefan condition, but the evaluation procedure is still problematic. And for the enthalpy method, good evaluation of liquid fraction and update techniques are still waiting to be developed. The enthalpy method is also weak when the phase front must be determined, such as the simulation of dendrite growth. What's more, for both methods, the advection/convection coupled problems are becoming hot topics.

In general, the author believes that the enthalpy methods have the advantages to deal with the solidification with advection/convection or other phenomena. This is due to the easy implementation into well-developed finite element methods. Scientists and engineers are able to focus more on the other aspects, such as advection, electro-magnetic effect, convection, etc. instead of putting much attention on dealing with complicated mathematics.

Chapter 3 The Theoretical Study on the Non-physical Enthalpy Method

3.1 General

The non-physical enthalpy method can be categorised as a fixed domain method. The term 'non-physical' means that, the enthalpy is not required to have any physical meaning, but it should still satisfy the mathematical laws related to the governing equations. This concept is developed from the effective capacitance method [39, 41] and the control volume capacitance method (CVCM) [66], and it was first introduced by Davey *et al* [62-63]. The non-physical method uses continuous but non-physical variables to replace the discontinuous physical variables. However, in this procedure, one or more source-like term will be generated, which can be difficult to implement with numerical methods. There are two reasons for the difficulties. Firstly, the non-physical jump is generated from the phase interface, however, in the fixed grid method, the phase interface is not tracked, and the non-physical jump has to be applied to the existing elements and nodes through approximations. Secondly, the non-physical jump is related to the latent heat energy which can be very large, and this may cause numerical temperature overflow during computation. The new non-physical variables are not unique because their definition is through transport equations, and they change if a different analysis type is applied. The method for the definition and the evaluation of non-physical enthalpy is still an open problem. This chapter starts from the study of the recently developed non-physical enthalpy method by Davey and Mondragon [62-63]. The analysis is conducted on the definition of non-physical enthalpy, which is provided in references [62-63]. This chapter adopts the same analysis as provided in references [62-63] for the non-weighted non-physical transport equation. As a matter of fact, it evolves four different velocities in the mathematical modelling. The material velocity $\underline{v}$ controls the motion of material which is for advection. The velocity $\underline{v}^*$ controls the shape and position of a control volume. It offers an opportunity to switch the transport equation between the Lagrangian description and the Eulerian description. The velocity $\underline{v}^+$ is used to describe the propagation of phase interface through the control volume Ω^+, which is moving with the phase interface. And the velocity $\underline{v}^\times$ is also for the phase interface but particularly

for the elemental control volume $\Omega^{\times}$. Unlike the analysis in references [62-63], a different analysis on the weighted non-physical transport equation is provided. This analysis considers a situation that, the weighting function can vary with time and space in the domain Ω^{+}, i.e. $D^{+}W/D^{+}t$ is non-zero. Moreover, a further study of the behaviour of non-physical source with prescribed temperature and various approximations of solid/liquid volume fraction is conducted. This study is aimed to examine the feasibility and capability of discontinuity isolation. Generally speaking, This chapter helps to achieve a better understanding of the idea of the non-physical enthalpy method.

3.2 The definition of non-physical enthalpy

A conservation law for enthalpy is of the form

$$\frac{D^{*}}{D^{*}t}\int_{\Omega}\ \rho h\, dV + \int_{\Gamma}\ \rho h\left(\underline{v}-\underline{v}^{*}\right)\cdot\underline{n}d\Gamma = -\int_{\Gamma}\ \underline{q}\cdot\underline{n}d\Gamma + \int_{\Omega}\ \rho Q\, dV \qquad (3—1)$$

where Ω is a control volume (CV) transported with velocity $\underline{v}^{*}$, the control surface Γ (CS) is the boundary of Ω, the vector $\underline{n}$ is the outward pointing unit normal to the boundary Γ, ρ is the density, h is the specific enthalpy, $\underline{q}$ is the heat flux and Q is the specific heat source [62-63]. The temporal derivative $D^{*}/D^{*}t$ outside the integration in the Equation (3—1) signifies the CV is moving, and its movement is governed by the velocity field $\underline{v}^{*}$. The velocity field $\underline{v}^{*}$ can be time and spatial dependent, i.e. $v^{*}(\boldsymbol{x},t)$, where $\boldsymbol{x}$ is the co-ordinates in the spatial reference system. The points $\boldsymbol{x}$ can be a function of vector $\boldsymbol{x}(\chi^{*},t)$, where a reference control volume Ω^{*} is regarded as a collection of points χ^{*}. The control volume Ω^{*} can change its shape due to the velocity v^{*}. Consequently, this velocity can be defined as $v^{*}(\boldsymbol{x}(\chi^{*},t),t) = D^{*}\boldsymbol{x}/D^{*}t = \partial\boldsymbol{x}(\chi^{*},t)/\partial t$, where $D^{*}/D^{*}t = \partial/\partial t + \underline{v}^{*}\cdot\nabla$ [62-63].

,Equations (3—1) can be transformed into more familiar forms by just letting $\underline{v}^{*} = \underline{v}$ if permitted or $\underline{v}^{*}\cdot\underline{n} = 0$, which is always permitted, so the Lagrangian and the Eulerian forms can be obtained as

$$\frac{D}{Dt}\int_{\Omega}\ \rho h\, dV = -\int_{\Gamma}\ \underline{q}\cdot\underline{n}d\Gamma + \int_{\Omega}\ \rho Q\, dV \qquad (3—2a)$$

and

$$\frac{\partial}{\partial t}\int_{\Omega}\ \rho h\, dV + \int_{\Gamma}\ \rho h\underline{v}\cdot\underline{n}d\Gamma = -\int_{\Gamma}\ \underline{q}\cdot\underline{n}d\Gamma + \int_{\Omega}\ \rho Q\, dV \qquad (3—2b)$$

The permission means that if the material velocity $\underline{v}$ is discontinuous in different phases due to material property difference, the relation $\underline{v}^* = \underline{v}$ cannot be set, because the domain velocity $\underline{v}^*$ is always considered as continuous. Setting $\underline{v}^* = \underline{0}$ is always permitted because zero is continuous and the problem becomes a fixed domain problem.

The Eulerian and Lagrangian descriptions of flow field can be understood as followed. If a field quantity, i.e. temperature T, is measured at two fixed computational points, and is vary with time. The change of this field quantity in a time period Δt can be described as $\Delta t(\partial T/\partial\, t) + \Delta\underline{v} \cdot \nabla T$, which is known as the Eulerian description of flow field. If the field quantity is measured at a material point, and this point is moving with the flow. The change of the field quantity in a time period Δt can be described as $\Delta t\left[\partial T/\partial\, t + \underline{v} \cdot \nabla T\right]$, which is known as the Lagrangian discerption of flow field. Both descriptions can be related by the identity that

$$\frac{D}{Dt} = \frac{\partial}{\partial t} + \underline{v} \cdot \nabla \tag{3—3}$$

where $\underline{v}$ is the material velocity field, $\nabla(\blacksquare) = \{\partial/\partial x\,, \partial/\partial y\,, \partial/\partial z\}$ is the gradient, and $\nabla \cdot (\blacksquare) = \partial/\partial x + \partial/\partial y + \partial/\partial z$ is the divergence. The Eulerian control volume is fixed. The heat change in the control volume is the difference between the heat flow in and the heat flow out. The Lagrangian control volume can change its shape. The material is tracked, and the shape changes because of the material velocity.

The non-physical enthalpy $\hat{h}$ is defined via the energy transport equation in references [62-63] as

$$\frac{D^*}{D^*t}\int_\Omega \hat{h}\, dV = \frac{D^*}{D^*t}\int_\Omega \rho h\, dV + \int_\Gamma \rho h\left(\underline{v} - \underline{v}^*\right) \cdot \underline{n} d\Gamma = -\int_\Gamma \underline{q} \cdot \underline{n} d\Gamma + \int_\Omega \rho Q\, dV \tag{3—4}$$

With this definition, the rate change of physical enthalpy and the change of advection/convection are accounted for by the rate change of non-physical enthalpy alone. The non-physical enthalpy is made continuous at a discontinuity and it gives rise to the possibility that a physical discontinuity can be represented by a continuous non-physical field on which a non-physical source is superimposed. The non-physical enthalpy method can be a fixed grid method by setting $\underline{v}^* = \underline{0}$, which means that, it can be easily implemented with existing finite-element programmes.

The sketch of the CV is depicted in Figure 3.1. The phase interface Γ_i separates the CV Ω into two phases, the solid phase Ω_s and the liquid phase Ω_l. When the material in the CV is solidifying, the interface Γ_i is propagating with the velocity $\underline{v}_i$. The symbols Γ_i^s and Γ_i^l denote the portions of the boundaries of the sub-domain Ω_s and Ω_l, which are alongside the phase interface, respectively. The vectors $\underline{n}_s$ and $\underline{n}_l$ are the outward pointing unit normal at Γ_i^s and Γ_i^l.

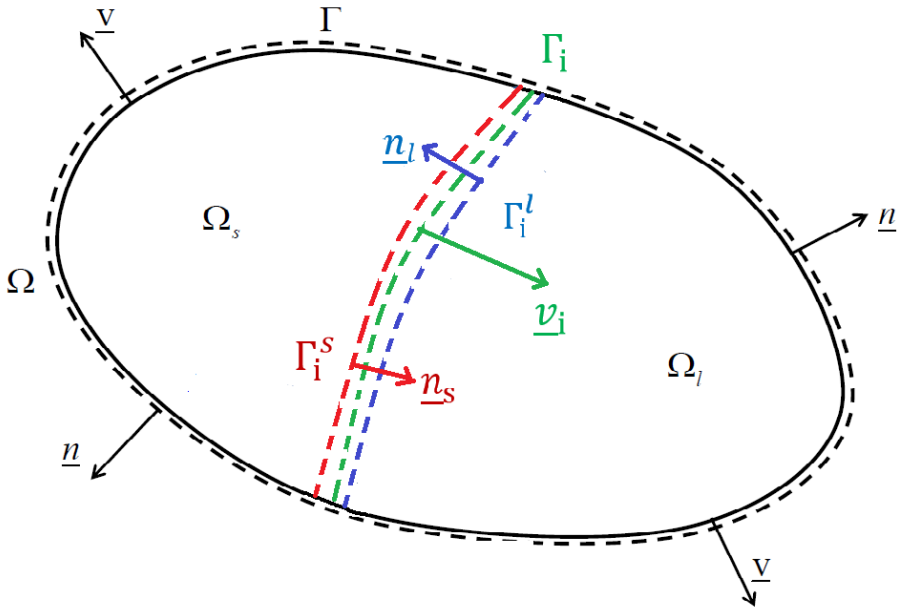

Figure 3.1: The control volume with phase change

Application of the Divergence theorem and the Reynold-type transport theorem to equation (3—4) gives

$$\frac{D^*}{D^*t}\hat{h} + \hat{h}\nabla\cdot\underline{v}^* = \frac{D^*h}{D^*t} + \rho\left(\underline{v}-\underline{v}^*\right)\nabla h = -\nabla\cdot\left(\underline{q}\right) + \rho Q \qquad (3—5)$$

The derivation of equation (3—5) from equation (3—4) can be found in the Appendix I—(b). It is readily apparent from equation (3—5) that the physical specific enthalpy h is not dependent on the velocity field $\underline{v}^*$, but the non-physical enthalpy $\hat{h}$ however is governed by the velocity $\underline{v}^*$. This is an important point as it highlights the non-physical nature of $\hat{h}$ being dependent on the analysis type.

Equation (3—4) cannot immediately be applied to find a relationship between the non-physical enthalpy $\hat{h}$ and the discontinuity embodied in the governing equation. This is because in equation (3—4), the condition of the discontinuous interface is not specified.

Thus, an analysis provided by Davey and Mondragon [62-63] is adopted here, which is to consider a new CV Ω^+ with particular features. The CV Ω^+ is transported with the phase interface, and its propagation is governed by a velocity field $\underline{v}^+$. As a consequence, the relationship $\underline{v}^+ \cdot \underline{n} = \underline{v}_i \cdot \underline{n}$ occurs at the interface boundary Γ_i. The transport equation with respect to the domain Ω^+ is

$$\frac{D^+}{D^+t}\int_{\Omega^+}\hat{h}\,dV + \int_{\Gamma^+}\hat{h}\left(\underline{v}^* - \underline{v}^+\right)\cdot\underline{n}d\Gamma = \frac{D^+}{D^+t}\int_{\Omega^+}\rho h\,dV + \int_{\Gamma^+}\rho h\left(\underline{v} - \underline{v}^+\right)\cdot\underline{n}d\Gamma = -\int_{\Gamma^+}\underline{q}\cdot\underline{n}d\Gamma + \int_{\Omega^+}\rho Q\,dV \quad (3—6)$$

where the boundary integral on the left hand side (LHS) of equation (3—6) is required to ensure $\hat{h}$ is identical to that found in equations (3—4) and (3—5). Equation (3—6) also ensures that the non-physical enthalpy $\hat{h}$ is independent on the velocity $\underline{v}^+$. Moreover, applying the Reynold transport theorem and the divergence theorem to the LHS term of equation (3—6) gives

$$\frac{D^+}{D^+t}\int_{\Omega^+}\hat{h}\,dV + \int_{\Gamma^+}\hat{h}\left(\underline{v}^* - \underline{v}^+\right)\cdot\underline{n}d\Gamma = \int_{\Omega^+}\frac{D^+}{D^+t}\hat{h} + \hat{h}\nabla\cdot\underline{v}^+ + \nabla\cdot\left(\hat{h}\left(\underline{v}^* - \underline{v}^+\right)\right)dV \quad (3—7)$$

Then, by the product rule of differentiation, it gives

$$\int_{\Omega^+}\frac{D^+}{D^+t}\hat{h} + \hat{h}\nabla\cdot\underline{v}^+ + \nabla\cdot\left(\hat{h}\left(\underline{v}^* - \underline{v}^+\right)\right)dV = \int_{\Omega^+}\frac{\partial}{\partial t}\hat{h} + \nabla\cdot(\hat{h}\underline{v}^+) + \nabla\cdot\left(\hat{h}\left(\underline{v}^* - \underline{v}^+\right)\right)dV \quad (3—8)$$

The velocity $\underline{v}^+$ is cancelled, then

$$\int_{\Omega^+}\frac{\partial}{\partial t}\hat{h} + \nabla\cdot(\hat{h}\underline{v}^+) + \nabla\cdot\left(\hat{h}\left(\underline{v}^* - \underline{v}^+\right)\right)dV = \int_{\Omega^+}\frac{\partial}{\partial t}\hat{h} + \nabla\cdot\left(\hat{h}\underline{v}^*\right)dV \quad (3—9)$$

Equation (3—9) proves that in the CV Ω^+, $D^+\left(\int_{\Omega^+}\hat{h}\,dV\right)/D^+t + \int_{\Gamma^+}\hat{h}\left(\underline{v}^* - \underline{v}^+\right)\cdot\underline{n}d\Gamma = D^*\left(\int_{\Omega^+}\hat{h}\,dV\right)/D^*t$, which is the LHS term of equation (3—4). The corresponding strong form (PDE) is

$$\frac{\partial\hat{h}}{\partial t} + \rho\left(\underline{v}^* - \underline{v}^+\right)\cdot\nabla\hat{h} = \rho\frac{D^+h}{D^+t} + \rho\left(\underline{v} - \underline{v}^+\right)\cdot\nabla(h) = -\nabla\cdot\underline{q} + \rho Q \quad (3—10)$$

From the previous section, the non-physical term is forced to be continuous at the phase interface, that is to say $\left]\hat{h}\underline{n}\right[= \hat{h}_l\underline{n}_l + \hat{h}_s\underline{n}_s = (\hat{h}_l - \hat{h}_s)\underline{n}_l = 0$, so the discontinuity is accounted for by the non-physical source $\hat{h}'$. This source term however facilitates the isolation of any discontinuity from the LHS of equation (3—4). So it is necessary to apply equation (3—6) to each sub-domain gives three transport equations which are

$$\frac{D^+}{D^+t}\int_{\Omega_i}\hat{h}\,dV + \int_{\Gamma-\Gamma_i^s-\Gamma_i^l}\hat{h}\left(\underline{v}^* - \underline{v}^+\right)\cdot\underline{n}d\Gamma + \int_{\Gamma_i^s}\hat{h}\left(\underline{v}^* - \underline{v}^+\right)\cdot\left(-\underline{n}\right)d\Gamma + \int_{\Gamma_i^l}\hat{h}\left(\underline{v}^* - \underline{v}^+\right)\cdot\left(-\underline{n}\right)d\Gamma = \frac{D^+}{D^+t}\int_{\Omega_i}\rho h\,dV + \int_{\Gamma-\Gamma_i^s-\Gamma_i^l}\rho h\left(\underline{v} - \underline{v}^+\right)\cdot\underline{n}d\Gamma + \int_{\Gamma_i^s}\rho h\left(\underline{v} - \underline{v}^+\right)\cdot\left(-\underline{n}\right)d\Gamma + \int_{\Gamma_i^l}\rho h\left(\underline{v} - \underline{v}^+\right)\cdot\left(-\underline{n}\right)d\Gamma = -\int_{\Gamma-\Gamma_i^s-\Gamma_i^l}\underline{q}\cdot\underline{n}d\Gamma - \int_{\Gamma_i^s}\underline{q}\cdot\left(-\underline{n}\right)d\Gamma - \int_{\Gamma_i^l}\underline{q}\cdot\left(-\underline{n}\right)d\Gamma + \int_{\Omega_i}\rho Q\,dV \tag{3—11a}$$

$$\frac{D^+}{D^+t}\int_{\Omega_l}\hat{h}\,dV + \int_{\Gamma_l}\hat{h}\left(\underline{v}^* - \underline{v}^+\right)\cdot\underline{n}d\Gamma + \int_{\Gamma_i^l}\hat{h}\left(\underline{v}^* - \underline{v}^+\right)\cdot\underline{n}d\Gamma = \frac{D^+}{D^+t}\int_{\Omega_l}\rho h\,dV + \int_{\Gamma_l}\rho h\left(\underline{v} - \underline{v}^+\right)\cdot\underline{n}d\Gamma + \int_{\Gamma_i^l}\rho h\left(\underline{v} - \underline{v}^+\right)\cdot\underline{n}d\Gamma = -\int_{\Gamma_l}\underline{q}\cdot\underline{n}d\Gamma - \int_{\Gamma_i^l}\underline{q}\cdot\underline{n}d\Gamma + \int_{\Omega_l}\rho Q \tag{3—11b}$$

and

$$\frac{D^+}{D^+t}\int_{\Omega_s}\hat{h}\,dV + \int_{\Gamma_s}\hat{h}\left(\underline{v}^* - \underline{v}^+\right)\cdot\underline{n}d\Gamma + \int_{\Gamma_i^s}\hat{h}\left(\underline{v}^* - \underline{v}^+\right)\cdot\underline{n}d\Gamma = \frac{D^+}{D^+t}\int_{\Omega_s}\rho h\,dV + \int_{\Gamma_s}\rho h\left(\underline{v} - \underline{v}^+\right)\cdot\underline{n}d\Gamma + \int_{\Gamma_i^s}\rho h\left(\underline{v} - \underline{v}^+\right)\cdot\underline{n}d\Gamma = -\int_{\Gamma_s}\underline{q}\cdot\underline{n}d\Gamma - \int_{\Gamma_i^s}\underline{q}\cdot\underline{n}d\Gamma + \int_{\Omega_s}\rho Q\,dV \tag{3—11c}$$

where $\Omega^+ = \Omega_i \cup \Omega_s \cup \Omega_l,\ \partial\Omega_s = \Gamma_s \cup \Gamma_i^s,\ \partial\Omega_l = \Gamma_l \cup \Gamma_i^l$.

A jump-like non-physical source term $\hat{h}'$ can be gained either by shrinking the Ω_i down, that is to say, $vol(\Omega_i) \to 0$ with $\Gamma_i \subset \Omega_i$, or by subtracting equations (3—11b) and (3—11c) from the equation (3—6). And the definition of $\hat{h}'$ is

$$\frac{D^+}{D^+t}\int_{\Gamma_i}\hat{h}'\,d\Gamma + \int_{\Sigma_i}\hat{h}'\left(\underline{v}^* - \underline{v}^+\right)\cdot\underline{t}\underline{n}d\Sigma + \int_{\Gamma_i}\left]\hat{h}\left(\underline{v}^* - \underline{v}^+\right)\cdot\left(-\underline{n}\right)\right[d\Gamma = \int_{\Gamma_i}\left]\rho h\left(\underline{v} - \underline{v}^+\right)\cdot\left(-\underline{n}\right)\right[d\Gamma = -\int_{\Gamma_i}\left]\underline{q}\cdot\left(-\underline{n}\right)\right[d\Gamma \tag{3—12}$$

where the bracket]■[signifies a jump term, Σ_i is the boundary of Γ_i, and $\underline{tn}$ is the outward pointing unit normal in the tangent plane of the Γ_i on the curve Σ_i. A sketch of $\underline{tn}$ is shown in the Figure 3.2. The vector $\underline{tn}$ indicates that the phase interface Γ_i may shrink or expand in the direction of $\underline{tn}$ to accommodate the shape of the external boundary Γ_i.

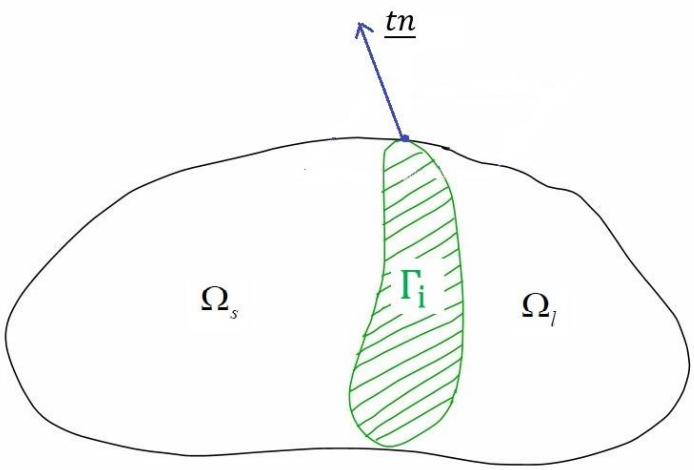

Figure 3.2: The tangent unit outward normal $\underline{tn}$

Equation (3—12) can be obtained either by letting the Ω_i shrinks down to a volume with infinitesimal thickness which is shown in equation (3—11a), or by summing equations (3—11b) and (3—11c), then compare with equation (3—6). All values are related to the volume, such as $\int_{\Gamma_i} \rho h \, d\Gamma$, because Γ_i in equation (3—12) has an infinitesimal thickness. Assuming that no additional heat is applied to the system at Γ_i, which gives $\int_{\Gamma_i} \rho Q \, d\Gamma = 0$. The non-physical enthalpy is considered to be continuous at the interface boundary Γ_i, thus the third term on the LHS of equation (3—12) has to be 0, i.e. $\int_{\Gamma_i}]\hat{h}(\underline{v}^* - \underline{v}^+) \cdot (-\underline{n})[d\Gamma = 0$. For fixed grid mesh, i.e. $\underline{v}^* = 0$.

3.3 Removal of the non-physical source term

In section 3.2, the non-physical source $\hat{h}'$ is defined through the transport equation. The sources equation is established for the isolation of discontinuity from the transport equation. A schematic sketch of the relationship between non-physical enthalpy $\hat{h}$ and non-physical source$\hat{h}'$ is depicted in Figure 2.5 (a). The isolation of discontinuity is achieved by noting that the relationship between the two transporting control volumes is

$$\frac{D^*}{D^*t}\int_\Omega \hat{h}\,dV = \frac{D^+}{D^+t}\int_\Omega \hat{h}\,dV + \int_\Gamma \hat{h}\left(\underline{v}^* - \underline{v}^+\right)\cdot\underline{n}d\Gamma \quad (3—13)$$

where $\underline{v}^* \cdot \underline{n} = \underline{v}^+ \cdot \underline{n}$ on Γ.

Thus, discontinuity exclusion for equation (3—5) can be achieved by

$$\frac{D^*}{D^*t}\int_{\Omega\backslash\Gamma_i}\hat{h}\,dV = \frac{D^+}{D^+t}\int_\Omega \hat{h}\,dV + \int_\Gamma \hat{h}\left(\underline{v}^* - \underline{v}^+\right)\cdot\underline{n}d\Gamma - \left(\frac{D^+}{D^+t}\int_{\Gamma_i}\hat{h}'\,d\Gamma + \int_{\Sigma_i}\hat{h}'\left(\underline{v}^* - \underline{v}^+\right)\cdot \underline{tn}d\Sigma\right) = -\int_\Gamma \underline{q}\cdot\underline{n}d\Gamma + \int_\Omega \rho Q\,dV - \left(\frac{D^+}{D^+t}\int_{\Gamma_i}\hat{h}'\,d\Gamma + \int_{\Sigma_i}\hat{h}'\left(\underline{v}^* - \underline{v}^+\right)\cdot\underline{tn}d\Sigma\right) \quad (3—14)$$

where the notation $\Omega\backslash\Gamma_i$ means that the boundary Γ_i is excluded from Ω. The term $D^+\left(\int_{\Gamma_i}\hat{h}'\,d\Gamma\right)/D^+t$ is correspond to the discontinuous interface of the CV integral $D^+\left(\int_\Omega \hat{h}\,dV\right)/D^+t$, and the term $\int_{\Sigma_i}\hat{h}'\left(\underline{v}^* - \underline{v}^+\right)\cdot\underline{tn}d\Sigma$ is corresponds to the discontinuous boundary of the CS integral $\int_\Gamma \hat{h}\left(\underline{v}^* - \underline{v}^+\right)\cdot\underline{n}d\Gamma$.

Substituting equation (3—12) into equations (3—14) gives

$$\frac{D^*}{D^*t}\int_{\Omega\backslash\Gamma_i}\hat{h}\,dV = \frac{D^*}{D^*t}\int_\Omega \rho h\,dV + \int_\Gamma \rho h\left(\underline{v} - \underline{v}^*\right)\cdot\underline{n}d\Gamma - \left(\int_{\Gamma_i}\right]\rho h\left(\underline{v} - \underline{v}^+\right)\cdot\left(-\underline{n}\right)\left[d\Gamma\right) = -\int_\Gamma \underline{q}\cdot\underline{n}d\Gamma + \int_\Omega \rho Q\,dV - \left(-\int_{\Gamma_i}\right]\underline{q}\cdot\left(-\underline{n}\right)\left[\,d\Gamma\right) \quad (3—15)$$

For the convenience of solution, equation (3—15) can be divided into two equations, which are

$$\frac{D^*}{D^*t}\int_{\Omega\backslash\Gamma_i}\hat{h}\,dV = \frac{D^*}{D^*t}\int_\Omega \rho h\,dV + \int_\Gamma \rho h\left(\underline{v} - \underline{v}^*\right)\cdot\underline{n}d\Gamma - \left(\int_{\Gamma_i}\right]\rho h\left(\underline{v} - \underline{v}^+\right)\cdot\left(-\underline{n}\right)\left[d\Gamma\right) \quad (3—16)$$

and

$$\frac{D^*}{D^*t}\int_{\Omega\backslash\Gamma_i}\hat{h}\,dV = -\int_\Gamma \underline{q}\cdot\underline{n}d\Gamma + \int_\Omega \rho Q\,dV - \left(-\int_{\Gamma_i}\right]\underline{q}\cdot\left(-\underline{n}\right)\left[\,d\Gamma\right) \quad (3—17)$$

The evaluation of non-physical enthalpy $\hat{h}$ can in principle be achieved via equation (3—16), which provides the relationship between the non-physical and physical enthalpy. Equation (3—17) can in principle be discretised and solved by numerical methods. On the LHS of this equation, the term is absent of any discontinuity. But the price is that, on the RHS of the equation, two extra terms have been generated through the discontinuity removal

procedure. The terms are non-linear and have the potential to cause problems for any numerical method. How to incorporate these terms into a numerical method needs to be further investigated.

3.4 The weighted non-physical governing equations

Equation (3—17) can be solved by the finite element method. To derive a finite element system, the weighted-residual approach is adopted, which is able to generate the characteristic matrices and vectors directly from the governing transport equations. And the Galerkin method is applied for the spatial discretization [108-112]. Unlike the recent non-physical enthalpy method, this section aims to analysis the weighted transport equation and the discontinuity isolation by considering a situation that (D^+W/D^+t) is non-zero. This new analysis avoid the consideration of the strong form of source equation.

The weighted form of equation (3—4) is given as

$$\frac{D^*}{D^*t}\int_\Omega W\hat{h}\,dV = \frac{D^*}{D^*t}\int_\Omega W\rho h\,dV + \int_\Gamma W\rho h(\underline{v}-\underline{v}^*)\cdot\underline{n}d\Gamma - \int_\Omega \rho h(\underline{v}-\underline{v}^*)\cdot\nabla W\,dV =$$
$$-\int_\Gamma W\underline{q}\cdot\underline{n}d\Gamma - \int_\Omega \underline{q}\cdot\nabla W d\Gamma + \int_\Omega \rho Q\,dV \qquad (3—18)$$

where W is the weighting function which in the first instance is assumed smooth or at least continuous up to the first derivative i.e., is in $C^1(\Omega)$. It is also transported invariantly with the domain Ω, i.e. $D^*W/D^*t = 0$.

Similarly, the weighted transport governing equation (3—6) for the domain Ω^+ is

$$\frac{D^+}{D^+t}\int_{\Omega^+} W\hat{h}\,dV - \int_{\Omega^+}\left(\frac{D^+W}{D^+t}\right)\hat{h}\,dV + \int_{\Gamma^+} W\hat{h}(\underline{v}^*-\underline{v}^+)\cdot\underline{n}d\Gamma - \int_{\Omega^+}\hat{h}(\underline{v}^*-\underline{v}^+)\cdot$$
$$\nabla W\,dV = \frac{D^+}{D^+t}\int_{\Omega^+}\rho h\,dV - \int_{\Omega^+}\left(\frac{D^+W}{D^+t}\right)\rho h\,dV + \int_{\Gamma^+} W\rho h(\underline{v}-\underline{v}^+)\cdot\underline{n}d\Gamma - \int_{\Omega^+}\rho h(\underline{v}-$$
$$\underline{v}^+)\cdot\nabla W\,dV = -\int_{\Gamma^+} W\underline{q}\cdot\underline{n}d\Gamma + \int_{\Omega^+}\underline{q}\cdot\nabla W\,dV + \int_{\Omega^+} W\rho Q\,dV \qquad (3—19)$$

The assumptions made for the weighting function W in the domain Ω apply to the domain Ω^+, but to accommodate for the possibility that $D^+W/D^+t \neq 0$ the terms $\int_{\Omega^+}(D^+W/D^+t)\hat{h}\,dV$ and $\int_{\Omega^+}(D^+W/D^+t)\rho h\,dV$ are required in equation (3—19).

The two derivatives involved for the weighting function are related by the identity

$$\frac{D^+W}{D^+t} = \frac{D^*W}{D^*t} + \left(\underline{v}^+ - \underline{v}^*\right)\cdot\nabla W = \left(\underline{v}^+ - \underline{v}^*\right)\cdot\nabla W \qquad (3—20)$$

where simplification arises because $D^*W/D^*t = 0$ as mentioned previously.

Substitution of equation (3—20) into equation (3—19) gives

$$\frac{D^+}{D^+t}\int_{\Omega^+} W\hat{h}\,dV - \int_{\Omega^+}\hat{h}\left(\underline{v}^+ - \underline{v}^*\right)\cdot\nabla W\,dV + \int_{\Gamma^+} W\hat{h}\left(\underline{v}^* - \underline{v}^+\right)\cdot\underline{n}d\Gamma - \int_{\Omega^+}\hat{h}\left(\underline{v}^* - \underline{v}^+\right)\cdot$$
$$\nabla W\,dV = \frac{D^+}{D^+t}\int_{\Omega^+}\rho h\,dV - \int_{\Omega^+}\rho h\left(\underline{v}^+ - \underline{v}^*\right)\cdot\nabla W\,dV + \int_{\Gamma^+} W\rho h\left(\underline{v} - \underline{v}^+\right)\cdot\underline{n}d\Gamma -$$
$$\int_{\Omega^+}\rho h\left(\underline{v} - \underline{v}^+\right)\cdot\nabla W\,dV = -\int_{\Gamma^+} W\underline{q}\cdot\underline{n}d\Gamma + \int_{\Omega^+}\underline{q}\cdot\nabla W\,dV + \int_{\Omega^+} W\rho Q\,dV \qquad (3—21)$$

which reduces to

$$\frac{D^+}{D^+t}\int_{\Omega^+} W\hat{h}\,dV + \int_{\Gamma^+} W\hat{h}\left(\underline{v}^* - \underline{v}^+\right)\cdot\underline{n}d\Gamma = \frac{D^+}{D^+t}\int_{\Omega^+}\rho h\,dV + \int_{\Gamma^+} W\rho h\left(\underline{v} - \underline{v}^+\right)\cdot\underline{n}d\Gamma -$$
$$\int_{\Omega^+}\rho h\left(\underline{v} - \underline{v}^*\right)\cdot\nabla W\,dV = -\int_{\Gamma^+} W\underline{q}\cdot\underline{n}d\Gamma + \int_{\Omega^+}\underline{q}\cdot\nabla W\,dV + \int_{\Omega^+} W\rho Q\,dV \qquad (3—22)$$

Consider again, applying the weighted transport equation (3—22) to a CV Ω_i which encloses to the phase interface Γ_i, to give

$$\frac{D^+}{D^+t}\int_{\Omega_i} W\hat{h}\,dV + \int_{\Gamma-\Gamma_i^s-\Gamma_i^l} W\hat{h}\left(\underline{v}^* - \underline{v}^+\right)\cdot\underline{n}d\Gamma + \int_{\Gamma_i^s} W\hat{h}\left(\underline{v}^* - \underline{v}^+\right)\cdot\left(-\underline{n}\right)d\Gamma +$$
$$\int_{\Gamma_i^l} W\hat{h}\left(\underline{v}^* - \underline{v}^+\right)\cdot\left(-\underline{n}\right)d\Gamma = \frac{D^+}{D^+t}\int_{\Omega_i} W\rho h\,dV + \int_{\Gamma-\Gamma_i^s-\Gamma_i^l} W\rho h\left(\underline{v} - \underline{v}^+\right)\cdot\underline{n}d\Gamma +$$
$$\int_{\Gamma_i^s} W\rho h\left(\underline{v} - \underline{v}^+\right)\cdot\left(-\underline{n}\right)d\Gamma + \int_{\Gamma_i^l} W\rho h\left(\underline{v} - \underline{v}^+\right)\cdot\left(-\underline{n}\right)d\Gamma - \int_{\Omega_i}\rho h\left(\underline{v} - \underline{v}^*\right)\cdot\nabla W\,dV =$$
$$-\int_{\Gamma-\Gamma_i^s-\Gamma_i^l} W\underline{q}\cdot\underline{n}d\Gamma - \int_{\Gamma_i^s} W\underline{q}\cdot\left(-\underline{n}\right)d\Gamma - \int_{\Gamma_i^l} W\underline{q}\cdot\left(-\underline{n}\right)d\Gamma + \int_{\Omega_i}\underline{q}\cdot\nabla W\,dV +$$
$$\int_{\Omega_i} W\rho Q\,dV \qquad (3—23)$$

In the limit $vol(\Omega_i)\to 0$ with $\Gamma_i \subset \Omega_i$, equation (3—23) shrinks to

$$\frac{D^+}{D^+t}\int_{\Gamma_i} W\hat{h}'\,d\Gamma + \int_{\Sigma_i} W\hat{h}'\left(\underline{v}^* - \underline{v}^+\right)\cdot\underline{t}\underline{n}d\Sigma = \int_{\Gamma_i}\rbrack\rho h\left(\underline{v} - \underline{v}^+\right)\cdot\left(-\underline{n}\right)\lbrack d\Gamma -$$
$$\lim_{vol(\Omega_i)\to 0}\int_{\Omega_i}\rho h\left(\underline{v} - \underline{v}^*\right)\cdot\nabla W\,dV = -\int_{\Gamma_i}\left\rbrack\underline{q}\cdot\left(-\underline{n}\right)\right\lbrack d\Gamma + \lim_{vol(\Omega_i)\to 0}\int_{\Omega_i}\underline{q}\cdot\nabla W\,dV \qquad (3—24)$$

However, the direct weighting of equation (3—12) provides

$$\frac{D^+}{D^+t}\int_{\Gamma_i} W\hat{h}'\,d\Gamma - \int_{\Gamma_i}\hat{h}'\left(\underline{v}^+ - \underline{v}^*\right)\cdot\nabla W d\Gamma + \int_{\Sigma_i} W\hat{h}'\left(\underline{v}^* - \underline{v}^+\right)\cdot\underline{t}\underline{n}d\Sigma - \int_{\Gamma_i}\hat{h}'\left(\underline{v}^* -$$
$$\underline{v}^+\right)_T\cdot\nabla_{\Gamma_i} W d\Gamma = \int_{\Gamma_i} W\rbrack\rho h\left(\underline{v} - \underline{v}^+\right)\cdot\left(-\underline{n}\right)\lbrack d\Gamma = -\int_{\Gamma_i} W\left\rbrack\underline{q}\cdot\left(-\underline{n}\right)\right\lbrack d\Gamma \qquad (3—25)$$

where the subscript T denotes the tangential component of velocities.

Substitution of equation (3—24) into equation (3—25) gives

$$\frac{D^+}{D^+t}\int_{\Gamma_i} W\hat{h}'\,d\Gamma + \int_{\Sigma_i} W\hat{h}'(\underline{v}^* - \underline{v}^+)\cdot \underline{tn}\,d\Sigma + \int_{\Gamma_i} \hat{h}'(\underline{v}^* - \underline{v}^+)_N \cdot \nabla_{\Gamma_i} W d\Gamma =$$
$$\int_{\Gamma_i} W\rho h(\underline{v} - \underline{v}^+)\cdot(-\underline{n})\big[d\Gamma = -\int_{\Gamma_i} W\,\big]\underline{q}\cdot(-\underline{n})\big[\,d\Gamma \qquad (3—26)$$

where the subscript N denotes the normal component of velocities. The relationship between the tangential component and normal component of velocities is depicted in Figure 3.3.

Comparison between equations (3—25) and (3—26) indicates that

$$\int_{\Gamma_i} \hat{h}'(\underline{v}^* - \underline{v}^+)_N \cdot \nabla_{\Gamma_i} W d\Gamma = \lim_{vol(\Omega_i)\to 0}\int_{\Omega_i} \rho h(\underline{v} - \underline{v}^*)\cdot\nabla W\,dV = -\lim_{vol(\Omega_i)\to 0}\int_{\Omega_i} \underline{q}\cdot$$
$$\nabla W\,dV \qquad (3—27)$$

where it is recognised that the limits in Equation (3—27) are ill-defined as a consequence of discontinuities at Γ_i.

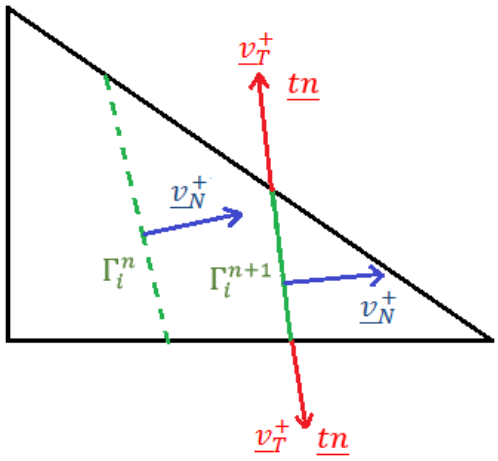

Figure 3.3: Discontinuity front moving in a finite element CV

The LHS of equation (3—24) reveals that the source terms are present in the LHS of equation (3—18). The source terms can be removed by subtracting equation (3—24) from equation (3—18), i.e.

$$\frac{D^*}{D^*t}\int_{\Omega\setminus\Gamma_i} W\hat{h}\,dV = \frac{D^*}{D^*t}\int_{\Omega}\ W\rho h\,dV + \int_{\Gamma}\ W\rho h\left(\underline{v}-\underline{v}^*\right)\cdot\underline{n}d\Gamma - \int_{\Gamma_i} W\Big]\rho h\left(\underline{v}-\underline{v}^+\right)\cdot$$
$$\left(-\underline{n}\right)\Big[d\Gamma - \int_{\Omega}\ \rho h\left(\underline{v}-\underline{v}^*\right)\cdot\nabla W\,dV + \int_{\Gamma_i}\ \hat{h}'\left(\underline{v}^*-\underline{v}^+\right)_N\ \cdot\nabla_{\Gamma_i} W d\Gamma = -\int_{\Gamma}\ W\underline{q}\cdot\underline{n}d\Gamma -$$
$$-\int_{\Gamma_i} W\Big]\underline{q}\cdot\left(-\underline{n}\right)\Big[\,d\Gamma - \int_{\Omega}\ \underline{q}\cdot\nabla W dV + \int_{\Gamma_i}\ \hat{h}'\left(\underline{v}^*-\underline{v}^+\right)_N\ \cdot\nabla_{\Gamma_i} W d\Gamma + \int_{\Omega}\ \rho Q\,dV \tag{3—28}$$

Equation (3—28) can be split into two equations, which are

$$\frac{D^*}{D^*t}\int_{\Omega\setminus\Gamma_i} W\hat{h}\,dV = \frac{D^*}{D^*t}\int_{\Omega}\ W\rho h\,dV + \int_{\Gamma}\ W\rho h\left(\underline{v}-\underline{v}^*\right)\cdot\underline{n}d\Gamma - \int_{\Gamma_i} W\Big]\rho h\left(\underline{v}-\underline{v}^+\right)\cdot$$
$$\left(-\underline{n}\right)\Big[d\Gamma - \int_{\Omega\setminus\Gamma_i}\rho h\left(\underline{v}-\underline{v}^*\right)\cdot\nabla W\,dV \tag{3—29}$$

and

$$\frac{D^*}{D^*t}\int_{\Omega\setminus\Gamma_i} W\hat{h}\,dV = -\int_{\Gamma}\ W\underline{q}\cdot\underline{n}d\Gamma - \Big(-\int_{\Gamma_i} W\Big]\underline{q}\cdot\left(-\underline{n}\right)\Big[\,d\Gamma\Big) - \int_{\Omega\setminus\Gamma_i}\underline{q}\cdot\nabla W dV +$$
$$\int_{\Omega}\ \rho Q\,dV \tag{3—30}$$

Equation (3—29) is the linkage equation which relates the non-physical enthalpy and the physical enthalpy, equation (3—30) is the weighted non-physical governing equation which requires to be solved by numerical methods. In equations (3—29) and (3—30), the terms $\int_{\Omega}\ \rho h\left(\underline{v}-\underline{v}^*\right)\cdot\nabla W\,dV$ and $\int_{\Omega}\ \underline{q}\cdot\nabla W dV$ also contain sources. According to equation (3—27), sources contained in both terms cancel with the term $\int_{\Gamma_i}\ \hat{h}'\left(\underline{v}^*-\underline{v}^+\right)_N\ \cdot\nabla_{\Gamma_i} W d\Gamma$.

3.5 The evaluation of each term in the finite element equations

3.5.1 Implementation of non-physical enthalpy method in the FEM

In the Galerkin method, the trial solution functions are assumed to be the elemental shape functions, and the unknown constants are regarded as the nodal degree of freedoms. A brief derivation of Galerkin weighted residual method can be seen in Appendix I—(c). The weighting functions are also shape functions in accordance with the Galerkin approach and consequently equation (3—30) can be rewritten as

$$\frac{D^*}{D^*t}\int_{\Omega_e\backslash\Gamma_i^e} N_\vartheta \tilde{h}_e \, dV = -\int_{\Gamma_e} N_\vartheta \underline{q}\cdot\underline{n} d\Gamma + \int_{\Omega_e} \underline{q}\cdot\nabla N_\vartheta d\Gamma + \int_{\Omega_e\backslash\Gamma_i^e} N_\vartheta \rho Q \, dV - \left(-\int_{\Gamma_i} N_\vartheta \left]\underline{q}\cdot\right.\right.$$
$$\left.\left.(-\underline{n})\right[d\Gamma\right) \quad (3—31)$$

where the subscript e denotes that this is in an elemental domain, and the ϑ refers to the number of simultaneous algebraic equations of an element. In references [62-63], the term $-\int_{\Gamma_i} N_\vartheta \left]\underline{q}\cdot(-\underline{n})\right[d\Gamma$ is accounted for as a source. The behaviour of this term as a source in the finite element system of equations requires to be studied. This is one of the objective of this chapter.

The corresponding approximate solution with respect to non-physical enthalpy is

$$\tilde{h}_e = \sum_{\varsigma=1}^{NN} N_\varsigma \hat{h}_\varsigma \quad (3—32)$$

where $\tilde{h}_e$ refers to the trial solution with respect to the element, and the upper-case letters NN refers to the local number of the element node.

The weighting function of the linkage equation (3—29) can be different to the governing equation (3—31), as the linkage equation can only be solved analytically. As a matter of fact, the weighing function for equation (3—29) is set to be 1, thus equation (3—29) reduces to

$$\frac{D^*}{D^*t}\int_{\Omega_e\backslash\Gamma_i^e} \hat{h}\, dV = \frac{D^*}{D^*t}\int_{\Omega_e} \rho h \, dV + \int_{\Gamma_e} \rho h\left(\underline{v}-\underline{v}^*\right)\cdot\underline{n} d\Gamma - \int_{\Gamma_i^e}\left]\rho h\left(\underline{v}-\underline{v}^{\times}\right)\cdot(-\underline{n})\right[d\Gamma$$

(3—33)

where the subscript/superscript e and a different velocity $\underline{v}^{\times}$ indicate that equation (3—33) is for an element domain. The velocity $\underline{v}^{\times}$ is similar to the velocity $\underline{v}^{+}$. The difference between them is that, the velocity $\underline{v}^{+}$ transports the propagation of the phase interface through arbitrary CV, but the velocity $\underline{v}^{\times}$ transports the interface in a finite elemental CV. In references [62-63], the material velocity $\underline{v}$ is set to be zero. The influence of non-zero material velocity to the change of non-physical capacitance needs to be further examined.

3.5.2 General simplifications

The non-uniqueness of the $\hat{h}$ is apparent from its definition. Through the definition of the non-physical enthalpy, extra terms have to be generated. These new terms require mathematical evaluation. Then the final solution (nodal temperatures) can be computed by the numerical method, such as the finite element method. The evaluation of the $\hat{h}$ can be

achieved via equation (3—33) in the last section, and the evaluation of the $\hat{h}'$ should be conducted via equation (3—12), but it is not necessary because the jump will be evaluated through the term $\int_{\Gamma_i^e} N_\vartheta]\rho h(\underline{v}-\underline{v}^\times)\cdot(-\underline{n})[d\Gamma$ directly in an element. Prior to solving equation (3—33), it is prudent to establish a direct mathematical relationship between the non-physical enthalpy $\hat{h}$ and the temperature T. The simplest approach is to set

$$\hat{h}=\hat{c}T \tag{3—34}$$

which is well defined for $T\neq 0$.

Substitution of equation (3—34) into equation (3—33) gives

$$\frac{D^*}{D^*t}\int_{\Omega_e\setminus\Gamma_i^e}\hat{c}T\,dV=\frac{D^*}{D^*t}\int_{\Omega_e}\rho h\,dV+\int_{\Gamma_e}\rho h(\underline{v}-\underline{v}^*)\cdot\underline{n}d\Gamma-\int_{\Gamma_i^e}]\rho h(\underline{v}-\underline{v}^\times)\cdot(-\underline{n})[d\Gamma \tag{3—35}$$

The easiest way to simplify equation (3—35) is to set the domain velocity $\underline{v}^*=0$, which is always permitted as mentioned before. And the mesh becomes a fixed grid. Equation (3—35) is rewritten as

$$\frac{\partial}{\partial t}\int_{\Omega_e\setminus\Gamma_i^e}\hat{c}T\,dV=\frac{\partial}{\partial t}\int_{\Omega_e}\rho h\,dV+\int_{\Gamma_e}\rho h\underline{v}\cdot\underline{n}d\Gamma-\int_{\Gamma_i^e}]\rho h(\underline{v}-\underline{v}^\times)\cdot(-\underline{n})[d\Gamma \tag{3—36}$$

The velocity $\underline{v}^\times$ presented indicates that equation (3—36) is evaluated in an elemental domain Ω_e, which boundary is Γ_e. The interface boundary Γ_i^e is also in the domain Ω_e.

Integration of equation (3—36) from time t^n to time t^{n+1} gives

$$\int_{t^n}^{t^{n+1}}\frac{\partial}{\partial t}\int_{\Omega_e\setminus\Gamma_i^e}\hat{c}T\,dV\,dt=\int_{\Omega_e^{n+1}}\rho^{n+1}h^{n+1}\,dV-\int_{\Omega_e^n}\rho^n h^n\,dV+\int_{t^n}^{t^{n+1}}\int_{\Gamma_e}\rho h\underline{v}\cdot\underline{n}d\Gamma\,dt-$$
$$\int_{t^n}^{t^{n+1}}\int_{\Gamma_i^e}]\rho h(\underline{v}-\underline{v}^+)\cdot(-\underline{n})[d\Gamma\,dt \tag{3—37}$$

Observing the first two terms on the RHS of equation (3—37), when the domain velocity $\underline{v}^*\neq 0$, the CV Ω_e expands and shrinks, thus $\Omega_e^{n+1}\neq\Omega_e^n$. But in this project, it is assumed that $\underline{v}^*=0$, which means the elemental CV is stationary, therefore $\Omega_e^{n+1}=\Omega_e^n$.

Evaluation of the third term on the RHS of equation (3—37) is achieved by

$$\int_{t^n}^{t^{n+1}}\int_{\Gamma_e}\rho h\underline{v}\cdot\underline{n}d\Gamma\,dt=\int_{\Gamma_e}\rho h(\underline{X}^{n+1}-\underline{X}^n)\cdot\underline{n}\,d\Gamma \tag{3—38}$$

where the position $\underline{X}^n$ is the original position of material at time t^n and the position $\underline{X}^{n+1}$ is the future position of material at time t^{n+1}. The simplest approximation can be $\left(\underline{X}^{n+1}-\underline{X}^n\right)=\underline{v}(t^{n+1}-t^n)\approx\int_{t^n}^{t^{n+1}}\underline{v}dt$. Further information on the evaluation of this term can be found in Appendix I—(d).

The non-physical capacitance is evaluated through the mean-value approach to the integration. Assuming that the non-physical capacitance $\hat{c}$ takes an intermediate value in each time interval, so it comes outside the integration. Thus, equation (3—37) returns to

$$\hat{c}=\frac{\int_{\Omega_e}\rho^{n+1}\mathrm{h}^{n+1}dV-\int_{\Omega_e}\rho^{n}\mathrm{h}^{n}dV+\int_{\Gamma_e}\rho h(\underline{X}^{n+1}-\underline{X}^n)\cdot\underline{n}d\Gamma-\int_{t^n}^{t^{n+1}}\int_{\Gamma_i^e}]\rho h(\underline{v}-\underline{v}^{\times})\cdot(-\underline{n})[d\Gamma dt}{\int_{\Omega_e}\mathrm{T}^{n+1}dV-\int_{\Omega_e}\mathrm{T}^{n}dV} \tag{3—39}$$

If there is no material movement ($\underline{v}=\underline{0}$), then equation (3—39) returns to

$$\hat{c}=\frac{\int_{\Omega_e}\rho^{n+1}h^{n+1}dV-\int_{\Omega_e}\rho^{n}h^{n}dV+\int_{t^n}^{t^{n+1}}\int_{\Gamma_i^e}]\rho h\underline{v}^{\times}\cdot(-\underline{n})[d\Gamma dt}{\int_{\Omega_e}T^{n+1}dV-\int_{\Omega_e}T^{n}dV} \tag{3—40}$$

As it has been mentioned before, there is no advective term appearing on the RHS of equation (3—31), because this is reflected in a change of non-physical enthalpy and therefore by a non-physical capacitance change which can be seen in equation (3—39). In equation (3—39), the advection is governed by the term $\int_{\Gamma_e}\rho h\left(\underline{X}^{n+1}-\underline{X}^n\right)\cdot\underline{n}\,d\Gamma$. Any change of this term will result in a change of non-physical capacitance, and furthermore the advection is accounted for by the change of non-physical capacitance.

The extraction of the jump term $\int_{t^n}^{t^{n+1}}\int_{\Gamma_i}]\rho h\left(\underline{v}-\underline{v}^{\times}\right)\cdot\left(-\underline{n}\right)[d\Gamma\,dt$ from equation (3—39) results an extra term appearing on the RHS of equation (3—31). Both terms require evaluation. The approximation to the term $\int_{t^n}^{t^{n+1}}\int_{\Gamma_i}]\rho h\left(\underline{v}-\underline{v}^{\times}\right)\cdot\left(-\underline{n}\right)[d\Gamma\,dt$ could follow the same approach adopted for the approximation of $\int_{t^n}^{t^{n+1}}\int_{\Gamma_e}\rho h\underline{v}\cdot\underline{n}\,d\Gamma\,dt$, i.e.

$$\int_{t^n}^{t^{n+1}}\int_{\Gamma_{ie}}]\rho h\left(\underline{v}-\underline{v}^{\times}\right)\cdot\left(-\underline{n}\right)[d\Gamma\,dt=\int_{t^n}^{t^{n+1}}\int_{\Gamma_i^e}\rho_l(h_s-h_l)\underline{v}_l\cdot\underline{n}_l d\Gamma\,dt+$$
$$\int_{t^n}^{t^{n+1}}\int_{\Gamma_i^e}(\rho_l h_l-\rho_s h_s)\underline{v}^{\times}\cdot\underline{n}_l d\Gamma\,dt \tag{3—41}$$

Detailed approach of equation (3—41) can be found in Appendix I—(e). The first term on the RHS of equation (3—41) mathematically represents the energy swept by the phase

interface by advection, and similarly, the second term on the RHS of equation (3—41) mathematically represents the energy swept by the phase interface due to the motion of interface itself.

The application of equations (3—39) and (3—40) for solidification problems requires a further evaluation of the volumetric enthalpy ρh as it appears many times in the numerator. The following relationships

$$h_s = h_{ref} + \int_{T_{ref}}^{T} \rho_s c_s(T')dT' \tag{3—42a}$$

and

$$h_l = h_{liq} + \int_{T_{liq}}^{T} c_l(T')dT' \tag{3—42b}$$

are currently used [39, 41, 62-63, 66]. The subscript s and l denote the solid phase and the liquid phase respectively. In addition $h_{ref} = c_s T_{ref}$, where T_{ref} represents the reference temperature. Moreover $h_{liq} = h_{sol} + L$, where L is the latent heat of solidification and $h_{sol} = c_s T_{sol}$ is the enthalpy of solidification.

In some studies, researchers set $T_{ref} = 0$ [37, 40, 46], other studies regard T_{ref} as the solidus temperature T_{sol} in equation (3—42a) and the liquidus temperature T_{liq} in equation (3—42b) [39, 41, 43, 62-63, 66]. This project prefers the second configuration, because this configuration allows the method to be easily applied to both isothermal solidification and mushy zone solidification. Thus equations (3—42a) and (3—42b) become

$$h_s = h_{sol} + \int_{T_{sol}}^{T} c_s(T')dT' \tag{3—43a}$$

and

$$h_l = h_{liq} + \int_{T_{liq}}^{T} c_l(T')dT' \tag{3—43b}$$

where the specific capacitance c_s, c_l are assumed to be constant. The material property of different phases are set to be different, i.e. $c_s \neq c_l$. This makes sure that the strong discontinuity in the change of enthalpy.

In the isothermal solidification, according to equations (3—43a) and (3—43b), for the integral $\int_{\Gamma_i^e}(\rho_l h_l - \rho_s h_s)\underline{v}^{\times} \cdot \underline{n}_l dA$ on the RHS of equation (3—41), the approximation applies

$$(\rho_l h_l - \rho_s h_s) \approx (\rho_l - \rho_s)h_{sol} + \rho_l L \tag{3—44}$$

In the previous studies, such as the enthalpy method reviewed by Voller *et al* [7], the density of the liquid ρ_l is assumed equal to the density of the solid ρ_s. With equation (3—31), the jump term returns a familiar form $\rho_l L(dX_i/dt) \cdot \underline{n} = \left]\underline{q} \cdot \underline{n}\right[$, which is identical to the Stefan condition.

For a material point, which contains both the solid phase and liquid phase, the enthalpy is represented by

$$\rho h = g_s \rho_s h_s + g_l \rho_l h_l \tag{3—45}$$

where g_s and g_l represent the solid volume fraction and liquid volume fraction respectively. There are various approaches for approximation of g_s and g_l, and the approach adopted can affect accuracy and stability; for all approaches however the identity $g_s + g_l = 1$ applies.

To explain the application of the non-physical variable methods and the above approximation approaches in details, a one-dimensional rod element is utilised as an example. Illustrated below is how the non-physical capacitance and the conductivity are evaluated in a one-dimensional element.

Substituting of equations (3—43a) and (3—43b) in to equation (3—45) and applying it into a one-dimensional elemental CV gives

$$\int_{\Omega_e} \rho^n h^n \, dV = \int_{\Omega_e} {g_s}^n \rho_s h_{sol} \, dV + \int_{\Omega_e} {g_s}^n \rho_s \int_{T_{sol}}^{T^n} c_s(T')dT' \, dV + \int_{\Omega_e} {g_l}^n \rho_l h_{sol} dV + \int_{\Omega_e} {g_l}^n \rho_l l \, dV + \int_{\Omega_e} {g_l}^n \rho_l \int_{T_{liq}}^{T^n} c_l(T')dT' \tag{3—46}$$

In equation (3—50), as well as the temperature, the solid volume fraction is also an important parameter for the computation of enthalpy. The methods utilised to predict and evaluate the solid fraction/liquid fraction dramatically affect the enthalpy methods such as the non-physical capacitance method, and the source-based method such as the non-physical source method [37, 46, 105]. It can be seen that the solid fraction/liquid fraction not only governs the magnitude of sensible heat but also controls the rate release of latent heat. In most

simulations, the fraction g_s or g_l are usually considered as a function of temperature. The numerical evaluation of fraction g_s or g_l are point based and usually applied to the methods such as FDM and FVM. Voller and Swaminathan [46] considered different approximations for the liquid fraction when $T_{sol} \neq T_{liq}$, and the relationships are shown in Table 3.1. They also indicated that the update of liquid fraction is very important to the source based method. However, for the isothermal solidification, the relationship $T_{liq} = T_{sol}$ makes all the equations in the Table 3.1 undefined. A Heaviside step function is applied for liquid fraction in reference [113], which is

Type	Value of g_l	Condition
Linear	$\frac{T - T_{liq}}{T_{sol} - T_{liq}}$	
Linear Eutectic	$\frac{(1 - g_E)T + g_E T_{sol} - T_{liq}}{T_{sol} - T_{liq}}$	$g_E = 0.2$
Scheil	$\left(\frac{T_{sol} - T}{T_{sol} - T_{liq}}\right)^{-\beta}$	$\beta = 1.163$
Power	$\left(\frac{T - T_{liq}}{T_{sol} - T_{liq}}\right)^{n}$	$n = 0.2\ or\ 5$

Table 3.1: Liquid Fraction of mushy zone solidification

$$g_l = \begin{cases} 1 & T \geq T_{sol} \\ 0 & T < T_{sol} \end{cases} \tag{3—47}$$

Clyne [135] indicates that the relationship between the liquid fraction and the temperature is greatly influenced by the solute redistribution, and this effect must be calculated. In some studies, a small artificial mushy region is created to replace the isothermal case by introducing the neighbourhood $\pm\delta T$ of the temperature T_{sol}, so the liquid fraction can be computed by

$$g_l = \begin{cases} 1 & T_{sol} + \delta T \leq T \\ \frac{\delta T + T_{sol} - T}{2\delta T} & T_{liq} - \delta T < T < T_{sol} + \delta T \\ 0 & T \leq T_{sol} - \delta T \end{cases} \tag{3—48}$$

One disadvantage with this approximation is that there is no precise definition of δT, The other problem is that, like equation (3—47), they are designed for node-based numerical methods such as the FVM, where usually only one node is positioned in the centre of the element. The substitution of nodal temperature into the above equations only results in one liquid fraction and one capacitance. However, for the FEM, there are usually more than one

node associated with an element, so applying the point based approximation of liquid fraction, at every node in an element will give different liquid fractions and capacitances. This makes the capacitance matrix difficult to construct and assemble. One possible solution to this problem is to substitute an averaged elemental temperature $T_e = (1/V_e)\int_{\Omega_e}\{N\}\{T\}^T\,dV$ in to the equations instead of the nodal temperatures. But this is a rather crude approximation; for example, for a two-node one-dimensional element, the nodal temperatures are $T_1 = 399℃$ and $T_2 = 405℃$. Assuming that the solidification is isothermal and the solidus temperature is $T_{sol} = 400℃$. In this situation, it is obvious that this one-dimensional element contains the phase interface, both solid and liquid coexist in the element. But the temperature $T_e = 402℃$, which is above the solidus temperature. If substituting the temperature T_e into equation (3—47), the equation will give the system wrong information that the element is staying in liquid. Accordingly, the point-based evaluation of liquid fraction cannot be directly applied to the FEM, and an element-based evaluation is required.

In reference [28], liquid fraction is regarded as a function of enthalpy. It can be used on an element base, but unfortunately, only applies to mushy-zone solidification. This thesis adopts an element-based evaluation of liquid fraction, but adapted for the simulation of isothermal solidification. However, it can also be applied to mushy-zone solidification. Figure 3.4 shows sketches of two phase changing elements in the solidification simulation. On the left is the isothermal solidification (pure metal solidification) and on the right is the mushy zone solidification (alloy solidification). To make a distinction between the point-based fraction and the element-based fraction, different notation is used. At time t^n, the volume of solid region is $\mathrm{V}_s = \Upsilon_s{}^n V_e$, and the volume of liquid region is $\mathrm{V}_l = \Upsilon_l{}^n V_e$, where V_e is the volume of the element, and $\Upsilon_s{}^n$ and $\Upsilon_l{}^n$ are the elemental solid volume fraction and elemental liquid volume fraction, respectively.

Figure 3.4: Isothermal solidification in 1D element (left) and Mushy zone solidification in 1D element (right)

For mushy zone solidification, the fraction of mushy zone is $\Upsilon_m{}^n = 1 - \Upsilon_s{}^n - \Upsilon_l{}^n$, so the volume of mushy zone is defined as $V_m = \Upsilon_m{}^n V_e$ and the identity $\Upsilon_s + \Upsilon_m + \Upsilon_l = 1$ applies.

For isothermal solidification, it is assumed that the temperature of the phase interface is the solidus temperature, thus, the nodal temperatures of an element can be used to approximate the solid fraction. For example, in one-dimensional case, the liquid fraction is given by

$$\Upsilon_s = \begin{cases} 1 & T_{sol} \le T_1 \le T_2 \\ \frac{T_{sol}-T_1}{T_2-T_1} & T_1 < T_{sol} \le T_2 \\ 0 & T_1 < T_2 < T_{sol} \end{cases} \quad (3—49)$$

where the temperature T_1 and T_2 are the nodal temperatures of node 1 and node 2 of an element.

If the position of the phase interface can be calculated, the solid fraction can also be evaluated as

$$\Upsilon_s = \begin{cases} 1 & X_i \le x_1 \le x_2 \\ \frac{X_i-x_1}{x_2-x_1} & x_1 < X_i \le x_2 \\ 0 & x_1 < x_2 < X_i \end{cases} \quad (3—50)$$

where x_1 and x_2 are the nodal coordinates of node 1 and node 2 of the element.

Equations (3—49) and (3—50) ensures that the elemental solid volume fraction $\Upsilon_s \in [0, 1]$, the 'over shoot/under shoot' correction considered by Voller *et. al.* [105] for the point-based approximation is not required.

Since the fraction $\Upsilon_s \in [0, 1]$, and from equation (3—50) it can be seen that the evaluation of elemental solid fraction Υ_s is conducted in a Cartesian coordinate system. Even through the temperature approach, it is assumed to be identical in the Cartesian coordinate system. However, the one-dimensional linear shape functions adopted requires the integration of equation (3—46) to be conducted in the natural coordinate system, i.e. $\xi \in [-1,1]$. As a consequence, a mapping of elemental solid fraction in the Cartesian coordinate system and the elemental solid fraction in the natural coordinate system is required to be established. Figure 3.5 shows the elemental solid fraction in the natural coordinate system.

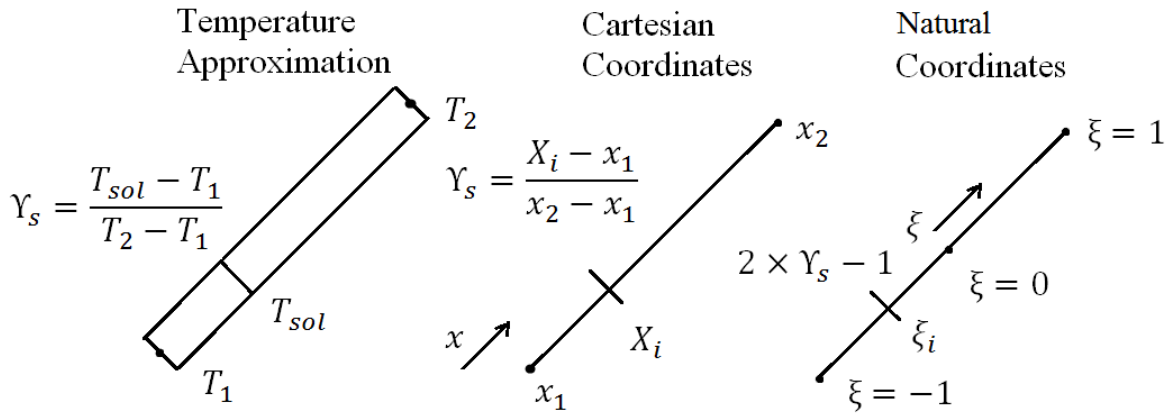

Figure 3.5: The elemental solid volume fraction in the natural coordinate system

With the relationship as shown in Figure 3.5, substitution of the shape functions to equation (3—46) gives

$$\int_{\Omega_e} \rho^n h^n \, dV \approx M_e^n h_{sol} + \rho_s c_s \frac{A_e L_e}{2} \Upsilon_s{}^n \left[2T_1{}^n - 2T_{sol} + \Upsilon_s{}^n \left(T_2{}^n - T_1{}^n\right)\right] + M_l^n L + \rho_l c_l \frac{A_e L_e}{2} (1 - \Upsilon_s{}^n)\left[T_1{}^n + T_2{}^n - 2T_{sol} + \Upsilon_s{}^n \left(T_2{}^n - T_1{}^n\right)\right] \quad (3—51)$$

where M_e is the total mass of material in the element, M_l is the total mass of liquid in the element, A_e is the element cross-sectional area, L_e is the element length. The superscript n refers to the time step. A complete approach from equation (3—46) to equation (3—51) can be found in Appendix I—(f).

The elemental integral $\int_{\Omega_e} T^n dV$ appearing in equations (3—39) and (3—40) can simply achieved by

$$\int_{\Omega_e} T^n dV = \int_{\Omega_e} N_1 T_1^n + N_2 T_2^n dV = A_e \frac{L_e}{2} \int_{-1}^{1} \frac{1-\xi}{2} T_1^n + \frac{1+\xi}{2} T_2^n d\xi = \frac{V_e}{2}(T_1^n + T_2^n) \quad (3—52)$$

In section 3.4, the discontinuity contained in the term $\int_\Omega \underline{q} \cdot \nabla W dV$ is annihilated by the term $\int_{\Gamma_i} \hat{h}'\left(\underline{v} - \underline{v}^+\right)_N \cdot \nabla W dA$. As a matter of fact, with relationship $q = -k\nabla T$, the thermal conductivity of material can be evaluated in a mixture approach [37, 46, 62-63, 105], which is

$$k^n = \Upsilon_s{}^n k_s + \Upsilon_l{}^n k_l \quad (3—53)$$

on the assumption that the thermal conductivity of solid k_s and the thermal conductivity of liquid k_l are both constant.

3.5.3 The behaviour of non-physical capacitance and source

In section 3.5.2 is given a mathematical derivation of non-physical capacitance and non-physical source terms. The approximations conducted in an element domain are given. However, the behaviour of non-physical properties in an element is not intuitive through complicated equations. Therefore, it is useful to use a prescribed temperature to substitute into the above equations to reveal their response. The temperature profiles are calculated from the exact solution as obtained in chapter 2. A finite-volume element and a finite element as shown in Figure 3.6 are used as examples for a point-based approximation and the element-based approximation, respectively. For the finite volume element, the node is positioned at $x = 0.02\ m$, and for the finite element, the node 1 is positioned at $x = 0.02\ m$ and the node 2 is positioned at $x = 0.03\ m$. Consequently, the length of the example finite element $L_e = 0.01\ m$. And the example finite volume element is set as the same length of the finite element. Moreover, since the examples are in one-dimension, the cross-sectional area A_e can be simply set as 1. Assuming the time step size is $\Delta t = 0.05\ sec$, with the known positions $x = 0.02\ m$ and $x = 0.03\ m$, the prescribed temperature for $\{T^{n+1}\}$ can be calculated through equation (2—7), which is

$$T(x,t) = \begin{cases} \left(\frac{T_{sol}-T_{amb}}{\frac{1}{h_c\sqrt{\pi\alpha_s t}}+\boldsymbol{erf}\left(\frac{X(t)}{2\sqrt{\alpha_s t}}\right)}\right)\boldsymbol{erf}\left(\frac{x}{2\sqrt{\alpha_s t}}\right)+\frac{T_{sol}+T_{amb}h_c\sqrt{\pi\alpha_s t}\,\boldsymbol{erf}\left(\frac{X(t)}{2\sqrt{\alpha_s t}}\right)}{1+h_c\sqrt{\pi\alpha_s t}\,\boldsymbol{erf}\left(\frac{X(t)}{2\sqrt{\alpha_s t}}\right)} & (x < X(t)) \\ T_{init}+(T_{sol}-T_{init})\dfrac{\boldsymbol{erfc}\left(\frac{x}{2\sqrt{\alpha_l t}}\right)}{\boldsymbol{erfc}\left(\lambda\sqrt{\frac{\alpha_s}{\alpha_l}}\right)} & (x \geq X(t)) \end{cases}$$

(3—54)

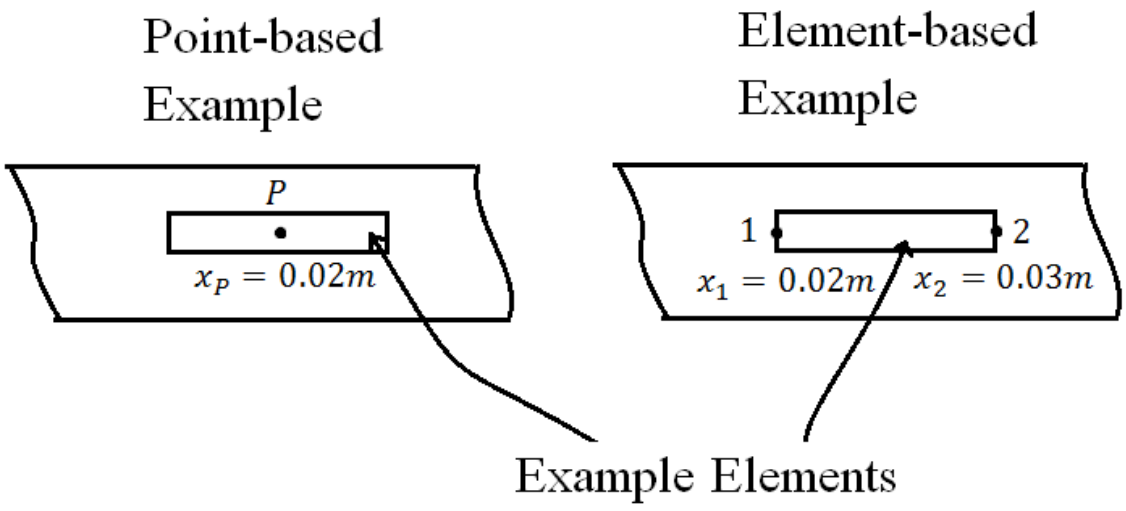

Figure 3.6: The example elements with prescribed temperature

The initial temperature (T_{init})	405℃
The forced convective term (h_c)	$12000W/m^2$℃
The ambient temperature (T_{amb})	25℃
Thermal diffusivity of solid (α_s)	$1.515 \times 10^{-5}\ m^2/sec$
Thermal diffusivity of liquid (α_l)	$3.623 \times 10^{-5}\ m^2/sec$
Latent Heat (L)	$130000J/kg$
Solidus temperature (T_{sol})	400℃
Liquidus temperature (T_{liq})	400℃

Table 3.2: The material properties

The reasons for using an analytical solution (3—55) as the prescribed temperature for substitution into the equations for non-physical variables are:

(1) It makes the non-physical capacitance and non-physical source behave exactly as they are in the numerical simulation of solidification;

(2) It avoid the effects from the numerical solvers such as solution method and the update method, and shows exactly how the non-physical variables behave with correct temperatures substituted;

(3) the behaviour of liquid fraction can be found for both point-based approximation and the element-based approximation, their influences on the non-physical variables can be easily identified.

Figure 3.7 shows a group of plots for point-based approximations of liquid fraction. The liquid fraction (vertical) is plotted against time (horizontal). In chapter 2, the position of phase interface is able to be calculated by equation $X_i(t) = 2\lambda\sqrt{\alpha_s t}$. Consequently, the liquid fraction of the given finite-volume element can be evaluated through the exact position of $X_i(t)$ from the analytical method. It is placed on the top left corner of Figure 3.3. The title "position approximation" means the evaluation of interface position is tracked via the analytical method. This evaluation assumes that the phase interface is distinct, thus the term "approximation" is used rather than "exact". On the top right of Figure 3.7 is the Heaviside step function which is given by equation (3—47). The bottom two plots are evaluated from equation (3—48) with different neighbourhood factor $\delta T = 0.5$℃ (left) and $\delta T = 1.5$℃ (right).

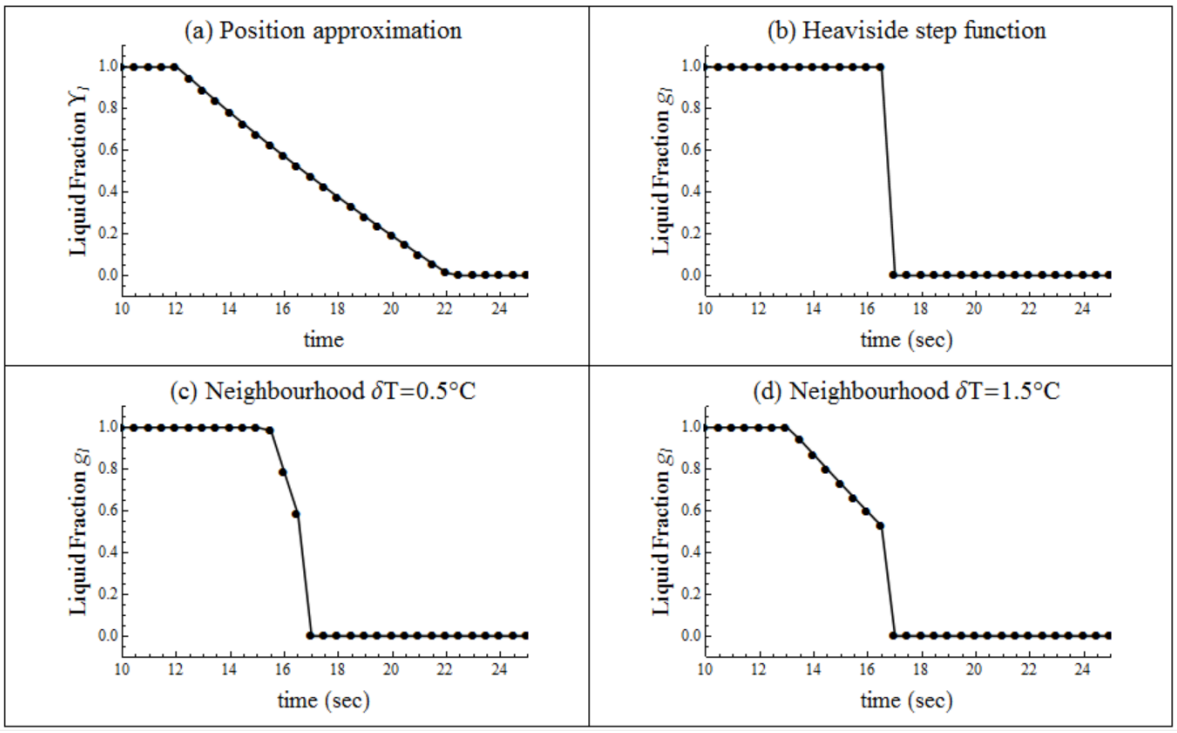

Figure 3.7: Point based Liquid fraction approximations of solidification

The liquid fraction $g_l = 1$ indicates that the finite volume is completely liquid, and when $g_l = 0$, the finite volume is completely solid. The position approximation shows that the decrease rate of the liquid fraction is almost constant. However, in the approximations, the

Heaviside side function (3—47) makes the liquid fraction suddenly jump down from 1 to 0, which is too abrupt; the "neighbourhood" method (3—48) is gentler, and larger value of δT makes the decrease of liquid fraction smoother. However, a problem can be easily identified is that the decreasing rate is uneven in the "neighbourhood" method. No matter how much the δT is, the liquid fraction drops down to 0 instantly after around 16.5 seconds. The nodal temperature profile displayed in the Figure 3.8 explains the reason why this problem happens. When $\delta T = 1.5$ ℃ and the time step size $\Delta T = 0.5\ seconds$, before the nodal temperature below the solidus temperature $T_{sol} = 400$ ℃, there are 7 time steps in which the nodal temperature is in the range $[T_{sol} + \delta T, T_{sol}]$. But when the Nodal temperature is just below the solidus temperature, the nodal temperature is 397.879 ℃ , which is out of the range $T_{sol}, T_{sol} - \delta T$. This is because of the different cooling rates of different phases, and the weak discontinuous (only kink appeared in the change of temperature) behaviour of the temperature profile.

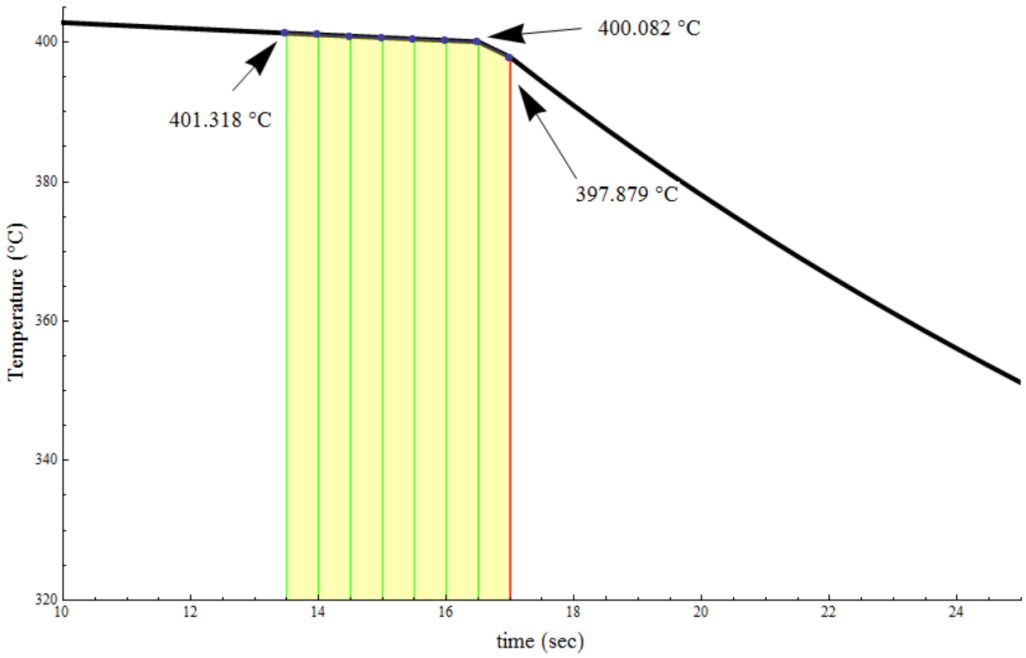

Figure 3.8: Nodal temperatures in the artificial mushy region

The different approximations of liquid fraction will give different behaviour of non-physical capacitance and non-physical source term in the numerical simulation.

Based on the assumption that the material is stationary, i.e. $\underline{v} = \underline{0}$, the non-physical capacitance and the non-physical jump can be evaluated through equation (3—40). It can be compared with the non-physical capacitance $\hat{c}$ that contains discontinuity, which is

$$\hat{c} = \frac{\int_{\Omega_e} \rho^{n+1} h^{n+1} dV - \int_{\Omega_e} \rho^n h^n dV}{\int_{\Omega_e} T^{n+1} dV - \int_{\Omega_e} T^n dV} \tag{3—55}$$

which is provided by Davey *et. al* [66].

Figure 3.9 shows the point-based non-physical capacitance according to equation (3—55), which is mainly applied to the control volume method. The term "point-based" means that the evaluations of liquid fraction and the non-physical variables are conducted through single node. The liquid fraction is consequently evaluated by the point-based approximation such as equations (3—47) and (3—48). The label "position approximations" means that the liquid fraction utilized for the evaluation of non-physical capacitance is evaluated through the interface position which is tracked by the analytical method. The top right plot of non-physical capacitance in Figure 3.9 is calculated by the substitution of liquid fraction from equation (3—47) and the bottom two plots of non-physical capacitance are calculated with equation (3—48). Each individual plot of the Figure 3.9 starts at the value $\hat{c} = \rho_l l_l = 330{,}000\, J/℃m^3$, which is maintained for a period of time, then the phase change makes the value increase. When the phase change is over, the non-physical capacitance ends at the value $\hat{c} = \rho_s c_s = 276{,}000\, J/℃m^3$. During phase change, the behaviour of the non-physical capacitance is corresponding to the evolution of liquid fraction. In the Heaviside step approximation, there is only one singularity in the plot. In the Neighbourhood approximations, greater δT makes the magnitude of non-physical capacitance smaller, but the increase of the number of time steps in the phase change period makes the range of the peak wider.

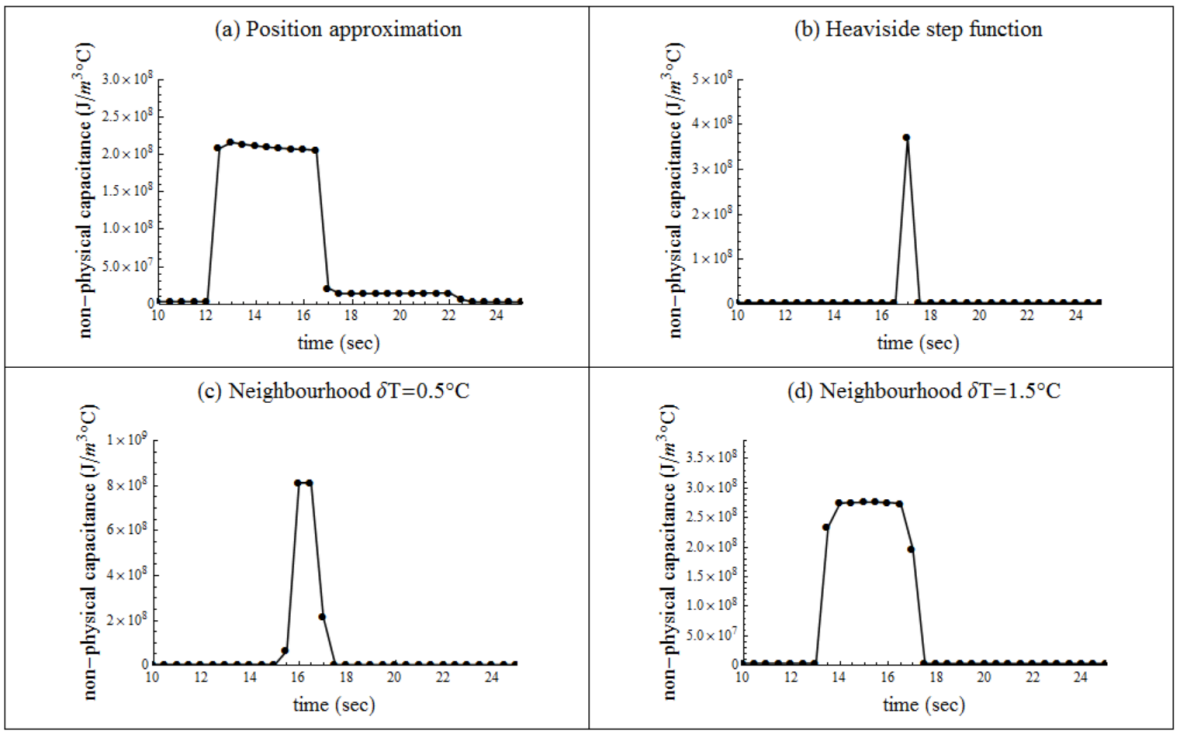

Figure 3.9: Point-based non-physical capacitance by CVCM

The application of equation (3—40) results in the removal of discontinuities from the enthalpy when the material velocity $\underline{v} = \underline{0}$. As a consequence, the peaks appearing in Figure 3.9 do not now appear. Figure 3.10 shows the node-based non-physical capacitance obtained after the discontinuity is removed. All four graphs show that the change of non-physical capacitance is smoother to that produced by equation (3—55). The aftermath of applying this method is that a non-physical source-term $\int_{\Gamma_{ie}}]\rho h(\underline{v} - \underline{v}^{\times}) \cdot (-\underline{n})[dA$ is generated, this source term is evaluated by equations (3—41) and (3—44) and is shown in the Figure 3.11. The change of the non-physical source terms shares the same characteristics as the non-physical capacitance. For example, in the Heaviside step approximation, the singular peak now is removed from the non-physical capacitance, but reappears as a source term. The behaviour of non-physical source also changes with different approximation of liquid fraction adopted.

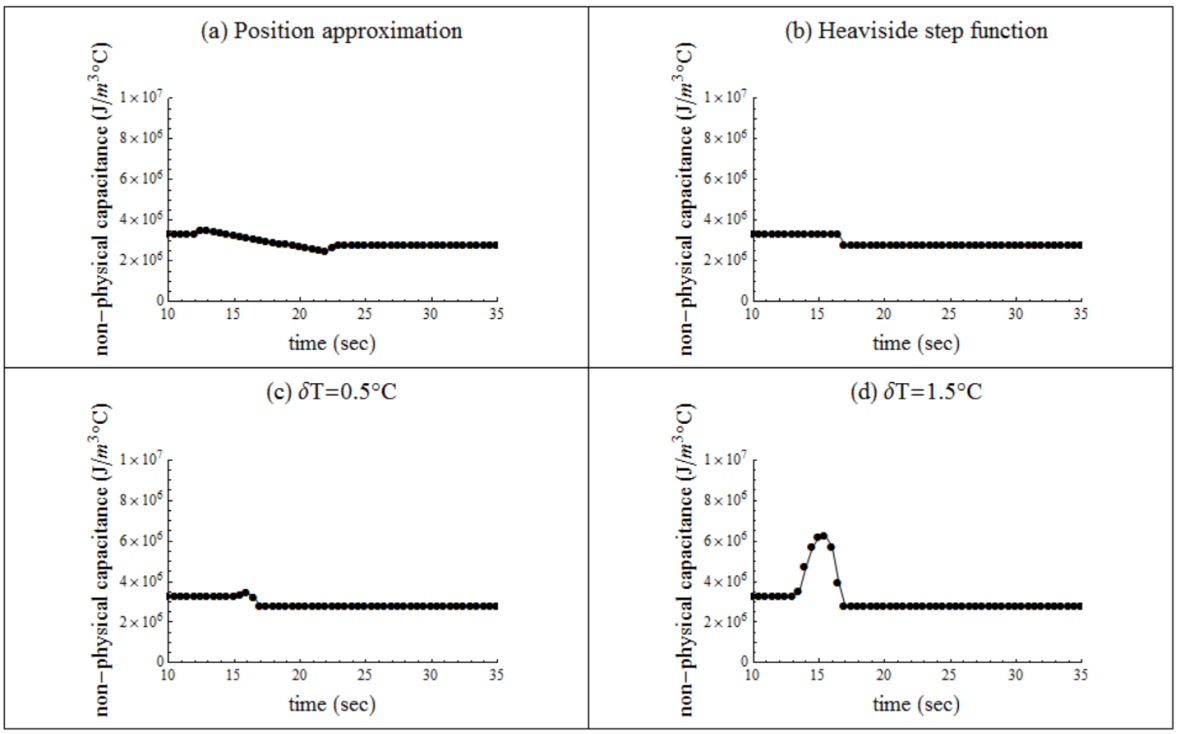

Figure 3.10: Node based non-physical capacitance without discontinuity

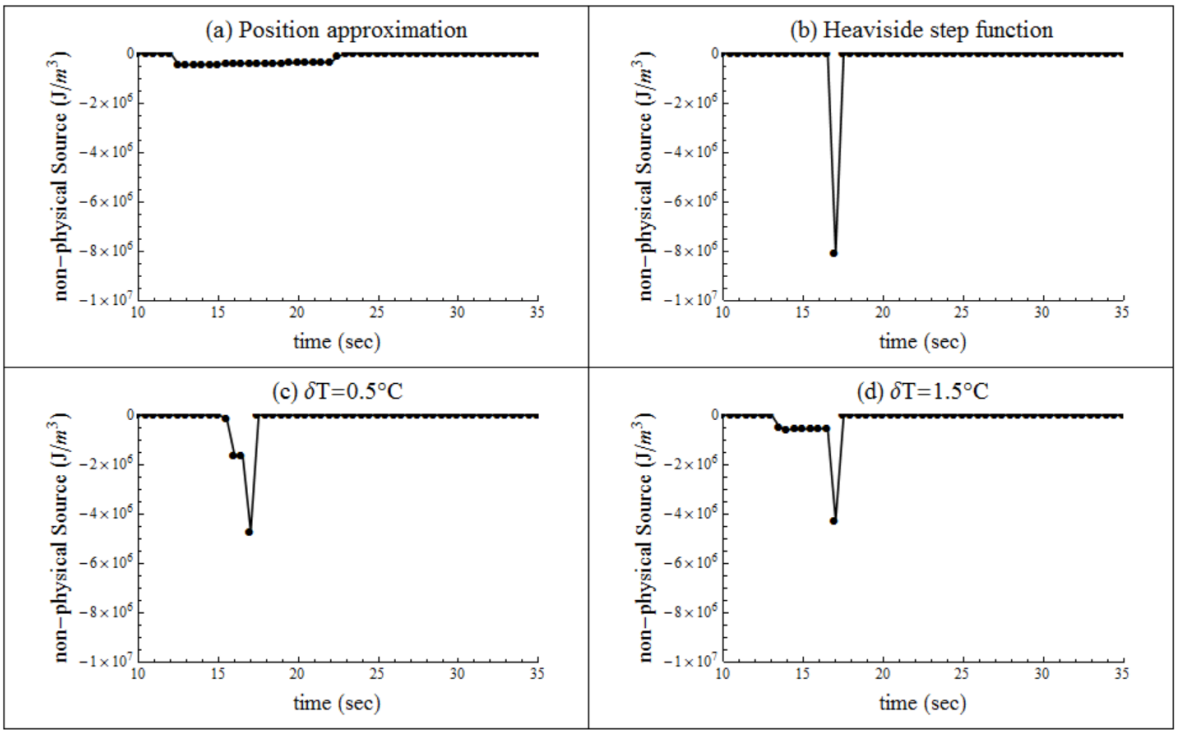

Figure 3.11: Node based non-physical source term

The above study shows the successful removal of the discontinuities from the non-physical capacitance in “ideal conditions” in which the temperature is correctly calculated by the analytical method. It shows the feasibility of the application of non-physical variable method

to the point-based numerical method such as FVM, though the FVM is not chosen in this project. This project uses the FEM, in which the approach is conducted on an element base and the element-based approximations are required.

The plot on the RHS of Figure 3.12 shows the element-based liquid fraction Υ_l. The fraction Υ_l is evaluated by the temperature approximation as shown in equation (3—49). The temperature substituted into equation (3—49) is calculated by the analytical method which is the same as used in the analysis of point-based approximations. The shape of the curve plotted by equation (3—49) is similar to a cumulative distribution function. It is different from the node based approximations that the phase change is not steep. The plot on the LHS of Figure 3.12 is the liquid fraction Υ_l evaluated by equation (3—50). The "position approximation" is conducted by equation (3—50), and the phase interface position X_i is from the analytical method, say $X_i(t) = 2\lambda\sqrt{\alpha_s t}$.

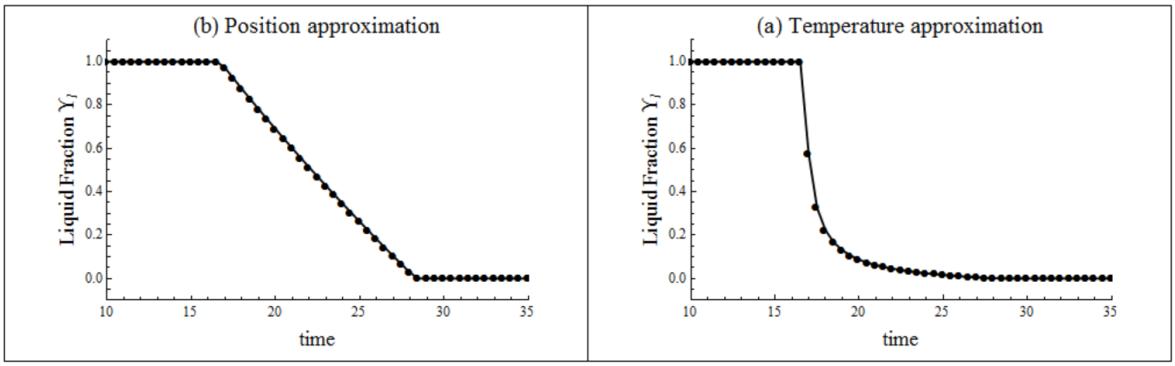

Figure 3.12: The element based approximation of liquid fraction

For both the position approximation and the temperature approximation, the phase interface is propagating through the example element from about 16 seconds to 28 seconds. But the behaviour of the liquid fractions is very different with different approaches. Through the position approximation, the decreasing rate of liquid fraction is almost constant, which leads to the non-physical capacitance of the element increasing gently during the phase change. However, in the temperature approximation, the decreasing rate of liquid fraction is cumulative, as a consequence, a spike is generated in the change of non-physical capacitance with equation (3—52). The peak of the non-physical capacitance through temperature approximation ($3 \times 10^8\ J/m^3$°C) is about 7.5 times higher than that obtained from position approximation ($4 \times 10^7\ J/m^3$°C).

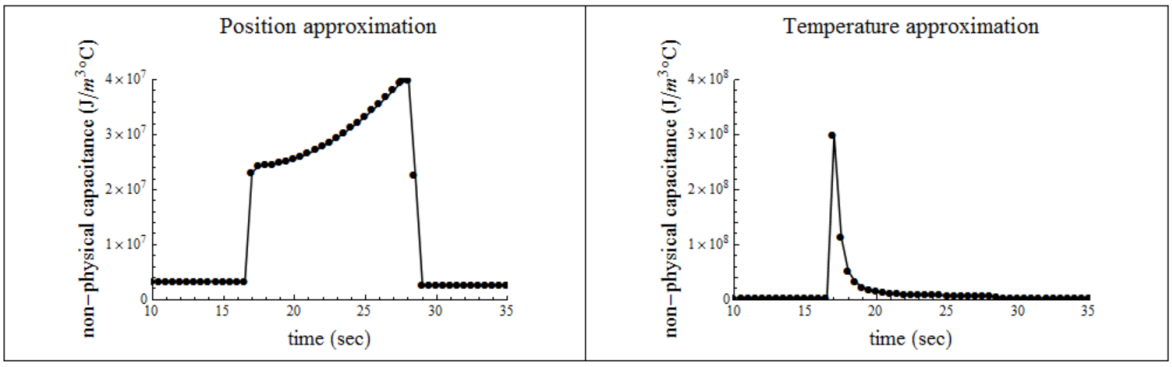

Figure 3.13: The element-based non-physical capacitance by CVCM

Figure 3.14 shows the non-physical capacitance evaluated by equation (3—37) in which the discontinuity is excluded. It confirms that the discontinuity can be removed from the enthalpy and capacitance via the non-physical variable method in a finite element domain. Figure 3.15 shows the non-physical source generated as the companion of removal procedure. Moreover, the behaviour of non-physical capacitance and non-physical enthalpy is related to the approximation of liquid fraction adopted.

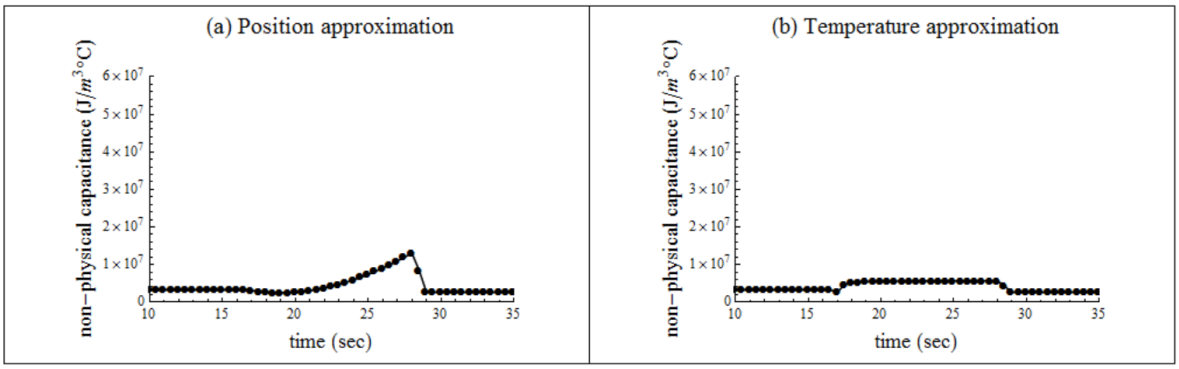

Figure 3.14: The element-based non-physical capacitance without discontinuity

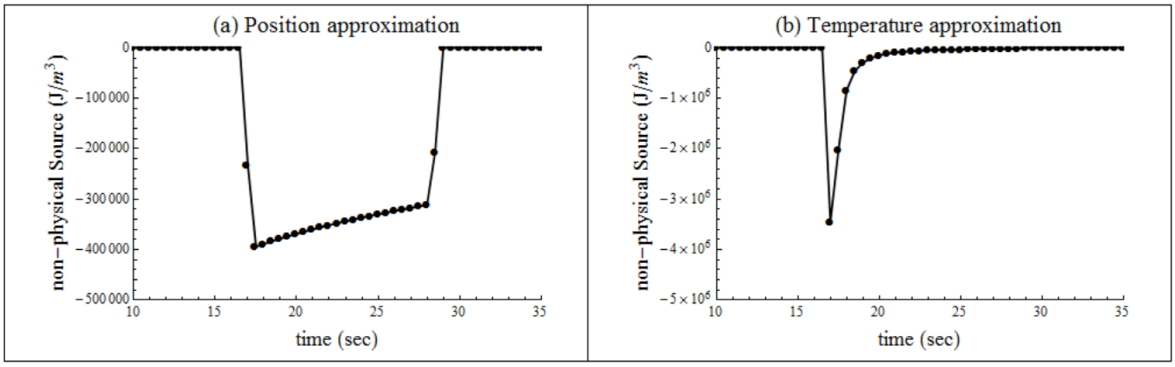

Figure 3.15: The element-based non-physical source

3.6 Summary

In this chapter, a detailed theoretical discussion of non-physical variable methods is given. The concept of non-physical variable method is introduced at the beginning of the chapter. This chapter provides a definition of non-physical enthalpy. Then, the volume analysis is conducted for both the weak form non-physical transport equation and the weighted weak form non-physical transport equation, which give rise to a jump that contains the discontinuity. The discontinuity removal from the weak form transport equation is attempted with respect to a finite element CV.

Through the substitution of prescribed temperature, which is calculated by the analytical method, to the non-physical variable method, it confirms that:

(1) The discontinuity in the enthalpy and the capacitance can be successfully removed by the non-physical variable method;
(2) The non-physical variable is not unique since it is defined without regard to initial conditions. The behaviour of non-physical variable is dependent on the approximation adopted for the liquid/solid fraction.

The above investigations give rise to further considerations, which are:

(1) How do non-physical variables actually behave in numerical methods with the involvement of approximations;
(2) The importance of the dependence of non-physical variables on the future temperature $\{T^{n+1}\}$ which appears to require an update procedure;
(3) The influences of the behaviour of non-physical variables on the stability and accuracy of the numerical methods;
(4) The effects of the peaks in the non-physical variables to the numerical simulation of solidification especially when advection is involved with solidification.

To illuminate these aspects, a numerical study is required.

Chapter 4 The Numerical Trials on the Non-physical Enthalpy Method and Its Solutions

4.1 General

In Chapter 3, a mathematical analysis of the recent non-physical enthalpy method [62-63] is provided. A situation, i.e. D^+W/D^+t is non-zero, is considered in the analysis of weighted transport equation. This leads to a same result as can be seen in references [62-63], which confirms the correctness of both analyses. A non-physical source $\widehat{h'}$ is obtained through the definition of non-physical enthalpy. The discontinuity removal approach generates three equations, which are:

$$\frac{D^*}{D^*t}\int_{\Omega_e\setminus\Gamma_i^e} N_\vartheta \hat{h}\, dV = -\int_{\Gamma_e} N_\vartheta \underline{q}\cdot\underline{n}d\Gamma + \int_{\Omega_e\setminus\Gamma_i^e} \underline{q}\cdot\nabla N_\vartheta dV + \int_{\Omega_e} N_\vartheta \rho Q\, dV - \left(\int_{\Gamma_i^e} N_\vartheta\right]\rho h\left(\underline{v}-\underline{v}^+\right)\cdot\left(-\underline{n}\right)\left[d\Gamma\right) \quad (4—1)$$

$$\frac{D^*}{D^*t}\int_{\Omega_e\setminus\Gamma_i^e} \hat{h}\, dV = \frac{D^*}{D^*t}\int_{\Omega_e} \rho h\, dV + \int_{\Gamma_e} \rho h\left(\underline{v}-\underline{v}^*\right)\cdot\underline{n}d\Gamma - \int_{\Gamma_i^e}\right]\rho h\left(\underline{v}-\underline{v}^\times\right)\cdot\left(-\underline{n}\right)\left[d\Gamma \quad (4—2)$$

and

$$\frac{D^\times}{D^\times t}\int_{\Gamma_i^e} N_\vartheta \hat{h}'\, dV + \int_{\Sigma_i^e} N_\vartheta \hat{h}'\left(\underline{v}^*-\underline{v}^\times\right)\cdot\underline{tn}d\Sigma + \int_{\Gamma_i^e} \hat{h}'\left(\underline{v}^*-\underline{v}^\times\right)\cdot\nabla N_\vartheta d\Gamma = \int_{\Gamma_i^e} N_\vartheta\right]\rho h\left(\underline{v}-\underline{v}^\times\right)\cdot\left(-\underline{n}\right)\left[d\Gamma = -\int_{\Gamma_i} N_\vartheta\left]\underline{q}\cdot\left(-\underline{n}\right)\right[d\Gamma \quad (4—3)$$

Equation (4—1) is the semi-discretised finite element equation which requires to be solved by the finite element method (FEM). Equation (4—2) is the linkage equation which is applied to evaluate the non-physical variables. Equation (4—3) is the source equation which facilitates the discontinuity removal from equation (4—1). The evaluation of (4—2) is already described in Chapter 3. The discontinuity removal approach is also confirmed available with the substitution of temperature from exact solution. The investigations in

Chapter 3 give rise to several further considerations. The development of non-physical enthalpy method should lead to concept as can be seen in Figure 4.1 (a) and Figure 4.1 (c), where discontinuity is completely or partially isolated from the non-physical enthalpy $\hat{h}$ and is accounted for by the non-physical source $\hat{h}'$. References [62-63] approximate the non-physical source $-\int_{\Gamma_i} N_\vartheta \left]\underline{q}\cdot(-\underline{n})\right[d\Gamma$ as a capacitance, which substitute the isolated discontinuity back to the non-physical enthalpy. This approximation returns the non-physical enthalpy method to a concept similar to Figure 4.1 (b), which is the control volume capacitance method provided by Davey *et. al.*[66]. It confirms the relationship between the non-physical enthalpy method and the control volume capacitance method, as the control volume capacitance method can also be categorised into the non-physical method, depending on how the non-physical enthalpy $\hat{h}$ is initially defined. However, the treatment of non-physical source $-\int_{\Gamma_i} N_\vartheta \left]\underline{q}\cdot(-\underline{n})\right[d\Gamma$ as a source term alone certainly required to be studied, which is one of the objectives of this chapter.

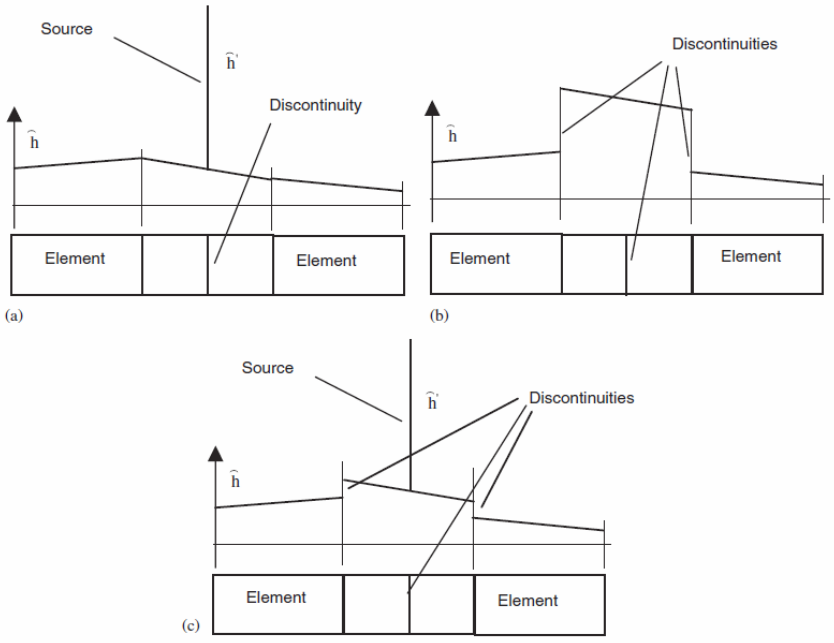

Figure 4.1: Non-physical behaviour on 1D elements: (a) moving source; (b) edge discontinuities; and (c) moving source and edge discontinuities [63].

Furthermore, as mentioned in Chapter 3, references [62-63] uses bisection method as the solution method. This method requires that the solution should be between the present value and predicted value. This criteria is not always guaranteed in the solution procedure and the programme may fail to converge. Thus, this chapter introduces three alternative solution

methods, which are the Predictor-Corrector method, the Secant method and the Homotopy method. Their application to other numerical methods can be seen in references [109, 113, 115, 124]. At last, the presence of advection, i.e. the material velocity is non-zero, requires exploration.

This chapter aims to illustrate the numerical solution of new transport equation (4—1). A complete procedure which includes the discretization with respect to one-dimensional linear finite element; the evaluation of non-physical variables and the updating procedure; and the solution methods adopted.

4.2 Discretization of time dependent solidification problem

In Chapter 3, a direct mathematical relationship between the non-physical enthalpy $\hat{h}$ and the temperature T is given as

$$\hat{h} = \hat{c}T \tag{4—4}$$

where $\hat{c}$ is the non-physical capacitance.

The evaluation of non-physical capacitance $\hat{c}$ is conducted via equation (3—39). The mean-value approach allows $\hat{c}$ to come outside of the integration. For that reason, an equivalent matrix form of equation (4—1) is expressed as

$$\left[\hat{C}\right]\{\dot{T}\} + [K]\{T\} = \{Q\} + \{q\} + \{\hat{q}\} \tag{4—5}$$

where [■] indicates the coefficient matrix and {■} indicates the term is either a field variable vector or a loading vector, and $\dot{T} = \partial T/\partial t$. Details of each term are discussed as below. The element capacitance matrix $\left[\hat{C}\right]_e$ is given by

$$\left[\hat{C}\right]_e = \int_{\Omega_e} \{N\}^T \{N\} \hat{c}\, dV \tag{4—6a}$$

where $\hat{c}$ is the non-physical capacitance, the operator $■^T$ is the transposition of matrix or vector. The element capacitance matrix $\left[\hat{C}\right]_e$ has a superposed $\hat{C}$ to denote the non-physical property. Similarly, the element conductivity matrix is

$$[K]_e = \int_{\Omega_e} \{\nabla N\}^T \begin{bmatrix} k_{xx} & 0 & 0 \\ 0 & k_{yy} & 0 \\ 0 & 0 & k_{zz} \end{bmatrix} \{\nabla N\} dV \tag{4—6b}$$

where an orthotropic material is assumed here in the matrix $[K]_e$. The elements k_{xx}, k_{yy} and k_{zz} are the conductivities in the principle directions. The element loading vectors are:

$$\{Q\} = \int_{\Omega_e} \{N\}^T \rho Q dV \tag{4—6c}$$

$$\{q\} = \int_{\Gamma_e} \{N\}^T q \, d\Gamma \tag{4—6c}$$

and

$$\{\hat{q}\} = \int_{\Gamma_i} \{N\}^T \left] \underline{q} \cdot (-\underline{n}) \right[d\Gamma \tag{4—6e}$$

Direct integration of equation (4—6a) gives a non-diagonal matrix, which is called a consistent matrix. An alternative form is a lumped capacitance matrix, which is diagonal. This is believed to be stable and computational cost effective [62]. Though it is an advection problem, no advective term appears on the RHS of equation (4—5), because this is reflected in a change of non-physical enthalpy and therefore by a non-physical capacitance change. The vector $\{Q\}$ is the heat source, and $\{q\}$ relates to heat loading at the boundary. The loading vector $\{\hat{q}\}$ is a jump at the phase interface, it has to been evaluated on an element base for the fixed grid finite element method.

Applying the forward Eulerian difference approximation and the θ method for temporal approximation gives

$$\{\dot{T}\} = \frac{\{T^{n+1}\} - \{T^n\}}{\Delta t} \tag{4—7}$$

and

$$\{T\} = \theta\{T^{n+1}\} + (1-\theta)\{T^n\} \tag{4—8}$$

where Δt is the time interval, and $\theta \in [0, 1]$ is a blending coefficient. By setting the θ to different numbers, different approximation can be obtained, standard choices are:

$\theta = 0$, the explicit method;

$\theta = 0.5$, the Crank-Nicolson method;

$\theta = \frac{2}{3}$, the Galerkin method;

$\theta = 1$, the implicit method [109, 125].

For a blending term $\theta \geq 0.5$, the method is unconditionally stable [125]. But when $\theta < 0.5$, such as the explicit method, particular restrictions must be satisfied; otherwise instability problems will occur [125]. A limitation on the time interval for $\theta < 0.5$ is provided by

$$\Delta t < \hat{c}\frac{(L_e)^2}{2k} \tag{4—9}$$

where the capacitance $\hat{c}$ can be physical or non-physical, L_e is the length of a finite element, and k is the thermal conductivity [125].

Substitution of equations (4—7) and (4—8) into equation (4—5) gives

$$\left[\hat{C}\right]\frac{\{T^{n+1}\}-\{T^n\}}{\Delta t} + (\theta[K^{n+1}]\{T^{n+1}\} + (1-\theta)[K^n]\{T^n\}) = \theta\{Q^{n+1}\} + (1-\theta)\{Q^n\} + \theta\{q^{n+1}\} + (1-\theta)\{q^n\} + \theta\{\hat{q}^{n+1}\} + (1-\theta)\{\hat{q}^n\} \tag{4—10}$$

Rearranging equation (4—10) gives

$$\left(\left[\hat{C}^{n+1}\right] + \theta\Delta t[K^{n+1}]\right)\{T^{n+1}\} = \left(\left[\hat{C}^n\right] - (1-\theta)\Delta t[K^n]\right)\{T^n\} + \Delta t(\theta\{Q^{n+1}\} + (1-\theta)\{Q^n\}) + \Delta t(\theta\{q^{n+1}\} + (1-\theta)\{q^n\}) + \Delta t(\theta\{\hat{q}^{n+1}\} + (1-\theta)\{\hat{q}^n\}) \tag{4—11}$$

The non-physical capacitance $\hat{c}$ for each time step is evaluated through the linkage equation (4—11), then the matrix $\left[\hat{C}\right]$ is constructed through equation (4—6a). The conductivity matrix $[K]$ can change with time, the superscript n and $n+1$ refer to the present time step and the future time step. The conductivity is linear because the source is absent as discussed in Section 3.4.2. The loading vector $\{Q\}$ can be pre-defined if additional heat energy rate is applied to the system. The flux $\{q\}$ arises at the boundary which can be applied as conduction, convection or radiation. The non-physical vector $\{\hat{q}\}$ is evaluated by the jump equation. All the three loading vectors can be time dependent, but direct relationship between them and the temperature may not exist, and an update technique may be required.

In this chapter, a one-dimensional numerical model is used. The reason is to better explain the non-physical variable method and to compare with known analytical solutions.

The shape functions for a one-dimensional linear rod element are

$$\lfloor N \rfloor = \lfloor N_1 \; N_2 \rfloor = \left\lfloor \frac{1-\xi}{2} \; \frac{1+\xi}{2} \right\rfloor \tag{4—12}$$

where ξ is a local co-ordinate in a natural coordinate space, the bracket $\lfloor \blacksquare \rfloor$ signifies a row vector.

With regard to a linear isoparametric element, the spatial approximation is

$$x_e = N_1 x_1 + N_2 x_2 = \lfloor N \rfloor \{x\} \tag{4—13}$$

with node coordinates x_1 and x_2, the bracket $\{x\}$ signifies a column vector. Furthermore the approximated solution for temperature T_e with the nodal variable T_1 and T_2 is

$$T_e = N_1 T_1 + N_2 T_2 = \lfloor N \rfloor \{T\} \tag{4—14}$$

Figure 4.2 shows a sketch of a one-dimensional linear element. When $\xi = -1$, the approximate solution $T_e = T_1$, which is the temperature at position $x = x_1$; and when $\xi = 1$, the approximate solution $T_e = T_2$, which is the temperature at position $x = x_2$.

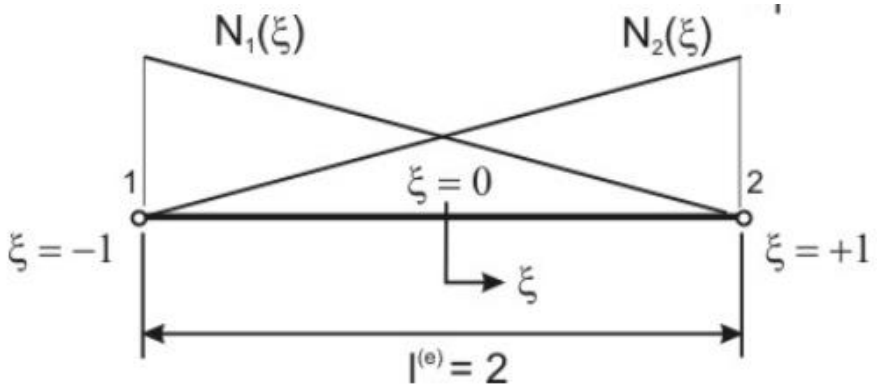

Figure 4.2: One-dimensional linear element

The non-physical element capacitance matrix $\left[\hat{C}\right]_e$ and the element conductivity matrix $[K]_e$ are estimated as

$$\left[\hat{C}\right]_e = \frac{\hat{c}L_e}{2} A_e \int_{-1}^{1} \begin{bmatrix} N_1 N_1 & N_1 N_2 \\ N_2 N_1 & N_2 N_2 \end{bmatrix} d\xi = \frac{\hat{c}A_e L_e}{2} \begin{bmatrix} \frac{2}{3} & \frac{1}{3} \\ \frac{1}{3} & \frac{2}{3} \end{bmatrix} \tag{4—15}$$

and

$$[K]_e = \frac{kL_e}{2} A_e \int_{-1}^{1} \left(\frac{\left\{ \frac{\partial N_1}{\partial \xi} \quad \frac{\partial N_2}{\partial \xi} \right\}}{\frac{1}{2} L_e} \right) \cdot \frac{1}{\frac{1}{2} L_e d\xi} \begin{Bmatrix} \frac{\partial N_1}{\partial \xi} \\ \frac{\partial N_2}{\partial \xi} \end{Bmatrix} d\xi = \frac{kA_e}{L_e} \begin{bmatrix} 1 & -1 \\ -1 & 1 \end{bmatrix} \tag{4—16}$$

respectively.

In the simulation of solidification, additional heat source is not under consideration, thus, $\{Q\} = \{0\}$. The vector $\{q\}$ is where the boundary conditions should apply, and is evaluated as

$$\{q\} = -\int_{\Gamma_e} \left(\begin{Bmatrix} N_1 \\ N_2 \end{Bmatrix} k\nabla \mathrm{T} \right) \cdot \underline{\mathrm{n}} d\Gamma = \begin{Bmatrix} q_i A_e \\ q_j A_e \end{Bmatrix} \quad (4—17)$$

It should be mentioned that, in the finite element approximation, two adjacent elements share the same boundary node, which will make the numerical flux q_j cancel for any node j shared by two elements after assembly. The cancellation of numerical flux is because that, at node j, the flux leaving the present element and the flux entering the next element are equal, but they have opposite direction and opposite signs in the equations. The jump term $\{\hat{q}\}$ is an integration over the phase interface Γ_i, but for the fixed grid finite element method, although the interface is able to be tracked by the temperature profile, but the information of interface such as position and velocity is not reflected in the mesh. In the FEM, all loading vectors are applied on the nodes, however, the interface position does not always coincide with the position of nodes. As a consequence, the term $\{\hat{q}\}$ needs to be approximated in another way, and its approximation should be coupled to the approach taken with the non-physical capacitance.

4.3 The solution procedure

It can be seen from equations (3—41) and (3—43) that, the non-physical enthalpy and the non-physical source are dependent on both the temperature of present time step and the temperature of future time step. An update procedure is required.

Assuming that the temperature of the present time $\{T^n\}$ step is known, with given material properties, BCs and ICs, the following steps are generally followed.

(1) Obtain the predicted temperature of the future time step, which is denoted as $\{T_p^{n+1}\}$. The approach can be the techniques such as explicit method, the predictor-corrector method, etc.;
(2) Obtain element liquid fraction Υ_l or element solid fraction Υ_s using equations (3—49);

(3) Evaluate each term appearing in equations (3—36) with the temperature $\{T^n\}$, $\{T_p^{n+1}\}$ and element solid fraction Υ_s via equations (3—38) (3—41), (3—46), and (3—53);

(4) Evaluate the non-physical capacitance $\hat{c}$ and source $\hat{q}$ through equations (3—39) and (3—41), evaluate the conductivity k^n through equation (3—53);

(5) Construct coefficient matrices and loading vectors via equations (4—15), (4—16) and (4—17);

(6) Solve the system of equations and obtain $\{T^{n+1}\}$,

(7) If $\{T^{n+1}\}$ satisfies the error criteria, go to the next time step, i.e. $\{T^{n+1}\} \rightarrow \{T^n\}$, if not $\{T^{n+1}\} \rightarrow \{T_p^{n+1}\}$, go through (1) to (7) again at the current time step.

4.4 Solution methods

Equation (4—11) can in principle be solved with a computational method. The determination of the non-physical capacitance and non-physical source (if discontinuity removal applied) however requires information from both the present time step and future time step; in other words, no explicit method is able to solve the equations. Thus, good iterative and convergent methods are required for the determination of accurate solutions. Previous studies made use of the bisection method along with the Successive-Over-relaxation method to solve the problem [62-63]. This approach is relatively straightforward and was able to provide good results. However, it failed to converge in certain case arising because the bisection method requires that the exact solution is in between of the predicted solution and the computed solution. Considered here are three alternative methods, which are the Predictor-Corrector method, the Secant method and the Homotopy method. It can be seen in equation (4—11) that the coefficient matrices are dependent on the unknown field variables. This makes the system of equations nonlinear, which means that the system of equations may have more than one solution, and the solution obtained may not be the desired solution [125]. For that reason, an iterative method is required. The Predictor-Corrector method is believed to be an accurate and time-efficient method which was firstly developed by Gresho *et. al.* [119], who originally applied it to the Navier-Stokes equations [109]. The predictor-corrector method is used to solve typical parabolic PDE (see Jacques [115]) and high order parabolic PDEs (see Houwen *et al*. [116]). Methods for improved stability are shown by Van et al. in reference [117] and Codina and Folch in reference [118]. The secant method is an extension of the Newton-Raphson Method. It inherits the advantage of Newton-Raphson method, which is

considered as a rapid convergence method, and it has been applied to the non-linear problems in solid-mechanics [126]. A potential disadvantage with the secant method is that it requires an effective guess at the initial value to start the procedure. The homotopy method developed by Liao [120] is believed to be a good way of finding a starting value. Practical applications of homotopy method can be found in [113, 121]. In this project, the predictor-corrector method is frequently adopted. The performance of it is generally acceptable, despite that oscillations may occur at the boundary where Robin boundary conditions are applied. The instability could be solved by using large number of iteration step (100); using a refined mesh; and setting the initial temperature of the boundary node slightly below the solidus temperature such as 399.99 ℃ if the solidus temperature is 400 ℃. The performance of secant method is limited by the matrix inversion routine from NAG Fortran library [127]. Only a maximum of 66×66 matrix can be inverted which limits the maximum element number to 65. The homotopy method is the slowest solver in the programme and it is also limited at 65. It can be utilised when the secant method fails to converge.

Details of the three solution methods are described below.

4.4.1 The predictor-corrector method

Equation (4—11) can be rewritten in the form

$$\left(\left[\hat{C}(T^{n+1},T^{n})\right]+\theta\Delta t[K(T^{n+1},T^{n})]\right)\{T^{n+1}\}=\left(\left[\hat{C}(T^{n+1},T^{n})\right]-(1-\theta)\Delta t[K(T^{n+1},T^{n})]\right)\{T^{n}\}+\Delta t(\theta\{Q^{n+1}\}+(1-\theta)\{Q^{n}\})+\Delta t(\theta\{q^{n+1}\}+(1-\theta)\{q^{n}\})+\Delta t(\theta\{\hat{q}^{n+1}\}+(1-\theta)\{\hat{q}^{n}\}) \quad (4—18)$$

which highlights which parameters are dependent on the present time-step temperature and the future time step temperature. The difficulty with equation (4—18) is the implicit nature of the problem with the future temperature T^{n+1} unknown. In the Predictor-Corrector method, the predictor computes a temperature field noted as T_p^{n+1}. Then, the predicted matrices $\left[\hat{C}\right]$ and $[K]$ are computed according to the temperature field T_p^{n+1}. In the next step, the new T^{n+1} is calculated by solving a linear system of equations. The relative error in T^{n+1} is determined and compared with ϵ by

$$\left|{T_k}^{n+1}-{T_{k-1}}^{n+1}\right|\leq\epsilon \quad (4—19)$$

where the subscript k refers to the kth iteration, and the tolerance ϵ is prescribed, i.e. $\epsilon = 1.0\times10^{-8}$.

If the temperature of future time step T^{n+1} satisfies equation (4—19), the program proceeds to the next time step, and if the error is not small enough, the new T^{n+1} will be regards as the T_p^{n+1} for the next iteration. In this study, a predictor which is outlined in reference [119], and it is commonly used for the solution of Navier-Stokes equations, is applied and is of the form

$$\{T_p^{n+1}\} = \{T^n\} + \frac{\Delta t_n}{2}\left(\left(2 + \frac{\Delta t_n}{\Delta t_{n-1}}\right)\{\dot{T}^n\} - \left(\frac{\Delta t_n}{\Delta t_{n-1}}\right)\{\dot{T}^{n-1}\}\right) \quad (4—20)$$

From equation (4—20), it can be see that, in order to compute the predicted future time-step temperature T_p^{n+1}, values of the temperature is required at least three time-steps prior to the future time-step t^{n+1}. At the initial two steps, there is insufficient data for the prediction to be performed, thus, it is reasonable to use alternative crude approximations. The initialisation procedure is as follow:

In the first time step, the initial temperature is set above the solidus temperature, the material is in liquid phase, and the material properties are constant in this step. So, the explicit method ($\theta = 0$) is used;

In the second time step, the explicit method is used as a predictor. The result from the explicit method will be used to update the material properties, and then the implicit method is used to get the 'true' values of the next time-step temperature;

For other time steps, the 3-time-step temperature is ready and can be substituted into the predictor (4—20).

Because the initial two steps use the explicit method, it is important that the time steps should be chosen conservatively. And they should satisfy the restriction as presented in equation (4—9). Equation (4—20) allows for variable time interval. To make the problem simpler, a constant time interval is used here, and equation (5—20) reduces to

$$\{T_p^{n+1}\} = \{T^n\} + \frac{\Delta t_n}{2}\left(3\{\dot{T}^n\} - \{\dot{T}^{n-1}\}\right) \quad (4—21)$$

and similarly to equation (5—18), the corrector is given as

$$\left(\left[\hat{C}\left(T_p^{n+1},T^n\right)\right]+\theta\Delta t\left[K\left(T_p^{n+1},T^n\right)\right]\right)\{T^{n+1}\}=\left(\left[\hat{C}\left(T_p^{n+1},T^n\right)\right]-(1-\theta)\Delta t\left[K\left(T_p^{n+1},T^n\right)\right]\right)\{T^n\}+\Delta t(\theta\{Q^{n+1}\}+(1-\theta)\{Q^n\})+\Delta t\left(\theta\left\{q_p^{n+1}\right\}+(1-\theta)\{q^n\}\right)+\Delta t\left(\theta\left\{\hat{q}_p^{n+1}\right\}+(1-\theta)\{\hat{q}^n\}\right) \quad (4—22)$$

where the presence of T_p^{n+1} is found.

Equation (4—22) provides a linear system of equations, and methods, such as the Successive Over-Relaxation method, the Gauss-Jordan method and the Lower-Upper (LU) decomposition method, can be used to solve it and thus provide a solution to equation (4—11).

4.4.2 The secant method

The secant method is an extension of the Newton-Raphson Method. The development of the methods starts from the Taylor-series expansion of a function $f(x)$, i.e.,

$$f(x)=f(x_0)+f'(x_0)(x-x_0)+\frac{f''(x_0)}{2!}(x-x_0)^2+\cdots \quad (4—23)$$

which on letting $f(x)=0$, the following approximation can be obtained:

$$f(x_0)+f'(x_0)(x-x_0)\approx 0 \quad (4—24)$$

An iterative procedure can be gained by rearranging equation (4—24)

$$x_{k+1}=x_k-\frac{f(x_k)}{f'(x_k)} \quad (4—25)$$

Since the solution x_{k+1} is not the exact solution, the iteration should stop when x_{k+1} satisfies the desired tolerance, for example $|f(x_{k+1})|\leq\epsilon$, where the subscript k refers to the kth iteration.

The Newton-Raphson Method described by equation (4—25) can be applied to equation (4—11) by letting

$$\{F(T^{n+1})\}=\left(\left[\hat{C}(T^{n+1},T^n)\right]+\theta\Delta t[K(T^{n+1},T^n)]\right)\{T^{n+1}\}-\left(\left[\hat{C}(T^{n+1},T^n)\right]-(1-\theta)\Delta t[K(T^{n+1},T^n)]\right)\{T^n\}-\Delta t(\theta\{Q^{n+1}\}+(1-\theta)\{Q^n\})-\Delta t(\theta\{q^{n+1}\}+(1-\theta)\{q^n\})-\Delta t(\theta\{\hat{q}^{n+1}\}+(1-\theta)\{\hat{q}^n\}) \quad (4—26)$$

and seeking the T^{n+1} that satisfies

$$F(T^{n+1}) = 0 \tag{4—27}$$

The generalized iterative equation should be

$$\{T_{k+1}^{n+1}\} = \{T_k^{n+1}\} - [J]^{-1}\{F(T_k^{n+1})\} \tag{4—28}$$

where

$$[J_{ij}] = \left[\frac{\partial F_i}{\partial T_j}\right] \tag{4—29}$$

is the Jacobian matrix, which is a $n \times n$ matrix. Where $i = 1, 2, \dots, n \; and \; j = 1, 2, \dots, n$

It is relatively easy to find the value of $F(T_k^{n+1})$, but the evaluation of $F'(T_k^{n+1})$ is the main barrier. As a consequence, the secant method is introduced. In the secant method, the derivative is approximated as

$$\frac{\partial F_i}{\partial T_j}(T_k^{n+1}) \approx \frac{F_i(T_k^{n+1}) - F_i(T_{k-1}^{n+1})}{{T_j}_k^{n+1} - {T_j}_{k-1}^{n+1}} \tag{4—30}$$

where the subscript i denotes the i th equation, and the subscript j denotes the jth nodal temperature.

Substituting equation (4—30) into equation (4—28) gives the generalized iterative equation of the secant method

$${T_j}_{k+1}^{n+1} = {T_j}_k^{n+1} - \frac{{T_j}_k^{n+1}}{F_i(T_k^{n+1}) - F_i(T_{k-1}^{n+1})}\left({T_j}_k^{n+1} - {T_j}_{k-1}^{n+1}\right) \tag{4—31}$$

The secant method avoids the evaluation of the derivative $\partial F_i(T_k^{n+1})/\partial T_j$, it however demands one additional initial value.

Rather than a single equation, in the finite element method, it usually contains a system with n equations that are required to be solved, where n is the total number of nodes. Consequently, in order to solve the system of non-linear equations, the Jacobian matrix of the system should be generated in the first place. Each element of Jacobian matrix can be approximated as

$$\frac{\partial F_i}{\partial T_j} \approx \frac{F_i\left(T_{1,k}^{n+1}, T_{2,k}^{n+1}, \dots, T_{j,k}^{n+1} + \Delta T, \dots, T_{n,k}^{n+1}\right) - F_i\left(T_{1,k}^{n+1}, T_{2,k}^{n+1}, \dots, T_{j,k}^{n+1}, \dots, T_{n,k}^{n+1}\right)}{\Delta T} \tag{4—32}$$

where the first number in the subscript of T^{n+1} denotes the nodal numbers, and the increment ΔT is user-defined.

4.4.3 The homotopy method

The linear homotopy equation for equation (4—26) is

$$\mathrm{H}(\mathrm{T}^{n+1},\lambda) = \lambda F(\mathrm{T}^{n+1}) + (1-\lambda)G(\mathrm{T}^{n+1}) \quad (4—33)$$

where the auxiliary function $G(\mathrm{T}^{n+1})$ is user-defined, which can lead to two well-known homotopy methods which are the fixed point homotopy method (FPH) [112, 121, 123]

$$G(\mathrm{T}^{n+1}) = T^{n+1} - \mathrm{T}_0^{n+1} \quad (4—34a)$$

and the Newton Homotopy method (NH) [122-123]

$$G(\mathrm{T}^{n+1}) = F(\mathrm{T}^{n+1}) - F(\mathrm{T}_0^{n+1}) \quad (4—34b)$$

where T_0^{n+1} is the is the initial assumption of T^{n+1}.

Substitution of equations (4—34a) and (4—34b) into equation (4—33) gives homotopy equations for each method as

$$\mathrm{H}(\mathrm{T}^{n+1},\lambda) = \lambda F(\mathrm{T}^{n+1}) + (1-\lambda)(T^{n+1} - T_0) = 0 \quad (4—35)$$

and

$$\mathrm{H}(\mathrm{T}^{n+1},\lambda) = F(\mathrm{T}^{n+1}) + (\lambda-1)F(\mathrm{T}_0^{n+1}) = 0 \quad (4—36)$$

Respectively, where $\lambda \in [0,1]$. For equation (4—35), when $\lambda = 0$, the function has a unique solution $T^{n+1} = \mathrm{T}_0^{n+1}$, and when $\lambda = 1$, $\mathrm{H}(\mathrm{T}^{n+1},1) = F(\mathrm{T}^{n+1})$. While equation (4—36) is slightly more complex than equation (4—35), but it widely used because it does not change the Jacobian matrix. The FPH failed to converge in the program of this subject, consequently, the NH is applied.

In order to solve the homotopy equation as shown in equation (4—36) the parameter λ should be discretised, such as $0 = \lambda_0 < \lambda_1 < \cdots < \lambda_m = 1$. Practically, the larger the m is, the more possibility the homotopy equation converges. The relationship of the homotopy method and secant method is depicted in Figure 4.3. For the secant method, if the initial

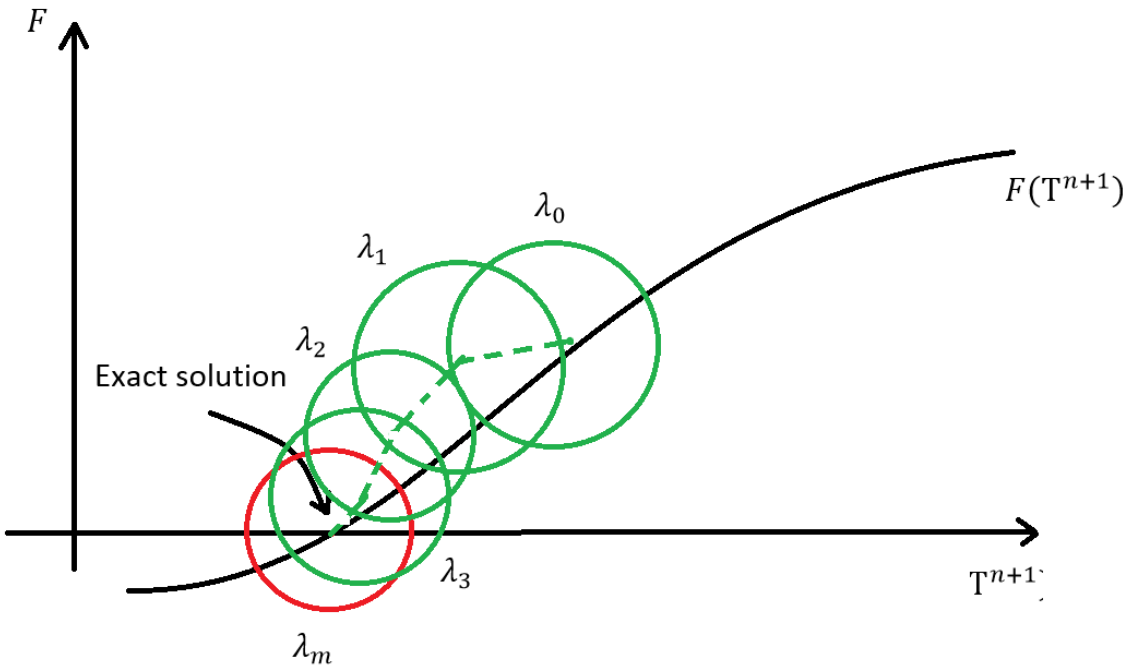

Figure 4.3: The homotopy method and the secant method

assumption of $\mathrm{T}_{\mathrm{p}}^{n+1}$ does not fall into the red circled area, the solution may not be found. The homotopy method is able to create a path for the predicted value $\mathrm{T}_{\mathrm{p}}^{n+1}(\lambda)$, and the path will lead the solutions to the exact solution.

For every value of λ_m, the secant method can be used. For example, when $m = 1$, the homotopy equation is

$$\mathrm{H}(\mathrm{T}^{n+1}, \lambda_1) = F(\mathrm{T}^{n+1}) + (\lambda_1 - 1)F(\mathrm{T}_0^{n+1}) \tag{4—37}$$

And its related Jacobian is

$$J_{ij} = \frac{\partial H_i}{\partial T_j} \approx \frac{H_i\left(T_{1,k}^{n+1}, T_{2,k}^{n+1}, \ldots, T_{j,k}^{n+1} + \Delta T, \ldots, T_{n,k}^{n+1}, \lambda_1\right) - H_i\left(T_{1,k}^{n+1}, T_{2,k}^{n+1}, \ldots, T_{j,k}^{n+1}, \ldots, T_{n,k}^{n+1}, \lambda_1\right)}{\Delta T} \tag{4—38}$$

So, the solution can be approximated as

$$\{T_{k+1}^{n+1}\} = \{T_k^{n+1}\} - [J]^{-1}\{H(T_k^{n+1}, \lambda_k)\} \tag{4—39}$$

Once the value of $\{T_{k+1}^{n+1}\}$ is calculated, it should be substituted back to the $\mathrm{H}(\mathrm{T}^{n+1}, \lambda)$, and if

$$|H(\mathrm{T}_{k+1}^{n+1}, \lambda)| \leq \epsilon \tag{4—40}$$

then set $T_0^{n+1} = T_{k+1}^{n+1}$ and $\lambda = \lambda_{k+1}$, Proceed in this manner until $\lambda = 1$, and a good numerical solution of $F(T^{n+1})$ is obtained.

The accuracy and the computational time for each method is presented in Table 4.1. The data is obtained on the basis of 50-element mesh, and the total number of times steps is 800. The percentage error is calculated on the basis of node 41 ($x = 0.02m$). It can be seen in the table that, the predictor-corrector method provides the fastest computation. However, during the experiments, this method sometimes suffers numerical oscillations. The secant method uses only 9 seconds longer than the predictor-corrector method, but due to the limitation of routine programmed, it only applies to the mesh with less than 66 nodes. The homotopy method takes the longest time for computation, but this method promises the highest possibility for convergence.

	x=0.02 m	
Solver	CPU time (sec)	Max. error (%)
Predictor-Corrector	141.26	2.71
Secant	150.01	3.89
Homotopy	22953.49	1.65

Table 4.1: Comparison of time efficiency and accuracy between solvers

4.5 The numerical experiments – stationary

4.5.1 Problem description

4.5.1.1 The experiment set-up

A one-dimensional material region is drawn in Figure 4.4. The material is pure zinc and its material properties are shown in the Table 4.2. The temperature of the material is initially uniform and above the liquidus temperature, which is $T_{init} = 405℃$. The boundary conditions are set to make the numerical tests match the analytical solution of Stefan problem

discussed in Chapter 2. The Robin boundary condition is applied to the left end of the material region, which is $k_s(\partial T/\partial x)|_{x=0} = h_c(T - T_{amb})$, where h_c is the forced convective coefficient and $T_{amb} = 25℃$ refers to the ambient temperature. On the other end, the boundary condition $k_s(\partial T/\partial x)|_{x=0.1} = 0$ is applied. For the rest of the material region, the boundary is insulated. The material will cool down from the left end, when the temperature drops below the liquidus temperature, the phase transformation begins, and the solid/liquid phase interface propagates from the left to the right. If the hot liquid material flows into the region from the right end, and colder material leaves the region from the left end, then the material velocity $\|\underline{v}\| \neq 0$, and the problem becomes a transient advection-diffusion problem, which will be discussed later. Firstly, the material velocity is set to 0.

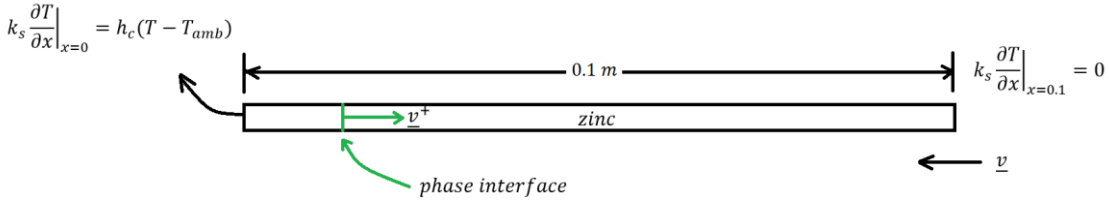

Figure 4.4: One dimensional solidification problem

Material Name	Pure Zinc
Thermal conductivity of solid (k_s)	$100W/m℃$
Thermal conductivity of liquid (k_l)	$50W/m℃$
Heat capacitance of solid (c_s)	$400J/kg℃$
Heat capacitance of liquid (c_l)	$500J/kg℃$
Density of solid (ρ_s)	$6900kg/m^3$
Density of liquid (ρ_l)	$6600kg/m^3$
Latent Heat (l)	$130000J/kg$
Solidus temperature (T_{sol})	400℃
Liquidus temperature (T_{liq})	400℃

Table 4.2: The material properties

4.5.1.2The mesh

The model as shown in Figure 4.5 is meshed with one-dimensional linear rod elements. It is commonly known that increasing the density of mesh will get more accurate results. In this group of test, 100, 200 and 400 elements are used to mesh the model. By testing with different mesh density, the influence of mesh size on the non-physical variable method can be identified. To make the results comparable between meshes, the nodes placed at $x = 0.02\ m$ and $x = 0.03\ m$ are picked. Because of different mesh sizes, the node numbers are different, for example, when the total element number (NELS) is 100, the example nodes are numbered 21 and 31; when the NELS is 200, the example nodes are numbered 41 and 61; and when the NELS is 400, the example nodes are numbered 81 and 121.

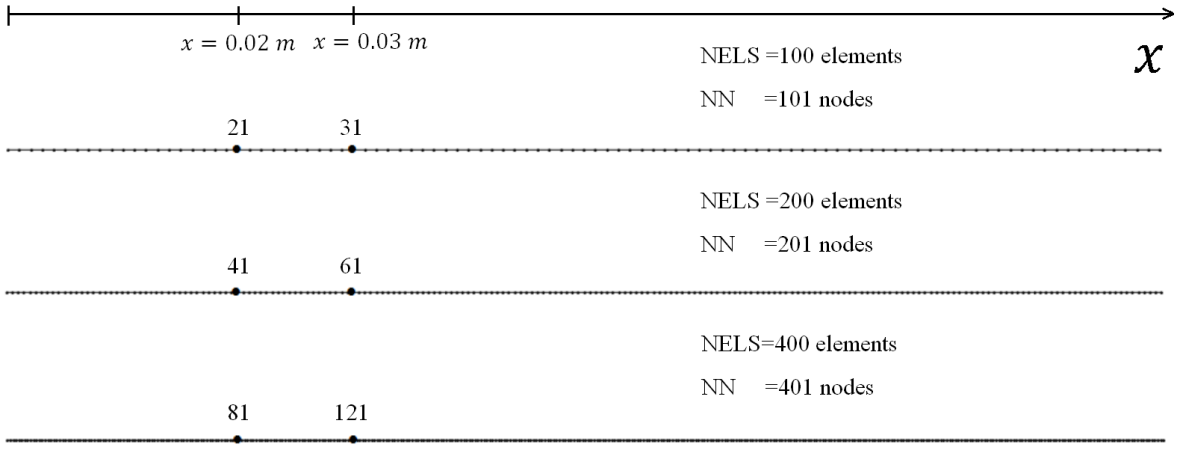

Figure 4.5: The one-dimensional mesh by FEM

The material is cooled over a period of 40 seconds. To examine the influence of time step size Δt, it is set as $\Delta t = 0.05\ sec$ or $\Delta t = 0.5\ sec$ respectively. Accordingly, there are 800 time steps or 80 time steps.

4.5.2 Results returned from non-physical capacitance method

The numerical results presented here are returned through programs written in Fortran 95 programming language. It has been indicated previously that the mesh density affects the performance of capacitance methods. With a crude mesh, the capacitance method suffers inaccuracy, wrong phase transformation time and oscillations in temperature after phase change [7, 28, 128]. In addition, it is illustrated previously that, when the material velocity $\underline{v} = \underline{0}$ and the discontinuity removal procedure does not apply, the non-physical enthalpy method returns to the non-physical capacitance method. The evaluation of the non-physical

capacitance or the control volume capacitance is provided by equation (3—55). The non-physical capacitance method is then categorised as a capacitance method. The following experiments test the performance of non-physical capacitance method with different time step sizes and mesh sizes.

Figure 4.6 and Figure 4.7 show the history of temperature at $x = 0.02\ m$ and $x = 0.03\ m$, respectively. The comparisons are conducted between the meshes: NELS=100, NELS=200 and NELS=400, which are shown in Figure 4.5. The results from different meshes are distinguished by different colours, and they are compared with the exact solution given in Chapter 2. The exact solution is plotted in black. It can be seen that, with a greater number of elements, such as 400, the method can provide more accurate results. However, somewhat surprisingly a mesh consisting of 100 elements provides greater accuracy than 200 elements.

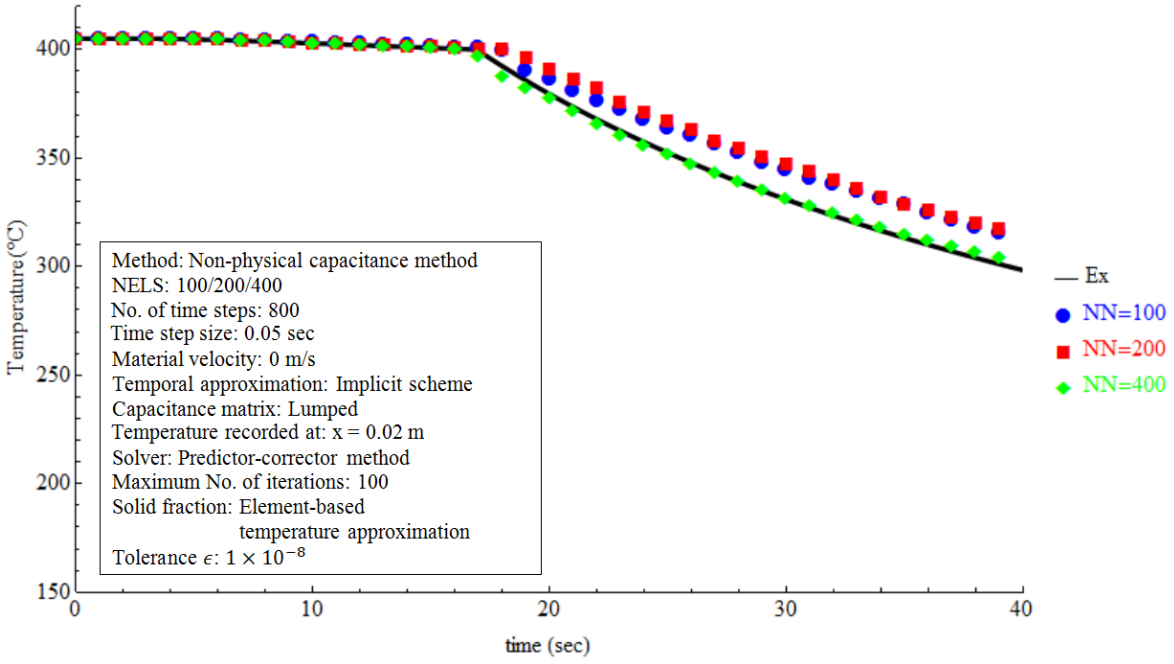

Figure 4.6: History of temperature at $x = 0.02\ m$, the non-physical capacitance method

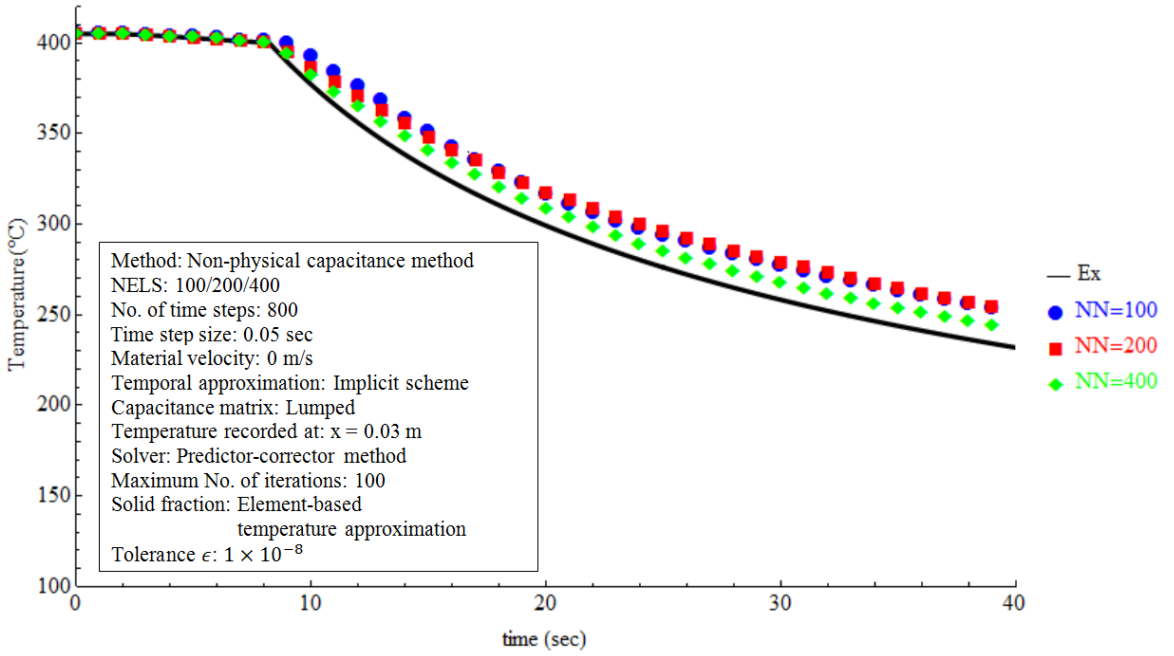

Figure 4.7: History of temperature at $x = 0.03\ m$, the non-physical capacitance method

Total number of elements	x = 0.02m		x = 0.03m		CPU time (sec)
	Max. difference (℃)	Max. error (%)	Max. difference (℃)	Max. error (%)	
100	22.52	8.33	15.58	4.98	347.85
200	21.37	8.93	17.23	5.47	1247.73
400	11.21	4.53	4.58	1.16	4980.05

Table 4.3: Error of the non-physical capacitance method with different mesh sizes

Table 4.3 presents the maximum difference and maximum percentage error of the non-physical capacitance method. When applying the Robin boundary conditions, the nodes close to the boundary provide greater error, i.e. the error of node 41 in a 200-element mesh is 8.93%. Increasing the mesh density will improve the accuracy, the mesh density is increased from 200 elements to 400 elements, the error is reduced from 8.93 % to 4.53 %, but with a cost of more time, i.e., it requires 4980.05 CPU time to run a 400-element methods, which is about 4 times longer than the 200-element mesh (only 1247.73 seconds required).

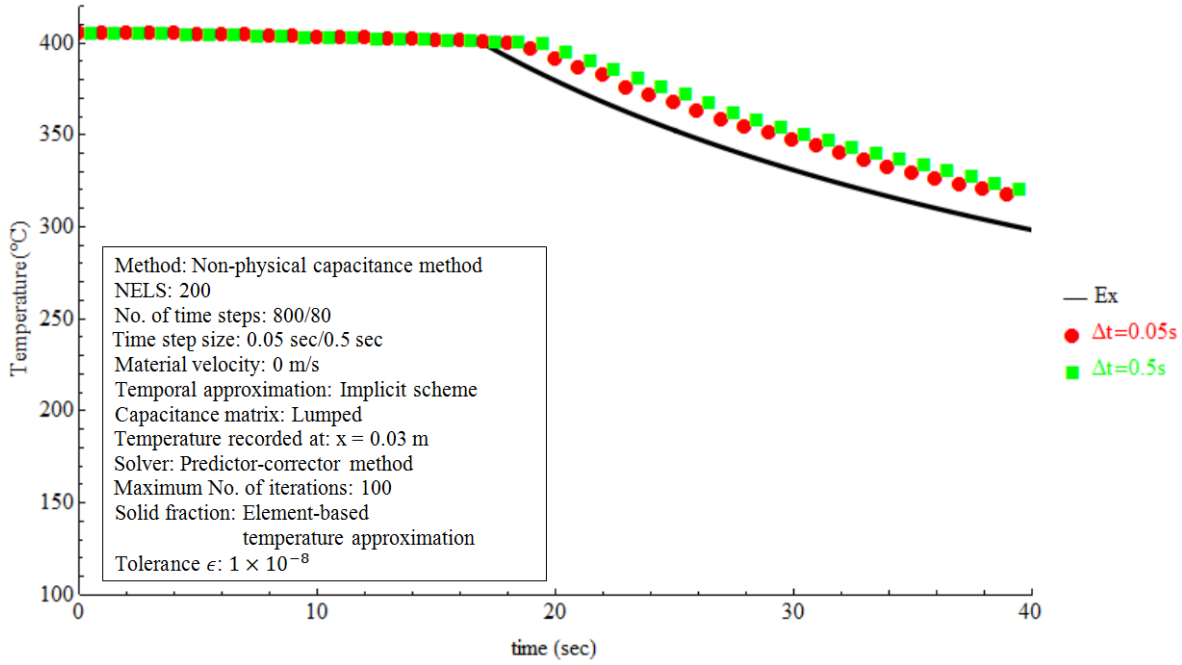

Figure 4.8: Numerical solutions with different time step sizes

Time step size Δt	x=0.03 m		CPU time (sec)
	Max. difference (℃)	Max. error (%)	
0.05	17.23	5.47	1247.73
0.50	22.31	7.13	123.43

Table 4.4: Error of the non-physical capacitance method with different time step sizes

The Figure 4.8 gives the plot of nodal temperature. The nodal temperatures are obtained by setting the time step size Δt to 0.5 s and 0.05 s, respectively. Reducing the time step size will increase the cost of CPU time, if the time step size is increased from 0.05 sec to 0.5 sec, the cost of CPU time drops from 1247.74 sec to just 123.43 sec,. However, the change of time step does not improve the accuracy that significantly, the error grows 1.66 % from 5.47 %.

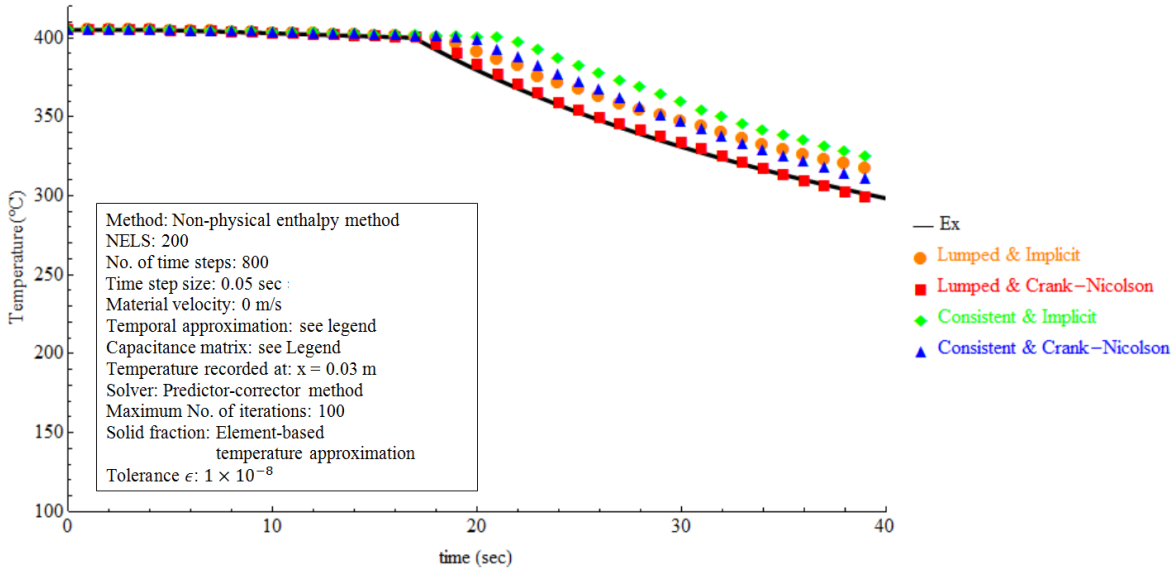

Figure 4.9: The format of matrix and the approximation of time derivative

Figure 4.9 shows how the combination of the matrix format and the approximation of time derivative can affect the numerical results. The phase transformation time is delayed in the simulated conducted with a consistent capacitance matrix, since very small oscillations are presented in the numerical solution. The Crank-Nicolson method is able to gain second order accuracy [109, 125]. The experiments show that it is more accurate than the implicit method which only provides first order accuracy [125]. This figure indicates that the Lumped capacitance matrix combined with the Crank-Nicolson time approximation provides the most accurate results, however there exists a small undulation in the result calculated with the lumped capacitance matrix just after the phase change. In Table 4.5, the Lumped matrix and the Crank-Nicolson method reduces the maximum percentage error to only 1.6199 %. However, the improvement does not require extra computational time.

	x=0.03 m		
Matrix format and temporal approximation	Max. difference (℃)	Max. error (%)	CPU time (sec)
Lumped and implicit	17.23	5.47	1247.73
Lumped and Crank-Nicolson	6.19	1.62	1259.55
Consistent and implicit	30.33	9.03	1259.85
Consistent and Crank-Nicolson	20.35	5.69	1263.98

Table 4.5: Error of the non-physical capacitance method with combination

The numerical experiments so far present the performance of non-physical capacitance method in one-dimensional simulation. In the non-physical capacitance method, the evaluation of non-physical capacitance as achieved by equation (3—55). It shows that the lumped capacitance matrix performs well with the non-physical capacitance method. And with the Crank-Nicolson method, the accuracy with maximum error equal to 1.62% can be achieved. The non-physical capacitance method works well with different meshes, it is accurate and the wrong phase transformation time of classical capacitance method does not affect the non-physical capacitance method.

4.5.3 Results returned from non-physical discontinuity annihilation method

In the subsequent numerical experiments, the non-physical source method is the focus of the study. In Section 3.5.2, the removal of discontinuity from the non-physical capacitance is presented. The non-physical capacitance becomes linear, and the change in it is small in its magnitude. However, the discontinuity returns as a source. The following numerical results show the performance of non-physical source method.

A temperature history at $x = 0.02\ m$ and $x = 0.03\ m$ calculated by the non-physical source method, are shown in Figures 4.10 and 4.11, respectively. The comparisons are conducted between the meshes: NELS=100, NELS=200 and NELS=400, which are shown in Figure 4.5. The results from different meshes are distinguished by different colours, and they are compared with the exact solution given in Chapter 2. The exact solution is plotted in black. The maximum error and the percentage error are presented in Table 4.6. To prevent the temperature overflow and inaccurate phase transformation time for non-physical source method, a blending parameter can be applied to the nodal temperatures between two iteration steps, i.e.:

$$\{T^{n+1}\}_p = \vartheta\{T_{k-1}^{n+1}\} + (1-\vartheta)\{T_k^{n+1}\} \qquad (4—41)$$

where the blending parameter $\vartheta \in [0,1]$ and in this project $\vartheta = 0.7$. Since the effect of latent heat may not be present in the predictor step, the predicted nodal value (i.e. temperature) may be lower than the true value. This blending technique artificially bringing the predicted value back to be closer to the true value. When the parameter $\vartheta = 0$, the predicted temperature is the result of present iteration. When the parameter $\vartheta = 1$, the predicted temperature is the result of previous iteration. The subscript k is the number of iteration step.

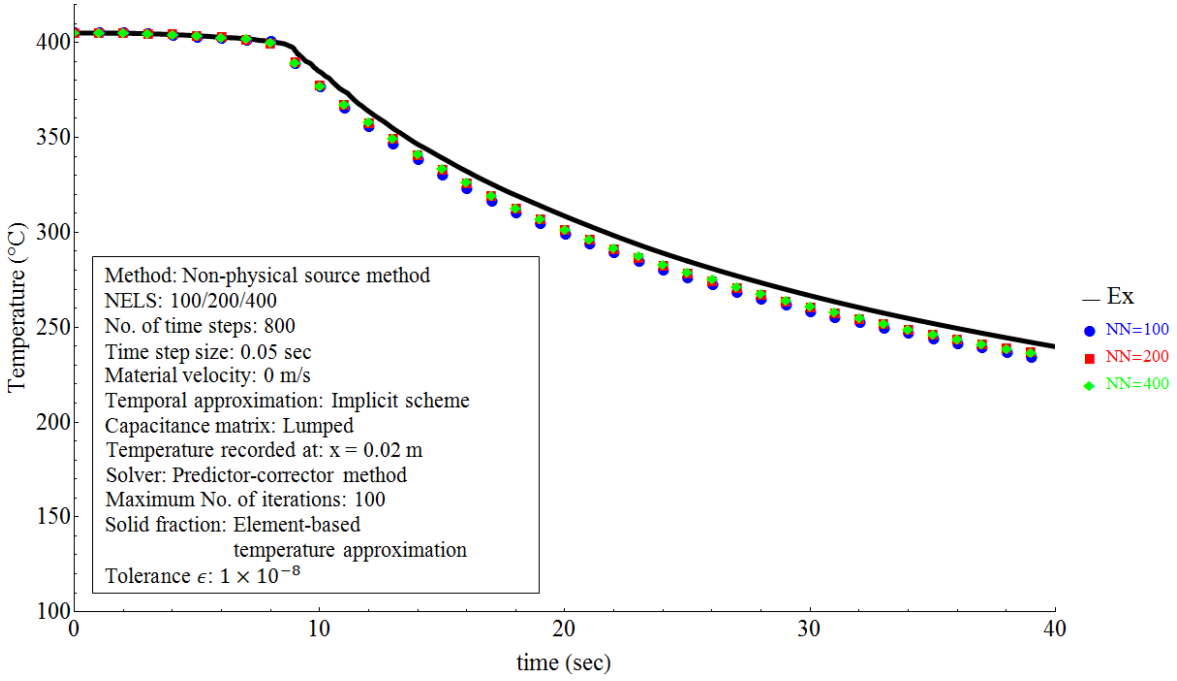

Figure 4.10: History of temperature at $x = 0.02\ m$, the non-physical source method

Comparison between Table 4.3 and Table 4.6, it can be seen that the non-physical source method is generally more accurate than the non-physical capacitance method. It is because most terms of equation (4—1) are now continuous. It means that continuous approximation of finite element method can be applied. The discontinuity is isolated in the non-physical source, and it can be treated analytically. For example, when the mesh is 100-element and at $x = 0.03m$, the maximum percentage error for the non-physical capacitance method is 4.98%, but the maximum percentage error is only 2.18% for non-physical source method. However, the non-physical source method requires 27.44% extra time for execution.

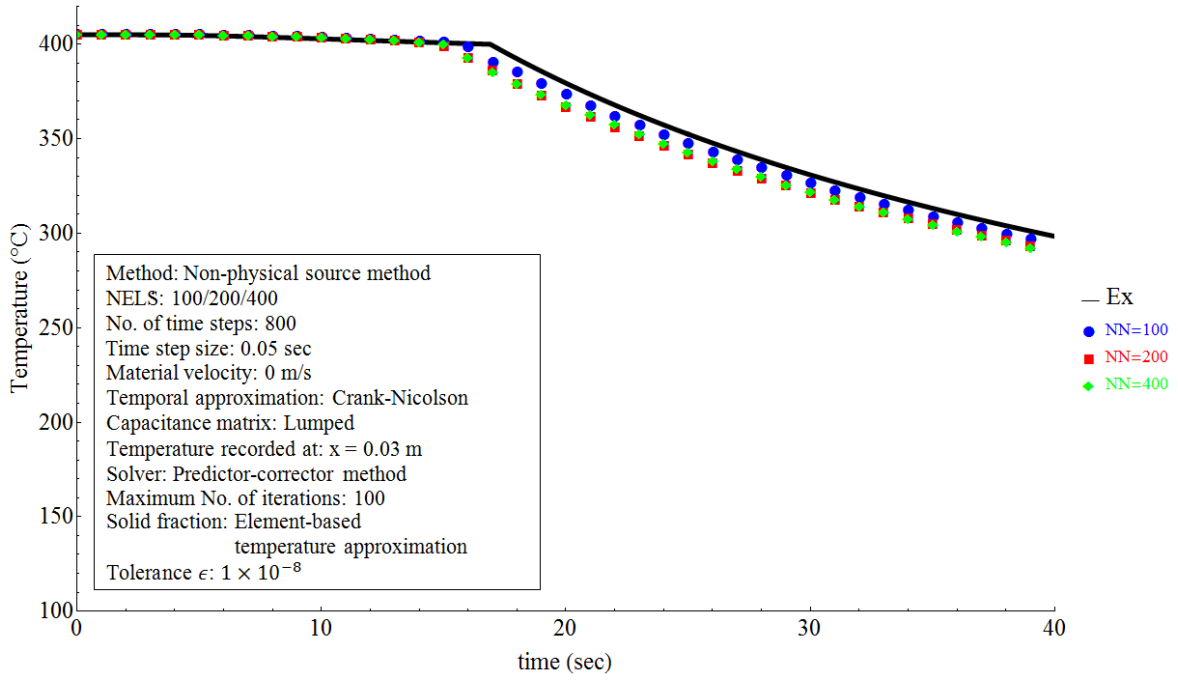

Figure 4.11: History of temperature at $x = 0.03\ m$, the non-physical source method

Total number of elements	x = 0.02m		x = 0.03m		CPU time (sec)
	Max. difference (℃)	Max. error (%)	Max. difference (℃)	Max. error (%)	
100	9.47	3.42	8.17	2.18	436.66
200	2.95	1.17	13.08	3.35	1533.91
400	3.59	1.10	14.16	3.56	6665.41

Table 4.6: Error of the non-physical source method with different mesh sizes

Figure 4.12 shows the non-physical capacitance calculated by equation (3—55), in which the discontinuity is embodied. The example elements are element 21 and element 31 from a 100-element mesh. It can be seen that the peak is generated due to phase change and the release of latent heat just like it is from the analysis by exact solution in Section 2.1. The application of non-physical source term method annihilates the discontinuity in the non-physical capacitance, and it can be seen in Figure 4.13.

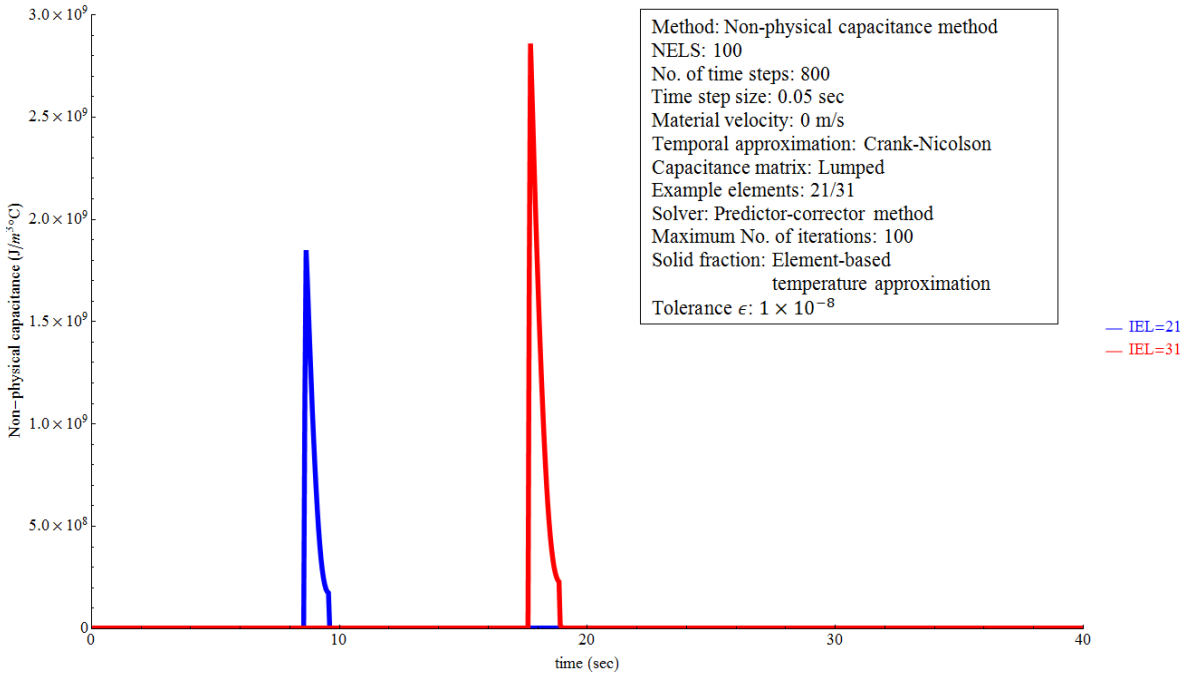

Figure 4.12: Non-physical capacitance embodies the discontinuity

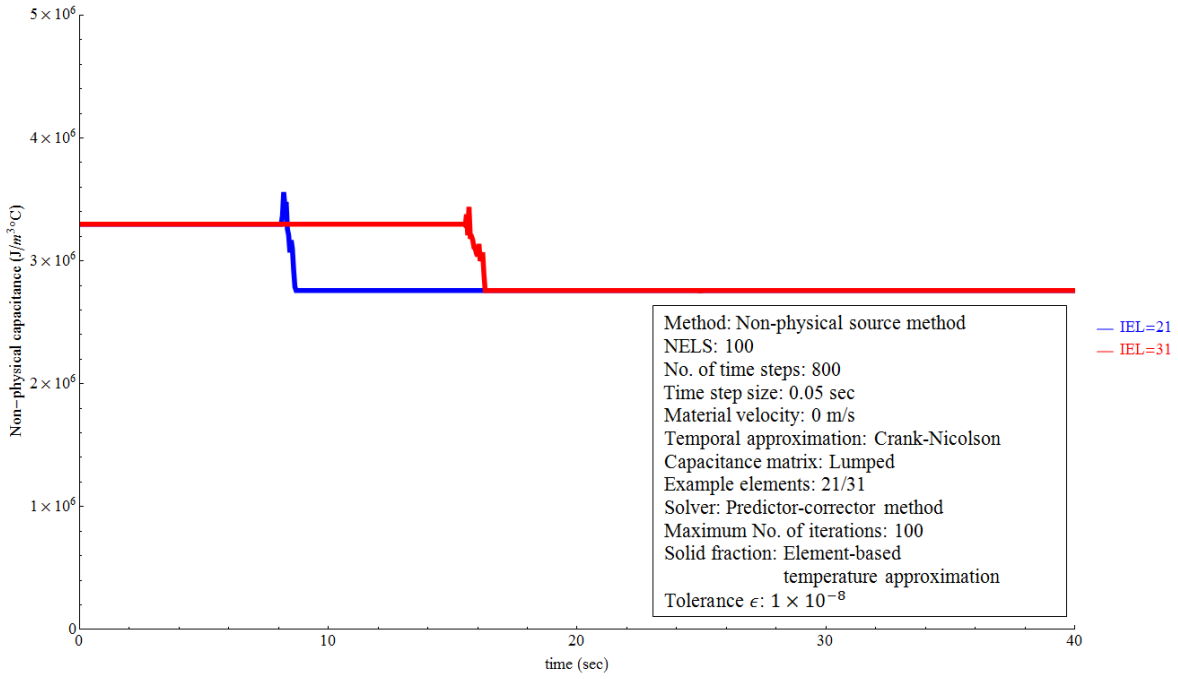

Figure 4.13: Non-physical capacitance, the discontinuity removed

In the previous tests, the discontinuity is not completed annihilated from the linkage equation (3—36). However, with the smoothed solid/liquid volume fraction and right combination of the capacitance matrix and the time derivative approximation, the percentage error can be controlled under 2%. As it can be seen in the Figure 4.9, the numerical solution and the analytical solution agree well with lumped capacitance matrix and the Crank-Nicolson time approximation. If applying the discontinuity annihilation method to the non-physical method, the discontinuity is removed from the linkage equation as shown in equation (3—36), and the aftermath is that a new source term embodies the discontinuity is generated from the new governing equation (3—37). In the numerical simulation, if the non-physical capacitance captures the discontinuity, the non-physical capacitance is evaluated through the mean-value approach. This approach arises the enthalpy of current time step and future time step together, and further it makes sure that the further time-step temperature is always smaller than the present time-step temperature in the solidification simulation. However, for the numerical simulations with the non-physical source method, it is essential to satisfy that the numerically approximated non-physical source must be smaller than the enthalpy loss of the elements during each time step of the simulation. If this criteria is not satisfied, the ‘cooling process’ is reversed to the ‘heating process’ and the solidification simulation fails. Theoretically, this criteria is ignorable, but in practical numerical simulations, unstable methods and crude approximations can make the numerical methods fail to satisfy the

criteria. In the numerical simulation, the approximation of solid/liquid volume fraction significantly influences the value of non-physical source. Moreover, for Stefan problems such as the solidification problem, the latent heat (large in magnitude for some materials, e.g. zinc) intensifies the effect of solid/liquid volume fraction. For example, through position approximation of solid faction in equation (3—50), the changing rate of liquid fraction with time is almost constant. This makes the release of the latent heat smooth, and the risk of temperature overflow is relatively small. However, if the temperature approximation is as shown in equation (3—49), the cumulative changing rate of solid volume fraction generates a peak in the non-physical source, which makes the temperature very possible to overflow. This phenomenon is common in the source based method, and updating of liquid fraction is essential for source based method [46, 105, 129]. For that reason, this project uses a blending parameter to the nodal variables (temperature) between iteration steps as shown in equation (4—41).

The non-physical source method has a strict requirement on the update procedure of liquid fraction. But for the material with low latent heat, the update procedure can be as simple as the non-physical capacitance method. To show this, consider a material of a pure Lead which has a low latent heat of fusion. The other material properties of Lead are shown in Table 4.7.

Material Name	Pure Lead
Thermal conductivity of solid (k_s)	$35W/m℃$
Thermal conductivity of liquid (k_l)	$16W/m℃$
Heat capacitance of solid (c_s)	$160J/kg℃$
Heat capacitance of liquid (c_l)	$180J/kg℃$
Density of solid (ρ_s)	$11340kg/m^3$
Density of liquid (ρ_l)	$10660kg/m^3$
Latent Heat (l)	$23000J/kg$
Solidus temperature (T_{sol})	$327℃$
Liquidus temperature (T_{liq})	$327℃$

Table 4.7: The thermal-physical material properties of Lead

The boundary conditions should be the same as the solidification of Zinc, such as the forced convective coefficient $h_c = 12000\ W/m^2$℃, and the ambient temperature $T_{amb} = 25$℃. But, the initial temperature is reduced to 340℃.

Plots of temperature histories at the point $x = 0.02m$ are shown in the Figure 4.14. They are calculated by the analytical method (Black), the non-physical capacitance method (Red) and the non-physical source term method (Blue), respectively. In a 50-element numerical model, the figure indicates that, once the criteria of low latent heat is satisfied, the non-physical source term method gives better accuracy than the non-physical capacitance method, moreover it does not require update techniques for liquid fraction such as the relaxation technique [46, 105, 129] and the blending technique, i.e. $\vartheta = 0$. In this case, the maximum percentage error is reduced from 15.79% to 2.61%. This is at a low costs of 127.89 seconds of CPU time to achieve this accuracy.

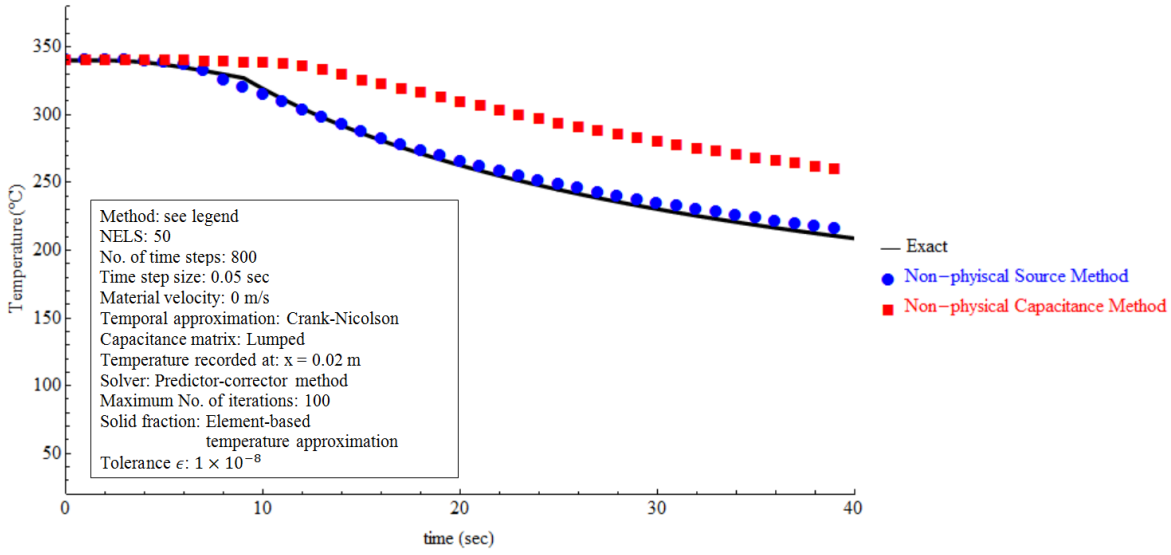

Figure 4.14: The non-physical source method vs. the non-physical capacitance method.

4.6 The numerical experiments – advection-diffusion

In the following tests, the material velocity is set to be $-0.0001\ m/s$, $-0.0005\ m/s$, $-0.001\ m/s$ and $-0.005\ m/s$, repectively. Thus solidifying material is transported. The negative sign "−" presents the direction of flow. The unknown field variables such as the temperature and the enthalpy are transported with the material flow. Moreover, for solidification problems, the latent heat of fusion, which is released at the phase interface, is transferred not only by the conduction but also by advection.

The advective effect of material flow can still be reflected by a change of non-physical capacitance. The influence of advection on non-physical capacitance is achieved by the term $\int_{\Gamma_e} \rho h\left(\underline{X}^{n+1} - \underline{X}^{n}\right) \cdot \underline{n}\, d\Gamma$ in equation (3—38). Further evaluation of this term can be found in Appendix I—(d). The non-physical capacitance method promises that no extra advective term is generated. This helps the simulation to be immune to the numerical instability as described in reference [71-74], which is caused by complex eigenvalue arising from large elemental Pecl ètnumbers [84-86]. Pecl ètnumber is a ratio of the diffusion and advection which can be computed as

$$Pe = \frac{L_e v}{2\alpha} \tag{4—42}$$

where L_e is the characteristic length of an element, v is the velocity of flow and α is the thermal diffusivity. Usually, when $Pe > 1$, instability will happen.

The temperature profiles depicted in the Figure 4.15 are the simulations of solidification with different material velocities. When the velocity field is negative, the material is moving from the right to the left. The greater the material velocity is, the more energy that will be transported into the system by advection. So, the cooling rate will be reduced. When the material velocity is $-0.001\ m/s$, the material flows into the system so fast that it is little time for the melt to cool down, so the temperature is maintained above 400℃. When the material velocity is $-0.0001\ m/s$ or $-0.0005\ m/s$, enough time is available to cool the material and the weak discontinuity in the temperature profiles as phase change occur is present in the figure.

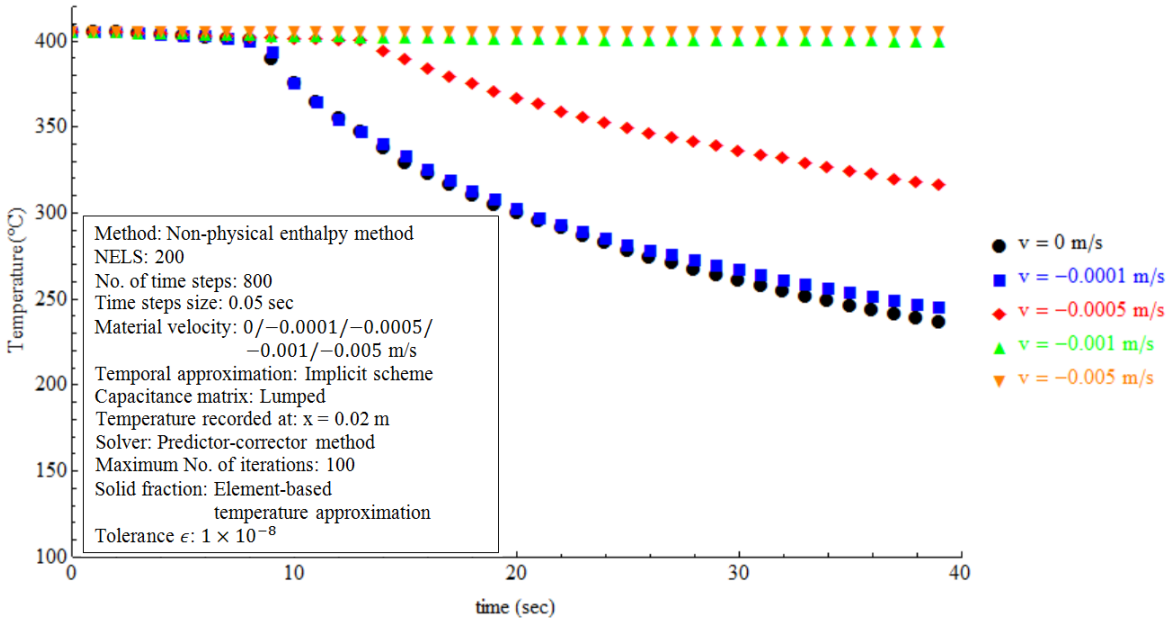

Figure 4.15: The temperature profiles when the velocities are negative

In a solidification simulation, the unknown field variables (enthalpy and the temperature) of the future time step must be smaller than the field variables of the present time step. This makes both $\int_{\Omega_e} \rho^{n+1} \mathrm{h}^{n+1} dV - \int_{\Omega_e} \rho^{n} \mathrm{h}^{n} dV$ and $\int_{\Omega_e} \mathrm{T}^{n+1} dV - \int_{\Omega_e} \mathrm{T}^{n} dV$ return negative values, and further give the non-physical capacitance $\hat{c}$ a positive value at each time step. When the material velocity is negative, $\int_{\Gamma_e} \rho h \left(\underline{X}^{n+1} - \underline{X}^{n}\right) \cdot \underline{n}\, d\Gamma$ returns negative values as well, which may intensify the peak of non-physical capacitance but it still keeps the numerical solution stable. However, when the velocity is positive (the material is flowing from the left to the right), the positive non-physical capacitance $\hat{c}$ cannot be guaranteed. Figure 4.16 shows the temperature profiles computed by non-physical capacitance method when the material velocities are positive. When the material velocity is very small, the method can still output the solution. In Figure 4.16 (for $v = 0.0001\ m/s$), the program runs normally until the 32 second, but when the material velocity is greater, disorder arises in the simulations. Experiment shows that a great many negative non-physical capacitances are generated by the method at different time. Figure 4.17 is the plot of non-physical capacitance vs. time when the material velocity is $0.0001\ m/s$. It can be seen that, once the non-physical capacitance is decreased at a certain level, it brings instability into the numerical simulations, and the following behaviour of the non-physical capacitance is in chaos.

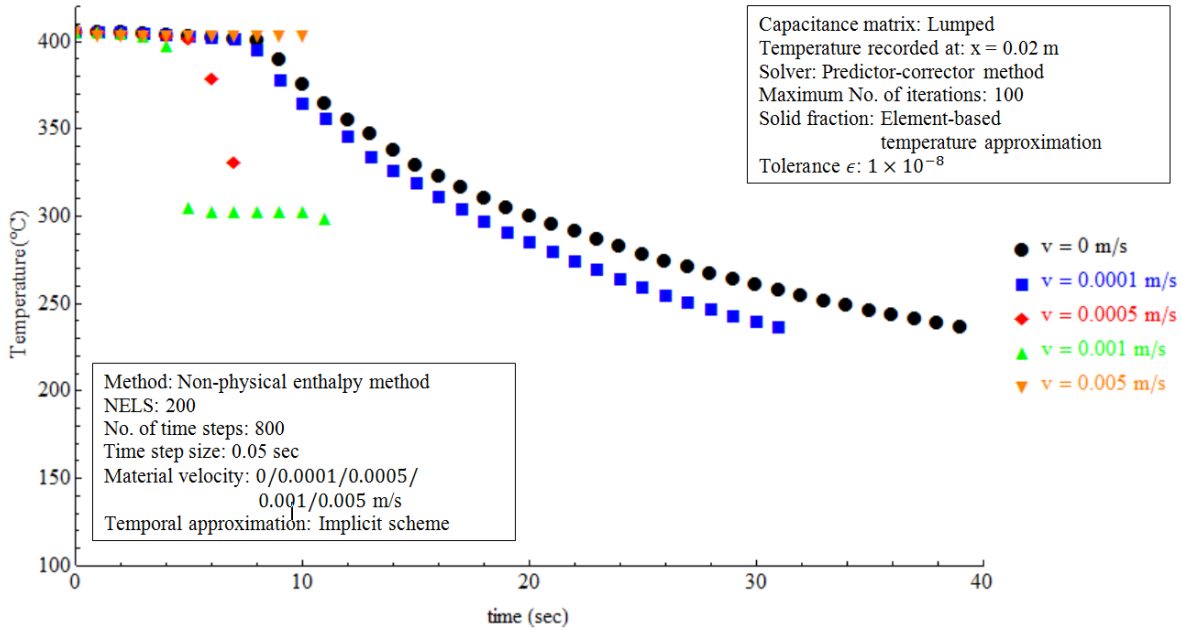

Figure 4.16: Numerical solution of non-physical capacitance method

However, the exclusion of the advective term of advection-diffusion problem is the major advantage of the non-physical capacitance term. This advantage helps to resolve the instability problem in the numerical methods when the velocity is too large.

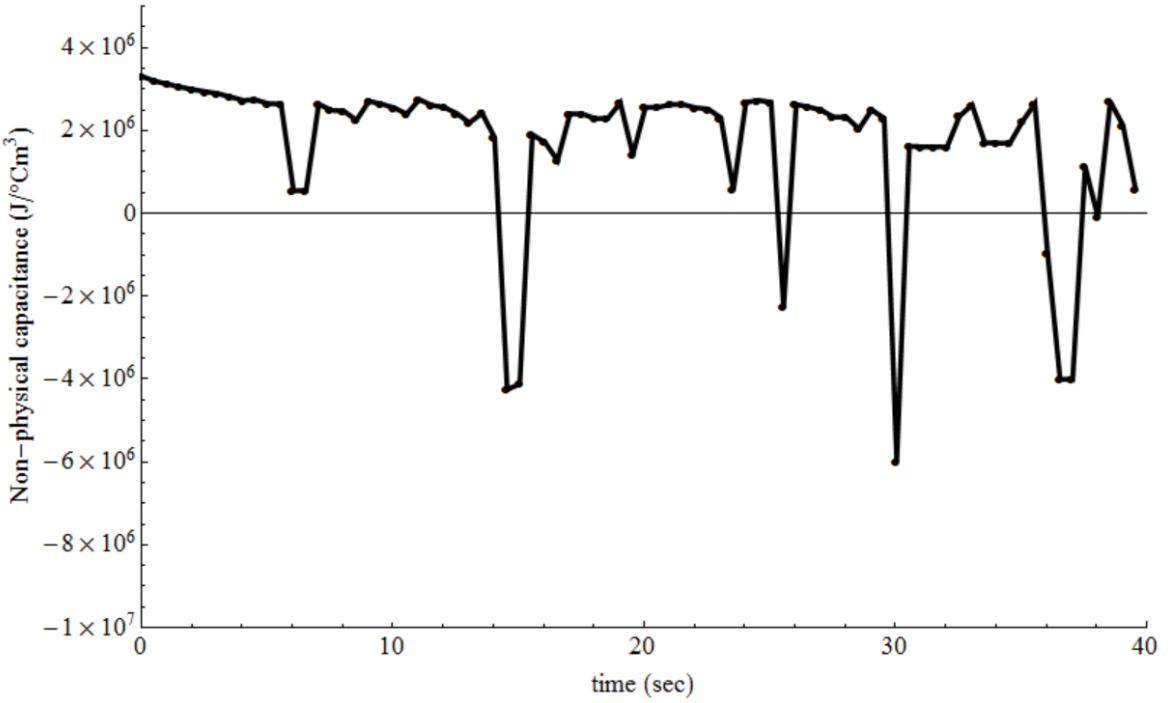

Figure 4.17: The instability of non-physical capacitance

In the numerical test, when the material velocity $v = -0.001\, m/s$, the cooling rate is significantly decelerated. The temperature is almost stable, but the element Pecl èt number is only 0.338 for a 200-element mesh. However, it is still necessary to show the capability of non-physical capacitance when $Pe > 1$. The results for this are compared against the central difference approximation in Figure 4.18 and Figure 4.19. The numerical model is now meshed with 10 elements to obtain large elemental Pecl èt Number. Both figures show the nodal temperatures of every node on the third time step (0.15 seconds). But $Pe = 16.875$ is for the first figure and $Pe = 168.75$ is for the second. It can be found that when the Pe is as high as 168.75, the non-physical capacitance method is still stable, but the standard Galerkin method (which gives central difference approximation) is unstable.

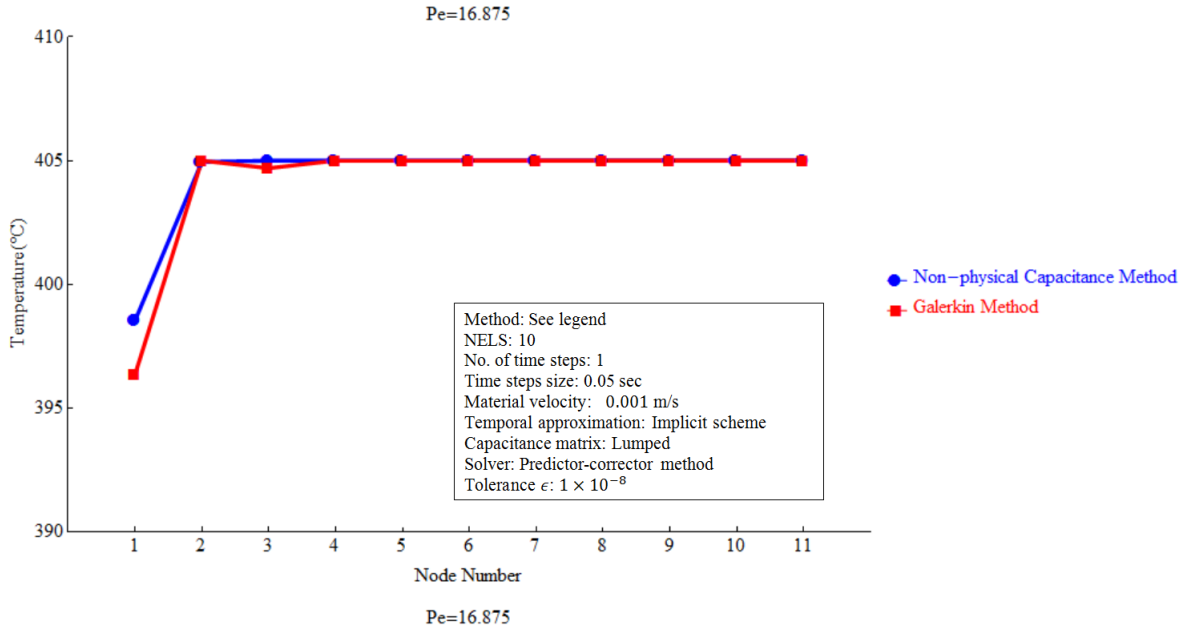

Figure 4.18: The non-physical capacitance method vs. the Galerkin method, $Pe = 16.875$

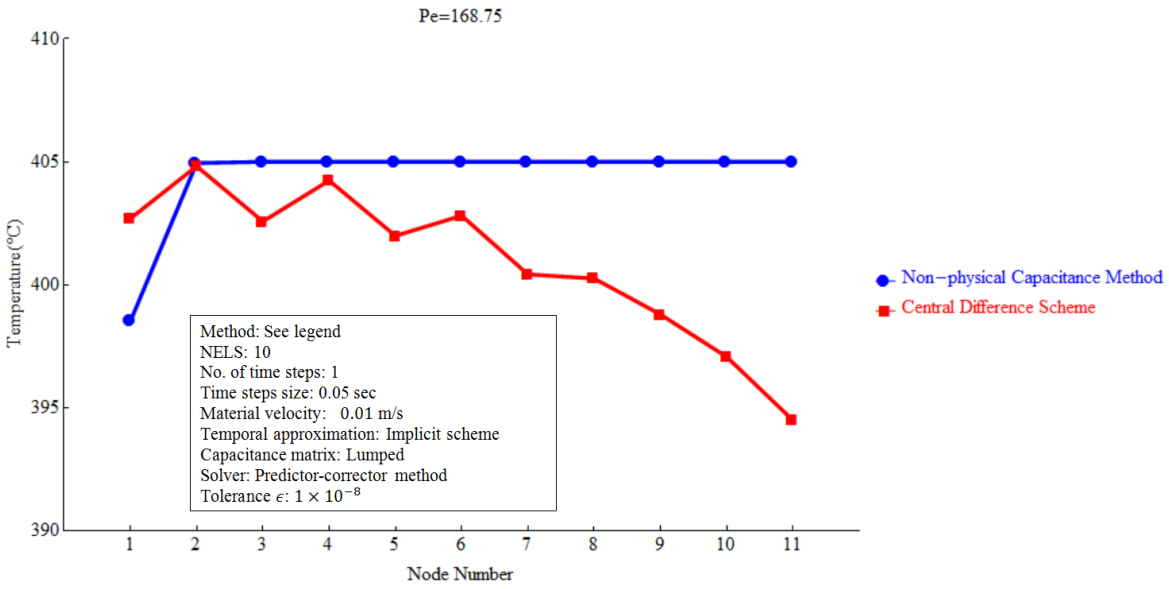

Figure 4.19: The non-physical capacitance method vs. the Galerkin method, $Pe = 168.75$

4.7 Summary

In this chapter, a detailed discussion of non-physical variable methods is given. The concept of non-physical variable method is introduced at the beginning of the chapter. A non-physical source $\widehat{h'}$ is obtained through the definition of non-physical enthalpy. Previous studies were conducted based on the zero material velocity, and the methods for convergence and solving the linear system of equations are bisection method and the SOR method, respectively. This chapter attempts three other solution techniques, which are:

the predictor-corrector method;

the secant method;

and the homotopy method.

This chapter also declares that the numerical approximation of solid/liquid fraction plays a very important role for the non-physical variable method, because it shapes the behaviour of the non-physical capacitance. The discussion of solid/liquid fraction is followed by the numerical tests, which include both stationary ($v = 0\ m/s$) and advection ($v \neq 0\ m/s$). The stationary tests shows that, in order to obtain high accuracy and stability, the non-physical capacitance method requires:

(1) sufficiently small mesh size and time step size;

(2) correct discretization of temporal derivatives;

(3) accurate numerical approximation of solid/liquid fractions;

(4) the secant method is more effective than the predictor-corrector method, and the homotopy method can be an alternative method if it is hard to find a prediction of future time step temperature (see Table 4.1).

In the advection-diffusion tests, the advective term is included into the calculation of non-physical capacitance. The results are stable and physically make sense. It also avoids the instability when the element Pecl è t number is greater than 1. However, it only works when the $\int_{\Gamma_e} \rho h\left(\underline{X}^{n+1} - \underline{X}^{n}\right) \cdot \underline{n}\, d\Gamma$ returns negative values.

Chapter 5 A New Definition for Non-physical Enthalpy for Isothermal Solidification Problems

5.1 General

Chapter 3 discussed the non-physical enthalpy method, which includes both the non-physical-capacitance method and the non-physical source-based method. Through a group of numerical experiments in chapter 4, their advantages were identified. Greater accuracy and stability can be obtained by the right combination of temporal and spatial discretization, the element-based approximation of solid/liquid volume fraction and the methods for solving the system of equations. Demonstrated is the ability of dealing with the solidification problems with material transportation. However, the non-physical capacitance method suffers instability when the material velocity makes the non-physical capacitance negative. The non-physical source-term method has better accuracy and greater efficiency, but it has restrictions on the range of material properties and it requires accurate approximation and precise update of the approximation of the solid/liquid volume fraction. Advection/Convection in solidification is a great challenge for numerical methods, but they also play an important role in the phenomena of solidification, such as macrosegregation, phase-interface stability, dendrite growth, etc. [82]. In some manufacturing technologies such as continuous casting, advection becomes significantly important as the liquid material and the solid material are all moving through a continuous casting machine. In this chapter, a new definition of non-physical enthalpy is established. This new definition is an extension of the control volume capacitance method [66] and the non-physical enthalpy method [62-63]. It is defined through a weak form of the enthalpy transport equation [62-63]. The new definition attempts to exclude the advection term from the non-physical capacitance method, and finally, to avoid the possible generation of negative capacitances. The details are discussed as follows.

5.2 The definition of non-physical enthalpy in weak form

Through the energy transport equation, the new non-physical enthalpy is defined as

$$\frac{D^*}{D^*t}\int_\Omega \hat{h}dV + \int_\Gamma \hat{h}\underline{v}\cdot\underline{n}d\Gamma = \frac{D^*}{D^*t}\int_\Omega \rho h dV + \int_\Gamma \rho h\left(\underline{v}-\underline{v}^*\right)\cdot\underline{n}d\Gamma = -\int_\Gamma \underline{q}\cdot\underline{n}\,d\Gamma + \int_\Omega \rho Q\,dV \quad (5—1)$$

where $\hat{h}$ is the non-physical enthalpy, h is the physical specific enthalpy, $\underline{v}$ is the material velocity field, $\underline{v}^*$ is the mesh velocity field, ρ is the density, and $\underline{n}$ is the outward pointing unit normal to the control surface (CS) Γ of the control volume (CV) Ω. Contrasting with the definition in chapter 3, the inclusion of the artificial advective term $\int_\Gamma \hat{h}\underline{v}\cdot\underline{n}d\Gamma$ is designed to isolate the non-physical capacitance from the effect of physical advection $\int_\Gamma \rho h\left(\underline{v}-\underline{v}^*\right)\cdot\underline{n}d\Gamma$. As will be shown, negative non-physical capacitance will not be generated through the new definition.

Two important temporal derivatives, which are derived in the material reference system (MRS) $\boldsymbol{X}$ and the computational reference system (CRS) $\boldsymbol{\chi}^*$, respectively are:

$$\frac{D}{Dt} = \frac{\partial}{\partial t} + \underline{v}\cdot\nabla \quad (5—2)$$

and

$$\frac{D^*}{D^*t} = \frac{\partial}{\partial t}\Big|_x + \underline{v}^*\cdot\nabla \quad (5—3)$$

where $\nabla(\blacksquare) = \{\partial/\partial x \quad \partial/\partial y \quad \partial/\partial z\}$, which is the gradient.

It is always permitted that, on setting $\underline{v}^* = \underline{0}$, the Eulerian description of transport equation can be obtained as

$$\frac{\partial}{\partial t}\int_\Omega \hat{h}dV + \int_\Gamma \hat{h}\underline{v}\cdot\underline{n}d\Gamma = \frac{\partial}{\partial t}\int_\Omega \rho h dV + \int_\Gamma \rho h\underline{v}\cdot\underline{n}d\Gamma = -\int_\Gamma \underline{q}\cdot\underline{n}\,d\Gamma + \int_\Omega \rho Q\,dV \quad (5—4)$$

If the material velocity $\underline{v}$ is discontinuous in different phases due to material property difference, then the relation $\underline{v}^* = \underline{v}$ cannot be set, because the domain velocity $\underline{v}^*$ is always considered as continuous. The setting $\underline{v}^* = \underline{0}$ is always permitted because $\underline{0}$ is continuous and the problem becomes a fixed grid problem.

Application of the Reynold-type transport theorem and the Divergence theorem to each term in equation (5—1), gives

$$\int_\Omega \left(\frac{D^*\hat{h}}{D^*t} + \hat{h}\nabla\cdot\underline{v}^*\right)dV + \int_\Omega \nabla\cdot\left(\hat{h}\underline{v}\right)dV = \int_\Omega \left(\frac{D^*\rho h}{D^*t} + \rho h\nabla\cdot\underline{v}^*\right)dV + \int_\Omega \nabla\cdot\Big(\rho h\big(\underline{v} - \underline{v}^*\big)\Big)dV = -\int_\Omega \nabla\cdot\left(\underline{q}\right)dV + \int_\Omega \rho Q\, dV \quad (5—5)$$

where $\nabla\cdot(\blacksquare) = \partial/\partial x + \partial/\partial y + \partial/\partial z$ is the divergence.

In equation (5—1), the non-physical enthalpy is defined in a weak formulation. And through equation (5—5), the definition of non-physical enthalpy $\hat{h}$ in the strong form can be found as

$$\frac{D^*\hat{h}}{D^*t} + \hat{h}\nabla\cdot\underline{v}^* + \nabla\cdot\left(\hat{h}\underline{v}\right) = \rho\frac{D^*h}{D^*t} + \rho\left(\underline{v} - \underline{v}^*\right)\cdot\nabla h = -\nabla\cdot\left(\underline{q}\right) + \rho Q \quad (5—6)$$

Comparing both definitions as shown in equations (5—1) and (5—6), it can be recognised that the non-physical enthalpy is not unique. Equation (5—1) indicates that, for fixed grid method, i.e. $\underline{v}^* = \underline{0}$, one possible formulation can be conducted by setting the non-physical enthalpy $\hat{h} = \rho h$. In this formulation, however the non-physical enthalpy contains a discontinuity. The formulation is identical to the CVCM. Alternatively the non-physical enthalpy can be forced continuous on the phase interface, that is to say, $\left]\hat{h}\underline{n}\right[= 0$, so that it generates an extra source term. It should be noted that no matter which evaluation is under consideration, the non-physical advective term $\int_\Gamma \hat{h}\underline{v}\cdot\underline{n}d\Gamma$ remains. This is not like the recent definition in references [62-63], which eliminates the advective term for finite element discretization. It is recognised however that the inclusion of the term $\int_\Gamma \hat{h}\underline{v}\cdot\underline{n}d\Gamma$ gives rise to a jump term of the form $\left]\hat{h}\underline{v}\cdot\underline{n}\right[$ at Γ_i. A possible approach to account for this is the incorporation of an additional non-physical term (a source term $\hat{Q}$) in equation (5—1), discussed in the section that follows.

5.3 The non-physical source term $\hat{Q}$

In order to find the relationships between the non-physical enthalpy, the non-physical source and the discontinuity front, it is necessary to consider a new CV, the motion of which is governed by the velocity field $\underline{v}^+$. The velocity field $\underline{v}^+$ matches the velocity of a discontinuity Γ_i passing through the domain Ω. Therefore, the governing equation for this CV (denoted as Ω^+) can be written as

$$\frac{D^+}{D^+t}\int_{\Omega^+}\hat{h}dV+\int_{\Gamma^+}\hat{h}\left(\underline{v}^*-\underline{v}^+\right)\cdot\underline{n}d\Gamma+\int_{\Gamma^+}\hat{h}\underline{v}\cdot\underline{n}d\Gamma+\int_{\Omega^+}\hat{Q}\,dV=\frac{D^+}{D^+t}\int_{\Omega^+}\rho hdV+$$
$$\int_{\Gamma^+}\rho h\left(\underline{v}-\underline{v}^+\right)\cdot\underline{n}d\Gamma=-\int_{\Gamma^+}\underline{q}\cdot\underline{n}d\Gamma+\int_{\Omega^+}\rho QdV \qquad (5—7)$$

where $\hat{Q}$ is a non-physical source term, which has similar characteristic as the non-physical enthalpy, i.e. it is user-defined for the convenience of the solution.

In equation (5—7), a new non-physical source $\hat{Q}$ is introduced. It transpires and is shown below that $\hat{Q}$ is necessary in order to remove the discontinuity that arises with the newly introduced non-physical advection term $\int_\Gamma\ \hat{h}\underline{v}\cdot\underline{n}d\Gamma$. Once the new non-physical source $\hat{Q}$ is defined, the non-physical $\hat{h}$ is required to change also to ensure energy conservation.

It can be seen that the non-physical enthalpy $\hat{h}$ is independent of the velocity $\underline{v}^+$. Application of equation (5—7) to a CV Ω_i, which encloses the discontinuity front Γ_i, gives

$$\frac{D^+}{D^+t}\int_{\Omega_i}\hat{h}dV+\int_{{\Gamma_i}^t-{\Gamma_i}^l-{\Gamma_i}^s}\hat{h}\left(\underline{v}^*-\underline{v}^+\right)\cdot\underline{n}d\Gamma+\int_{\Gamma_i^l}\hat{h}\left(\underline{v}^*-\underline{v}^+\right)\cdot\left(-\underline{n}_l\right)d\Gamma+$$
$$\int_{\Gamma_i^s}\hat{h}\left(\underline{v}^*-\underline{v}^+\right)\cdot\left(-\underline{n}_s\right)d\Gamma+\int_{{\Gamma_i}^t-{\Gamma_i}^l-{\Gamma_i}^s}\hat{h}\underline{v}\cdot\underline{n}d\Gamma+\int_{\Gamma_i^l}\hat{h}\underline{v}\cdot\left(-\underline{n}_l\right)d\Gamma+\int_{\Gamma_i^s}\hat{h}\underline{v}\cdot$$
$$\left(-\underline{n}_s\right)d\Gamma+\int_{\Omega_i}\hat{Q}\,dV=\frac{D^+}{D^+t}\int_{\Omega_i}\rho hdV+\int_{{\Gamma_i}^t-{\Gamma_i}^l-{\Gamma_i}^s}\rho h\left(\underline{v}-\underline{v}^+\right)\cdot\underline{n}d\Gamma+\int_{\Gamma_i^l}\rho h\left(\underline{v}-\underline{v}^+\right)\cdot$$
$$\left(-\underline{n}_l\right)d\Gamma+\int_{\Gamma_i^s}\rho h\left(\underline{v}-\underline{v}^+\right)\cdot\left(-\underline{n}_s\right)d\Gamma=-\int_{{\Gamma_i}^t-{\Gamma_i}^l-{\Gamma_i}^s}\underline{q}\cdot\underline{n}d\Gamma-\int_{\Gamma_i^l}\underline{q}\cdot\left(-\underline{n}_l\right)d\Gamma-$$
$$\int_{\Gamma_i^s}\underline{q}\cdot\left(-\underline{n}_s\right)d\Gamma+\int_{\Omega_i}\rho QdV \qquad (5—8)$$

where $\Omega^+=\Omega_i\cup\Omega_s\cup\Omega_l$, $\partial\Omega_s=\Gamma_s\cup\Gamma_i^s$, $\partial\Omega_l=\Gamma_l\cup\Gamma_i^l$. The subscript i denotes the phase interface, and the subscript/superscript l and s refer to the liquid and solid. The relationship of the CVs and the CSs can be seen in Figure 5.1.

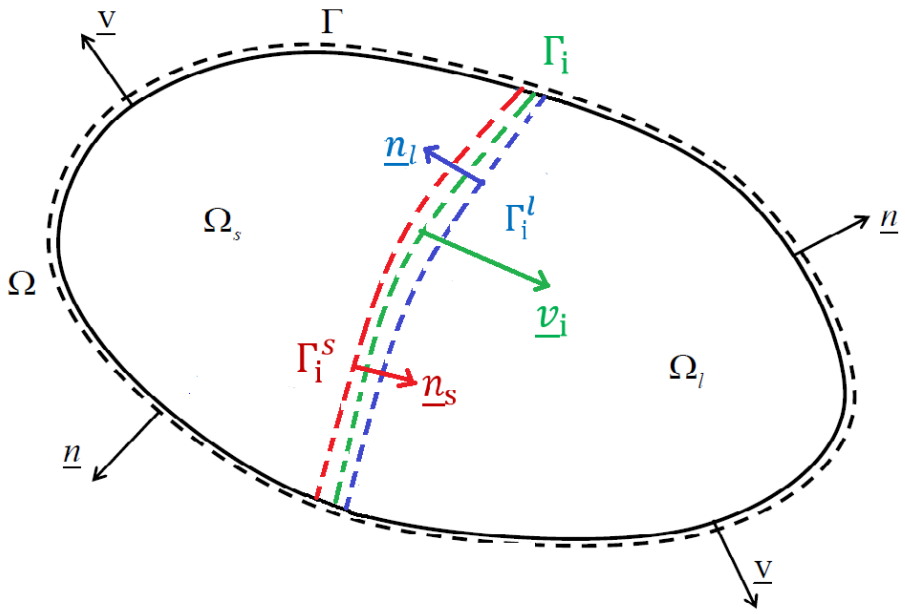

Figure 5.1: The control volume with phase change

By letting $vol(\Omega_i) \to 0$ with $\Gamma_i \subset \Omega_i$, and $\Gamma_i^l, \Gamma_i^s \to \Gamma_i$, Equation (5—8) gives

$$\frac{D^+}{D^+t}\int_{\Gamma_i} \hat{h}' d\Gamma + \int_{\Sigma_i} \hat{h}'(\underline{v}^* - \underline{v}^+)\cdot \underline{tn} d\Sigma - \int_{\Gamma_i}]\hat{h}(\underline{v}^* - \underline{v}^+)\cdot \underline{n}[d\Gamma + \int_{\Sigma_i} \hat{h}'\underline{v}\cdot \underline{tn} d\Sigma -$$
$$\int_{\Gamma_i}]\hat{h}\underline{v}\cdot \underline{n}[d\Gamma + \int_{\Gamma_i} \hat{Q}' d\Gamma = -\int_{\Gamma_i}]\rho h(\underline{v} - \underline{v}^+)\cdot \underline{n}[d\Gamma = \int_{\Gamma_i} \left]\underline{q}\cdot \underline{n}\right[d\Gamma \qquad (5—9)$$

where the bracket]■[signifies a jump term, Σ_i is the boundary of Γ_i, and $\underline{tn}$ is the outward pointing unit normal on Σ_i in the tangent plane of Γ_i. The term $\int_{\Sigma_i} \hat{h}'\underline{v}\cdot \underline{tn} d\Sigma$ is included in equation (5—9) for convenience but requires special consideration since $\underline{v}$ is not defined on Σ_i. A sketch showing the orientation of $\underline{tn}$ is provided in the Figure 3.2. The vector $\underline{tn}$ appears in equation (5—9) to account for the fact that the phase interface Γ_i may shrink or expand in the direction of $\underline{tn}$ to accommodate the shape of the external boundary Γ. The jumps $]\hat{h}\underline{v}\cdot \underline{n}[= -\hat{h}_s\underline{v}_s\cdot \underline{n}_l + \hat{h}_l\underline{v}_l\cdot \underline{n}_l$, $]\rho h(\underline{v} - \underline{v}^+)\cdot \underline{n}[= -\rho_s h_s(\underline{v}_s - \underline{v}^+)\cdot \underline{n}_l + \rho_l h_l(\underline{v}_l - \underline{v}^+)\cdot \underline{n}_l$, and $\left]\underline{q}\cdot \underline{n}\right[= -\underline{q}_s\cdot \underline{n}_l + \underline{q}_l\cdot \underline{n}_l$. The velocities $\underline{v}^*$ and $\underline{v}^+$ are continuous on the interface Γ_i, with the identity $]\hat{h}\underline{n}[= 0$. Note that the jump term containing $\hat{h}$, $\underline{v}^*$ and $\underline{v}^+$ on the LHS of equation (5—9) disappears because

$$\int_{\Gamma_i}]\hat{h}(\underline{v}^* - \underline{v}^+)\cdot \underline{n}[d\Gamma = \int_{\Gamma_i}]\hat{h}\underline{n}[\cdot(\underline{v}^* - \underline{v}^+) d\Gamma = 0 \qquad (5—10)$$

Observe that the source terms $\hat{h}'$ and $\hat{Q}'$ only exist on the CS Γ_i. The motion of Γ_i is described by the velocity field $\underline{v}^+$ and the source $\hat{h}'$ is assumed to vary spatially on Γ_i to reflect the physical behaviour of the physical jump conditions at Γ_i. Consequently, the value of $\hat{h}'$ on Σ_i should not depend on the material velocity field $\underline{v}$ at Σ_i. Moreover, it can be assumed that the velocity $\underline{v} = \underline{0}$ outside the domain $\Omega_s \cup \Omega_l$. For these reasons, the term $\int_{\Sigma_i} \hat{h}'\underline{v} \cdot \underline{tn} d\Sigma$, which is poorly defined (since $\underline{v}$ is not defined on Σ_i) can be set to zero. Thus, equation (5—9) becomes

$$\frac{D^+}{D^+t}\int_{\Gamma_i} \hat{h}' d\Gamma + \int_{\Sigma_i} \hat{h}'(\underline{v}^* - \underline{v}^+) \cdot \underline{tn} d\Sigma - \int_{\Gamma_i}]\hat{h}\underline{v} \cdot \underline{n}[d\Gamma + \int_{\Gamma_i} \hat{Q}' d\Gamma = -\int_{\Gamma_i}]\rho h(\underline{v} - \underline{v}^+) \cdot \underline{n}[d\Gamma = \int_{\Gamma_i}]\underline{q} \cdot \underline{n}[\, d\Gamma \tag{5—11}$$

Equation (5—11) indicates that if the non-physical enthalpy $\hat{h}$ is considered to be continuous at the phase interface Γ_i, then $\hat{h}'$ is a source whose strength does not now depend solely on the jump in ρh at Γ_i.

The corresponding partial differential equation of equation (5—11) is

$$\frac{D^+\hat{h}'}{D^+t} + \hat{h}'\nabla_{\Gamma_i} \cdot \underline{v}^+ + \nabla_{\Gamma_i} \cdot \left(\hat{h}'(\underline{v}^* - \underline{v}^+)_T\right) -]\hat{h}\underline{v} \cdot \underline{n}[+ \hat{Q}' = -]\rho h(\underline{v} - \underline{v}^+) \cdot \underline{n}[=]\underline{q} \cdot \underline{n}[\tag{5—12}$$

where the subscript T denotes the tangential component of velocities $\underline{v}^*$ and $\underline{v}^+$, the operator ∇_{Γ_i} is the gradient operator intrinsic to the surface Γ_i.

Detailed derivation of equation (5—12) from equation (5—11) can be found in Appendix I—(g). Both the strong and the weak definitions for $\hat{h}'$ indicate that for $\hat{h}$ to have the desirable property $]\hat{h}\underline{n}[= 0$ at Γ_i, and for $\hat{h}'$ to depend solely on the jump in ρh at Γ_i requires that $\hat{Q}'$ should be non-zero. Note that for $]\hat{h}\underline{n}[= 0$, then $]\hat{h}\underline{v} \cdot \underline{n}[\neq 0$, as a consequence of the difference between solid and liquid densities at Γ_i. This is apparent on consideration of

$$\int_{\Gamma_i}]\hat{h}\underline{v} \cdot \underline{n}[d\Gamma = \int_{\Gamma_i}]\hat{h}(\underline{v} - \underline{v}^+) \cdot \underline{n}[d\Gamma = \int_{\Gamma_i} \hat{h}]\frac{1}{\rho}\rho\underline{v} \cdot \underline{n}[\, d\Gamma = \int_{\Gamma_i} \hat{h}\dot{m}(\frac{1}{\rho_s} - \frac{1}{\rho_l}) d\Gamma \tag{5—13}$$

where $\dot{m}$ is the solid mass flux rate, the term $\int_{\Gamma_i}]\hat{h}\underline{v}^+ \cdot \underline{n}[d\Gamma$ in equation (5—13) is zero because $\underline{v}^+$ is continuous along with $\hat{h}$.

It is of interest to observe from equations (5—11) and (5—12) that a possible choice for $\hat{Q}'$ is that $\hat{Q}' =]\hat{h}\underline{v} \cdot \underline{n}[$, which has the effect of reducing these equations to

$$\frac{D^+}{D^+t}\int_{\Gamma_i} \hat{h}' d\Gamma + \int_{\Sigma_i} \hat{h}'(\underline{v}^* - \underline{v}^+) \cdot \underline{tn} d\Sigma = -\int_{\Gamma_i}]\rho h(\underline{v} - \underline{v}^+) \cdot \underline{n}[d\Gamma = \int_{\Gamma_i} \left]\underline{q} \cdot \underline{n}\right[d\Gamma \tag{5—14}$$

and

$$\frac{D^+\hat{h}\prime}{D^+t} + \hat{h}'\nabla_{\Gamma_i} \cdot \underline{v}^+ + \nabla_{\Gamma_i} \cdot \left(\hat{h}'(\underline{v}^* - \underline{v}^+)_T\right) = -]\rho h(\underline{v} - \underline{v}^+) \cdot \underline{n}[= \left]\underline{q} \cdot \underline{n}\right[\tag{5—15}$$

thus ensuring that the source $\hat{h}'$ depends only on a physical jump condition.

In principle this choice would ensure that any physical discontinuity would be solely accounted for by the magnitude of non-physical jump $\hat{h}'$. This source term facilitates the removal of any discontinuity from the LHS of equation (5—1), as required. Recall that for the non-physical variable method, the CV Ω refers to the computational reference system. The CV Ω^+ is identically equal to Ω when viewed as a collection of points but was created to analyze the discontinuity on the phase interface. The difference between the two domains is that the transport of Ω is governed by the velocity field $\underline{v}^*$ yet the transport of Ω^+ is governed by the velocity field $\underline{v}^+$. Note however the overall movement of the two domains is matched provided $\underline{v}^* \cdot \underline{n} = \underline{v}^+ \cdot \underline{n}$ on Γ, i.e. on the common boundary for Ω and Ω^+. The two approaches can be related in transport form by the identity

$$\frac{D^*}{D^*t}\int_\Omega \hat{h} dV - \int_\Gamma \hat{h}\underline{v}^* \cdot \underline{n} d\Gamma = \frac{D^+}{D^+t}\int_{\Omega^+} \hat{h} dV - \int_\Gamma \hat{h}\underline{v}^+ \cdot \underline{n} d\Gamma \tag{5—16}$$

This identity also provides

$$\frac{D^*}{D^*t}\int_\Omega \hat{h}dV + \int_\Gamma \hat{h}\underline{v}\cdot\underline{n}d\Gamma = \frac{D^+}{D^+t}\int_{\Omega^+}\hat{h}dV + \int_\Gamma \hat{h}(\underline{v}^* - \underline{v}^+)\cdot\underline{n}d\Gamma + \int_\Gamma \hat{h}\underline{v}\cdot\underline{n}d\Gamma \quad (5—17)$$

This equation provides a mean to remove the source from equation (5—17), i.e.

$$\frac{D^*}{D^*t}\int_{\Omega\backslash\Gamma_i}\hat{h}dV + \int_{\Gamma\backslash\Sigma_i}\hat{h}\underline{v}\cdot\underline{n}d\Gamma + \int_\Omega \hat{Q}\,dV = \frac{D^*}{D^*t}\int_\Omega \rho h dV + \int_\Gamma \rho h(\underline{v} - \underline{v}^*)\cdot\underline{n}d\Gamma - \left(\frac{D^+}{D^+t}\int_{\Gamma_i}\hat{h}'d\Gamma + \int_{\Sigma_i}\hat{h}'(\underline{v}^* - \underline{v}^+)\cdot\underline{t}\underline{n}d\Sigma\right) \quad (5—18)$$

where it is understood that $\hat{Q}$ is so defined so that $\hat{Q}' =]\hat{h}\underline{v}\cdot\underline{n}[$ to ensure that cancellation on the left hand side of equation (5—18) which ensures the RHS is absent of any discontinuity. The CV $\Omega\backslash\Gamma_i$ and CS $\Gamma\backslash\Sigma_i$ indicate that sources have been excluded from LHS of equation (5—18). The term $-]\hat{h}\underline{v}\cdot\underline{n}[$ in equation (5—11) is not a source of course yet has been removed with the inclusion of the non-physical source $\hat{Q}$.

5.4 The finite element discretization

5.4.1 The new weighted non-physical governing equation

Application of weighted-residual method to the governing equation (5—1) gives

$$\frac{D^*}{D^*t}\int_\Omega W\hat{h}dV + \int_\Gamma W\hat{h}\underline{v}\cdot\underline{n}d\Gamma - \int_\Omega \hat{h}\underline{v}\cdot\nabla W dV + \int_\Omega W\hat{Q}dV = \frac{D^*}{D^*t}\int_\Omega \rho h dV + \frac{D^*}{D^*t}\int_\Omega W\rho h dV + \int_\Gamma W\rho h(\underline{v} - \underline{v}^*)\cdot\underline{n}d\Gamma - \int_\Omega \rho h(\underline{v} - \underline{v}^*)\cdot\nabla W dV = -\int_\Gamma W\underline{q}\cdot\underline{n}\,d\Gamma + \int_\Omega \underline{q}\cdot\nabla W dV + \int_\Omega W\rho Q\,dV \quad (5—19)$$

where W is a weighting function and it is assumed smooth and is transported invariantly with Ω, i.e. $D^*W/D^*t = 0$.

If the weighing function W transported with the CV Ω varies with time then, the derivatives $\int_\Omega (D^*W/D^*t)\hat{h}dV$ and $\int_\Omega (D^*W/D^*t)\rho h dV$ are required to be subtracted from the weighted equation, i.e.

$$\frac{D^*}{D^*t}\int_\Omega W\hat{h}dV - \int_\Omega \frac{D^*W}{D^*t}\hat{h}dV + \int_\Gamma W\hat{h}\underline{v}\cdot\underline{n}d\Gamma - \int_\Omega \hat{h}\underline{v}\cdot\nabla W dV + \int_\Omega W\hat{Q}dV = \frac{D^*}{D^*t}\int_\Omega W\rho h dV - \int_\Omega \frac{D^*W}{D^*t}\rho h dV + \int_\Gamma W\rho h(\underline{v} - \underline{v}^*)\cdot\underline{n}d\Gamma - \int_\Omega \rho h(\underline{v} - \underline{v}^*)\cdot\nabla W dV = -\int_\Gamma W\underline{q}\cdot\underline{n}\,d\Gamma + \int_\Omega \underline{q}\cdot\nabla W dV + \int_\Omega W\rho Q\,dV \quad (5—20)$$

It is necessary to conduct the volume analysis, which is applied for the equation (5—1), to the weighted governing equation (5—20). Consider then a control volume Ω^+, which is transported with the velocity field $\underline{v}^+$. The weighted equation in the CV Ω^+ is

$$\frac{D^+}{D^+t}\int_{\Omega^+} W\hat{h}dV - \int_{\Omega^+}\frac{D^+W}{D^+t}\hat{h}dV + \int_{\Gamma^+} W\hat{h}(\underline{v}^* - \underline{v}^+)\cdot\underline{n}d\Gamma - \int_{\Omega^+}\hat{h}(\underline{v}^* - \underline{v}^+)\cdot\nabla W dV + \int_{\Gamma^+} W\hat{h}\underline{v}\cdot\underline{n}d\Gamma - \int_{\Omega^+}\hat{h}\underline{v}\cdot\nabla W dV + \int_{\Omega^+} W\hat{Q}\,dV = \frac{D^+}{D^+t}\int_{\Omega^+} W\rho h dV - \int_{\Omega^+}\frac{D^+W}{D^+t}\rho h dV + \int_{\Gamma^+} W\rho h(\underline{v} - \underline{v}^+)\cdot\underline{n}d\Gamma - \int_{\Omega^+}\rho h(\underline{v} - \underline{v}^+)\cdot\nabla W dV = -\int_{\Gamma^+} W\underline{q}\cdot\underline{n}\,d\Gamma + \int_{\Gamma^+}\underline{q}\cdot\nabla W dV + \int_{\Omega^+} W\rho Q\,dV \quad (5—21)$$

On setting $D^*W/D^*t = 0$, the two derivatives of the weighing function W can be related by the identity

$$\frac{D^+W}{D^+t} = \frac{D^*W}{D^*t} + (\underline{v}^+ - \underline{v}^*)\cdot\nabla W = (\underline{v}^+ - \underline{v}^*)\cdot\nabla W \quad (5—22)$$

Substitution of equation (5—21) into equation (5—20) gives

$$\frac{D^+}{D^+t}\int_{\Omega^+} W\hat{h}dV - \int_{\Omega^+}\hat{h}(\underline{v}^+ - \underline{v}^*)\cdot\nabla W dV + \int_{\Gamma^+} W\hat{h}(\underline{v}^* - \underline{v}^+)\cdot\underline{n}d\Gamma - \int_{\Omega^+}\hat{h}(\underline{v}^* - \underline{v}^+)\cdot\nabla W dV + \int_{\Gamma^+} W\hat{h}\underline{v}\cdot\underline{n}d\Gamma - \int_{\Omega^+}\hat{h}\underline{v}\cdot\nabla W dV + \int_{\Omega^+} W\hat{Q}\,dV = \frac{D^+}{D^+t}\int_{\Omega^+} W\rho h dV - \int_{\Omega^+}\rho h(\underline{v}^+ - \underline{v}^*)\cdot\nabla W dV + \int_{\Gamma^+} W\rho h(\underline{v} - \underline{v}^+)\cdot\underline{n}d\Gamma - \int_{\Omega^+}\rho h(\underline{v} - \underline{v}^+)\cdot\nabla W dV = -\int_{\Gamma^+} W\underline{q}\cdot\underline{n}\,d\Gamma + \int_{\Gamma^+}\underline{q}\cdot\nabla W dV + \int_{\Omega^+} W\rho Q\,dV \quad (5—23)$$

Simplification of equation (5—23) gives

$$\frac{D^+}{D^+t}\int_{\Omega^+} W\hat{h}dV + \int_{\Gamma^+} W\hat{h}(\underline{v}^* - \underline{v}^+)\cdot\underline{n}d\Gamma + \int_{\Gamma^+} W\hat{h}\underline{v}\cdot\underline{n}d\Gamma - \int_{\Omega^+}\hat{h}\underline{v}\cdot\nabla W dV + \int_{\Omega^+} W\hat{Q}\,dV = \frac{D^+}{D^+t}\int_{\Omega^+} W\rho h dV + \int_{\Gamma^+} W\rho h(\underline{v} - \underline{v}^+)\cdot\underline{n}d\Gamma - \int_{\Omega^+}\rho h(\underline{v} - \underline{v}^*)\cdot\nabla W dV = -\int_{\Gamma^+} W\underline{q}\cdot\underline{n}\,d\Gamma + \int_{\Gamma^+}\underline{q}\cdot\nabla W dV + \int_{\Omega^+} W\rho Q\,dV \quad (5—24)$$

Consider again, applying the weighted transport equation (5—24) to a CV Ω_i which encloses to the phase interface Γ_i, it gives

$$\frac{D^+}{D^+t}\int_{\Omega_i} W\hat{h}dV + \int_{\Gamma-\Gamma_i^s-\Gamma_i^l} W\hat{h}(\underline{v}^* - \underline{v}^+)\cdot\underline{n}d\Gamma + \int_{\Gamma_i^s} W\hat{h}(\underline{v}^* - \underline{v}^+)\cdot(-\underline{n})d\Gamma + \int_{\Gamma_i^l} W\hat{h}(\underline{v}^* - \underline{v}^+)\cdot(-\underline{n})d\Gamma + \int_{\Gamma-\Gamma_i^s-\Gamma_i^l} W\hat{h}\underline{v}\cdot\underline{n}d\Gamma + \int_{\Gamma_i^s} W\hat{h}\underline{v}\cdot(-\underline{n})d\Gamma + \int_{\Gamma_i^l} W\hat{h}\underline{v}\cdot$$

$$(-\underline{n})d\Gamma - \int_{\Omega_i} \hat{h}\underline{v}\cdot\nabla W dV + \int_{\Omega_i} W\hat{Q}\, dV = \frac{D^+}{D^+t}\int_{\Omega_i} W\rho h dV + \frac{D^+}{D^+t}\int_{\Gamma-\Gamma_i^s-\Gamma_i^l} W\rho h\left(\underline{v}-\underline{v}^+\right)\cdot \underline{n}d\Gamma + \int_{\Gamma_i^s} W\rho h\left(\underline{v}-\underline{v}^+\right)\cdot(-\underline{n})d\Gamma + \int_{\Gamma_i^l} W\rho h\left(\underline{v}-\underline{v}^+\right)\cdot(-\underline{n})d\Gamma - \int_{\Omega_i}\rho h\left(\underline{v}-\underline{v}^*\right)\cdot \nabla W\, dV = -\int_{\Gamma-\Gamma_i^s-\Gamma_i^l} W\underline{q}\cdot\underline{n}d\Gamma - \int_{\Gamma_i^s} W\underline{q}\cdot(-\underline{n})d\Gamma - \int_{\Gamma_i^l} W\underline{q}\cdot(-\underline{n})d\Gamma + \int_{\Omega_i}\underline{q}\cdot \nabla W\, dV + \int_{\Omega_i} W\rho Q\, dV \quad (5—25)$$

On limiting $vol(\Omega_i)\to 0$ with $\Gamma_i \subset \Omega_i$, equation (5—25) returns to

$$\frac{D^+}{D^+t}\int_{\Gamma_i} W\hat{h}'\, d\Gamma + \int_{\Sigma_i} W\hat{h}'\left(\underline{v}^*-\underline{v}^+\right)\cdot \underline{tn}d\Sigma = \int_{\Gamma_i} W\rbrack\rho h\left(\underline{v}-\underline{v}^+\right)\cdot(-\underline{n})\lbrack d\Gamma - \lim_{vol(\Omega_i)\to 0}\int_{\Omega_i}\rho h\left(\underline{v}-\underline{v}^*\right)\cdot\nabla W\, dV = -\int_{\Gamma_i} W\left\rbrack\underline{q}\cdot(-\underline{n})\right\lbrack d\Gamma + \lim_{vol(\Omega_i)\to 0}\int_{\Omega_i}\underline{q}\cdot\nabla W\, dV \quad (5—26)$$

The terms $-\int_{\Gamma_i} W\rbrack\hat{h}\underline{v}\cdot\underline{n}\lbrack d\Gamma$ and $\int_{\Gamma_i} W\hat{Q}'d\Gamma$ are not present in equation because of the setting $\hat{Q}' = \rbrack\hat{h}\underline{v}\cdot\underline{n}\lbrack$. The term $\lim_{vol(\Omega_i)\to 0}\int_{\Omega_i}\hat{h}\underline{v}\cdot\nabla W\, dV = 0$, which is similar to the term $\int_{\Sigma_i}\hat{h}'\underline{v}\cdot\underline{tn}d\Sigma = 0$. Detailed discussion about the terms $\lim_{vol(\Omega_i)\to 0}\int_{\Omega_i}\rho h\left(\underline{v}-\underline{v}^*\right)\cdot\nabla W\, dV$ and $\lim_{vol(\Omega_i)\to 0}\int_{\Omega_i}\underline{q}\cdot\nabla W\, dV$ is provided in Appendix I—(h) [130].

An alternative procedure to arrive at an equation similar to equation (5—26) is the direct weighting of equation (5—11), i.e.

$$\frac{D^+}{D^+t}\int_{\Gamma_i} W\hat{h}'d\Gamma - \int_{\Gamma_i}\left(\frac{D^+W}{D^+t}\right)\hat{h}'d\Gamma + \int_{\Sigma_i} W\hat{h}'\left(\underline{v}^*-\underline{v}^+\right)\cdot\underline{tn}d\Sigma - \int_{\Gamma_i}\hat{h}'\left(\underline{v}^*-\underline{v}^+\right)_T\cdot \nabla_{\Gamma_i^+}W d\Gamma - \int_{\Gamma_i} W\rbrack\hat{h}\underline{v}\cdot\underline{n}\lbrack d\Gamma + \int_{\Gamma_i} W\hat{Q}'d\Gamma = -\int_{\Gamma_i} W\rbrack\rho h\left(\underline{v}-\underline{v}^+\right)\cdot\underline{n}\lbrack d\Gamma = \int_{\Gamma_i} W\left\rbrack\underline{q}\cdot\underline{n}\right\lbrack d\Gamma \quad (5—27)$$

where the subscript T denotes the tangential component of the velocities $\underline{v}^*$ and $\underline{v}^+$, which appearance is due to Stoke Theorem and the tangential outward pointing normal $\underline{tn}$ from the boundary curve Σ_i^+.

In equation (5—27), If the weighing function W is transported with the CS Γ_i^+, the derivatives $\int_{\Gamma_i^+}(D^+W/D^+t)\hat{h}'d\Gamma$, is required to be subtracted off. Substitution of the identity (5—22) into equation (5—27) gives

$$\frac{D^+}{D^+t}\int_{\Gamma_i} W\hat{h}'d\Gamma - \int_{\Gamma_i} \hat{h}'\left(\underline{v}^+ - \underline{v}^*\right)\cdot\nabla W d\Gamma + \int_{\Sigma_i} W\hat{h}'\left(\underline{v}^* - \underline{v}^+\right)\cdot \underline{tn}d\Sigma - \int_{\Gamma_i} \hat{h}'\left(\underline{v}^* - \underline{v}^+\right)_T \cdot \nabla_{\Gamma_i^+} W d\Gamma - \int_{\Gamma_i} W\right]\hat{h}\underline{v}\cdot\underline{n}\left[d\Gamma + \int_{\Gamma_i} W\hat{Q}'d\Gamma = -\int_{\Gamma_i} W\right]\rho h\left(\underline{v} - \underline{v}^+\right)\cdot\underline{n}\left[d\Gamma = \int_{\Gamma_i} W\left]\underline{q}\cdot\underline{n}\right[d\Gamma \quad (5—28)$$

Observing the terms on the LHS of equation (5—28), cancellation can be made so that

$$\frac{D^+}{D^+t}\int_{\Gamma_i} W\hat{h}'d\Gamma - \int_{\Gamma_i} \hat{h}'\left(\underline{v}^+ - \underline{v}^*\right)_N\cdot\nabla W d\Gamma + \int_{\Sigma_i} W\hat{h}'\left(\underline{v}^* - \underline{v}^+\right)\cdot \underline{tn}d\Sigma - \int_{\Gamma_i} W\right]\hat{h}\underline{v}\cdot \underline{n}\left[d\Gamma + \int_{\Gamma_i} W\hat{Q}'d\Gamma = -\int_{\Gamma_i} W\right]\rho h\left(\underline{v} - \underline{v}^+\right)\cdot\underline{n}\left[d\Gamma = \int_{\Gamma_i} W\left]\underline{q}\cdot\underline{n}\right[d\Gamma \quad (5—29)$$

where N denotes normal component at Γ_i.

In section 5.3, the non-physical jump is defined as $\hat{Q}' = \left]\hat{h}\underline{v}\cdot\underline{n}\right[$. With this identity, it is obvious that equation (5—25) reduces to

$$\frac{D^+}{D^+t}\int_{\Gamma_i} W\hat{h}'d\Gamma - \int_{\Gamma_i} \hat{h}'\left(\underline{v}^+ - \underline{v}^*\right)_N\cdot\nabla W d\Gamma + \int_{\Sigma_i} W\hat{h}'\left(\underline{v}^* - \underline{v}^+\right)\cdot \underline{tn}d\Sigma = -\int_{\Gamma_i} W\right]\rho h\left(\underline{v} - \underline{v}^+\right)\cdot\underline{n}\left[d\Gamma = \int_{\Gamma_i} W\left]\underline{q}\cdot\underline{n}\right[d\Gamma \quad (5—30)$$

Comparison between equations (5—26) and (5—30) provides

$$\int_{\Gamma_i} \hat{h}'\left(\underline{v}^+ - \underline{v}^*\right)_N\cdot\nabla W d\Gamma = -\lim_{vol(\Omega_i)\to 0}\int_{\Omega_i}\rho h\left(\underline{v} - \underline{v}^*\right)\cdot\nabla W dV = \lim_{vol(\Omega_i)\to 0}\int_{\Omega_i}\underline{q}\cdot\nabla W dV \quad (5—31)$$

which confirms the existence of the limits.

Equation (5—30) is the definition of non-physical jump $\hat{h}'$ via the weighted governing equation, which facilitate the removal of the discontinuity. Discontinuity removal requires the matching of two CVs Ω and Ω^+ for the weighted transported equation. The overall movement of the CV Ω and the CV Ω^+ is matched provided $\underline{v}^*\cdot\underline{n} = \underline{v}^+\cdot\underline{n}$ on Γ. The two approaches can be related in transport form by the identity

$$\frac{D^*}{D^*t}\int_\Omega W\hat{h}dV - \int_\Omega \left(\frac{D^*W}{D^*t}\right)\hat{h}dV - \int_\Gamma W\hat{h}\underline{v}^*\cdot\underline{n}\,d\Gamma + \int_\Omega W\hat{h}\underline{v}^*\cdot\nabla W dV = \frac{D^+}{D^+t}\int_{\Omega^+} W\hat{h}dV — \int_{\Omega^+}\left(\frac{D^+W}{D^+t}\right)\hat{h}dV - \int_{\Gamma^+} W\hat{h}\underline{v}^+\cdot\underline{n}\,d\Gamma + \int_{\Omega^+} W\hat{h}\underline{v}^+\cdot\nabla W dV \quad (5—32)$$

The matching with weighted equation is slightly different to the unweighted equation and the derivation of equation (5—32) is shown in Appendix I—(i).

According to the identity as shown in equation (5—22), equation (5—32) reduces to

$$\frac{D^*}{D^*t}\int_\Omega W\hat{h}dV - \int_\Gamma W\hat{h}\underline{v}^*\cdot\underline{n}\,d\Gamma + \int_\Omega W\hat{h}\underline{v}^*\cdot\nabla W dV = \frac{D^+}{D^+t}\int_{\Omega^+} W\hat{h}dV - \int_{\Omega^+}\hat{h}(\underline{v}^+ - \underline{v}^*)\cdot\nabla W dV - \int_{\Gamma^+} W\hat{h}\underline{v}^+\cdot\underline{n}\,d\Gamma + \int_{\Omega^+} W\hat{h}\underline{v}^+\cdot\nabla W dV \quad (5—33)$$

Re-arrangement of equation (5—33) gives

$$\frac{D^*}{D^*t}\int_\Omega W\hat{h}dV = \frac{D^+}{D^+t}\int_\Omega W\hat{h}dV - \int_\Omega \hat{h}(\underline{v}^+ - \underline{v}^*)\cdot\nabla W dV + \int_\Gamma W\hat{h}(\underline{v}^* - \underline{v}^+)\cdot\underline{n}\,d\Gamma + \int_\Omega W\hat{h}(\underline{v}^+ - \underline{v}^*)\cdot\nabla W dV \quad (5—34)$$

Cancellation can now be made so that

$$\frac{D^*}{D^*t}\int_\Omega W\hat{h}dV = \frac{D^+}{D^+t}\int_\Omega W\hat{h}dV + \int_\Gamma W\hat{h}(\underline{v}^* - \underline{v}^+)\cdot\underline{n}\,d\Gamma \quad (5—35)$$

The identity derived from equation (5—32) to equation (5—35) allows the discontinuity to be removed from the LHS of equation (5—19) by subtracting $(D^+/D^+t)\int_{\Gamma_i} W\hat{h}'\,d\Gamma + \int_{\Sigma_i} W\hat{h}'(\underline{v}^* - \underline{v}^+)\cdot\underline{tn}d\Sigma$, i.e.

$$\frac{D^*}{D^*t}\int_{\Omega\setminus\Gamma_i} W\hat{h}dV + \int_{\Gamma\setminus\Sigma_i} W\hat{h}\underline{v}\cdot\underline{n}d\Gamma - \int_{\Omega\setminus\Gamma_i}\hat{h}\underline{v}\cdot\nabla W dV + \int_\Omega W\hat{Q}dV = \frac{D^*}{D^*t}\int_\Omega W\rho h dV + \int_\Gamma W\rho h(\underline{v} - \underline{v}^*)\cdot\underline{n}d\Gamma - \int_\Omega \rho h(\underline{v} - \underline{v}^*)\cdot\nabla W dV - \left(\frac{D^+}{D^+t}\int_{\Gamma_i} W\hat{h}'\,d\Gamma + \int_{\Sigma_i} W\hat{h}'(\underline{v}^* - \underline{v}^+)\cdot\underline{tn}d\Sigma\right) = -\int_\Gamma W\underline{q}\cdot\underline{n}\,d\Gamma + \int_\Omega \underline{q}\cdot\nabla W dV + \int_\Omega W\rho Q\,dV - \left(\frac{D^+}{D^+t}\int_{\Gamma_i} W\hat{h}'\,d\Gamma + \int_{\Sigma_i} W\hat{h}'(\underline{v}^* - \underline{v}^+)\cdot\underline{tn}d\Sigma\right) \quad (5—36)$$

Substitution of equation (5—26) into equation (5—36) provides

$$\frac{D^*}{D^*t}\int_{\Omega\setminus\Gamma_i} W\hat{h}dV + \int_{\Gamma\setminus\Sigma_i} W\hat{h}\underline{v}\cdot\underline{n}d\Gamma - \int_{\Omega\setminus\Gamma_i}\hat{h}\underline{v}\cdot\nabla W dV + \int_\Omega W\hat{Q}dV = \frac{D^*}{D^*t}\int_\Omega W\rho h dV + \int_\Gamma W\rho h(\underline{v} - \underline{v}^*)\cdot\underline{n}d\Gamma - \int_{\Gamma_i} W\Big]\rho h(\underline{v} - \underline{v}^+)\cdot(-\underline{n})\Big[d\Gamma - \int_\Omega \rho h(\underline{v} - \underline{v}^*)\cdot\nabla W dV - \left(-\lim_{vol(\Omega_i)\to 0}\int_{\Omega_i}\rho h(\underline{v} - \underline{v}^*)\cdot\nabla W\,dV\right) = -\int_\Gamma W\underline{q}\cdot\underline{n}\,d\Gamma + \int_\Omega \underline{q}\cdot\nabla W dV - \left(-\int_{\Gamma_i} W\Big]\underline{q}\cdot(-\underline{n})\Big[\,d\Gamma\right) + \int_\Omega W\rho Q\,dV - \lim_{vol(\Omega_i)\to 0}\int_{\Omega_i}\underline{q}\cdot\nabla W\,dV \quad (5—37)$$

On substitution the identity provided in equation (5—31), equation (5—37) becomes

$$\frac{D^*}{D^*t}\int_{\Omega\setminus\Gamma_i} W\hat{h}dV + \int_{\Gamma\setminus\Sigma_i} W\hat{h}\underline{v}\cdot\underline{n}d\Gamma - \int_{\Omega\setminus\Gamma_i} \hat{h}\underline{v}\cdot\nabla W dV + \int_{\Omega} W\hat{Q}dV = \frac{D^*}{D^*t}\int_{\Omega} W\rho h dV + \int_{\Gamma} W\rho h(\underline{v}-\underline{v}^*)\cdot\underline{n}d\Gamma - \int_{\Gamma_i} W\rho h(\underline{v}-\underline{v}^+)\cdot(-\underline{n})d\Gamma - \int_{\Omega} \rho h(\underline{v}-\underline{v}^*)\cdot\nabla W dV - \int_{\Gamma_i} \hat{h}'(\underline{v}^+-\underline{v}^*)_N\cdot\nabla W d\Gamma = -\int_{\Gamma} W\underline{q}\cdot\underline{n}\,d\Gamma + \int_{\Omega} \underline{q}\cdot\nabla W dV - \left(-\int_{\Gamma_i} W\right]\underline{q}\cdot(-\underline{n})\Big[d\Gamma\Big) + \int_{\Omega} W\rho Q\,dV - \int_{\Gamma_i} \hat{h}'(\underline{v}^+-\underline{v}^*)_N\cdot\nabla W d\Gamma \quad (5—38)$$

Similar to what has been done in chapter 3, equation (5—38) can be split into two equations, which are

$$\frac{D^*}{D^*t}\int_{\Omega\setminus\Gamma_i} W\hat{h}dV + \int_{\Gamma\setminus\Sigma_i} W\hat{h}\underline{v}\cdot\underline{n}d\Gamma - \int_{\Omega\setminus\Gamma_i} \hat{h}\underline{v}\cdot\nabla W dV + \int_{\Omega} W\hat{Q}dV = \frac{D^*}{D^*t}\int_{\Omega} W\rho h dV + \int_{\Gamma} W\rho h(\underline{v}-\underline{v}^*)\cdot\underline{n}d\Gamma - \int_{\Gamma_i} W\rho h(\underline{v}-\underline{v}^+)\cdot(-\underline{n})d\Gamma - \int_{\Omega} \rho h(\underline{v}-\underline{v}^*)\cdot\nabla W dV - \int_{\Gamma_i} \hat{h}'(\underline{v}^+-\underline{v}^*)_N\cdot\nabla W d\Gamma \quad (5—39)$$

and

$$\frac{D^*}{D^*t}\int_{\Omega\setminus\Gamma_i} W\hat{h}dV + \int_{\Gamma\setminus\Sigma_i} W\hat{h}\underline{v}\cdot\underline{n}d\Gamma - \int_{\Omega\setminus\Gamma_i} \hat{h}\underline{v}\cdot\nabla W dV + \int_{\Omega} W\hat{Q}dV = -\int_{\Gamma} W\underline{q}\cdot\underline{n}\,d\Gamma + \int_{\Omega} \underline{q}\cdot\nabla W dV - \left(-\int_{\Gamma_i} W\right]\underline{q}\cdot(-\underline{n})\Big[d\Gamma\Big) + \int_{\Omega} W\rho Q\,dV - \int_{\Gamma_i} \hat{h}'(\underline{v}^+-\underline{v}^*)_N\cdot\nabla W d\Gamma \quad (5—40)$$

Equation (5—39) is the linkage equation which relates the non-physical enthalpy and the physical enthalpy, equation (5—40) is the weighted non-physical governing equation which requires to be solved by numerical methods. In equations (5—39) and (5—40), the terms $\int_{\Omega} \rho h(\underline{v}-\underline{v}^*)\cdot\nabla W\,dV$ and $\int_{\Omega} \underline{q}\cdot\nabla W dV$ also contain sources. According to equation (5—31), Sources contained in both terms cancel with the term $\int_{\Gamma_i} \hat{h}'(\underline{v}^*-\underline{v}^+)_N\cdot\nabla_{\Gamma_i} W d\Gamma$.

5.4.2 Implementation of non-physical enthalpy method in the FEM

The analysis in section 5.4.1 provides three equations, which are

$$\frac{D^*}{D^*t}\int_{\Omega\setminus\Gamma_i} W\hat{h}dV + \int_{\Gamma\setminus\Sigma_i} W\hat{h}\underline{v}\cdot\underline{n}d\Gamma - \int_{\Omega\setminus\Gamma_i} \hat{h}\underline{v}\cdot\nabla W dV + \int_{\Omega} W\hat{Q}dV = \frac{D^*}{D^*t}\int_{\Omega} W\rho h dV + \int_{\Gamma} W\rho h(\underline{v}-\underline{v}^*)\cdot\underline{n}d\Gamma - \left(-\int_{\Gamma_i} W\right]\rho h(\underline{v}-\underline{v}^+)\cdot\underline{n}\Big[d\Gamma\Big) - \int_{\Omega\setminus\Gamma_i} \rho h(\underline{v}-\underline{v}^*)\cdot\nabla W dV$$

(5—41)

$$\frac{D^*}{D^*t}\int_{\Omega\backslash\Gamma_i} W\hat{h}dV + \int_{\Gamma\backslash\Sigma_i} W\hat{h}\underline{v}\cdot\underline{n}d\Gamma - \int_{\Omega\backslash\Gamma_i}\hat{h}\underline{v}\cdot\nabla W dV + \int_{\Omega} W\hat{Q}dV = -\int_{\Gamma} W\underline{q}\cdot\underline{n}\,d\Gamma +$$
$$\int_{\Omega\backslash\Gamma_i}\underline{q}\cdot\nabla W dV - \left(\int_{\Gamma_i} W\right]\underline{q}\cdot\underline{n}\Big[\,d\Gamma\right) + \int_{\Omega} W\rho Q\,dV \qquad (5—42)$$

and

$$\int_{\Gamma_i} W\hat{Q}'dA = \int_{\Gamma_i} W\big]\hat{h}\underline{v}\cdot\underline{n}\big[d\Gamma \qquad (5—43)$$

According to equation (5—31), the discontinuity contained in the weighted terms $\int_{\Omega}\rho h(\underline{v}-\underline{v}^*)\cdot\nabla W dV$ and $\int_{\Omega}\underline{q}\cdot\nabla W dV$ is cancelled with the term $\int_{\Gamma_i}\hat{h}'(\underline{v}^*-\underline{v}^+)_N\cdot\nabla_{\Gamma_i}Wd\Gamma$. The notation $\Omega\backslash\Gamma_i$ means that the boundary Γ_i is excluded from Ω. Though the non-physical jump $\hat{h}'$ is non-zero in the analysis, it is absent from both the linkage equation and the weighted governing equation, however, several jump terms remain which require evaluation, which are $-\int_{\Gamma_i} W\big]\rho h(\underline{v}-\underline{v}^+)\cdot\underline{n}\big[d\Gamma$, $\int_{\Gamma_i} W\left]\underline{q}\cdot\underline{n}\right[\,d\Gamma$ and $\int_{\Gamma_i} W\big]\hat{h}\underline{v}\cdot\underline{n}\big[d\Gamma$.

The weighted governing equation (5—42) can be solved by the numerical method, such as the FEM. In the Galerkin finite element approach, the weighting functions are also the shape functions, thus the weighed governing equation of (5—42) becomes

$$\frac{D^*}{D^*t}\int_{\Omega_e\backslash\Gamma_i^e} N_\vartheta\tilde{h}dV + \int_{\Gamma_e\backslash\Sigma_i^e} N_\vartheta\tilde{h}\underline{v}\cdot\underline{n}d\Gamma - \int_{\Omega_e\backslash\Gamma_i^e}\tilde{h}\underline{v}\cdot\nabla N_\vartheta dV + \int_{\Omega_e} N_\vartheta\hat{Q}dV = -\int_{\Gamma_e} N_i\underline{q}\cdot$$
$$\underline{n}\,d\Gamma + \int_{\Omega_e\backslash\Gamma_i^e}\underline{q}\cdot\nabla N_\vartheta dV - \left(-\int_{\Gamma_i} N_\vartheta\right]\rho h(\underline{v}-\underline{v}^{\times})\cdot\underline{n}\big[d\Gamma\Big) + \int_{\Omega_e} N_\vartheta\rho Q\,dV \qquad (5—44)$$

where N_ϑ denote the shape functions, $\tilde{h}$ is the trial solution, the subscript ϑ refers to the ith simultaneous algebraic equation of an element and the subscript e denotes that this is in an elemental domain. The semi-discretized governing equation (5—44) is defined in an element domain. The velocity $\underline{v}^{\times}$ is defined in a similar fashion as the velocity $\underline{v}^+$, the superscript $\times$ signifies the velocity $\underline{v}^{\times}$ is for an element domain, i.e. $\underline{v}^{\times}\cdot\underline{n}=\underline{v}_i\cdot\underline{n}$ at interface Γ_i^e. The term $\int_{\Omega_e\backslash\Gamma_i^e}\underline{q}\cdot\nabla N_\vartheta dV$ is without source and arises as a consequence of the cancellation of the source contained in the term $\int_{\Omega_e}\underline{q}\cdot\nabla N_\vartheta dV$ with $\int_{\Gamma_i}\hat{h}'(\underline{v}^*-\underline{v}^+)_N\cdot\nabla_{\Gamma_i}Wd\Gamma$ according to the identity as shown in equation (5—31).

For standard Galerkin method, the trial solution with respect to non-physical enthalpy can be defined as

$$\tilde{h} \approx \sum_{\varsigma=1}^{NN} N_\varsigma \hat{h}_\varsigma \tag{5—45}$$

where ς is the local nodal number an element, NN is the total number of nodes of the element, and $\hat{h}_\varsigma$ is the nodal field variable of node ς.

The solution of equation (5—44) requires that, the linkage equation (5—39) can be solved analytically, which on setting the weighting function $W = 1$ gives

$$\frac{D^*}{D^*t}\int_{\Omega_e\setminus\Gamma_i^e} \hat{h}dV + \int_{\Gamma_e\setminus\Sigma_i^e} \hat{h}\underline{v}\cdot\underline{n}d\Gamma + \int_{\Omega_e} \hat{Q}dV = \frac{D^*}{D^*t}\int_{\Omega_e} \rho h dV + \int_{\Gamma_e} \rho h\left(\underline{v}-\underline{v}^*\right)\cdot\underline{n}d\Gamma - \left(-\int_{\Gamma_i^e}\right]\rho h\left(\underline{v}-\underline{v}^{\times}\right)\cdot\underline{n}\left[d\Gamma\right) \tag{5—46}$$

where the subscript e and the velocity $\underline{v}^{\times}$ indicates that equation (5—44) is solved analytically within an element CV.

The simplest setting that makes the problem easier to be solved by the FEM is to let the mesh be fixed, i.e. $\underline{v}^* = \underline{0}$. Also assuming that no additional heat is applied externally, say $\int_{\Omega_e} N_\vartheta \rho Q\, dV = 0$, as a consequence, equation (5—44) returns to

$$\frac{\partial}{\partial t}\int_{\Omega_e\setminus\Gamma_i^e} N_\vartheta \tilde{h}dV + \int_{\Gamma_e\setminus\Sigma_i^e} N_\vartheta \tilde{h}\underline{v}\cdot\underline{n}d\Gamma - \int_{\Omega_e\setminus\Gamma_i^e} \tilde{h}\underline{v}\cdot\nabla N_\vartheta dV + \int_{\Omega_e} N_\vartheta \hat{Q}dV = -\int_{\Gamma_e} N_\vartheta \underline{q}\cdot\underline{n}\,d\Gamma + \int_{\Omega_e\setminus\Gamma_i^e} \underline{q}\cdot\nabla N_\vartheta dV - \left(-\int_{\Gamma_i} N_\vartheta\right]\rho h\left(\underline{v}-\underline{v}^{\times}\right)\cdot\underline{n}\left[d\Gamma\right) \tag{5—47}$$

Similarly, for the linkage equation, it gives

$$\frac{\partial}{\partial t}\int_{\Omega_e\setminus\Gamma_i^e} \hat{h}dV + \int_{\Gamma_e\setminus\Sigma_i^e} \hat{h}\underline{v}\cdot\underline{n}d\Gamma + \int_{\Omega_e} \hat{Q}dV = \frac{\partial}{\partial t}\int_{\Omega_e} \rho h dV + \int_{\Gamma_e} \rho h\underline{v}\cdot\underline{n}d\Gamma - \left(-\int_{\Gamma_i^e}\right]\rho h\left(\underline{v}-\underline{v}^{\times}\right)\cdot\underline{n}\left[d\Gamma\right) \tag{5—48}$$

Recall the identity that $\hat{h} = \hat{c}T$ when $T \neq 0$, where $\hat{c}$ is non-physical capacitance and T is temperature, equation (5—48) becomes

$$\frac{\partial}{\partial t}\int_{\Omega_e\setminus\Gamma_i^e} \hat{c}TdV + \int_{\Gamma_e\setminus\Sigma_i^e} \hat{c}T\underline{v}\cdot\underline{n}d\Gamma + \int_{\Omega_e} \hat{Q}dV = \frac{\partial}{\partial t}\int_{\Omega_e} \rho h dV + \int_{\Gamma_e} \rho h\underline{v}\cdot\underline{n}d\Gamma - \left(-\int_{\Gamma_i^e}\right]\rho h\left(\underline{v}-\underline{v}^{\times}\right)\cdot\underline{n}\left[d\Gamma\right) \tag{5—49}$$

The non-physical source $\hat{Q}$ is user-defined, which can be written as

$$\int_{\Omega_e} \hat{Q} dV = \int_{\Omega_e \backslash \Gamma_i^e} \hat{Q} dV + \int_{\Gamma_i^e} \hat{Q}' d\Gamma \tag{5—50}$$

In equation (5—50), the term $\int_{\Gamma_i^e} \hat{Q}' d\Gamma$ is defined as $\int_{\Gamma_i^e} \hat{Q}' d\Gamma = \int_{\Gamma_i^e}]\hat{h}\underline{v} \cdot \underline{n}[d\Gamma$, which is introduced for the convenience of the development of non-physical theory. It can be seen that the non-physical source $\hat{Q}$ in the element domain $\Omega_e \backslash \Gamma_i^e$ is still undefined. This helps the evaluation of non-physical capacitance $\hat{c}$ through equation (5—50). On setting that

$$\int_{\Omega_e \backslash \Gamma_i^e} \hat{Q} dV = \int_{\Omega_e \backslash \Gamma_i^e} \nabla \cdot (\rho h \underline{v}) dV - \int_{\Omega_e \backslash \Gamma_i^e} \nabla \cdot (\hat{c} T \underline{v}) dV \tag{5—51}$$

and noting identities

$$\int_{\Omega_e \backslash \Gamma_i^e} \nabla \cdot (\rho h \underline{v}) dV = \int_{\Gamma_e} \rho h \underline{v} \cdot \underline{n} d\Gamma - \left(- \int_{\Gamma_i^e}]\rho h \underline{v} \cdot \underline{n}[d\Gamma \right) \tag{5—52}$$

and

$$\int_{\Omega_e \backslash \Gamma_i^e} \nabla \cdot (\hat{c} T \underline{v}) dV = \int_{\Gamma_e} \hat{c} T \underline{v} \cdot \underline{n} d\Gamma - \left(- \int_{\Gamma_i^e}]\hat{h} \underline{v} \cdot \underline{n}[d\Gamma \right) \tag{5—53}$$

Substitution of equations (5—52) and (5—53) into equation (5—51), and application of divergence theorem gives

$$\int_{\Omega_e \backslash \Gamma_i^e} \hat{Q} dV = \int_{\Gamma_e} \rho h \underline{v} \cdot \underline{n} d\Gamma + \int_{\Gamma_i^e}]\rho h \underline{v} \cdot \underline{n}[d\Gamma - \int_{\Gamma_e} \hat{c} T \underline{v} \cdot \underline{n} d\Gamma - \int_{\Gamma_i^e}]\hat{h} \underline{v} \cdot \underline{n}[d\Gamma \tag{5—54}$$

Further, substitution of equation (5—54) into equation (5—50) gives

$$\int_{\Omega_e} \hat{Q} dV = \int_{\Gamma_e} \rho h \underline{v} \cdot \underline{n} d\Gamma + \int_{\Gamma_i^e}]\rho h \underline{v} \cdot \underline{n}[d\Gamma - \int_{\Gamma_e} \hat{c} T \underline{v} \cdot \underline{n} d\Gamma - \int_{\Gamma_i^e}]\hat{h} \underline{v} \cdot \underline{n}[d\Gamma + \int_{\Gamma_i^e}]\hat{h} \underline{v} \cdot \underline{n}[d\Gamma = \int_{\Gamma_e} \rho h \underline{v} \cdot \underline{n} d\Gamma + \int_{\Gamma_i^e}]\rho h \underline{v} \cdot \underline{n}[d\Gamma - \int_{\Gamma_e} \hat{c} T \underline{v} \cdot \underline{n} d\Gamma \tag{5—55}$$

Substitution of equation (5—55) into equation (5—49) provides the equation for the evaluation of non-physical capacitance $\hat{c}$, which is

$$\int_{\Omega_e \backslash \Gamma_i^e} (\hat{c} T^{n+1} - \hat{c} T^n) dV = \int_{\Omega_e} \rho^{n+1} h^{n+1} dV - \int_{\Omega_e} \rho^n h^n dV - \int_{t^n}^{t^{n+1}} \int_{\Gamma_i^e}]\rho h \underline{v}^{\times} \cdot \underline{n}[d\Gamma \, dt \tag{5—56}$$

With the mean-value theorem applied to the integration, the mean non-physical capacitance for the time period t^n to t^{n+1} can be placed outside of the integration. Equation (5—56) can be re-arranged as

$$\hat{c} = \frac{\int_{\Omega_e} \rho^{n+1} h^{n+1} dV - \int_{\Omega_e} \rho^n h^n dV - \int_{t^n}^{t^{n+1}} \int_{\Gamma_i^e}]\rho h \underline{v}^{\times} \cdot \underline{n}[dA dt}{\int_{\Omega_e \setminus \Gamma_i^e} T^{n+1} dV - \int_{\Omega_e \setminus \Gamma_i^e} T^n dV} \tag{5—57}$$

The non-physical source term $\hat{Q}$ is now fully defined in the element CV Ω_e, and the evaluation of non-physical capacitance $\hat{c}$ is developed corresponding to the definition of $\hat{Q}$. The non-physical source term $\hat{Q}$ is defined as the difference of the physical enthalpy change due to advection and the non-physical enthalpy change due to numerical advection. Equation (5—55) is established with two benefits: firstly, it shows that the introduction of $\hat{Q}' =]\hat{h}\underline{v} \cdot \underline{n}[$ in the theory is justified; secondly, it establishes the purpose of non-physical variable $\hat{Q}$, that is, no matter how the non-physical enthalpy $\hat{h}$ is defined, the non-physical source $\hat{Q}$ will adjust itself through the theory, to satisfy the conservation equation.

In equation (5—55), it can be seen that the evaluation of non-physical source $\int_{\Omega_e} \hat{Q} dV$ is dependent on the non-physical capacitance $\hat{c}$, consequently, the non-physical capacitance $\hat{c}$ is required to be determined by equation (5—57) first. The evaluation and approximation of each term on the RHS of equation (5—57) are conducted as follows.

5.5 The evaluation of non-physical variables

The specific enthalpy for solid and liquid follow the identities, which are

$$h_s = h_{sol} + \int_{T_{sol}}^{T} c_s(T')\, dT' \tag{5—58a}$$

$$h_l = h_{liq} + \int_{T_{liq}}^{T} c_l(T')\, dT' \tag{5—58b}$$

where $h_{sol} = c_s T_{sol}$ and $h_{liq} = h_{sol} + L$ are the phase change enthalpy, and L is the latent heat of fusion. T_{sol} is the solidus temperature and T_{liq} is the liquidus temperature [39, 41, 62-63, 66]. For isothermal solidification, the identity $T_{sol} = T_{liq}$ applies. So, the enthalpy ρh can be represented by

$$\rho h = \Upsilon_s \rho_s h_s + \Upsilon_l \rho_l h_l \tag{5—59}$$

where Υ_s and Υ_l are element-based solid fraction and element-based liquid fraction, respectively. The identity$\Upsilon_s + \Upsilon_l = 1$ applys to the isothermal solidification and eutectic solidification. If the solidification is mushy zone solidification, such as alloy solidification, the solidus temperature T_{sol} and liquidus temperature T_{liq} are not equal. The fraction of mushy zone Υ_m should satisfy the identity$\Upsilon_s + \Upsilon_m + \Upsilon_l = 1$.

For fixed grid simulation of isothermal solidification, assuming that the element liquid fraction for time t^{n+1} is Υ^{n+1} and the liquid fraction for time t^n is Υ^{n}. The volumetric enthalpy for both steps can be approximated as

$$\int_{\Omega_e} \rho^{n+1} h^{n+1} dV = \int_{\Omega_e} {\Upsilon_s}^{n+1} \rho^{n+1} \left(h_{sol} + \int_{T_{sol}}^{T^{n+1}} c_s(T') dT' \right) + {\Upsilon_l}^{n+1} \rho^{n+1} \left(h_{liq} + \int_{T_{liq}}^{T^{n+1}} c_l(T') dT' \right) \quad (5—60)$$

Also, assuming that the material properties of each phase are constant, consequently, equation (5—60) returns to

$$\int_{\Omega_e} \rho^{n+1} h^{n+1} dV = \int_{\Omega_e} {\Upsilon_s}^{n+1} \rho_s \left(h_{sol} + c_s (T^{n+1} - T_{sol}) \right) + {\Upsilon_l}^{n+1} \rho_l \left(h_{liq} + c_l (T^{n+1} - T_{sol}) \right) dV \quad (5—61)$$

Since $h_{liq} = h_{sol} + L$, $h_{sol} = c_s T_{sol}$ and $T_{liq} = T_{sol}$ for isothermal solidification, equation (5—61) reduces to

$$\int_{\Omega_e} \rho^{n+1} h^{n+1} dV = \int_{\Omega_e} \left({\Upsilon_s}^{n+1} \rho_s c_s T^{n+1} + {\Upsilon_l}^{n+1} \rho_l (c_s - c_l) T_{sol} + {\Upsilon_l}^{n+1} \rho_l L + {\Upsilon_l}^{n+1} \rho_l c_l T^{n+1} \right) dV \quad (5—62)$$

Assuming that the all the parameters are spatially invariant at time t^{n+1} and the integral $\int_{\Omega_e} dV = V_e$, where V_e is the element volume, thus, equation (5—62) returns to

$$\int_{\Omega_e} \rho^{n+1} h^{n+1} dV = {\Upsilon_s}^{n+1} \rho_s c_s T^{n+1} V_e + {\Upsilon_l}^{n+1} \rho_l (c_s - c_l) T_{sol} V_e + {\Upsilon_l}^{n+1} \rho_l L V_e + {\Upsilon_l}^{n+1} \rho_l c_l T^{n+1} V_e \quad (5—63)$$

Observing equation (5—63), the RHS of equation (5—63) can be divided into three parts, the summation ${\Upsilon_s}^{n+1} \rho_s c_s T^{n+1} V_e + {\Upsilon_l}^{n+1} \rho_l c_l T^{n+1} V_e = \left({\Upsilon_s}^{n+1} \rho_s c_s + {\Upsilon_l}^{n+1} \rho_l c_l \right) T^{n+1} V_e$ is the sensible enthalpy at time t^{n+1}, where it can be seen that terms in the bracket is the

mixture physical material properties. The term $\Upsilon_l^{n+1}\rho_l(c_s - c_l)T_{sol}V_e$ is the discontinuity which relates to the material property difference, and the term $\Upsilon_l^{n+1}\rho_l LV_e$ is the discontinuity which relates to the release of latent heat.

Similar to equation (5—63), the enthalpy at time t^n can be evaluated as

$$\int_{\Omega_e}\rho^n h^n dV = \Upsilon_s{}^n\rho_s c_s T^n V_e + \Upsilon_l{}^n\rho_l(c_s - c_l)T_{sol}V_e + \Upsilon_l{}^n\rho_l LV_e + \Upsilon_l{}^n\rho_l c_l T^n V_e \qquad (5—64)$$

Subtraction of equation (5—64) from equation (5—63) gives

$$\int_{\Omega_e}\rho^{n+1}h^{n+1}dV - \int_{\Omega_e}\rho^n h^n dV = \left(\Upsilon_s{}^{n+1}\rho_s c_s T^{n+1}V_e + \Upsilon_l{}^{n+1}\rho_l c_l T^{n+1}V_e\right) - (\Upsilon_s{}^n\rho_s c_s T^n V_e + \Upsilon_l{}^n\rho_l c_l T^n V_e) + \left(\Upsilon_l{}^{n+1} - \Upsilon_l{}^n\right)(\rho_l(c_s - c_l)T_{sol} + \rho_l L)V_e \qquad (5—65)$$

Moreover, the evaluation of the jump term $\int_{t^n}^{t^{n+1}}\int_{\Gamma_i^e}]\rho h\underline{v}^{\times}\cdot\underline{n}[d\Gamma\,dt$ can be conducted as

$$\int_{t^n}^{t^{n+1}}\int_{\Gamma_i^e}]\rho h\underline{v}^{\times}\cdot\underline{n}[d\Gamma\,dt = \int_{\Gamma_i^e}\left((\rho_l h_l - \rho_s h_s)\int_{t^n}^{t^{n+1}}\underline{v}^{\times}\cdot\underline{n}\right)d\Gamma \qquad (5—66)$$

With the identity$(\rho_l h_l - \rho_s h_s) = (\rho_l - \rho_s)h_{sol} + \rho_l L$, and the assumption that $\int_{t^n}^{t^{n+1}}\underline{v}^{\times}\cdot\underline{n} \approx \left(\Upsilon_l{}^{n+1} - \Upsilon_l{}^n\right)V_e$, equation (5—66) becomes

$$\int_{\Gamma_i^e}]\rho h\underline{v}^{\times}\cdot\underline{n}[d\Gamma\,dt = \left(\Upsilon_l{}^{n+1} - \Upsilon_l{}^n\right)\left((\rho_l - \rho_s)h_{sol} + \rho_l L\right)V_e \qquad (5—67)$$

By comparing equation (5—67) and equation (5—65), it can be seen that the approximation of non-physical capacitance using equation (5—57) should remove most of the discontinuity from the capacitance, however, a discontinuity remains which is much lower due to material property difference, because

$$\int_{\Omega_e}\rho^{n+1}h^{n+1}dV - \int_{\Omega_e}\rho^n h^n dV + \int_{\Gamma_i^e}]\rho h\underline{v}^{\times}\cdot\underline{n}[d\Gamma\,dt = \left(\Upsilon_s{}^{n+1}\rho_s c_s T^{n+1}V_e + \Upsilon_l{}^{n+1}\rho_l c_l T^{n+1}V_e\right) - (\Upsilon_s{}^n\rho_s c_s T^n V_e + \Upsilon_l{}^n\rho_l c_l T^n V_e) + \left(\Upsilon_l{}^{n+1} - \Upsilon_l{}^n\right)(\rho_l(c_s - c_l)T_{sol} + \rho_l L)V_e - \left(\Upsilon_l{}^{n+1} - \Upsilon_l{}^n\right)\left((\rho_l - \rho_s)h_{sol} + \rho_l L\right)V_e \qquad (5—68)$$

If the densities $\rho_l \approx \rho_s$ and the specific capacities $c_l \approx c_s$ or the capacitance $\rho_l c_l \approx \rho_s c_s$ can both make the last two terms on the RHS of equation (5—68) be zero, i.e.

$$\left(\Upsilon_l^{n+1}-\Upsilon_l^{n}\right)(\rho_l(c_s-c_l)T_{sol}+\rho_l L)V_e-\left(\Upsilon_l^{n+1}-\Upsilon_l^{n}\right)\left((\rho_l-\rho_s)h_{sol}+\rho_l L\right)V_e\approx 0 \tag{5—69}$$

Thus equation (5—69) reduces to

$$\int_{\Omega_e}\rho^{n+1}h^{n+1}dV-\int_{\Omega_e}\rho^{n}h^{n}dV-\int_{\Gamma_i^e}\rho h\underline{v}^{\times}\cdot\underline{n}\,d\Gamma\,dt\approx\left(\Upsilon_s{}^{n+1}\rho_s c_s T^{n+1}V_e+\Upsilon_l{}^{n+1}\rho_l c_l T^{n+1}V_e\right)-\left(\Upsilon_s{}^{n}\rho_s c_s T^{n}V_e+\Upsilon_l{}^{n}\rho_l c_l T^{n}V_e\right) \tag{5—70}$$

which is obviously the difference of sensible enthalpy.

Thus the approximation of equation (5—57) returns the non-physical capacitance as the mixture physical capacitance, e.g.

$$\hat{c}=\frac{(\Upsilon_s{}^{n+1}\rho_s c_s+\Upsilon_l{}^{n+1}\rho_l c_l)T^{n+1}-(\Upsilon_s{}^{n}\rho_s c_s+\Upsilon_l{}^{n}\rho_l c_l)T^{n}}{T^{n+1}-T^{n}} \tag{5—71}$$

Once the non-physical capacitance $\hat{c}$ is known for a time increment, the non-physical source $\hat{Q}$ can be evaluated. In equation (5—54), the non-physical $\hat{Q}$ is a volumetric term, and the terms on the LHS of equation are boundary terms. The term $\int_{\Gamma e}\hat{c}T\underline{v}\cdot\underline{n}dA$ can be evaluated numerically as

$$\int_{t^n}^{t^{n+1}}\int_{\Gamma e}\hat{c}T\underline{v}\cdot\underline{n}dA\,dt\approx\theta\left[K_v{}^{n+1}\right]\{T^{n+1}\}+(1-\theta)[K_v{}^{n}]\{T^{n}\}=\theta\Delta t\int_{\Omega_e}\{N\}\hat{c}v\left\{\frac{\partial N}{\partial x}\right\}\{T^{n+1}\}dV+(1-\theta)\Delta t\int_{\Omega_e}\{N\}\hat{c}v\left\{\frac{\partial N}{\partial x}\right\}\{T^{n}\}dV \tag{5—72}$$

where θ is a blending factor of theta method for time discretization, $[K_v]$ is the element advective coefficient matrix.

The term

$$\int_{t^n}^{t^{n+1}}\int_{\Gamma_e}\rho h\underline{v}\cdot\underline{n}d\Gamma\,dt\approx\int_{\Gamma_e}\rho h\left(\int_{t^n}^{t^{n+1}}\underline{v}\cdot\underline{n}\,dt\right)d\Gamma\approx\int_{\Omega_{\mathrm{f}}^e}\rho h dV \tag{5—73}$$

where Ω_{f}^e is the virtual CV swept by element boundary with velocity $\underline{v}$, say $vol(\Omega_{\mathrm{f}}^e)\approx A_e\left(\underline{v}\cdot\underline{n}\right)(t^{n+1}-t^n)$. This technique has been used in reference [66], it is also used in chapter 4, which detailed procedure can be seen in Appendix I—(d).

The jump term $\int_{t^n}^{t^{n+1}}\int_{\Gamma_i^e}\rho h\underline{v}\cdot\underline{n}\,d\Gamma\,dt$ should be evaluated separately as

$$\int_{t^n}^{t^{n+1}} \int_{\Gamma_i^e}]\rho h \underline{v} \cdot \underline{n}[d\Gamma\, dt = \int_{t^n}^{t^{n+1}} \int_{\Gamma_i^e} (\rho_l h_l \underline{v}_l - \rho_s h_s \underline{v}_s) \cdot \underline{n} d\Gamma\, dt \quad (5—74)$$

The mass of liquid swept by the interface Γ_i^e is equal to the mass of solid swept by the interface in a period of time, thus an identity can be established as

$$\rho_l \underline{v}_l A_i \Delta t = \rho_s \underline{v}_s A_i \Delta t \quad (5—75)$$

where A_i is the area of interface Γ_i^e.

Substitution of equation (5—75) into equation (5—74) gives

$$\int_{t^n}^{t^{n+1}} \int_{\Gamma_i^e}]\rho h \underline{v} \cdot \underline{n}[d\Gamma\, dt = \int_{t^n}^{t^{n+1}} \int_{\Gamma_i^e} (\rho_s h_l \underline{v}_s - \rho_s h_s \underline{v}_s) \cdot \underline{n} d\Gamma\, dt = \rho_s \int_{t^n}^{t^{n+1}} \int_{\Gamma_i^e} (h_l - h_s) \underline{v}_s \cdot \underline{n} d\Gamma\, dt \quad (5—76)$$

Assuming that $\int_{t^n}^{t^{n+1}} \underline{v}_s \cdot \underline{n} dt = (\underline{v}_s \cdot \underline{n})(t^{n+1} - t^n) = (X_s^{n+1} - X_s^n)_i$, consequently, on recalling the identity that $(h_l - h_s) = h_{sol} + L - h_{sol} = L$, equation (5—73) becomes

$$\int_{t^n}^{t^{n+1}} \int_{\Gamma_i^e}]\rho h \underline{v} \cdot \underline{n}[d\Gamma\, dt = (X_s^{n+1} - X_s^n)_i \rho_s L A_i \quad (5—77)$$

Subtraction of equations (5—72) and (5—73) provides a quantity, which can be applied to the numerical system as the non-physical source $\hat{Q}$.

In order to examine the feasibility of all evaluations described above, two situations of nodal temperatures for a one-dimensional two-node linear element is prescribed in Table 5.1. The material properties are shown in Table 4.2. The nodal temperature of situation 1 ensures that the simple element is always liquid during the period t^n to t^{n+1}; and the nodal temperature of simulation 2 ensures that the simple element is completely liquid at time t^n, and then, the discontinuity is present because the temperature drops below the solidus temperature. Assuming that the element length is $1 \times 10^{-3} m$, the material velocity is pre-set as $-0.05\ m/s$, a sketch of the two situations is shown in Figure 5.2.

Situation	Time step	Node 1	Node 2
Situation 1	n	405 ℃	405 ℃
	$n+1$	401 ℃	404 ℃
Situation 2	n	401 ℃	404 ℃
	$n+1$	394 ℃	402 ℃

Table 5.1: Prescribed nodal temperatures of a simple 1D finite element

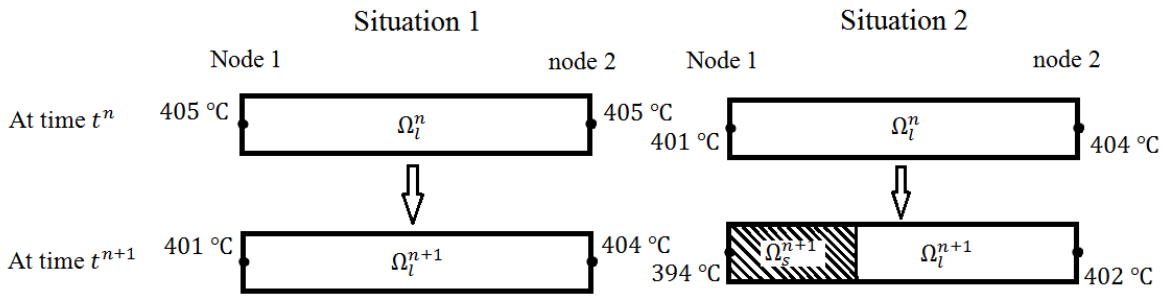

Figure 5.2: Sketch of prescribed situations

In Table 5.2, the values for all terms are evaluated on the basis of nodal temperature of situation 1, these values show that the approximations and evaluations are established properly. As a discontinuity is not present in situation 1, the jump term is zero, the non-physical capacitance is identical to the physical capacitance of liquid material ($\rho_l c_l = 3.3 \times 10^6\ J/m^3$℃). Moreover, the magnitude of physical advection and numerical advection are equal to each other, which proves that the analytical strategy is correct.

Situation 1			
Definition	Term	Evaluation	Value
Element-based solid volume fraction at time t^{n+1}	Υ_s^{n+1}	Element based temperature approximation	0
Element-based solid volume fraction at time t^{n}	Υ_s^{n}	Element based temperature approximation	0
Element volumetric enthalpy at time t^{n+1}	$\int_{\Omega_e} \rho^{n+1} h^{n+1} dV$	(5—63)	$1.922 \times 10^6\ J$
Element volumetric enthalpy at time t^{n}	$\int_{\Omega_e} \rho^{n} h^{n} dV$	(5—63)	$1.931 \times 10^6\ J$
Discontinuity	$\int_{t^n}^{t^{n+1}} \int_{\Gamma_i^e}]\rho h \underline{v}^{\times} \cdot \underline{n}[d\Gamma\, dt$	(5—67)	0
Non-physical capacitance	$\hat{c}$	(5—57)	$3.3 \times 10^6\ J/m^3℃$
Mixture physical capacitance	c	(5—68)	$3.3 \times 10^6\ J/m^3℃$
Numerical advection	$\int_{t^n}^{t^{n+1}} \int_{\Gamma^e} \hat{c} T \underline{v} \cdot \underline{n} d\Gamma\, dt$	(5—72)	$-1.238 \times 10^4\ J$
Physical advection	$\int_{t^n}^{t^{n+1}} \int_{\Gamma_i^e} \rho h \underline{v} \cdot \underline{n} d\Gamma\, dt$	(5—73)	$1.238 \times 10^4\ J$
Non-physical source	$\int_{\Omega_e} \hat{Q} dV$	(5—55)	$0\ J$

Table 5.2: Value of each term on the basis of situation 1

Next, the nodal temperatures of situation 2 are substituted into the evaluations, which values are provided in Table 5.3.

Situation 2			
Definition	Term	Evaluation	Value
Element-based solid volume fraction at time t^{n+1}	Υ_s^{n+1}	Element based temperature approximation	0
Element-based solid volume fraction at time t^{n}	Υ_s^{n}	Element based temperature approximation	0.75
Element volumetric enthalpy at time t^{n+1}	$\int_{\Omega_e} \rho^{n+1} h^{n+1} dV$	(5—63)	$1.301 \times 10^6\ J$
Element volumetric enthalpy at time t^{n}	$\int_{\Omega_e} \rho^{n} h^{n} dV$	(5—63)	$1.922 \times 10^6\ J$
Discontinuity	$\int_{t^n}^{t^{n+1}} \int_{\Gamma_i^e}]\rho h \underline{v}^{\times} \cdot \underline{n}[d\Gamma\, dt$	(5—67)	$-6.075 \times 10^5\ J$
Non-physical capacitance	$\hat{c}$	(5—57)	$3.03 \times 10^6\ J/m^3$℃
Mixture physical capacitance	c	(5—68)	$3.098 \times 10^6\ J/m^3$℃
Numerical advection	$\int_{t^n}^{t^{n+1}} \int_{\Gamma^e} \hat{c} T \underline{v} \cdot \underline{n} d\Gamma\, dt$	(5—72)	$-4.166 \times 10^4\ J$
Physical advection	$\int_{t^n}^{t^{n+1}} \int_{\Gamma_i^e} \rho h \underline{v} \cdot \underline{n} d\Gamma\, dt$	(5—73)	$1.779 \times 10^6\ J$
Non-physical source	$\int_{\Omega_e} \hat{Q} dV$	(5—55)	$1.737 \times 10^6\ J$

Table 5.3: Value of each term on the basis of situation 2

Phase transformation is occurring in the simple element now because of situation 2. It can be seen in Table 5.3 that, the element volume solid fraction at t^{n+1} is no longer zero because

the solid and liquid co-exist in the simple element. The jump term is not zero as a result of latent heat release. The non-physical capacitance $\hat{c}$ and the mixture physical capacitance c are approximately equal to each other when the blending factor $\theta = 0.5$. It has to be mentioned that the mixture physical capacitance c is actually between $2.895 \times 10^6\ J/m^3$℃ to $3.3 \times 10^6\ J/m^3$℃ depending on how the factor θ is set for the θ-method. In situation 2, the discontinuity transports into the element through the element boundary, which results a difference in the physical advection and the continuous numerical advection, this difference is accounted for by the non-physical source, thus the conservation equation is satisfied.

5.6 Summary

This chapter aims to solve the instability of the non-physical enthalpy method when involving advection-diffusion. A new definition of the non-physical enthalpy has been given by the transport equation (5—1). Through this definition, the physical advection is isolated from the non-physical temporal term. As a consequence, no negative non-physical capacitance will be obtained. However, with this definition remains an advective term which includes the non-physical term. Through the derivation of the new non-physical theory, it give rise to a new non-physical term which is the non-physical source $\hat{Q}$. The non-physical source $\hat{Q}$ is fully defined in the development of the theory and the establishment of evaluation strategies. In section 5.5, the evaluations and approximations are provided in detail, their feasibility and correctness are proved by the prescribed situations of a simple element.

Comparison between the classical non-physical enthalpy formulation and the new non-physical enthalpy formulation shows that, the new non-physical enthalpy formulation has an advective term and a non-physical source term. In chapters 2 and 3, it had been mentioned that when the advective term is involved in the numerical solution, numerical oscillation is a feature because of complex eigenvalue from the large elemental Peclèt number, consequently stabilization techniques are required. In the following chapter 6, the new non-physical enthalpy method will be implemented into the one-dimensional FEM. It will describe how the advection and the non-physical source are treated.

In order to deal with the new advective term, three concepts are described. In the first concept, the non-physical capacitance is used to construct the matrix of advection. The advection term in FEM is a known issue for numerical instability. As a matter of fact, the upwind method,

such as the Petrov-Galerkin method, is applied with this concept. Nevertheless, numerical experiments show that there is incompatibility between the non-physical capacitance and the upwind scheme, as disorder can be found in the computation of capacitances. Thus, the second concept was introduced. In the second concept, the discontinuity is forced to be removed from the advection, and a new source term is introduced to account for the discontinuity and to maintain the consistency of energy. It was demonstrated by the numerical experiments that the stability had been dramatically enhanced. In the last concept, the advective term is completely replaced by a source term. This is in preparation for the multi-dimensional FEM, in which discontinuous weighing functions may be hard to construct. Moreover, at the very end of chapter 7, the potential capability of the non-physical variable method, which can solve the strong discontinuity, is demonstrated by the plots of enthalpy.

Chapter 6 Numerical Trials on the New Non-physical Enthalpy Method for 1D Isothermal Solidification Problems

6.1 General

In chapter 5, a new numerical methodology for solidification problems is established. It involved a new definition of non-physical enthalpy via energy transport equation, which is equation (5—1). With this definition, the negative non-physical capacitance is avoided, however it give raise to a new non-physical source $\hat{Q}$ which can be related to advection. Moreover, with advection now involved any numerical solution procedure is required to be stable particularly when the element Pecl ètNumber is greater than 1. This chapter aims to describe how the new non-physical enthalpy method is implemented with FEM method; one-dimensional (1D) case studies are examined. Aspects considered in this chapter include: firstly, a full discretization of the governing equation; secondly, the construction of finite element coefficient matrices and loading vectors; thirdly, the evaluation of each term and their updating procedure; fourthly, the stabilization of advection and the solvers utilised.

6.2 The full discretization

In chapter 5, a semi-discretized finite element equation was established as

$$\frac{\partial}{\partial t}\int_{\Omega_e\backslash\Gamma_i^e} N_\vartheta \tilde{h} dV + \int_{\Gamma_e\backslash\Sigma_i^e} N_\vartheta \tilde{h}\underline{v}\cdot\underline{n} d\Gamma - \int_{\Omega_e\backslash\Gamma_i^e} \tilde{h}\underline{v}\cdot\nabla N_\vartheta dV = -\int_{\Gamma_e} N_\vartheta \underline{q}\cdot\underline{n}\, d\Gamma + \int_{\Omega_e\backslash\Gamma_i^e} \underline{q}\cdot\nabla N_\vartheta dV - \left(\int_{\Gamma_i} N_\vartheta\right]\rho h\left(\underline{v}-\underline{v}^{\times}\right)\cdot(-\underline{n})\left[d\Gamma\right) - \int_{\Omega_e} N_\vartheta \hat{Q} dV \quad (6—1)$$

Since the problem is time dependent, the forward Euler method and the θ method are applied, so equation (6—1) becomes

$$\frac{\int_{\Omega_e\setminus\Gamma_i} N_\vartheta \hat{h}^{n+1} dV - \int_{\Omega_e\setminus\Gamma_i} N_\vartheta \hat{h}^{n} dV}{\Delta t} + \theta \int_{\Gamma_e\setminus\Sigma_i} N_\vartheta \hat{h}^{n+1} \underline{v} \cdot \underline{n} d\Gamma + (1-\theta) \int_{\Gamma_e\setminus\Sigma_i} N_\vartheta \hat{h}^{n} \underline{v} \cdot \underline{n} d\Gamma -$$
$$\theta \int_{\Omega_e\setminus\Gamma_i} \hat{h}^{n+1} \cdot \nabla N_\vartheta dV - (1-\theta) \int_{\Omega_e\setminus\Gamma_i} \hat{h}^{n} \cdot \nabla N_\vartheta dV = -\theta \int_{\Gamma_e} N_\vartheta \underline{q}^{n+1} \cdot \underline{n}\, d\Gamma - (1 -$$
$$\theta) \int_{\Gamma_e} N_\vartheta \underline{q}^{n} \cdot \underline{n}\, d\Gamma + \theta \int_{\Omega_e\setminus\Gamma_i^e} \underline{q}^{n+1} \cdot \nabla N_\vartheta dV + (1-\theta) \int_{\Omega_e\setminus\Gamma_i^e} \underline{q}^{n} \cdot \nabla N_\vartheta dV -$$
$$\int_{t^n}^{t^{n+1}} \left(\int_{\Gamma_i} N_\vartheta \right] \rho h \underline{v}^{\times} \cdot \underline{n} \left[d\Gamma + \int_{\Omega_e} N_\vartheta \hat{Q}\, dV \right) dt \qquad (6—2)$$

where the superscript n is the number of time steps, and Δt is the time increment between two adjacent time steps. It is known that by setting θ from 0 to 1, the explicit scheme, the Crank-Nicolson scheme or the implicit method is obtained [109, 125]. The numerical experiments in chapter 4 show that the Crank-Nicolson scheme provides accurate results. Also in this study, the Crank-Nicolson scheme is preferred since is able to achieve second order accuracy [109, 125].

Prior to solving equation (6—2), it is prudent to establish a direct mathematical relationship between the non-physical enthalpy $\hat{h}$ and the temperature T. The simplest approach is to set $\hat{h} = \hat{c}T$. The trial solution for temperature is given as

$$T_e \approx \sum_{\varsigma=1}^{NN} N_\varsigma T_\varsigma \qquad (6—3)$$

where T_e is the trial solution and T_ς is the nodal temperature of node ς.

Thus, equation (6—2) can be written as a system of equations of the form

$$\frac{[\hat{C}^{n+1}]\{T^{n+1}\} - [\hat{C}^{n}]\{T^{n}\}}{\Delta t} + \left(\theta \left[K_v{}^{n+1}\right]\{T^{n+1}\} + (1-\theta)[K_v{}^{n}]\{T^{n}\}\right) = -(\theta[K^{n+1}]\{T^{n+1}\} +$$
$$(1-\theta)[K^{n}]\{T^{n}\}) - \theta\left\{\tilde{Q}^{n+1}\right\} - (1-\theta)\left\{\tilde{Q}^{n}\right\} + \theta\{q^{n+1}\} + (1-\theta)\{q^{n}\} \qquad (6—4)$$

where the loading vector $\left\{\tilde{Q}\right\}$ with a tilde is generated as a consequence of the last term in equation (6—2).

Reorganization of equation (6—4) gives

$$\left(\left[\hat{C}^{n+1}\right] + \theta\Delta t\left[{K_v}^{n+1}\right] + \theta\Delta t[K^{n+1}]\right)\{T^{n+1}\} = \left(\left[\hat{C}^{n}\right] - (1-\theta)\Delta t[{K_v}^{n}] - (1-\theta)\Delta t[K^{n}]\right)\{T^{n}\} + \theta\Delta t\left\{\tilde{Q}^{n+1}\right\} - (1-\theta)\Delta t\left\{\tilde{Q}^{n}\right\} + \Delta t(\theta\{q^{n+1}\} + (1-\theta)\{q^{n}\}) \quad (6—5)$$

where $\left[\hat{C}\right]$ is the capacitance matrix, $[K_v]$ is the advective matrix, $[K]$ is the conductive matrix, and $\{q\}$ is the heat flux. The superscript n and $n+1$ refer to time steps.

An alternative way of getting second order accuracy can be achieved by the application of Taylor-Galerkin method, which is developed in [125]. It can be seen in Appendix I—(j).

6.3 Solidification in 1D

In order to understand the capability and feasibility of the non-physical variable method, the method is implemented into the 1D linear element. The 1D finite element is sketched in Figure 6.1 Its shape functions are

$$N_1 = \frac{1-\xi}{2} \quad (6—6a)$$

$$N_2 = \frac{1+\xi}{2} \quad (6—6b)$$

where ξ is a local co-ordinate in a natural co-ordinate space.

The two nodes of the element are located at $\xi = -1$, and $\xi = 1$. And the point $\xi = 0$ is the centre of the element.

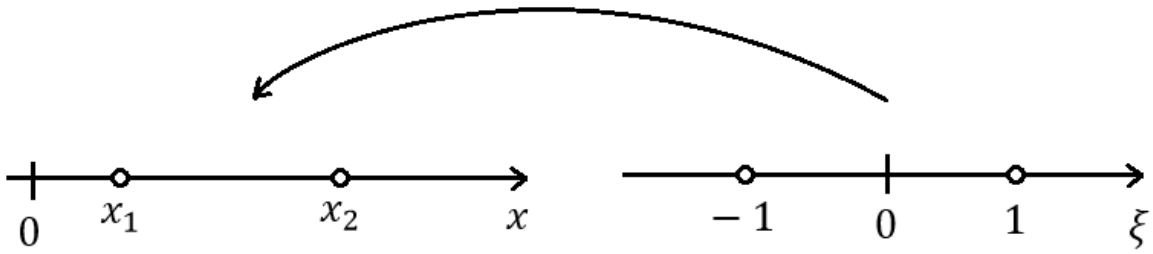

Figure 6.1: Mapping of the physical domain and the computational domain

Assuming that the volume of solid exists in the elemental CV (as depicted in Figure 6.2), at time t^n, the volume of solid $\mathrm{V}_s = {\Upsilon_s}^n V_e$, where V_e is the volume of the element. The solid volume fraction ${\Upsilon_s}^n$ is evaluated through the element-based temperature approximation. For the isothermal solidification, it is

$$\Upsilon_s{}^n = \frac{T_{sol} - T_1{}^n}{T_2{}^n - T_1{}^n} \tag{6—7}$$

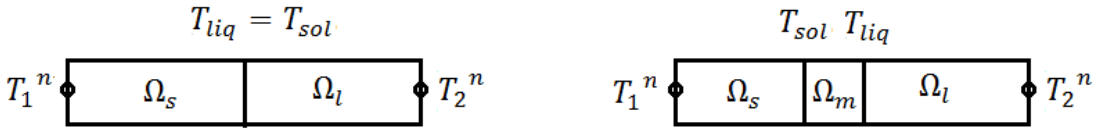

Figure 6.2: Isothermal solidification in 1D element (left) and mushy zone solidification in 1D element (right)

In one-dimensional modelling, the evaluation of equation (5—61) is

$$\int_{\Omega_e} \rho^n h^n \, dV \approx M_e^n h_{sol} + \rho_s c_s \frac{A_e L_e}{2} \Upsilon_s{}^n \left[2T_1{}^n - 2T_{sol} + \Upsilon_s{}^n \left(T_2{}^n - T_1{}^n\right)\right] + M_l^n L + \rho_l c_l \frac{A_e L_e}{2} \left(1 - \Upsilon_s{}^n\right)\left[T_1{}^n + T_2{}^n - 2T_{sol} + \Upsilon_s{}^n \left(T_2{}^n - T_1{}^n\right)\right] \tag{6—8}$$

where M_e is the total mass of material in the element, M_l is the total mass of liquid in the element, A_e is the cross-sectional area of element, L_e is the length of element. The superscript n refers to the time step. It is identical to the approach adopted for equation (3—51) in chapter 3, which can be seen in Appendix I—(e).

6.3.1 The rod capacitance and conductivity matrix

With the shape functions (6—6a) and (6—6b), the trial solution T_e is given by the Galerkin weighted residual method in the form

$$T_e = \lfloor N_1 \quad N_2 \rfloor \begin{Bmatrix} T_1 \\ T_2 \end{Bmatrix} = N_1 T_1 + N_2 T_2 \tag{6—9}$$

where the subscript e denotes the element and the subscripts 1 and 2 denote the local node numbers of the element. The bracket $\lfloor \blacksquare \rfloor$ signifies a row vector and the bracket $\{\blacksquare\}$ signifies a column vector.

The space x is also discretized by the FEM as

$$x_e = \lfloor N_1 \quad N_2 \rfloor \begin{Bmatrix} x_1 \\ x_2 \end{Bmatrix} = N_1 x_1 + N_2 x_2 \tag{6—10}$$

where x_1 and x_2 are the coordinates of the element nodes, respectively.

In the discretization, the cross-sectional area of the element A_e is assumed to be constant for 1D modelling. The volume of the element can be approximate as

$$\int_{\Omega_e} dV = \int_x \int_{\Gamma_e} d\Gamma dx = A_e \int_x dx = A_e \int_{-1}^{1} \frac{1}{2}(x_1 - x_2)d\xi = A_e L_e \tag{6—11}$$

According to the chain rule, $dx = (d(N_1 x_1 + N_2 x_2)/d\xi)d\xi = (x_2 - x_1)d\xi/2 = L_e d\xi/2$, and the length $L_e = x_2 - x_1$ is the length of element.

Since the mean-value approach to the integration is applied, the non-physical capacitance $\hat{c}$ is invariant in each time step, thus its relative matrix can be constructed as

$$\left[\hat{C}\right]_e = \frac{\hat{c}L_e}{2} A_e \int_{-1}^{1} \begin{bmatrix} N_1 N_1 & N_1 N_2 \\ N_2 N_1 & N_2 N_2 \end{bmatrix} d\xi = \frac{\hat{c}A_e L_e}{2} \begin{bmatrix} \frac{2}{3} & \frac{1}{3} \\ \frac{1}{3} & \frac{2}{3} \end{bmatrix} \tag{6—12}$$

where $\left[\hat{C}\right]_e$ is a consistent element capacitance matrix.

As to conductivity, since the source term $\lim_{vol(\Omega_i)\to 0} \int_{\Omega_i} \underline{q} \cdot \nabla N_\vartheta \, dV$ is excluded in the term $\int_{\Omega_e \backslash \Gamma_i^e} \underline{q} \cdot \nabla N_\vartheta dV$ by the analysis in section 5.4.1, thus the conductivity matrix can be constructed as

$$[K]_e = \frac{\hat{k}L_e}{2} A_e \int_{-1}^{1} \begin{pmatrix} \left[\frac{\partial N_1}{\partial \xi} \quad \frac{\partial N_2}{\partial \xi}\right] \\ \frac{1}{2}L_e \end{pmatrix} \cdot \frac{1}{\frac{1}{2}L_e d\xi} \begin{Bmatrix} \frac{\partial N_1}{\partial \xi} \\ \frac{\partial N_2}{\partial \xi} \end{Bmatrix} d\xi = \frac{\hat{k}A_e}{L_e} \begin{bmatrix} 1 & -1 \\ -1 & 1 \end{bmatrix} \tag{6—13}$$

where $[K]_e$ is the element conductivity matrix, and $\hat{k}$ is the mixture conductivity, i.e. $\hat{k} = \Upsilon_s{}^n k_s + \Upsilon_l{}^n k_l$.

The vectors $\{q^{n+1}\}_e$ and $\{q^n\}_e$ are related to the boundary conditions. For example, when the Robin boundary condition is considered only, the load vector of an element can be expressed as

$$\{q^n\}_e = \begin{Bmatrix} A_e q_1 \\ A_e q_2 \end{Bmatrix} = \begin{Bmatrix} A_e h_c (T_{amb} - T_1^n) \\ A_e h_c (T_{amb} - T_2^n) \end{Bmatrix} \tag{6—14}$$

6.3.2 The advection-diffusion in 1D

In the new definition of the non-physical method, the advective term is not accounted for in the change of non-physical enthalpy. This helps to prevent negative capacitances, and further

to enhance the stability of the method. Its evaluation is part of the non-physical approach. But when implementing it into the finite element method, it is required to be treated independently, and further stability action needs to be taken. This is because it is known that for the elemental Peclèt number $Pe > 1$, complex eigenvalues are generated in the difference equations which result in numerical oscillations [84-86]. In this section, two schemes are adopted for the advection-diffusion terms. The first one is a classical upwind method, called the Petrov-Galerkin method. This method is well-known, and can be easily applied with the standard Galerkin method, as it only replaces the standard weighting functions by modified weighting functions. However difficulties can be foreseen in that Petrov-Galerkin weighting functions are hard to obtain for higher dimensional elements. An alternative method is to treat the advective term analytically, which can be adopted for the evaluation of equation (5—70) as mentioned in section 5.5.

6.3.2.1 The Petrov-Galerkin method

In the fixed grid FEM, the application of standard Galerkin method to advection-diffusion terms in equation (6—5), it gives

$$[K]_e\{T\}_e + [K_v]_e\{T\}_e \approx \frac{kA_e}{\Delta x}\int_{-1}^{1}\begin{Bmatrix} \frac{d\frac{1-\xi}{2}}{d\xi} \\ \frac{d\frac{1+\xi}{2}}{d\xi} \end{Bmatrix}\begin{bmatrix} \frac{d\frac{1-\xi}{2}}{d\xi} & \frac{d\frac{1+\xi}{2}}{d\xi} \end{bmatrix} d\xi \begin{Bmatrix} T_1 \\ T_2 \end{Bmatrix} +$$

$$\hat{c}vA_e\int_{-1}^{1}\begin{Bmatrix} \frac{1-\xi}{2} \\ \frac{1+\xi}{2} \end{Bmatrix}\begin{bmatrix} \frac{d\frac{1-\xi}{2}}{d\xi} & \frac{d\frac{1+\xi}{2}}{d\xi} \end{bmatrix} d\xi \begin{Bmatrix} T_1 \\ T_2 \end{Bmatrix} \qquad (6—15)$$

After integration, equation (6—15) becomes

$$[K]_e\{T\}_e + [K_v]_e\{T\}_e \approx \frac{kA_e}{\Delta x}\begin{bmatrix} 1 & -1 \\ -1 & 1 \end{bmatrix}\begin{Bmatrix} T_1 \\ T_2 \end{Bmatrix} + \frac{\hat{c}vA_e}{2}\begin{bmatrix} -1 & 1 \\ -1 & 1 \end{bmatrix}\begin{Bmatrix} T_1 \\ T_2 \end{Bmatrix} \qquad (6—16)$$

where $\Delta x = L_e$ is the length between two nodes of a 1D element.

Assuming that the conductivity k and the velocity v are constant, the assembled conductivity matrix $[K]$ and the assembled advective matrix $[K_v]$ are

$$[K] \approx \frac{kA_e}{\Delta x}\begin{bmatrix} 1 & -1 & 0 \\ -1 & 2 & -1 \\ 0 & -1 & 1 \end{bmatrix} \qquad (6—17)$$

and

$$[K_v] \approx \frac{\hat{c}vA_e}{2}\begin{bmatrix}-1 & 1 & 0\\ -1 & 0 & 1\\ 0 & -1 & 1\end{bmatrix} \tag{6—18}$$

According to equations (6—17) and (6—18) the advection-diffusion in the jth system of equation is given as

$$[K]_{2,\varsigma}\{T\} + [K_v]_{2,\varsigma}\{T\} \approx \frac{kA_e}{\Delta x}\lfloor -1 \quad 2 \quad -1\rfloor\begin{Bmatrix}T_{\varsigma-1}\\ T_{\varsigma}\\ T_{\varsigma+1}\end{Bmatrix} + \frac{\hat{c}vA_e}{2}\lfloor -1 \quad 0 \quad 1\rfloor\begin{Bmatrix}T_{\varsigma-1}\\ T_{\varsigma}\\ T_{\varsigma+1}\end{Bmatrix} \tag{6—19}$$

or, equation (6—18) can be written in another form, which is

$$[K]_{2,\varsigma}\{T\} + [K_v]_{2,\varsigma}\{T\} \approx kA_e\frac{-T_{\varsigma-1}+2T_{\varsigma}-T_{\varsigma+1}}{\Delta x} + \hat{c}vA_e\frac{T_{\varsigma+1}-T_{\varsigma-1}}{2} \tag{6—20}$$

It can be seen in equation (6—20) that the discretization of advection term by the 1D linear shape functions is identical to the central difference scheme of the finite difference method. Figure 6.3 shows the typical discretization of the finite difference method. Its approximations of the differentiations are

$$\frac{dT}{dx} \approx \frac{T_{\varsigma+1}-T_{\varsigma-1}}{2\Delta x} \tag{6—21}$$

and

$$\frac{d^2T}{dx^2} \approx \frac{T_{\varsigma+1}-2T_{\varsigma}+T_{\varsigma-1}}{\Delta x^2} \tag{6—22}$$

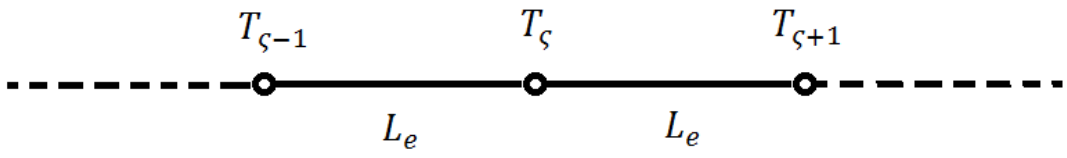

Figure 6.3: Central difference scheme

To formulate the Petrov-Galerkin shape functions, equation (6—22) is rewritten as

$$[K]_{2,\varsigma}\{T\} + [K_v]_{2,\varsigma}\{T\} \approx (1+P_e)T_{\varsigma-1} - 2T_{\varsigma} + (1-P_e)T_{\varsigma+1} \tag{6—23}$$

where P_e is defined as the element Pecl$\grave{e}$t number， i.e. $P_e = vL_e/(2\alpha)$, where v is the advective parameter (velocity), L_e is the length of an element, and α is the diffusive

coefficient. If the Pecl ât number $P_e > 1$, the central difference technique becomes unstable, e.g. when $P_e = 2.5$ in Figure 6.4 [125, 131].

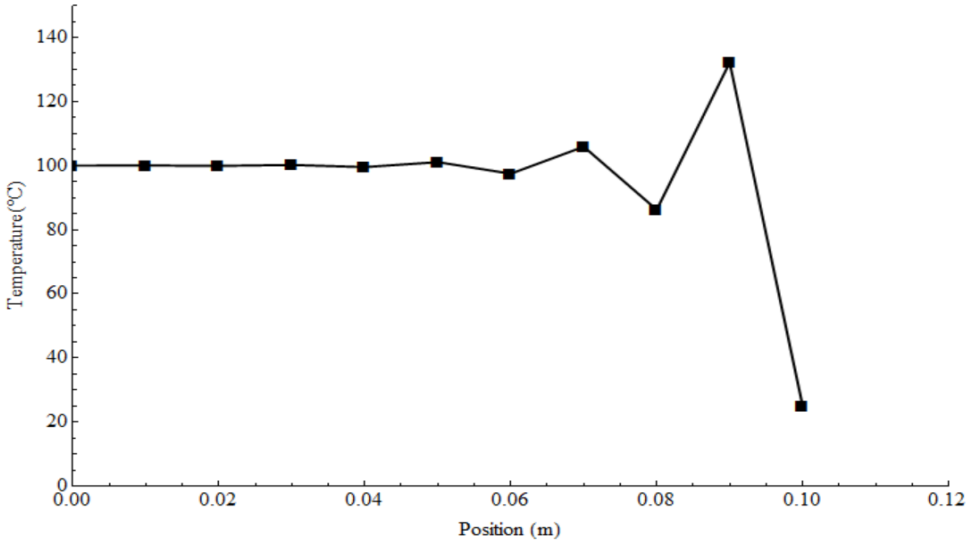

Figure 6.4: Central difference scheme for 2nd order ODE, $P_e = 2.5$

One way of resolving the oscillation problem is to use the upwind difference scheme instead of central difference scheme. In the finite difference method, the upwind approximation is

$$\frac{dT}{dx} \approx \frac{T_\varsigma - T_{\varsigma-1}}{\Delta x} \tag{6—24}$$

The RHS term of equation (6—24) can be extended as

$$\frac{T_\varsigma - T_{\varsigma-1}}{\Delta x} = \frac{T_{\varsigma+1} - T_{\varsigma-1}}{2\Delta x} - \left(\frac{\Delta x}{2}\right)\frac{T_{\varsigma+1} - 2T_\varsigma + T_{\varsigma-1}}{\Delta x^2} \tag{6—25}$$

From equation (5—83), it generates an artificial conductivity which is $k_{up} = v\Delta x/2$. With this term, it is possible to switch between the central difference scheme and the upwind scheme. Therefore, it can be rewritten as

$$v\frac{dT}{dx} - k_{up}\frac{d^2T}{dx^2} \approx v\frac{T_\varsigma - T_{\varsigma-1}}{\Delta x} - v\frac{T_{\varsigma+1} - 2T_\varsigma + T_{\varsigma-1}}{\Delta x^2} \tag{6—26}$$

where the term dT/dx is upwinded because the artificial conductivity is introduced.

Figure 6.5 shows that the fully upwinded finite element method can eliminate the oscillations, however the result is a little under diffused [125, 131].

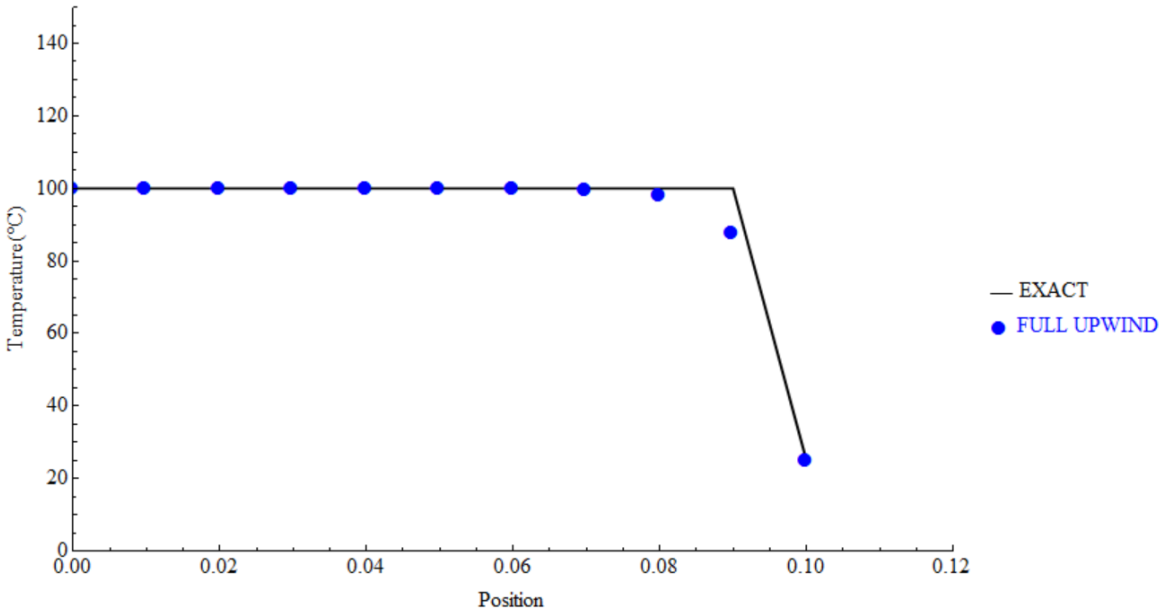

Figure 6.5: Upwind difference scheme for second order ODE, $P_e = 2.5$

In order to correct the under diffusion as appeared in Figure 6.5, a blending factor β is used to control the degree of upwind, so the advective-diffusive terms can be written as

$$\hat{c}v\frac{dT_\varsigma}{dx} - \left(k + \beta k_{up}\right)\frac{d^2T_\varsigma}{dx^2} \approx (1 + (\beta - 1)P_e)T_{\varsigma+1} - 2(1+\beta)T_\varsigma + (1 - (1+\beta)P_e)T_{\varsigma-1} \tag{6—27}$$

where the blending factor $\beta = \coth(P_e) - 1/P_e$ [125].

It transpires that equation (6—27) can be obtained by applying the 1D Petrov-Galerkin weighing functions to the finite element method. The weighting functions are shown below.

$$W_1'(\xi) = \frac{1-\xi}{2} - \frac{3}{4}\beta(1-\xi^2) \tag{6—28a}$$

$$W_2'(\xi) = \frac{1+\xi}{2} + \frac{3}{4}\beta(1-\xi^2) \tag{6—28b}$$

It is also known as the Petrov-Galerkin method [91-92, 125]. The plot of Petrov-Galerkin weighting function is shown in Figure 6.6.

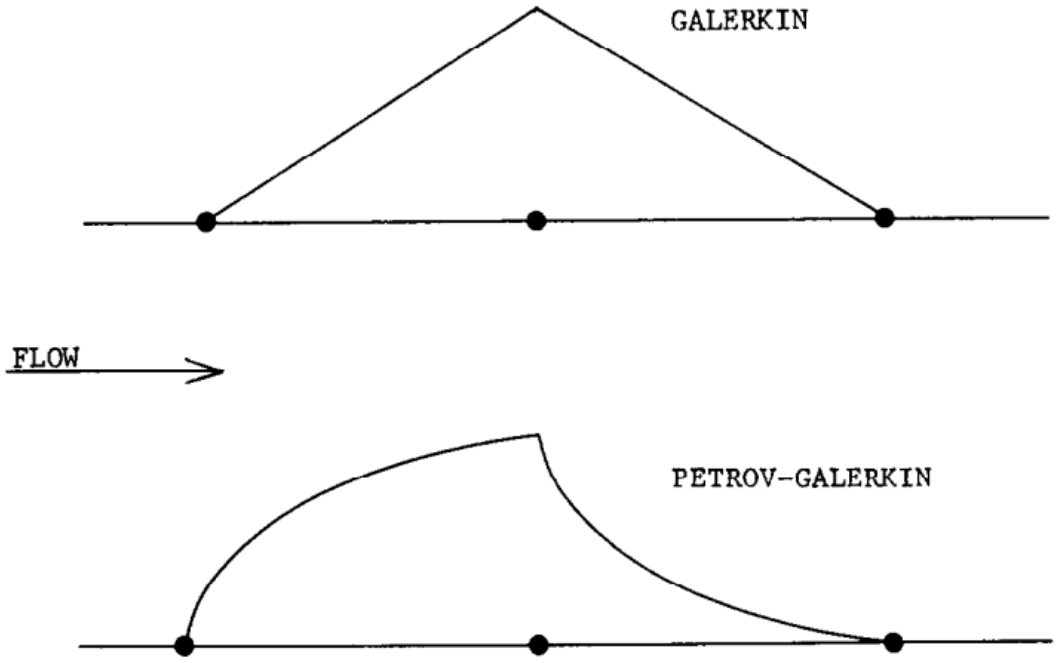

Figure 6.6: Upwind Petrov-Galerkin weighting function [125]

Application of Petrov-Galerkin weighting functions to the advective term gives

$$\int_{\Omega_e}\{W'\}\hat{c}v\left[\frac{\partial N}{\partial x}\right]\{T\}dV = A_e\hat{c}v\int_{-1}^{1}\begin{Bmatrix}\frac{1-\xi}{2}-\frac{3}{4}\beta(1-\xi^2)\\ \frac{1+\xi}{2}+\frac{3}{4}\beta(1-\xi^2)\end{Bmatrix}\frac{1}{\frac{L_e}{2}}\begin{bmatrix}\frac{d\frac{1-\xi}{2}}{d\xi} & \frac{d\frac{1+\xi}{2}}{d\xi}\end{bmatrix}\frac{L_e}{2}d\xi\begin{Bmatrix}T_1\\T_2\end{Bmatrix} =$$

$$\frac{A_e\hat{c}v}{2}\begin{bmatrix}-1+\beta & 1-\beta\\ -1-\beta & 1+\beta\end{bmatrix}\begin{Bmatrix}T_1\\T_2\end{Bmatrix} \qquad (6—29)$$

It can be observed from equation (6—29) that, if the blending factor $\beta = 0$, the advective term returns to central difference technique, if the blending factor $\beta = \coth(P_e) - 1/P_e$, the Petrov-Galerkin method is applied and if the blending factor $\beta = 1$, the full upwind method applies. The relationship between β and P_e is shown in Figure 6.7.

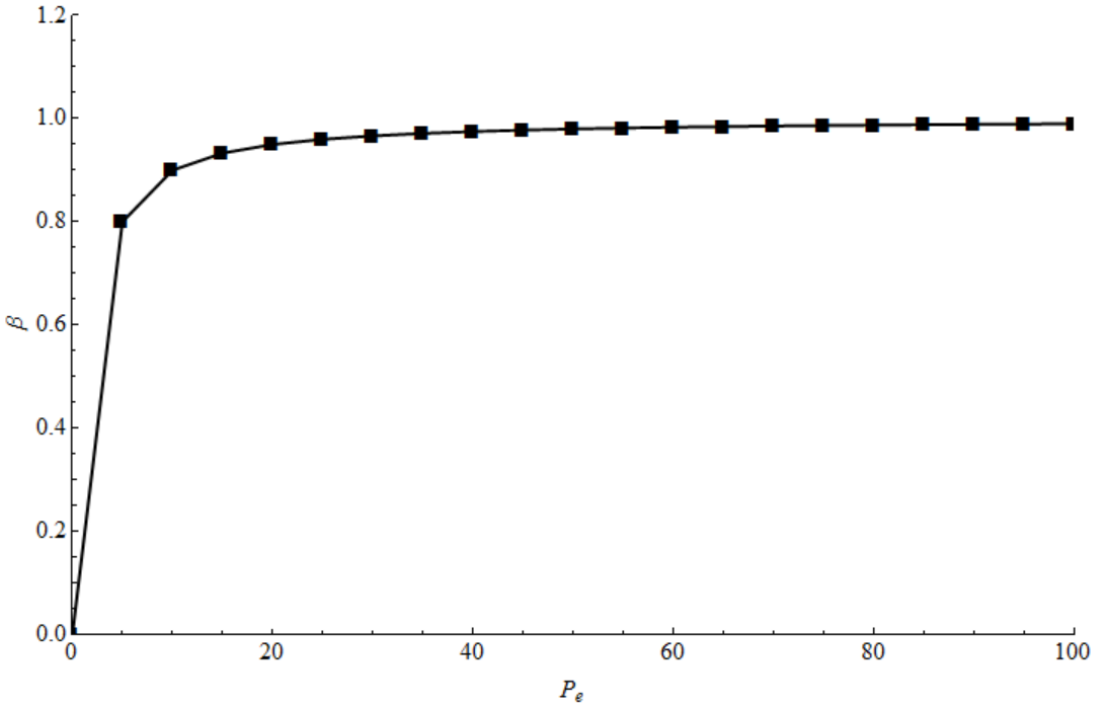

Figure 6.7: The relationship between β and P_e

If assembling the Petrov-Galerkin upwind advective term for a two-element system, the relationship is obtained as below.

$$[K_v] \approx \frac{A_e \hat{c} v}{2} \begin{bmatrix} -1+\beta & 1-\beta & 0 \\ -1-\beta & 2\beta & 1-\beta \\ 0 & -1-\beta & 1+\beta \end{bmatrix} \begin{Bmatrix} T_{\varsigma-1} \\ T_{\varsigma} \\ T_{\varsigma+1} \end{Bmatrix} \tag{6—30}$$

If the blending factor $\beta = 0$, equation (6—30) is the same as that of central difference technique, i.e.

$$[K_v] \approx \frac{A_e \hat{c} v}{2} \begin{bmatrix} -1 & 1 & 0 \\ -1 & 0 & 1 \\ 0 & -1 & 1 \end{bmatrix} \begin{Bmatrix} T_{\varsigma-1} \\ T_{\varsigma} \\ T_{\varsigma+1} \end{Bmatrix} \tag{6—31}$$

and if the blending factor $\beta = 1$, equation (6—31) is the same as that of the full upwind difference technique, i.e.

$$[K_v] \approx \frac{A_e \hat{c} v}{2} \begin{bmatrix} 0 & 0 & 0 \\ -2 & 2 & 0 \\ 0 & -2 & 2 \end{bmatrix} \begin{Bmatrix} T_{\varsigma-1} \\ T_{\varsigma} \\ T_{\varsigma+1} \end{Bmatrix} \tag{6—32}$$

6.3.2.2: The analytical scheme

It is mentioned in section 5.5 that an artificial region is generated by the swept of elemental boundary with the relative velocity in a time interval, which is denoted as Ω_f. The evaluation of the volume of Ω_f is conducted as

$$V_f = A_e \int_{t^n}^{t^{n+1}} \underline{v} \cdot \underline{n} dt \tag{6—33}$$

The swept volume Ω_f can be regarded as a 1D elemental domain (though it is not an element), and the two corresponding nodal temperatures are T_1^n and T_1^{n+1}, where the number 1 denotes this is for the boundary 1 of the real element (not the swept volume). Thus a similar relationship as equation (6—8), can be used to calculate the amount of enthalpy transported by advection through the associated elemental boundary.

$$\int_{\Omega_f} \hat{h} dV \approx \int_{\Omega_f} \Upsilon_s{}^f \rho^n \left(h_{sol} + \int_{T_{sol}}^{T} c_s(T') dT' \right) + \Upsilon_l{}^n \rho^n \left(h_{liq} + \int_{T_{liq}}^{T} c_l(T') dT' \right) dV =$$
$$M_e^f h_{sol} + M_l{}^f l + \rho_s c_s \frac{V_f}{2} g_s^f \left(2T_1{}^{n+1} - 2T_{sol} + \Upsilon_s{}^f \left(T_1{}^n - T_1{}^{n+1} \right) \right) + \rho_l c_l \frac{V_f}{2} \Upsilon_s{}^f \left(T_1{}^n + T_1{}^{n+1} - 2T_{liq} + \Upsilon_s{}^f \left(T_1{}^n - T_1{}^{n+1} \right) \right) \tag{6—34}$$

where $\Upsilon_s{}^f$ is the element-based temperature approximation for solid volume fraction of swept volume, if the discontinuity front is passing through the boundary in the period t^n to t^{n+1}. $M_e^f = \Upsilon_s{}^f \rho_s V_1^f + (1 - \Upsilon_s{}^f) \rho_l V_f$ is the mass in the Ω_f, and $M_l{}^f = (1 - \Upsilon_s{}^f) \rho_l V_f$ is the mass of liquid through the boundary 1.

6.3.3 The loading vector $\{\tilde{Q}\}$

The 2×1 loading vector $\{\tilde{Q}\}$ is essential to the non-physical source method, since the jump and source which relate to the discontinuities are now accounted for in this loading vector. In equation (6—1), the term $\int_{\Omega_e} N_\vartheta \hat{Q} dV$ on the LHS of the equation and the term $\left(- \int_{\Gamma_i^e} N_\vartheta \right] \rho h \left(\underline{v} - \underline{v}^\times \right) \cdot \underline{n} \left[d\Gamma \right)$ on the RHS of the equation require further consideration for finite elements.

According to the definition of non-physical source $\hat{Q}$ via equation (5—54), a relationship can be established as

$$\int_{\Omega_e} N_\vartheta \hat{Q} dV - \int_{\Gamma_i^e} N_\vartheta \rceil \rho h \underline{v} \cdot \underline{n} \lceil d\Gamma = \int_{\Gamma_e} N_\vartheta \rho h \underline{v} \cdot \underline{n} d\Gamma + \int_{\Gamma_i^e} N_\vartheta \rceil \rho h \underline{v} \cdot \underline{n} \lceil d\Gamma - \int_{\Gamma_e} N_\vartheta \hat{c} T \underline{v} \cdot \underline{n} d\Gamma - \int_{\Gamma_i^e} N_\vartheta \rceil \rho h \underline{v} \cdot \underline{n} \lceil d\Gamma = \int_{\Gamma_e} N_\vartheta \rho h \underline{v} \cdot \underline{n} d\Gamma - \int_{\Gamma_e} N_\vartheta \hat{c} T \underline{v} \cdot \underline{n} d\Gamma \quad (6—35)$$

Equation (6—35) can be loaded to a finite element system by a 2×1 column vector $\{\tilde{Q}\}_e$. It is known that the term $\int_{\Gamma_e} N_\vartheta \rho h \underline{v} \cdot \underline{n} d\Gamma$ can be evaluated analytically regarded as a 2×1 vector $\{Q_f\}_e$, and a numerical evaluation can be conducted for $\int_{\Gamma_e} N_\vartheta \hat{c} T \underline{v} \cdot \underline{n} d\Gamma$ once the non-physical $\hat{c}$ is provided by equation (5—56), and the matrices for this term are given by equation (6—30). Change of the non-physical enthalpy due to $\int_{\Gamma_e} N_\vartheta \hat{c} T \underline{v} \cdot \underline{n} d\Gamma$ is then numerically evaluated as

$$\{Q_{num}\}_e = \left(\theta \left[{K_v}^{n+1}\right]_e \left\{T_p^{n+1}\right\}_e + (1-\theta)[{K_v}^n]_e \{T^n\}_e\right) \quad (6—36)$$

Where $\{Q_{num}\}_e$ is a 2×1 column vector, and $\left\{T_p^{n+1}\right\}_e$ are the predicted further time step temperature, which are directly returned from updating techniques such as predictor-corrector method.

With equation (6—35), equation (6—1) now only remains one term which is the jump $\left(\int_{\Gamma_i^e} N_\vartheta \rceil \rho h \underline{v}^\times \cdot \underline{n} \lceil d\Gamma\right)$. This term is tricky for fixed grid FEM. In Tables 5.2 and 5.3, it can be known that this term returns a single value, which is related to the phase interface. However, in the fixed grid FEM, no information about the phase interface can be provided from the grid, all values are given to the nodes, simple equal division and application to every node of an element is rough, and may cause temperature overflow. However, how this single value is distributed to the nodes is hard to establish. One strategy which can avoid the establishment of the distribution and the possible temperature overflow is to introduce another capacitance as

$$c_i = \frac{\int_{t^n}^{t^{n+1}} \int_{\Gamma_i^e} \rceil \rho h \underline{v}^\times \cdot \underline{n} \lceil d\Gamma dt}{\int_{\Omega_e} T^{n+1} dV - \int_{\Omega_e} T^n dV} \quad (6—37)$$

Then a matrix is constructed in a similar manner as equation (5—56), which is denoted as $[C_i]_e$, consequently, the jump $\int_{t^n}^{t^{n+1}} \int_{\Gamma_i^e} \rceil \rho h \underline{v}^\times \cdot \underline{n} \lceil d\Gamma \, dt$ is treated as

$$\{Q_i\}_e = [C_i]_e \left(\left\{T_p^{n+1}\right\}_e - \{T^n\}_e\right) \quad (6—38)$$

Finally, the loading vector $\{\tilde{Q}\}$ can be evaluated as

$$\{\tilde{Q}\}_e = \{Q_f\}_e + \{Q_{num}\}_e + \{Q_i\}_e \tag{6—39}$$

As mentioned, the predicted temperature vector $\{T_p^{n+1}\}_e$ is obtained by the methods such as the predictor-corrector method. In a time step, the predictor-corrector method has several loops to generate the predicted temperature for future time step. At each loop, the system of equations are considered as linear system of equations, and the cooling rate is potentially faster than it should be. Because, it is known that the cooling rate for phase change solidification is slower than the cooling rate of single phase material if the boundary conditions are the same, because of latent heat release when the phase changes. Thus, it is artificially slowed as below.

$$\{T_p^{n+1}\}_e = R\{T_{\tau-1}^{n+1}\}_e + (1-R)\{T_\tau^{n+1}\}_e \tag{6—40}$$

where τ denotes the τth loop, and the factor $R \in [0,1]$, which adjust the dependence of predicted temperature $\{T_p^{n+1}\}_e$ on the temperatures returned from two adjacent loops. A parametric study on the factor R can be seen in Appendix IV.

6.4 Solver and solution procedure

6.4.1 The solver

(1) The Successive Over-Relaxation method (SOR)

This is the method used in the previous studies of CVCM [39, 31] and non-physical enthalpy method [62-63]. For a set of linear equations as shown below,

$$\begin{bmatrix} a_{11} & a_{12} & \cdots & a_{1u} \\ a_{21} & a_{22} & \cdots & a_{2u} \\ \vdots & \vdots & \ddots & \vdots \\ a_{v1} & a_{v2} & \cdots & a_{vu} \end{bmatrix} \begin{Bmatrix} x_1 \\ x_2 \\ \vdots \\ x_{nu} \end{Bmatrix} = \begin{Bmatrix} b_1 \\ b_2 \\ \vdots \\ b_u \end{Bmatrix} \tag{6—41}$$

the solution of this method can be written as,

$$x_i{}^{n+1} = x_i{}^n - \omega \left[\frac{\sum_{j=1}^{j=i-1} a_{ij} x_j{}^{n+1} + \sum_{j=i}^{j=u} a_{ij} x_j{}^n + b_j}{a_{ii}} \right] \tag{6—42}$$

where $\omega \in (0,2)$ is the relaxation factor, and the selecting of ω can be via $\omega = 4/\left(2+\sqrt{4+\left(\cos\left(\frac{\pi}{n}\right)+\cos\left(\frac{\pi}{n}\right)\right)^2}\right)$ for a $n \times n$ matrix. The advantage of this method is that, it is easily implemented with any program. The convergence of this method requires that the relaxation factor $\omega \in (0,2)$ and the matrix has to be positive definite [132-133]. In the program, it does not converge with some settings of mesh.

(2) The Gauss- Jordan elimination method (GJM)

The GJM requires the system of equations become an augmented matrix. Then row operations are taken to make the augmented matrix solved [134]. For example, in order to resolve equation (6—41), the augmented matrix is built as,

$$\left[\begin{array}{cccc|c} a_{11} & a_{12} & \cdots & a_{1u} & b_1 \\ a_{21} & a_{22} & \cdots & a_{2u} & b_2 \\ \vdots & \vdots & \ddots & \vdots & \vdots \\ a_{v1} & a_{v2} & \cdots & a_{vu} & b_u \end{array}\right] \tag{6—43}$$

Row and column operations will be conducted on the above matrix, until the left part of the matrix becomes a unit matrix, then the right part will be the solution of equation (5—36).

$$\left[\begin{array}{cccc|c} 1 & 0 & \cdots & 0 & x_1 \\ 0 & 1 & \cdots & 0 & x_2 \\ \vdots & \vdots & \ddots & \vdots & \vdots \\ 0 & 0 & \cdots & 1 & x_{nu} \end{array}\right] \tag{6—44}$$

The advantage of this method is that, it is very stable and able to deal with most of the linear equations. However, in the experiment, it is observed that, row and column operations require a lot of time for computation.

(3) Routine from NAG Fortran Library (NAG)

This method is from a commercial Fortran library. The name of the routine is F07AAF (DGESV) [77]. This method is based on the LU decomposition with partial pivoting. Here L denotes the lower triangular matrix and U denotes the upper triangular matrix. A coefficient matrix can be manipulated as,

$$\begin{bmatrix} a_{11} & a_{12} & \cdots & a_{1u} \\ a_{21} & a_{22} & \cdots & a_{2u} \\ \vdots & \vdots & \ddots & \vdots \\ a_{v1} & a_{v2} & \cdots & a_{vu} \end{bmatrix} = \begin{bmatrix} l_{11} & 0 & \cdots & 0 \\ l_{21} & l_{22} & \cdots & 0 \\ \vdots & \vdots & \ddots & \vdots \\ l_{v1} & l_{v2} & \cdots & l_{vu} \end{bmatrix} \begin{bmatrix} u_{11} & u_{12} & \cdots & u_{1u} \\ 0 & u_{22} & \cdots & u_{2u} \\ \vdots & \vdots & \ddots & \vdots \\ 0 & 0 & \cdots & u_{vu} \end{bmatrix} \tag{6—45}$$

Both the matrices $[L]$ and $[U]$ are arbitrary and unknown. A usual way of finding unique LU composition is to set the diagonal elements of $[L]$ as one.

Thus, the coefficient matrix can be divided into two equations,

$$\begin{bmatrix} l_{11} & 0 & \cdots & 0 \\ l_{21} & l_{22} & \cdots & 0 \\ \vdots & \vdots & \ddots & \vdots \\ l_{v1} & l_{v2} & \cdots & l_{vu} \end{bmatrix} \begin{Bmatrix} y_1 \\ y_2 \\ \vdots \\ y_u \end{Bmatrix} = \begin{bmatrix} 1 & 0 & \cdots & 0 \\ 0 & 1 & \cdots & 0 \\ \vdots & \vdots & \ddots & \vdots \\ 0 & 0 & \cdots & 1 \end{bmatrix} \begin{Bmatrix} b_1 \\ b_2 \\ \vdots \\ b_u \end{Bmatrix} \tag{6—46a}$$

and

$$\begin{bmatrix} u_{11} & u_{12} & \cdots & u_{1u} \\ 0 & u_{22} & \cdots & u_{2u} \\ \vdots & \vdots & \ddots & \vdots \\ 0 & 0 & \cdots & u_{vu} \end{bmatrix} \begin{Bmatrix} x_1 \\ x_2 \\ \vdots \\ x_{nu} \end{Bmatrix} = \begin{Bmatrix} y_1 \\ y_2 \\ \vdots \\ y_u \end{Bmatrix} \tag{6—46b}$$

The forward and backward substitution can be directly applied to equations (6—46a) and (6—46b), and the set of linear equations is resolved.

The update methods applied here are those described in the chapter 4. They are the predictor-corrector method, the secant method and the homotopy method. This method itself is not able to check the convergence and consistency. And it prevents the infinite loop. All the three methods have their own criterion to judge whether the results is converged at each time step. For the predictor-corrector method, the relative error in T^{n+1} is determined and compared with the relative error ϵ by

$$\left|{T_k}^{n+1} - {T_{k-1}}^{n+1}\right| \leq \epsilon \tag{6—47}$$

where the subscript k refers to the kth iteration, and the tolerance ϵ is prescribed, i.e. $\epsilon = 1.0 \times 10^{-8}$.

For the secant method presented in chapter 5, the system of equations were constructed as

$$\{F(T^{n+1})\} = \left(\left[\hat{C}(T^{n+1}, T^n)\right] + \theta\Delta t[K(T^{n+1}, T^n)]\right)\{T^{n+1}\} - \left(\left[\hat{C}(T^{n+1}, T^n)\right] - (1-\theta)\Delta t[K(T^{n+1}, T^n)]\right)\{T^n\} - \Delta t(\theta\{Q^{n+1}\} + (1-\theta)\{Q^n\}) - \Delta t(\theta\{q^{n+1}\} + (1-\theta)\{q^n\}) - \Delta t(\theta\{\hat{q}^{n+1}\} + (1-\theta)\{\hat{q}^n\}) \tag{6—48}$$

For each nodal unknown (temperatures) obtained in a loop, it will be substituted back to equation (6—48) to check whether it satisfies

$$\left|F_j\left(T_j^{n+1}\right)\right| \leq \epsilon \tag{6—49}$$

where $|\blacksquare|$ is the absolute value, and ϵ is the tolerance, for instance, $\epsilon = 1.0 \times 10^{-8}$.

Similarly, for the homotopy method, a similar equation is established as

$$\mathrm{H}(\mathrm{T}^{n+1}, \lambda_1) = F(\mathrm{T}^{n+1}) + (\lambda_1 - 1)F(\mathrm{T}_0^{n+1}) \tag{6—50}$$

As a matter of fact, at each loop, the results must satisfy

$$\left|\mathrm{H}_j\left(\mathrm{T}_\mathrm{j}^{n+1}, \lambda_m\right)\right| \leq \epsilon \tag{6—51}$$

where m is the mth partition for the factor λ.

6.4.2 The solution procedure

A flow chart of the program is shown in Figure 6.8, which presents the general procedure of the non-physical variable method. In every time step, the non-physical variables are calculated according to the temperature distributions gained from the present time step and the future time step. The calculation of solid fraction is achieved via the element-based temperature approximation in equation (6—7). The evaluation of each non-physical variables are described in section 5.5. The construction of matrices for 1D tests are illustrated in the section 6.4.1 and section 6.4.2. And the optional methods for solving the system of equations are shown in this previous section. The temperature distribution of the future time step can be computed by the Predictor-Corrector method, the secant method or the homotopy method as discussed in chapter 4. Then the non-physical variables are substituted into the classic finite element equation to compute the temperature distribution for the next convergence loop.

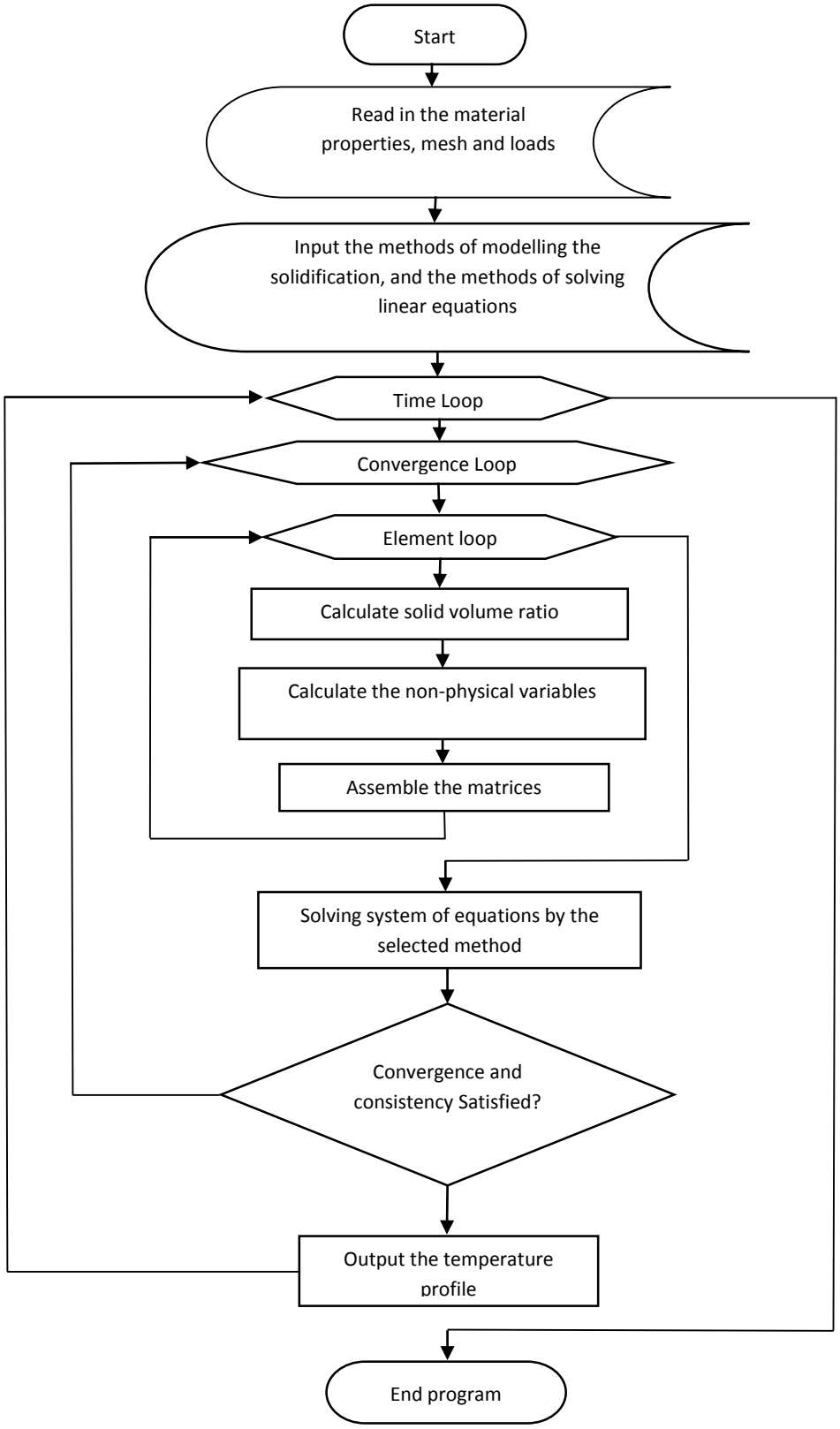

Figure 6.8: Programming flow chart

6.5 Numerical results

6.5.1 General set-up

The model is a 1D tube, which is shown in Figure 6.9. The length of the slab is $0.1m$. The numerical experiments are designed to investigate the non-physical variable methods. The material is pure zinc. The forced convective coefficient $h_c = 12000\, W/m^2$℃ and the ambient temperature $T_{amb} = 25$℃. They are used in the boundary conditions to instigate a cooling process. And the boundary conditions are given as

$$-k_s \frac{\partial T}{\partial x}\Big|_{x=0} = h_c(T - T_{amb}) \qquad (6—52a)$$

and

$$k_s \frac{\partial T}{\partial x}\Big|_{x=0.01} = 0 \qquad (6—52b)$$

The model is partitioned into 200 elements, which also can be seen in Figure 6.9. In this project, the solid produced in the tube is also moving because the incoming liquid pushes it out. This phenomenon can commonly be related to the continuous casting and squeezing casting. For that reason, the terminology “advection” is used rather than “convection”.

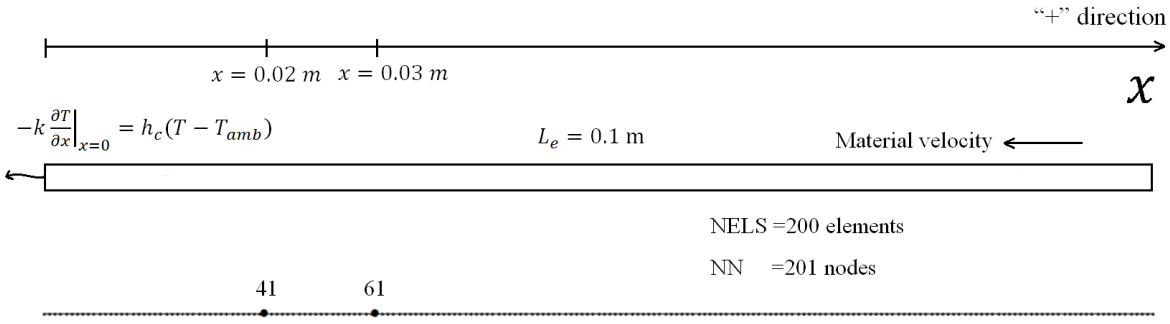

Figure 6.9: Experimental model

In the numerical simulations, the cooling and solidification starts from the left end of the zinc slab. The material velocity are set to be $0/-0.0001/-0.0005/-0.001/-0.005\, m/s$, the liquid zinc flows into the tube from one end and flow out from the other. The rate of cooling and the direction of the flow are dependent on the material velocities and their “$+/-$” signs.

When the material velocity $\|\underline{v}\| \geq 0.001\ m/s$, and the direction of it is negative (with the "$-$"), the cooling rate of the model becomes very slow, and the phase change is not initiated. But experiments with high material velocity help the examination of numerical stability.

The model set up above can be solved numerically by three methods which belong to the family of non-physical theory. The three methods are the control volume capacitance method, classic the non-physical enthalpy method and the new non-physical variable method. Their concepts can be seen in Figure 6.10.

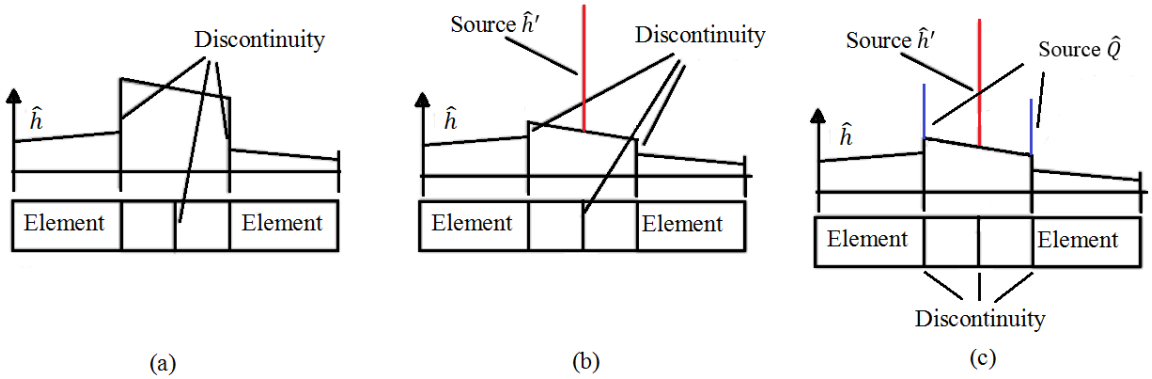

Figure 6.10: The concepts of non-physical methods

The CVCM can be regarded as the non-physical capacitance method, because in the classic definition of non-physical enthalpy, the jump $\hat{h}' = 0$ so it will not facilitate the removal of discontinuity, and consequently, the discontinuity is accounted for by the change of capacitance alone. In graph (a) of Figure 6.10, the capacitance of the element with discontinuity is different from its two adjacent elements. The control volume capacitance can be evaluated as

$$\hat{c} = \frac{\int_{\Omega_e} \rho^{n+1} h^{n+1} dV - \int_{\Omega_e} \rho^n h^n dV}{\int_{\Omega_e} T^{n+1} dV - \int_{\Omega_e} T^n dV} \tag{6—53}$$

After the evolution of $\hat{c}$ via equation (6—53), it can be substituted into the temporal term. As to the advective term, it can be solved numerically by substitution of $\hat{c}$ into discretised advective term; or it can be solved analytically via the strategy described in section 6.3.2.2.

Graph (b) in Figure 6.10 is a schematic sketch for the classic non-physical enthalpy method. Through the definition (3—4) in chapter 3, the non-physical jump $\hat{h}'$ is non-zero and is defined by equation (3—12). Equation (3—12) facilities the removal of most of the

discontinuity from the LSH of equation (3—4), it leaves a much smaller discontinuity which still results in a difference between the capacitances of the element in phase change and its neighbouring elements, the difference however is much reduced if it is compared with the control volume capacitance. This has been shown in section 3.5.3.

The classic non-physical enthalpy method has a problem with advection, which can be seen in the numerical experiment in chapter 4, consequently, a new definition has been given as equation (5—1) in chapter 5. Schematic sketch for the new definition is shown in Graph (c) in Figure 6.10. Through the development of the new methodology, the non-physical $\hat{h}'$ still facilities the removal of discontinuity from governing equation (5—1), and a new non-physical source $\hat{Q}$ is established through the derivation to treat the advection. Since it is considered that discontinuity can be transported into the element by advection, the source $\hat{Q}$ should appears at the boundary of an element.

In the following numerical experiments, the non-physical capacitance method with numerical advection, the non-physical capacitance method with analytical advection and the new non-physical variable method are applied. Also, the material velocities with different directions are examined. The influence of the directions is dependent on the boundary conditions applied. For example, in the presented experimental set-up, the Newton's law of cooling is applied on the left end of the tube. As a matter of fact, if the material is flowing into the tube from the left end, it will raise the energy level within the tube and slow the cooling rate. As it is defined, a positive direction (the material velocity is signed with "+") is from left to the right, the example described above should be a negative value being input into the computer program. The velocity with positive sign means that the material is flowing in through the cooling end. Although this does not physically make sense, results are still provided to show the capability of the method and the program.

6.5.2 Numerical results

Figure 6.11 is the temperature history of the node 41 at $x = 0.02\,m$. The non-physical capacitance method corresponds to the concept (a) in Figure 6.10. It can be seen that the rise in the quantity of the material velocity makes the cooling rate reduced. When the material velocity $\|\underline{v}\| = 0.001\,m/s$, the temperature of material refuses to drop because the hot material is flowing in so fast that there is no time to cool down. In this graph, some defects can be spotted. For instance, when the velocity $\|\underline{v}\| = 0.0001\,m/s$, the temperature is lower

than the stationary solidification just after the phase change. This could be an error. Furthermore, when the velocity $\|\underline{v}\| = 0.0005\, m/s$, an undulated behaviour in the temperature profile indicates that there is instability.

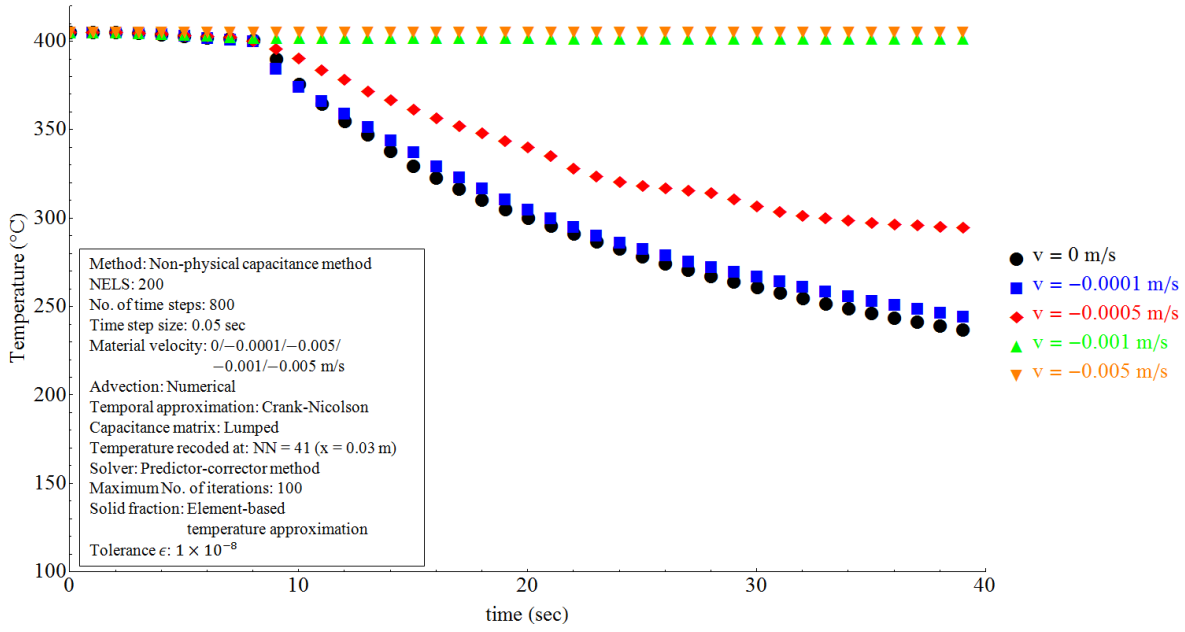

Figure 6.11: Temperature histories at $x = 0.02\, m$, with non-physical capacitance method and numerical advection

In the chapter 4, concept (a) was demonstrated by numerical examples to work well for solidification problems with stationary material on a fixed mesh. Also, the Petrov-Galerkin upwind scheme is shown to be able to deal with advection-diffusion problems in the continuous simulations (i.e. single material properties, no phase change and no discontinuity) [135]. As a matter of fact, it is possible that the problem is embodied in the advective term with the variable non-physical capacitance. Figure 6.12 shows the non-physical capacitance directly computed and output from the program. There are three spikes, and the black one is the capacitance of the stationary case. The phase transformation time is around 8 seconds. The red one and the blue one are the capacitances on setting that the material velocity $\|\underline{v}\| = 0.0001\, m/s$ and $\|\underline{v}\| = 0.0005\, m/s$, respectively. This graphs shows that the phase transformation time for $\|\underline{v}\| = 0.0005\, m/s$ is earlier and even greater than the phase transformation time for $\|\underline{v}\| = 0.0001\, m/s$. Accordingly, it is possible that incompatibility is contained between rapid changing non-physical capacitance and the upwind technique.

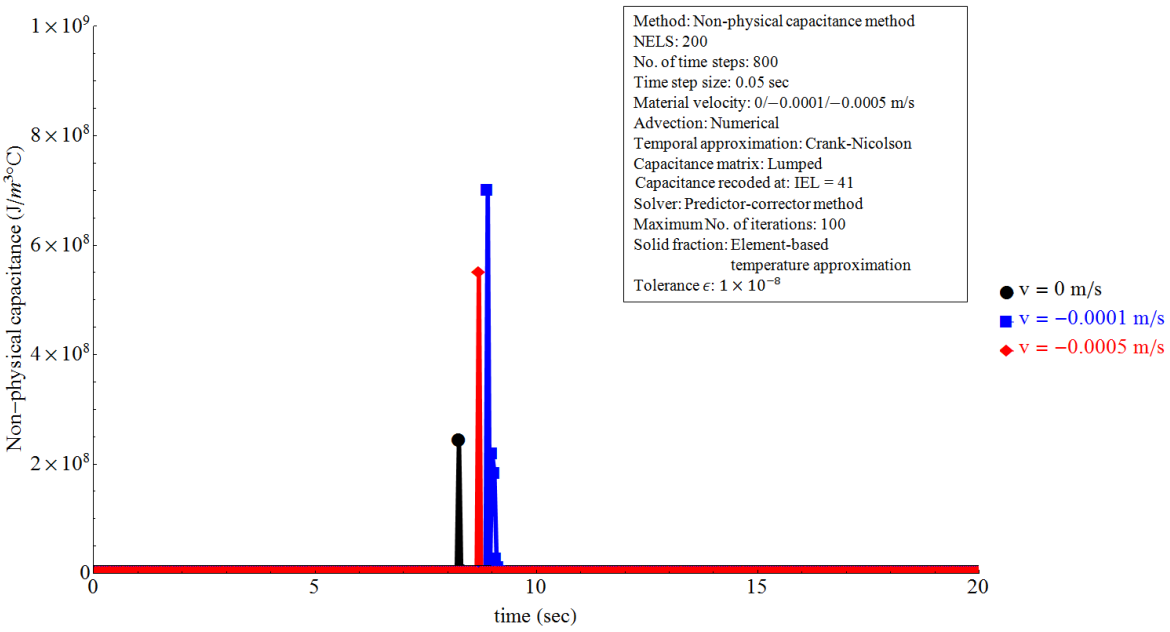

Figure 6.12: The change of non-physical capacitance, with non-physical capacitance method and numerical advection

In the following numerical experiments, the new non-physical variable method is applied. In the new method, the non-physical capacitance is computed via equation (5—56). It is then substituted into the capacitance matrix. Also, the capacitance is substituted into equation (6—30), which is already an upwind advection matrix by Petro-Galerkin method. Meanwhile, the non-physical source $\hat{Q}$ captures the discontinuity, which is the difference between the physical advection and the numerical advection. The physical advection is evaluated via the approach illustrated in Appendix I—(d). The implementation of this idea gives temperature history as shown in Figure 6.13. It can be seen that the behaviour of the temperature profiles is better than it appeared in Figure 6.11. Moreover, the non-physical capacitance as shown in Figure 6.14 shows that the discontinuity has been removed. Nevertheless, the removal of discontinuity from capacitance give rise to the non-physical source which is shown in Figure 6.15. Figure 6.16 shows the comparison between the temperature profile of node 61 ($x = 0.03\ m$) obtained by non-physical capacitance method and the new non-physical variable method. The material velocity $\|\underline{v}\| = 0.0005\ m/s$, and it shows new non-physical variable method improves the numerical stability and solves the incompatibility issue.

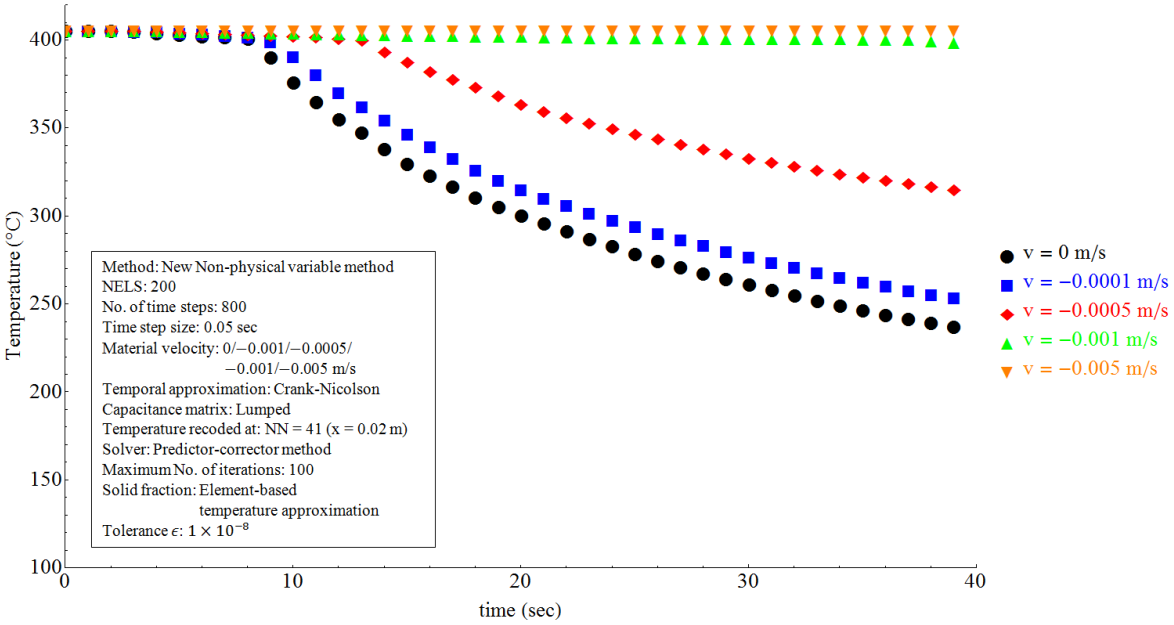

Figure 6.13: Temperature histories at $x = 0.02\ m$, with new non-physical variable method

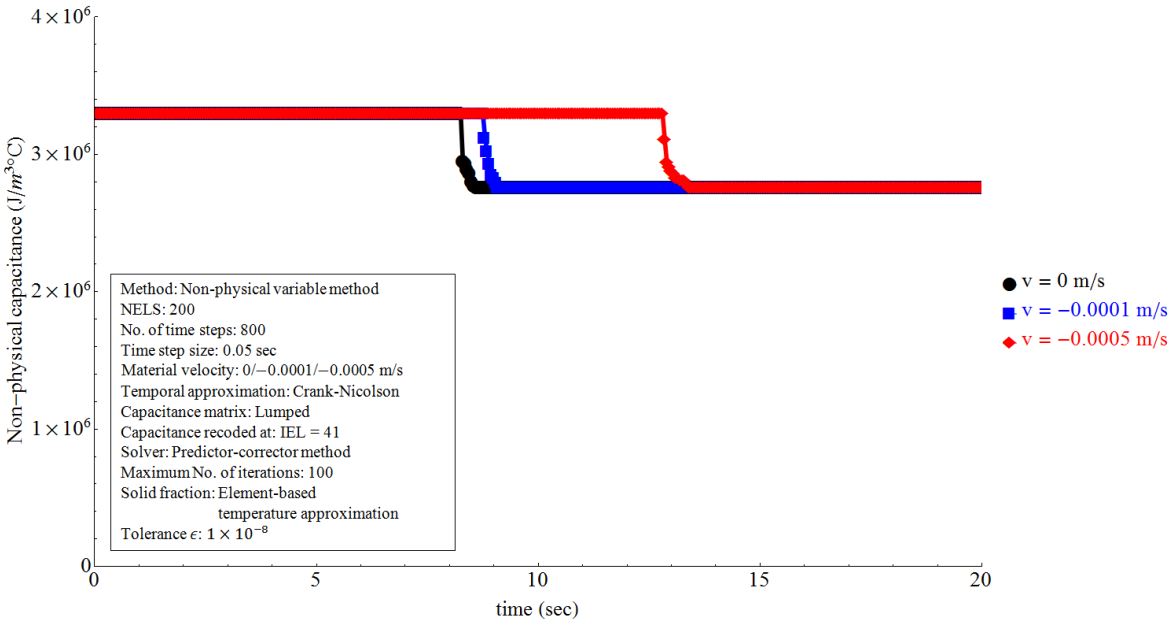

Figure 6.14: The change of non-physical capacitance, with new non-physical variable method

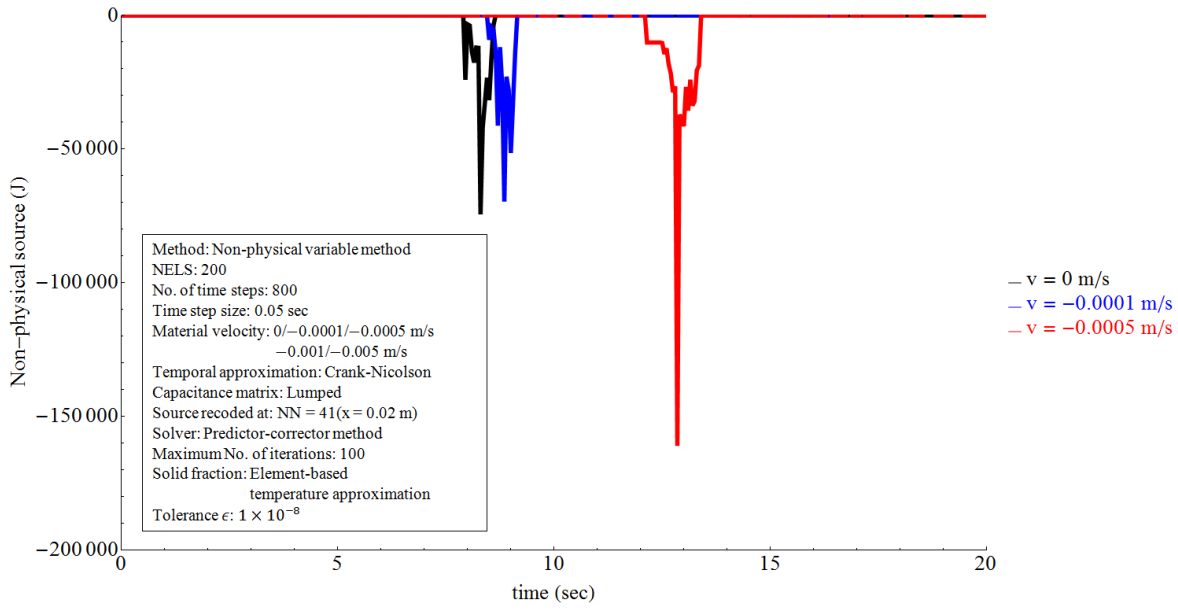

Figure 6.15: The change of non-physical source, with new non-physical variable method

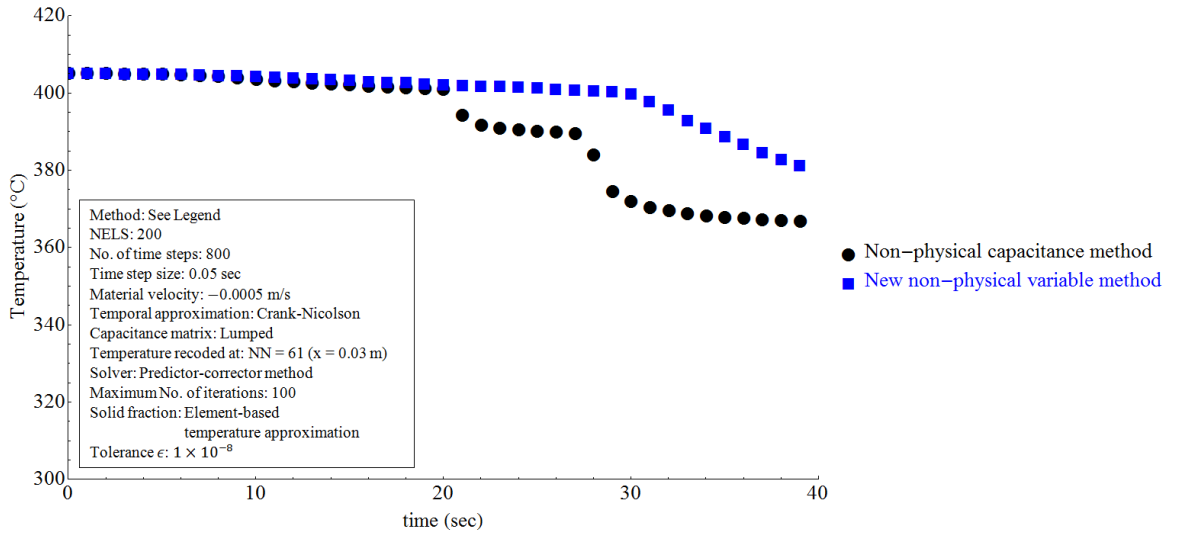

Figure 6.16: Non-physical capacitance method vs. new non-physical variable method with $\left]\hat{h}\underline{n}\right[= 0$ on Γ_i

It is obvious that the advection term can be evaluated completely through analytical approach in Appendix I—(d). This treatment eliminates the advective terms in the assembled equations. Instead, analytical evaluation of the advection is applied to the system of equations as a source. This is good for the advective-diffusive solidification problems in multi-dimension, because it may be hard to construct discontinuous weighting functions like the Petrov-Galerkin scheme in 1D. Figure 6.17 is the temperature history received from non-physical capacitance with analytical advection. The behaviour of temperature profile is also

stable, though for high velocity, such as the velocity $\|\underline{v}\| = 0.001\ m/s$, the curve has little undulation.

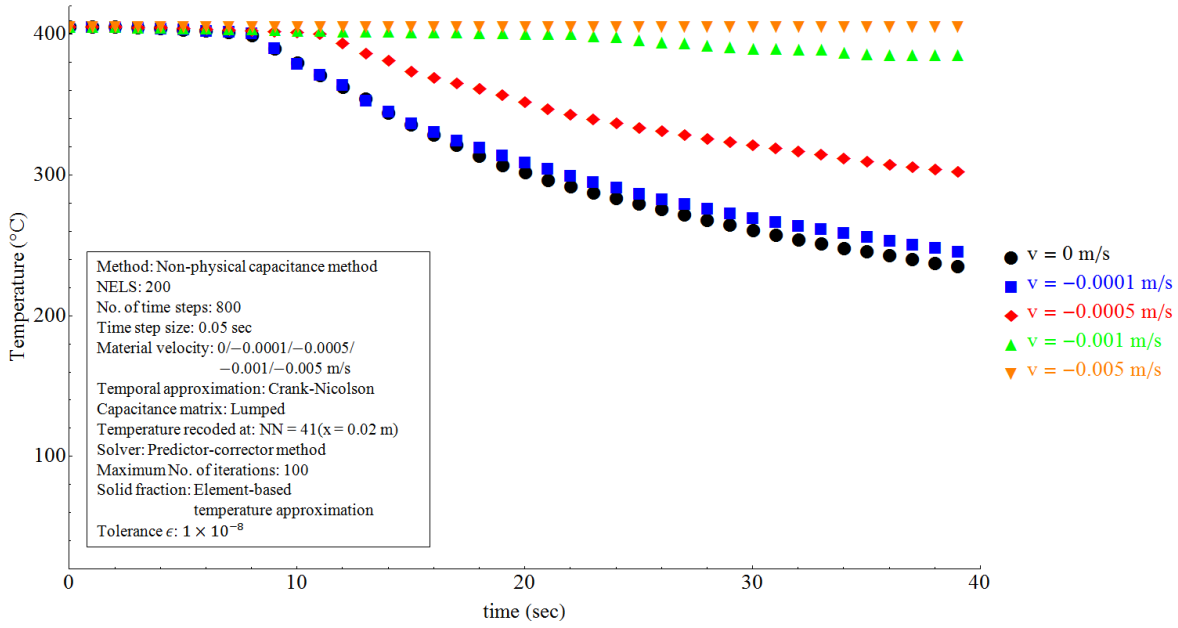

Figure 6.17: Temperature histories at $x = 0.02\ m$, with non-physical capacitance method and analytical advection

In continuous casting, in order to prevent the solidifying shell to stick on the mould, the mould is usually moved sinusoidally up and down (for vertical continuous casting machine) [136]. Thus, it is necessary to examine the non-physical variable method with the velocity in all directions. From Figure 6.18 to Figure 6.20, are the numerical results when the material velocity is positive. The figures indicate that all the three strategies show great stability and feasibility for positive velocity.

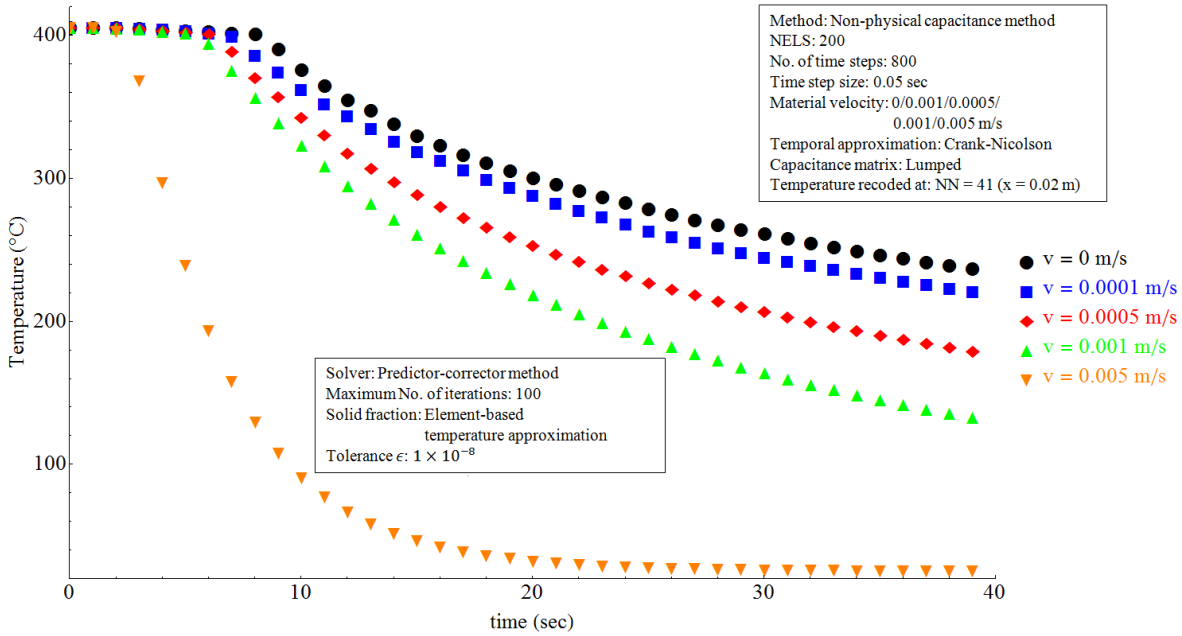

Figure 6.18: Temperature histories at $x = 0.02\ m$, with numerical advection and positive velocities

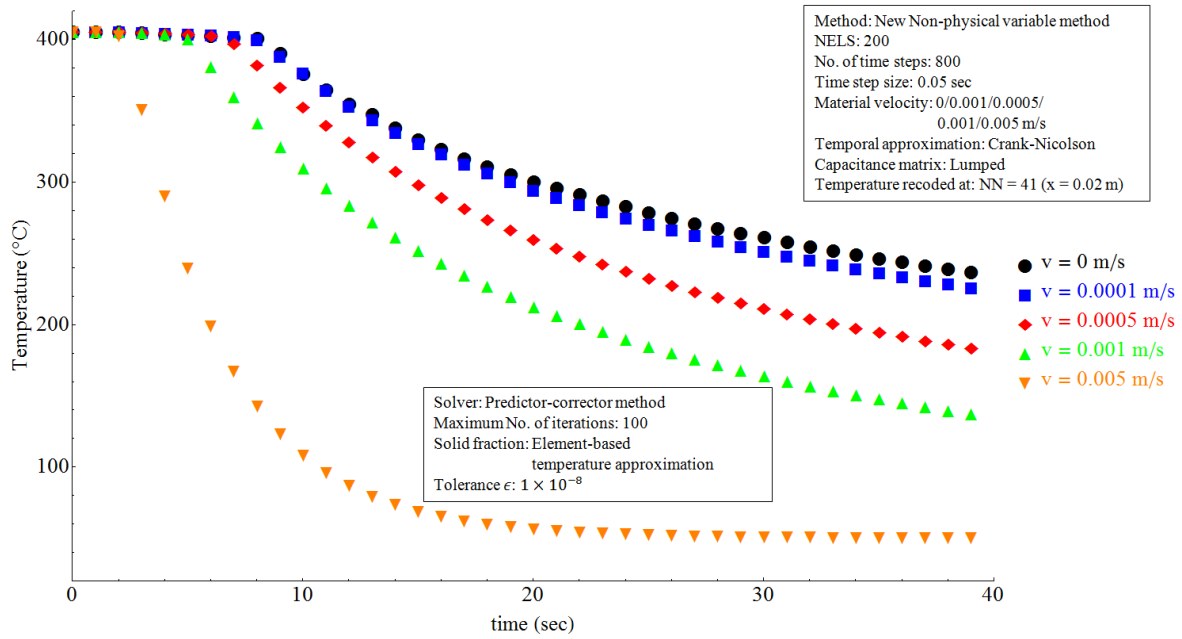

Figure 6.19: Temperature histories at $x = 0.02\ m$, new non-physical variable method with $\left]\hat{h}\underline{n}\right[= 0$ on Γ_i and positive velocity

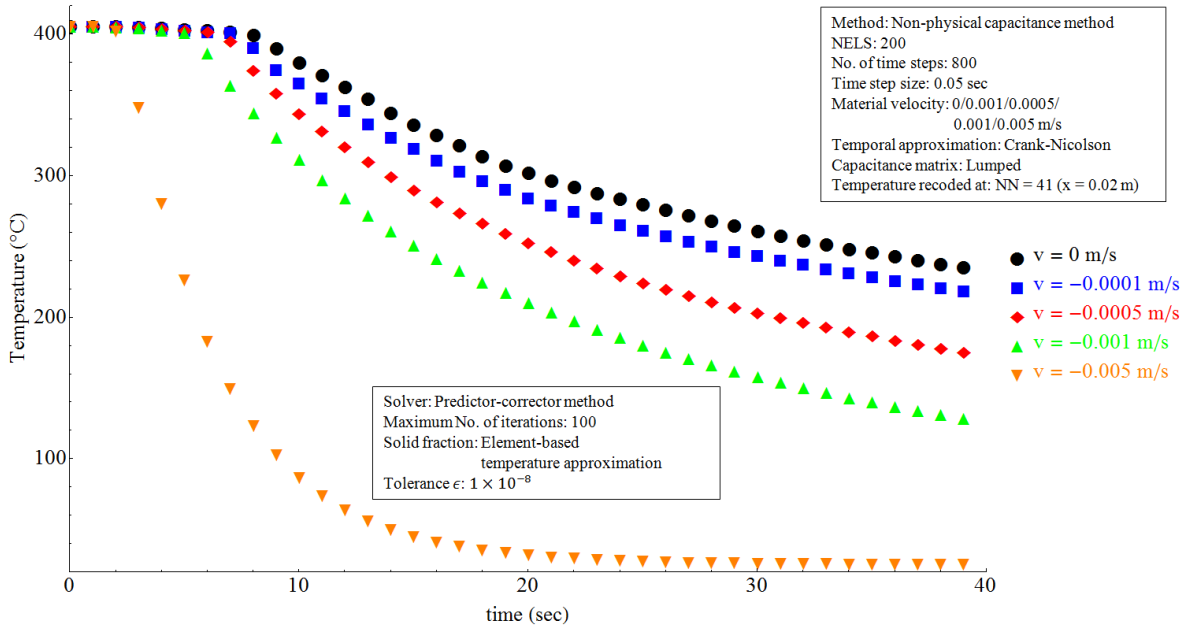

Figure 6.20: Temperature histories at $x = 0.02\ m$, with analytical advection and positive velocities

6.6 Summary

This chapter aims to solve the instability of the non-physical enthalpy method when involving the advection-diffusion. A new definition of the non-physical enthalpy has been given by the transport equation (5—1). Through this definition, the physical advection is isolated from the non-physical temporal term. As a consequence, no negative non-physical capacitance will be obtained. In order to deal with the new non-physical advective term, the upwind method, such as the Petrov-Galerkin method, was applied with this concept.

This chapter provides a detailed procedure on the implementation of the new non-physical variable method to the 1D FEM. Numerical model has been set up, and it is solved by three methods which belong to the family of non-physical theory. In the numerical experiments, it shows that the CVCM has incompatibility issue with the Petrov-Galerkin method, as disorder can be found in the computation of capacitances. The disorder may arise from the great change of non-physical capacitance. The new non-physical variable method just resolves this issue because the discontinuity is forced to be removed from the temporal term, which makes the non-physical capacitance does not vary significantly. However, the new method give rise to a new source term introduced to keep the discontinuity and to maintain the consistency of energy. It was demonstrated by the numerical experiments that the stability had been dramatically improved.

Chapter 7 The non-physical variable method for solidification in 2D

7.1 General

In the previous two chapters, the solidification problems were solved by the non-physical variable method with one-dimensional linear finite elements. The one-dimensional modelling is used to test of the theory underpinning the non-physical variable method. Specifically, the implementation of the non-physical variable approach in the FEM illustrated how the non-physical variables behave and perform in the test cases considered. Results provided directly from the program were used to compare against existing analytical solutions. In practice, many problems in two or three dimensions can be simplified to equivalent one-dimensional problems, although this requires the geometry and boundary conditions to be sufficiently simple. However, it is of interest to investigate how the non-physical variable method deals with complex geometry and boundary conditions, this chapter attempts to solve solidification problems by utilising the non-physical variable approach and two-dimensional linear triangular elements. The difficulties involved are the approximation of solid fraction by the element based temperature approximation**,** the evaluation of non-physical variables and the stabilization of the advective terms.

7.2 The non-physical variable method in 2D

7.2.1 The semi-discretization

The implementation of non-physical variable method in 2D follows the theory developed in chapter 5. In that chapter, the definition of non-physical was defined through the weak form of the energy conservation equation, which is

$$\frac{D^*}{D^*t}\int_\Omega \hat{h}dV + \int_\Gamma \hat{h}\underline{v}\cdot\underline{n}d\Gamma = \frac{D^*}{D^*t}\int_\Omega \rho h dV + \int_\Gamma \rho h\left(\underline{v}-\underline{v}^*\right)\cdot\underline{n}d\Gamma = -\int_\Gamma \underline{q}\cdot\underline{n}\,d\Gamma + \int_\Omega \rho Q\,dV \qquad (7—1)$$

where $\hat{h}$ is the non-physical enthalpy, $\underline{v}$ is the material velocity field, $\underline{v}^*$ is the grid velocity field, ρ is the density, h is the specific enthalpy, $\underline{q}\cdot\underline{n}$ denotes the heat flux and Q is the specific external heat source. The derivative $D^*/D^*t = \partial/\partial t|_x + \underline{v}^*\cdot\nabla$, and the operator $\nabla(\blacksquare) = \{\partial/\partial x \quad \partial/\partial y \quad \partial/\partial z\}$ is the gradient.

Application of equation (7—1) to a control volume (CV) Ω^+, in which motion is governed by the velocity field $\underline{v}^+$, gives

$$\frac{D^+}{D^+t}\int_{\Omega^+}\hat{h}dV + \int_{\Gamma^+}\hat{h}\left(\underline{v}^* - \underline{v}^+\right)\cdot\underline{n}d\Gamma + \int_{\Gamma^+}\hat{h}\underline{v}\cdot\underline{n}d\Gamma + \int_{\Omega^+}\hat{Q}\,dV = \frac{D^+}{D^+t}\int_{\Omega^+}\rho h dV + \int_{\Gamma^+}\rho h\left(\underline{v} - \underline{v}^+\right)\cdot\underline{n}d\Gamma = -\int_{\Gamma^+}\underline{q}\cdot\underline{n}d\Gamma + \int_{\Omega^+}\rho Q dV \quad (7—2)$$

where $\hat{Q}$ is non-physical source, which is defined for the convenience of the solution.

The CV Ω^+ encloses the phase interface Γ_i, and the velocity $\underline{v}^+$ satisfies the identity $\underline{v}^+\cdot\underline{n} = \underline{v}_i\cdot\underline{n}$, where $\underline{v}_i$ is the velocity of the phase interface.

From equation (7—2), by defining $\hat{Q}' = \left]\hat{h}\underline{v}\cdot\underline{n}\right[$, a source-like jump term $\hat{h}'$ is obtained as

$$\frac{D^+}{D^+t}\int_{\Gamma_i}\hat{h}'d\Gamma + \int_{\Sigma_i}\hat{h}'\left(\underline{v}^* - \underline{v}^+\right)\cdot\underline{t}\underline{n}d\Sigma = -\int_{\Gamma_i}\left]\rho h\left(\underline{v} - \underline{v}^+\right)\cdot\underline{n}\right[d\Gamma = \int_{\Gamma_i}\left]\underline{q}\cdot\underline{n}\right[d\Gamma \quad (7—3)$$

where $]\blacksquare[$ signifies a jump.

Detailed derivation can be seen in section 5.3 of chapter 5. Equation (7—3) defines the discontinuity on the interface boundary Γ_i, which facilitates the removal of the discontinuity from left hand side (LHS) of equation (7—1).

Through equation (7—3), the non-physical source $\hat{Q}$ is only defined on the phase interface Γ_i. A complete definition is achieved by the analysis for the weighted governing equation of (7—1), which is

$$\frac{D^*}{D^*t}\int_\Omega W\hat{h}dV + \int_\Gamma W\hat{h}\underline{v}\cdot\underline{n}d\Gamma - \int_\Omega \hat{h}\underline{v}\cdot\nabla W dV + \int_\Omega W\hat{Q}dV = \int_\Omega W\rho h dV + \int_\Gamma W\rho h\left(\underline{v} - \underline{v}^*\right)\cdot\underline{n}d\Gamma - \int_\Omega \rho h\left(\underline{v} - \underline{v}^*\right)\cdot\nabla W dV = -\int_\Gamma W\underline{q}\cdot\underline{n}\,d\Gamma + \int_\Omega \underline{q}\cdot\nabla W dV + \int_\Omega W\rho Q\,dV \quad (7—4)$$

where W is the weighting function.

Through the analysis provided in section 5.4.1, the linkage equation is obtained as

$$\frac{D^*}{D^*t}\int_{\Omega\backslash\Gamma_i} W\hat{h}dV + \int_{\Gamma\backslash\Sigma_i} W\hat{h}\underline{v}\cdot\underline{n}d\Gamma - \int_{\Omega\backslash\Gamma_i}\hat{h}\underline{v}\cdot\nabla W dV + \int_{\Omega} W\hat{Q}dV = \frac{D^*}{D^*t}\int_{\Omega} W\rho h dV + \int_{\Gamma} W\rho h(\underline{v}-\underline{v}^*)\cdot\underline{n}d\Gamma - \left(-\int_{\Gamma_i} W\right]\rho h(\underline{v}-\underline{v}^+)\cdot\underline{n}\left[d\Gamma\right) - \int_{\Omega\backslash\Gamma_i}\rho h(\underline{v}-\underline{v}^*)\cdot\nabla W dV \tag{7—5}$$

It also provides a weighted governing equation of the form

$$\frac{D^*}{D^*t}\int_{\Omega\backslash\Gamma_i} W\hat{h}dV + \int_{\Gamma\backslash\Sigma_i} W\hat{h}\underline{v}\cdot\underline{n}d\Gamma - \int_{\Omega\backslash\Gamma_i}\hat{h}\underline{v}\cdot\nabla W dV + \int_{\Omega} W\hat{Q}dV = -\int_{\Gamma} W\underline{q}\cdot\underline{n}\,d\Gamma + \int_{\Omega\backslash\Gamma_i}\underline{q}\cdot\nabla W dV - \left(\int_{\Gamma_i} W\right]\underline{q}\cdot\underline{n}\left[d\Gamma\right) + \int_{\Omega} W\rho Q\,dV \tag{7—6}$$

Equation (7—5) can be evaluated analytically, it is not necessary to be weighted. Thus, choice of weighting function for equation (7—5) can be simply made as $W = 1$, which gives

$$\frac{\partial}{\partial t}\int_{\Omega_e\backslash\Gamma_i^e}\hat{h}dV + \int_{\Gamma_e\backslash\Sigma_i^e}\hat{h}\underline{v}\cdot\underline{n}d\Gamma + \int_{\Omega_e}\hat{Q}dV = \frac{\partial}{\partial t}\int_{\Omega_e}\rho h dV + \int_{\Gamma_e}\rho h\underline{v}\cdot\underline{n}d\Gamma - \left(-\int_{\Gamma_i^e}\right]\rho h(\underline{v}-\underline{v}^{\times})\cdot\underline{n}\left[d\Gamma\right) \tag{7—7}$$

where $\Omega\backslash\Gamma_i$ and $\Gamma\backslash\Sigma_i$ mean no discontinuities are embodied in those terms. The curve Σ_i is the boundary of interface Γ_i, and the vector $\underline{tn}$ is the outward pointing unit normal on the tangent plane of Σ_i.

Equation (7—6) can be solved numerically, for standard Galerkin weighted residual method, the weighting function $W = N_\vartheta$, consequently, equation (7—6) becomes

$$\frac{\partial}{\partial t}\int_{\Omega_e\backslash\Gamma_i^e} N_\vartheta\tilde{h}dV + \int_{\Gamma_e\backslash\Sigma_i^e} N_\vartheta\tilde{h}\underline{v}\cdot\underline{n}d\Gamma - \int_{\Omega_e\backslash\Gamma_i^e}\tilde{h}\underline{v}\cdot\nabla N_\vartheta dV + \int_{\Omega_e} N_\vartheta\hat{Q}dV = -\int_{\Gamma_e} N_\vartheta\underline{q}\cdot\underline{n}\,d\Gamma + \int_{\Omega_e\backslash\Gamma_i^e}\underline{q}\cdot\nabla N_\vartheta dV - \left(-\int_{\Gamma_i^e} N_\vartheta\right]\rho h(\underline{v}-\underline{v}^{\times})\cdot\underline{n}\left[d\Gamma\right) \tag{7—8}$$

where $\tilde{h}$ is the trial solution for enthalpy, N_ϑ are the finite element shape functions.

On defining the non-physical source that,

$$\int_{\Omega_e}\hat{Q}dV = \int_{\Gamma_e}\rho h\underline{v}\cdot\underline{n}d\Gamma + \int_{\Gamma_i^e}\right]\rho h\underline{v}\cdot\underline{n}\left[d\Gamma - \int_{\Gamma_e}\hat{c}T\underline{v}\cdot\underline{n}d\Gamma \tag{8—9}$$

and with the identity $\hat{h} = \hat{c}T$ for $T \neq 0$, subtraction of equation (7—9) from equation (7—7) and application of mean-value approach to the integration provides

$$\hat{c} = \frac{\int_{\Omega_e} \rho^{n+1} h^{n+1} dV - \int_{\Omega_e} \rho^n h^n dV - \int_{t^n}^{t^{n+1}} \int_{\Gamma_i^e}]\rho h \underline{v}^{\times} \cdot \underline{n}[d\Gamma dt}{\int_{\Omega_e \backslash \Gamma_i^e} T^{n+1} dV - \int_{\Omega_e \backslash \Gamma_i^e} T^n dV} \tag{7—10}$$

The non-physical source $\hat{Q}$ is non-unique. Whatever the definition of $\hat{h}$ is, the non-physical source is the difference between the physical advection and numerical advection. It guarantees that the energy conservation and consistency are always satisfied.

Equation (7—10) is adopted to evaluate the non-physical capacitance $\hat{c}$. Equation (7—9) is then applied to compute the non-physical source $\hat{Q}$. No discretization is required to be applied to equations (7—9) and (7—10) as they are only evaluated analytically. However, the evaluation has to be conducted on an elemental domain. Finally, the non-physical capacitance and the non-physical source are both substituted into equation (7—8) which is solved by the finite element method (FEM).

7.2.2 The linear triangular element and assembly

This chapter uses the 3-noded linear triangular finite element for the numerical experiments. Its sketch is shown in Figure 7.1. The shape functions are constructed as

$$\lfloor N \rfloor = \lfloor N_1 \quad N_2 \quad N_3 \rfloor = \lfloor 1 - \xi - \eta \quad \xi \quad \eta \rfloor \tag{7—11}$$

where ξ and η are the natural co-ordinates, the sign $\lfloor \blacksquare \rfloor$ signifies a row vector.

It is known that, the weighting functions are also shape functions for the standard Galerkin method, consequently

$$\{W\} = \begin{Bmatrix} W_1 \\ W_2 \\ W_3 \end{Bmatrix} = \begin{Bmatrix} 1 - \xi - \eta \\ \xi \\ \eta \end{Bmatrix} \tag{7—12}$$

where $\{\blacksquare\}$ signifies a column vector.

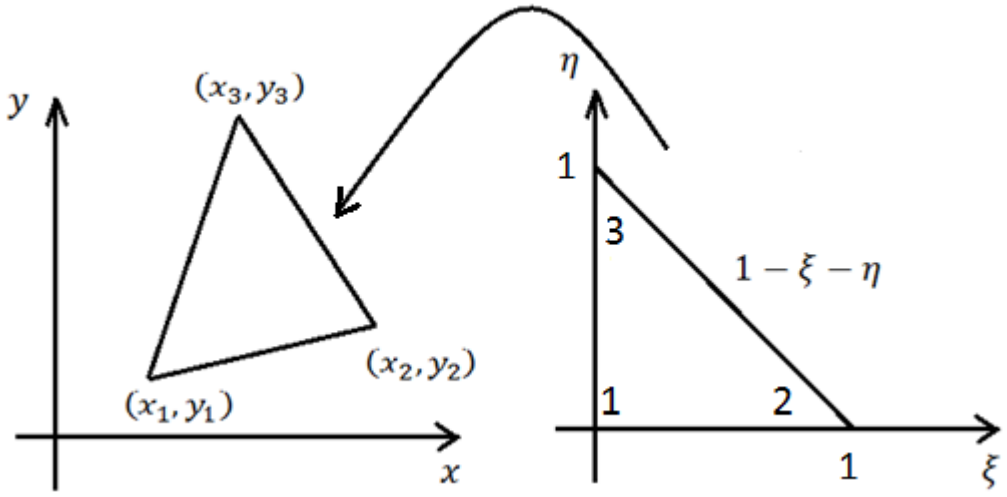

Figure 7.1: A linear triangular finite element

A trial solution with respect to temperature is given as

$$T_e = N_1T_1 + N_2T_2 + N_3T_3 = \lfloor N \rfloor \{T\} \tag{7—13}$$

where the subscripts 1, 2 and 3 are the local node number of an element.

In addition, for an isoparametric element

$$x_e = N_1x_1 + N_2x_2 + N_3x_3 = \lfloor N \rfloor \{x\} \tag{7—14a}$$

and

$$y_e = N_1y_1 + N_2y_2 + N_3y_3 = \lfloor N \rfloor \{y\} \tag{7—14b}$$

where (x_1, y_1), (x_2, y_2) and (x_3, y_3) are the nodal co-ordinates of a triangular element in the Cartesian co-ordinate system.

The volumetric integration in the triangular finite element domain is conducted as

$$\iint dV = \iint dxdy = \int_0^1 \int_0^{1-\eta} |[J]| d\xi d\eta = \int_0^1 \int_0^{1-\eta} \left| \begin{bmatrix} \frac{\partial x}{\partial \xi} & \frac{\partial x}{\partial \eta} \\ \frac{\partial y}{\partial \xi} & \frac{\partial y}{\partial \eta} \end{bmatrix} \right| d\xi d\eta \tag{7—15}$$

where $[J]$ is the Jacobian matrix, and the operator $|\blacksquare|$ signifies the determinant of a matrix. The finite element programme requires the $|[J]|$ to be always positive, which is achieved by order of numbering the local nodes to be anticlockwise.

As mentioned in chapter 5, the approximation of non-physical capacitance $\hat{c}$ is conducted through a mean-value approach. It is assumed that the non-physical $\hat{c}$ is constant for each time step. Moreover, on setting that the mesh is stationary, i.e. the velocity $\underline{v}^* = \underline{0}$, equation (7—8) is discretised and is written in a matrix form as

$$\left[\hat{C}\right](\{T^{n+1}\} - \{T^n\})/\Delta t + \left(\theta\left[K_v{}^{n+1}\right]\{T^{n+1}\} + (1-\theta)[K_v{}^n]\{T^n\}\right) = -(\theta[K^{n+1}]\{T^{n+1}\} + (1-\theta)[K^n]\{T^n\}) - \theta\left\{\tilde{Q}^{n+1}\right\} - (1-\theta)\left\{\tilde{Q}^n\right\} + \theta\{q^{n+1}\} + (1-\theta)\{q^n\} \quad (7—16)$$

where θ is a blending factor for θ-method, and the superscripts n and $n+1$ refer to the time step, the bracket [■] signifies a matrix. The forward Eularian approximation is applied for the temporal term. The constructions of each matrix and each loading vector are presented below.

As regards the elemental capacitance matrix, there are two methods for construction, i.e. the consistent capacitance matrix and the lumped capacitance matrix.

The consistent capacitance matrix can be constructed as

$$\left[\hat{C}\right]_e = \int_{\Omega_e}\{W\}\hat{c}\lfloor N\rfloor\, dV \approx \hat{c}\int_{\Omega_e}\{W\}\lfloor N\rfloor\, dV =$$

$$\hat{c}\int_0^1\int_0^{1-\eta}\begin{Bmatrix}1-\xi-\eta\\ \xi\\ \eta\end{Bmatrix}\lfloor 1-\xi-\eta \quad \xi \quad \eta\rfloor\left|\begin{bmatrix}\frac{\partial x}{\partial \xi} & \frac{\partial x}{\partial \eta}\\ \frac{\partial y}{\partial \xi} & \frac{\partial y}{\partial \eta}\end{bmatrix}\right| d\xi d\eta =$$

$$\hat{c}\int_0^1\int_0^{1-\eta}\begin{bmatrix}(1-\xi-\eta)^2 & (1-\xi-\eta)\xi & (1-\xi-\eta)\eta\\ \xi(1-\xi-\eta) & \xi^2 & \xi\eta\\ \eta(1-\xi-\eta) & \eta\xi & \eta^2\end{bmatrix}\left|\begin{bmatrix}x_2-x_1 & x_3-x_1\\ y_2-y_1 & y_3-y_1\end{bmatrix}\right| d\xi d\eta =$$

$$\hat{c}|[J]|\begin{bmatrix}\frac{1}{12} & \frac{1}{24} & \frac{1}{24}\\ \frac{1}{24} & \frac{1}{12} & \frac{1}{24}\\ \frac{1}{24} & \frac{1}{24} & \frac{1}{12}\end{bmatrix} = \frac{\hat{c}|[J]|}{12}\begin{bmatrix}1 & \frac{1}{2} & \frac{1}{2}\\ \frac{1}{2} & 1 & \frac{1}{2}\\ \frac{1}{2} & \frac{1}{2} & 1\end{bmatrix} \quad (7—17)$$

The lumped matrix capacitance is much simpler, and it can be constructed as

$$\left[\hat{C}\right]_e \approx \frac{\hat{c}A_e}{3}\begin{bmatrix}1 & 0 & 0\\ 0 & 1 & 0\\ 0 & 0 & 1\end{bmatrix} \quad (7—18)$$

where A_e is the area of an element.

In the numerical experiments conducted in the previous chapters, the consistent capacitance matrix results in delay of phase transformation time and it also experiences numerical oscillations. However, the lumped capacitance matrix shows good stability as well as the ability to provide accurate results. Consequently, the lumped capacitance matrix is preferred in this project.

For the conductivity matrix, the identity $\underline{q} = -k\nabla T$ is applied for the flux in equation (7—1). Since this is a two-dimensional problem and the thermal conductivity can be anisotropic, the conductive term can be expressed as

$$\{q\} = -\begin{bmatrix} k_{xx} & 0 \\ 0 & k_{yy} \end{bmatrix} \begin{Bmatrix} \frac{\partial T}{\partial x} \\ \frac{\partial T}{\partial y} \end{Bmatrix} = -[k](\nabla\{T\}) \tag{7—19}$$

where k_{xx} and k_{yy} refer to the thermal conductivity in the principal directions for an orthotropic material. If the material is orthotropic, the conductivities follow $k_{xx} \neq k_{yy}$; and if the material is isotropic, the conductivities $k_{xx} = k_{yy}$.

The thermal conductivity matrix is constructed as

$$[K]_e = \int_{\Omega_e} \left\{ \frac{\partial N}{\partial x} \quad \frac{\partial N}{\partial y} \right\} [k] \left[\frac{\partial N}{\partial x} \quad \frac{\partial N}{\partial y} \right] dV = \int_{\Omega_e} [B]^T [k][B]\, dV \tag{7—20}$$

where the superscript T signifies a transpose matrix.

The matrix $[B]$ arises from the gradients of shape and weighting functions. Construction of the thermal conductivity matrix via equation (7—20) requires transform of the Cartesian co-ordinates into the natural co-ordinates. Here, the Jacobian matrix is involved again. Suppose the matrix $[B]$ is the derivative of the shape functions with respect to the Cartesian co-ordinate system, i.e.

$$[B] = \begin{bmatrix} \frac{\partial N_1}{\partial x} & \frac{\partial N_2}{\partial x} & \frac{\partial N_3}{\partial x} \\ \frac{\partial N_1}{\partial y} & \frac{\partial N_2}{\partial y} & \frac{\partial N_3}{\partial y} \end{bmatrix} \tag{7—21}$$

Then, suppose the matrix $[D]$ is the derivative of the shape functions with respect to the natural co-ordinate system, i.e.

$$[D] = \begin{bmatrix} \frac{\partial N_1}{\partial \xi} & \frac{\partial N_2}{\partial \xi} & \frac{\partial N_3}{\partial \xi} \\ \frac{\partial N_1}{\partial \eta} & \frac{\partial N_2}{\partial \eta} & \frac{\partial N_3}{\partial \eta} \end{bmatrix} = \begin{bmatrix} -1 & 1 & 0 \\ -1 & 0 & 1 \end{bmatrix} \tag{7—22}$$

Consequently, the mapping of matrices [D] and [B] can be conducted through the Jacobian matrix, which is

$$[D] = [J]^T[B] = \begin{bmatrix} \frac{\partial x}{\partial \xi} & \frac{\partial y}{\partial \xi} \\ \frac{\partial x}{\partial \eta} & \frac{\partial y}{\partial \eta} \end{bmatrix} \begin{bmatrix} \frac{\partial N_1}{\partial x} & \frac{\partial N_2}{\partial x} & \frac{\partial N_2}{\partial x} \\ \frac{\partial N_1}{\partial y} & \frac{\partial N_2}{\partial y} & \frac{\partial N_2}{\partial y} \end{bmatrix} \tag{7—23}$$

With the identity $[B] = ([J]^T)^{-1}[D]$ from equation (7—23), the thermal conductivity can be written as

$$[K]_e = \int_{\Omega_e} [B]^T [\mathrm{k}][B]\, dV\{T\} = \int_{\Omega_e} [J]^{-1}[D]^T [\mathrm{k}]([J]^T)^{-1}[D] dV\{T\} \tag{7—24}$$

As to the advective term, the velocity $\underline{v}$ is a vector which can be projected on the x-direction and the y-direction in a Cartesian co-ordinate system. Thus, in the numerical methods the velocity can be expressed as

$$[v] = \begin{bmatrix} v_{xx} & 0 \\ 0 & v_{yy} \end{bmatrix} \tag{7—25}$$

where the v_{xx} is the scalar of the component of $\underline{v}$ on the x-direction and the v_{yy} is the scalar of the component on the y-direction. The material velocity matrix $[v]$ is established on the assumption that the difference of density between the solid and liquid is effectively small, so that the material velocity is constant.

Similar to the conductive term, the matrix of advection arises from

$$[K_v]_e = \hat{\mathrm{c}} \int_\Omega \{W\} : [v] \left[\frac{\partial N}{\partial x} \quad \frac{\partial N}{\partial y} \right] dV = \hat{\mathrm{c}} \int_0^1 \int_0^{1-\eta} \{W\} : [v][B]|[J]| d\xi d\eta =$$
$$\hat{\mathrm{c}} \int_0^1 \int_0^{1-\eta} \{W\} : [v]([J]^T)^{-1}[D]|[J]| d\xi d\eta = [Kv]_{xx} + [Kv]_{yy} \tag{7—26}$$

where ■: ■ signifies the Frobenius inner product of a vector and matrix. Thus, the above equation generates two separate matrices with respect to the velocity components v_{xx} and v_{yy}, respectively.

$$[Kv]_{xx} = \frac{\hat{\mathrm{c}} v_{xx}}{6} \begin{bmatrix} y_2 - y_3 & y_3 - y_1 & y_1 - y_2 \\ y_2 - y_3 & y_3 - y_1 & y_1 - y_2 \\ y_2 - y_3 & y_3 - y_1 & y_1 - y_2 \end{bmatrix} \tag{7—27a}$$

and

$$[Kv]_{yy} = \frac{\hat{c}v_{yy}}{6}\begin{bmatrix} x_3 - x_2 & x_1 - x_3 & x_2 - x_1 \\ x_3 - x_2 & x_1 - x_3 & x_2 - x_1 \\ x_3 - x_2 & x_1 - x_3 & x_2 - x_1 \end{bmatrix} \tag{7—27b}$$

The advective term above are interpolated by the central difference technique. Detailed derivation from equation (7—26) to equations (7—27a) and (7—27) can be seen in Appendix I—(k). It is known that, when the elemental Peclèt number is greater than 1, oscillations will occur in the numerical methods. In chapter 5, the Petrov-Galerkin method was adopted as the solution for numerical oscillation. And a discontinuous one-dimensional weighing function was applied. A general form of the Petrov-Galerkin modified weighing functions is shown in [137-138] is

$$\{W'_{xx}\} = \{N\} + \frac{\beta v_{xx} h}{2\|\underline{v}\|}\left\{\frac{\partial N}{\partial x}\right\} \tag{7—28a}$$

and

$$\left\{W'_{yy}\right\} = \{N\} + \frac{\beta v_{yy} h}{2\|\underline{v}\|}\left\{\frac{\partial N}{\partial y}\right\} \tag{7—28b}$$

where the parameter $\beta = \coth(Pe) - 1/Pe$. In references [75, 110], the streamline Petrov-Galerkin method is applied to the 3-node triangular elements.

In this project, for a linear triangular element as shown in Figure 7.1, the characteristic length of the element is regarded as the minimum height of the triangle, i.e.

$$h = \boldsymbol{min}(h_1, h_2, h_3) \tag{7—29}$$

Then, an artificial conductive matrix can be introduced to implement the upwind effect to the system of equations. The artificial conductive matrix is constructed as

$$\left[K_{up}\right]_e = \int_{\Omega_e}\left\{\frac{\partial N}{\partial x} \quad \frac{\partial N}{\partial y}\right\}\left[k_{up}\right]\left|\frac{\partial N}{\partial x} \quad \frac{\partial N}{\partial y}\right| dV \tag{7—30}$$

where the artificial conductivity matrix is evaluated as

$$\left[k_{up}\right] = \frac{\beta h}{2|\underline{v}|}\begin{bmatrix} v_{xx}^2 & v_{xx}v_{yy} \\ v_{yy}v_{xx} & v_{yy}^2 \end{bmatrix} \tag{7—31}$$

A similar approach adopted for equations from (7—20) to (7—24) can be applied to equation (7—30). Thus the semi-discretized artificial conductivity matrix for the upwind scheme is

$$\left[K_{up}\right]_e = \int_{\Omega_e}[D]^T[J]^{-1}\left[k_{up}\right]([J]^T)^{-1}[D]dV\{T\} \quad (7—32)$$

When the Petrov-Galerkin method is applied, the system of equations as shown in equation (7—16) becomes

$$\left[\hat{C}\right]\frac{(\{T^{n+1}\}-\{T^n\})}{\Delta t} + \left(\theta\left[{K_v}^{n+1}\right]\{T^{n+1}\} + (1-\theta)[{K_v}^n]\{T^n\}\right) + \left(\theta\left[{K_{up}}^{n+1}\right]\{T^{n+1}\} + (1-\theta)\left[{K_{up}}^n\right]\{T^n\}\right) = -(\theta[K^{n+1}]\{T^{n+1}\} + (1-\theta)[K^n]\{T^n\}) - \theta\{\tilde{Q}^{n+1}\} - (1-\theta)\{\tilde{Q}^n\} + \theta\{q^{n+1}\} + (1-\theta)\{q^n\} \quad (7—33)$$

So far, the constructions of all coefficient matrices are illustrated, the capacitance matrix $[\hat{C}]$ is constructed by equations (7—10), (7—17) and (7—18); the advective matrix is constructed by equations (7—10), (7—27a) and (7—27b); the Petrov-Galerkin artificial conductivity matrix is constructed by equations (7—31) and (7—32); and the conductivity matrix is constructed by equation (7—24), in which the conductivities are evaluated as $[k] = \Upsilon_s[k]_s + \Upsilon_l[k]_l$.

Equation (7—33) also contains several loading vectors that are required to be evaluated. The vector $\{q\}$ relates to the boundary conditions, and the vector $\{\tilde{Q}\}$ relates to the jump terms and non-physical source $\hat{Q}$.

7.2.3 Boundary conditions - Robin boundary conditions

The relationship of the number of surfaces and the number of nodes is sketched in Figure 7.2.

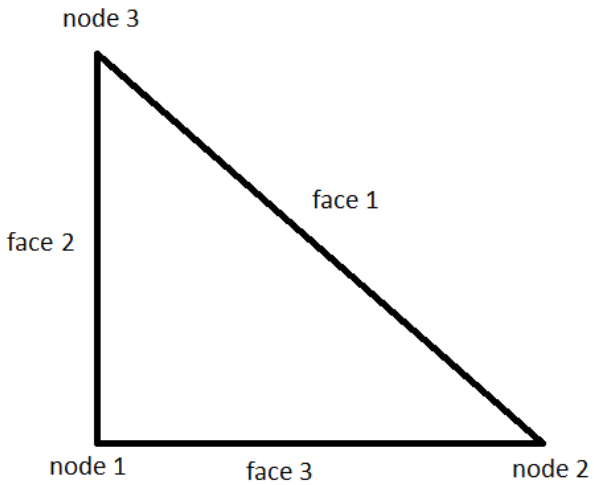

Figure 7.2: The numbering of nodes and faces

The vectors $\{q\}^n$ and $\{q\}^{n+1}$ are 3×1 column vectors in the system of equations for a triangular elements, they are nodal variables. As showed in Figure 7.2, a linear triangular element has three faces (boundaries), each boundary relates to two nodes, e.g. the face 2 relates to node 1 and node 3. Consequently, the boundary condition for face 2 can be regarded as a 2×1 column vector, noted as

$$\{q\}_2 = \begin{Bmatrix} q_1 \\ q_3 \end{Bmatrix} \tag{7—34}$$

where q_1 is the load at node 1 and q_3 is the load at node 3.

Moreover, the element boundary can be geometrically regarded as a line. Therefore, the boundary conditions can be calculated by considering each face as a one-dimensional rod element, and the shape functions are

$$\emptyset_1 = \frac{1-\zeta}{2} \quad and \; \emptyset_2 = \frac{1+\zeta}{2} \tag{7—35}$$

A different notation $\emptyset$ rather than N is used to highlight that these shape functions are only for the boundary. It is the same as the natural co-ordinate ζ instead of ξ.

With the shape functions as shown in equation (7—35) being adopted, the loading vector of boundary condition for face 2 becomes

$$\{q\}_2 = \begin{Bmatrix} q_1 \\ q_3 \end{Bmatrix} \approx \int_{-1}^{1} \emptyset_\vartheta \, q_{c2} \frac{L_2}{2} \mathrm{d}\zeta \tag{7—36}$$

where $q_{c2} = h_c(T - T_{amb})$ is the Robin boundary condition applied on face 2, the factor h_c is the convective coefficient and the temperature T_{amb} is the ambient temperature.

The length of the boundary surface L_2 can be evaluated as

$$\begin{Bmatrix} L_1 \\ L_2 \\ L_3 \end{Bmatrix} = \begin{Bmatrix} \sqrt{(y_3 - y_2)^2 + (x_3 - x_2)^2} \\ \sqrt{(y_3 - y_1)^2 + (x_3 - x_1)^2} \\ \sqrt{(y_2 - y_1)^2 + (x_2 - x_1)^2} \end{Bmatrix} \tag{7—37}$$

Below is an example showing how to calculate the Robin boundary condition for the surface 2.

$$\{q\}_2 = \begin{Bmatrix} q_1 \\ q_3 \end{Bmatrix} = \int_{-1}^{1} \begin{Bmatrix} \frac{1-\zeta}{2} \\ \frac{1+\zeta}{2} \end{Bmatrix} h_c (T - T_{amb}) \frac{L_2}{2} d\zeta = h_c \int_{-1}^{1} \begin{Bmatrix} \frac{1-\zeta}{2} \\ \frac{1+\zeta}{2} \end{Bmatrix} \begin{bmatrix} \frac{1-\zeta}{2} & \frac{1+\zeta}{2} \end{bmatrix} \begin{Bmatrix} T_1 \\ T_3 \end{Bmatrix} \frac{L_2}{2} d\zeta -$$

$$h_c \int_{-1}^{1} \begin{Bmatrix} \frac{1-\zeta}{2} \\ \frac{1+\zeta}{2} \end{Bmatrix} T_{amb} \frac{L_2}{2} = h_c \frac{L_2}{2} \begin{bmatrix} \frac{2}{3} & \frac{1}{3} \\ \frac{1}{3} & \frac{2}{3} \end{bmatrix} \begin{Bmatrix} T_1 \\ T_3 \end{Bmatrix} - h_c \frac{L_2}{2} \begin{Bmatrix} 1 \\ 1 \end{Bmatrix} T_{amb} \quad (7—38)$$

As it can be seen in equation (7—38), a direct integration of the heat flux with Robin boundary condition results in a 2 by 2 matrix, which is potentially difficult to assembly. An alternative way of constructing the boundary conditions for the numerical method is to lump the matrix again, which makes it as a vector, for example

$$\{q\}_2 = \begin{Bmatrix} q_1 \\ q_3 \end{Bmatrix} = \int_{-1}^{1} \begin{Bmatrix} \frac{1-\zeta}{2} \\ \frac{1+\zeta}{2} \end{Bmatrix} q_{c2} \frac{L_2}{2} d\zeta = \frac{L_2}{2} \begin{Bmatrix} 1 \\ 1 \end{Bmatrix} q_{c2} = \frac{L_2}{2} \begin{Bmatrix} 1 \\ 1 \end{Bmatrix} h_c \left(\frac{T_1 + T_3}{2} - T_{amb} \right) \quad (7—39)$$

In equation (7—37), the boundary condition $q_{c2} = h_c(T_{f2} - T_{amb})$, and T_{f2} an average temperature for surface 2, i.e.

$$T_{f2} = \frac{1}{L_2} \int_{-1}^{1} \left(\frac{1-\zeta}{2} T_1 + \frac{1+\zeta}{2} T_3 \right) \frac{L_2}{2} d\zeta = \frac{T_1 + T_3}{2} \quad (7—40)$$

7.2.4 The loading vector $\{\tilde{Q}\}$

The loading vector $\{\tilde{Q}\}$ is essential to the non-physical source method, since the jump and source which relate to the discontinuities are now accounted for in this loading vector. In equation (7—8), the term $\int_{\Omega_e} N_\vartheta \hat{Q} dV$ on the LHS of the equation and the term $\left(- \int_{\Gamma_i^e} N_\vartheta \right] \rho h (\underline{v} - \underline{v}^{\times}) \cdot \underline{n} [d\Gamma \Big)$ on the RHS of the equation require further consideration for finite elements.

According to the definition of non-physical source $\hat{Q}$ via equation (7—9), a relationship can be established as

$$\int_{\Omega_e} N_\vartheta \hat{Q} dV - \int_{\Gamma_i^e} N_\vartheta] \rho h \underline{v} \cdot \underline{n} [d\Gamma = \int_{\Gamma_e} N_\vartheta \rho h \underline{v} \cdot \underline{n} d\Gamma + \int_{\Gamma_i^e} N_\vartheta] \rho h \underline{v} \cdot \underline{n} [d\Gamma - \int_{\Gamma_e} N_\vartheta \hat{c} T \underline{v} \cdot$$

$$\underline{n} d\Gamma - \int_{\Gamma_i^e} N_\vartheta] \rho h \underline{v} \cdot \underline{n} [d\Gamma = \int_{\Gamma_e} N_\vartheta \rho h \underline{v} \cdot \underline{n} d\Gamma - \int_{\Gamma_e} N_\vartheta \hat{c} T \underline{v} \cdot \underline{n} d\Gamma \quad (7—41)$$

Equation (7—41) can be loaded to a finite element system by a 3×1 column vector $\{\tilde{Q}\}_e$. It is known that the term $\int_{\Gamma_e} N_\vartheta \rho h \underline{v} \cdot \underline{n} d\Gamma$ can be evaluated analytically as a 3×1 vector

$\{Q_f\}_e$ (the shape functions N_ϑ can be ignored here, and detailed evaluation is provided later in this chapter), and a numerical evaluation can be conducted for $\int_{\Gamma_e} N_\vartheta \hat{c} T \underline{v} \cdot \underline{n} d\Gamma$ once the non-physical $\hat{c}$ is provided by equation (7—10), and the matrices for this term are given by equations (7—27a), (7—27b) and (7—32). Change of the enthalpy due to $\int_{\Gamma_e} N_\vartheta \hat{c} T \underline{v} \cdot \underline{n} d\Gamma$ is then numerically evaluated as

$$\{Q_{num}\}_e = \left(\theta \left[{K_v}^{n+1}\right]_e \{T_p^{n+1}\}_e + (1-\theta)[{K_v}^n]_e \{T^n\}_e\right) + \left(\theta \left[{K_{up}}^{n+1}\right]_e \{T_p^{n+1}\}_e + (1-\theta)\left[{K_{up}}^n\right]_e \{T^n\}\right) \quad (7—42)$$

Where $\{Q_{num}\}_e$ is a 3×1 column vector, and $\{T_p^{n+1}\}_e$ is the predicted further time step temperature, which are directly returned from updating techniques such as predictor-corrector method.

With equation (7—41), equation (7—8) now has only one remaining term to consider which is the jump $\left(\int_{\Gamma_i^e} N_\vartheta\right] \rho h \underline{v}^{\times} \cdot \underline{n}\left[d\Gamma\right)$. This term is tricky for fixed grid FEM. In Tables 5.2 and 5.3, it can be known that this term returns a single value, which is related to the phase interface. However, in the fixed grid FEM, no information about the phase interface can be provided from the grid, all values are given to the nodes, simple equal division and application to every node of an element is rough, and may cause temperature overflow. However, how this single value is distributed to the nodes is hard to establish. One strategy which can avoid the establishment of the distribution and the possible temperature overflow is to introduce another capacitance as

$$c_i = \frac{\int_{t^n}^{t^{n+1}} \int_{\Gamma_i^e}] \rho h \underline{v}^{\times} \cdot \underline{n}[d\Gamma dt}{\int_{\Omega_e} T^{n+1} dV - \int_{\Omega_e} T^n dV} \quad (7—43)$$

Then a matrix is constructed in a similar manner as equation (7—18), which is denoted as $[C_i]_e$, consequently, the jump $\int_{t^n}^{t^{n+1}} \int_{\Gamma_i^e}] \rho h \underline{v}^{\times} \cdot \underline{n}\left[d\Gamma\, dt\right.$ is treated as

$$\{Q_i\}_e = [C_i]_e \left(\{T_p^{n+1}\}_e - \{T^n\}_e\right) \quad (7—44)$$

Finally, the loading vector $\{\tilde{Q}\}$ can be evaluated as

$$\{\tilde{Q}\}_e = \{Q_f\}_e + \{Q_{num}\}_e + \{Q_i\}_e \quad (7—45)$$

As mentioned, the predicted temperature vector $\{T_p^{n+1}\}_e$ is obtained by the methods such as the predictor-corrector method. In a time step, the predictor-corrector method has several loops to generate the predicted temperature for future time step. At each loop, the system of equations are considered as linear system of equations, and the cooling rate is potentially faster than it should be. Because, it is known that the cooling rate for phase change solidification is slower than the cooling rate of single phase material if the boundary conditions are the same, because latent heat is released when phase changes. Thus, it is artificially slowed as below.

$$\{T_p^{n+1}\}_e = R\{T_{\tau-1}^{n+1}\}_e + (1-R)\{T_\tau^{n+1}\}_e \tag{7—46}$$

where τ denotes the τth loop, and the factor $R \in [0,1]$, which adjust the dependence of predicted temperature $\{T_p^{n+1}\}_e$ on the temperatures returned from two adjacent loops.

7.3 The non-physical variable method in triangular elements

7.3.1 The evaluation of solid fraction

The evaluation of solid volume fraction for a triangular element is similar to the one-dimensional case. The element based temperature approximation is applied. For example, in the modelling of isothermal solidification, if the nodal temperature of node 1 is less than the solidus temperature T_{sol}, and the nodal temperatures of node 2 and node 3 are greater than T_{sol}, then the solid domain and liquid domain within the element can be sketched as Figure 7.3. The solid volume fraction of this element can be approximated as $\Upsilon_s \approx V_s/V_e$. In order to evaluate the volume V_s, the shaded area is required to be evaluated. This evaluation is conducted via the assumptions $f_s^1 = (T_{sol} - T_1)/(T_2 - T_1)$ and $f_s^2 = (T_{sol} - T_1)/(T_3 - T_1)$ as shown in Figure 7.3.

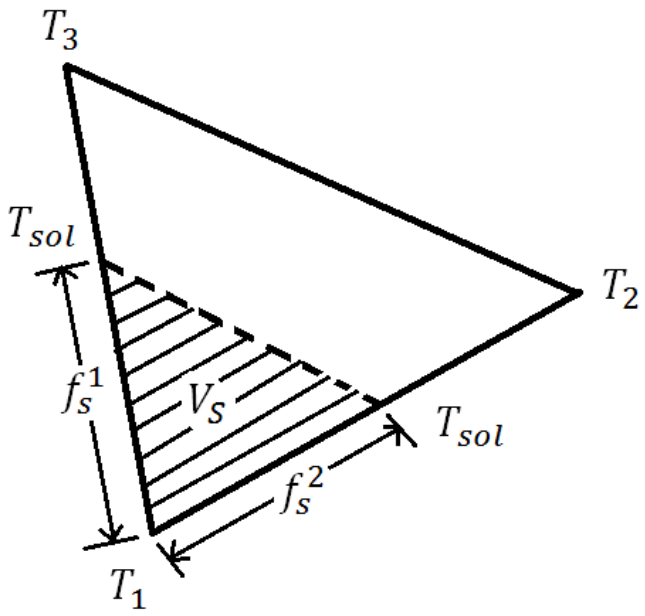

Figure 7.3: Solid fraction of an element

As a consequence, the volume of solid domain can be approximated as

$$V_s \approx \frac{1}{2} f_s^1 L_2 * f_s^2 L_3 \, \boldsymbol{sin}(\beta_1) \tag{7—47}$$

and

$$V_e \approx \sqrt{P(P-L_1)(P-L_2)(P-L_3)} \tag{7—48}$$

where β_1 is the angle between face 2 and face 3, L is the length of face and P is the semi-parimeter. The subscripts 1, 2 and 3 refer to the local face number of element. The evaluation of each parameter is shown in Appendix I—(l).

However, there may be another situation as shown in Figure 7.4. In this situation, the nodal temperatures T_1 and T_2 are both less than T_{sol}, but T_3 is greater than T_{sol}. It means the portion of element in the solid region is quadrilateral, which makes it difficult to calculate the area. The strategy applied is that, the liquid fraction Υ_l can be calculated by evaluating $f_l^1 = (T_3 - T_{sol})/(T_3 - T_1)$ and $f_l^2 = (T_3 - T_{sol})/T_3 - T_2$, the solid fraction is then calculated with respect to the identity $\Upsilon_s = 1 - \Upsilon_l$ for isothermal solidification.

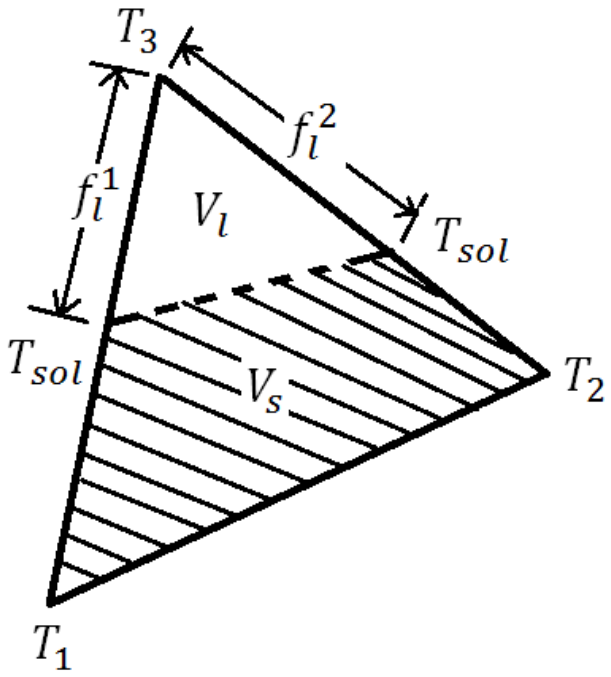

Figure 7.4: Quadrilateral solid region

7.3.2 The evaluation of enthalpy

Once the solid/liquid fractions are evaluated, the linkage equation can be recalled to evaluate the non-physical enthalpy and the non-physical capacitance. Application of the mixture enthalpy $\rho h = \Upsilon_s \rho_s h_s + \Upsilon_l \rho_l h_l$ gives

$$\int_{\Omega_e} \rho h \, dV = \int_{\Omega_e} \Upsilon_s \rho_s h_{sol} \, dV + \int_{\Omega_e} \Upsilon_s \, \rho_s \int_{T_{sol}}^{T} c_s(T') dT' \, dV + \int_{\Omega_e} \Upsilon_l \, \rho_l h_{sol} dV +$$
$$\int_{\Omega_e} \Upsilon_l \rho_l l \, dV + \int_{\Omega_e} \Upsilon_l \rho_l \int_{T_{liq}}^{T} c_l(T') dT' \, dV \qquad (7—49)$$

Assuming that the capacitances and the densities are constant, equation (7—49) becomes

$$\int_{\Omega_e} \rho h \, dV = \int_{\Omega_e} \Upsilon_s \rho_s h_{sol} \, dV + \int_{\Omega_e} \Upsilon_s \, \rho_s c_s (T - T_{sol}) dV + \int_{\Omega_e} \Upsilon_l \, \rho_l h_{sol} dV +$$
$$\int_{\Omega_e} \Upsilon_l \rho_l l \, dV + \int_{\Omega_e} \Upsilon_l \rho_l \, c_l \big(T - T_{liq}\big) dV \qquad (7—50)$$

Computation of equation (7—50) requires the integration of temperature over the solid and liquid region, respectively. In the one-dimensional cases, the integrations are conducted directly to the interpolated temperatures. For two dimensional and three dimensional elements, an averaging strategy provided by Mondragon [139] can be applied. For instance, if the situation is the same as Figure 7.3, then

$$\int_{\Omega_e} \Upsilon_s \, T dV \approx \frac{\Upsilon_s V_e}{3}(T_1 + 2T_{sol}) \tag{7—51}$$

and

$$\int_{\Omega_e} \Upsilon_s \, \rho_s c_s (T - T_{sol}) dV \approx \rho_s c_s \left[\frac{\Upsilon_s V_e}{3}(T_1 + 2T_{sol}) - \Upsilon_s V_e T_{sol}\right] \tag{7—52}$$

Similarly, in the liquid phase

$$\int_{\Omega_e} \Upsilon_l \, T dV \approx \frac{V_e}{3}(T_1 + T_2 + T_3) - \frac{\Upsilon_l V_e}{3}(T_1 + 2T_{liq}) \tag{7—53}$$

and

$$\int_{\Omega_e} \Upsilon_l \rho_l \, c_l \big(T - T_{liq}\big) dV \approx \rho_l c_l \left[\frac{V_e}{3}(T_1 + T_2 + T_3) - \frac{\Upsilon_l V_e}{3}\big(T_i + 2T_{liq}\big) - \Upsilon_l V_e T_{liq}\right] \tag{7—54}$$

An alternative approach in this project is to conduct direct integrations to the temperatures over the finite element domain. Thus equations (7—52) and (7—54) become

$$\int_{\Omega_e} g_s \, (T - T_{sol}) dV \approx \int_0^{f_s^1} \int_0^{f_s^2 (1-\eta)} (N_1 T_1 + N_2 T_2 + N_3 T_3 - T_{sol}) |[J]| \, d\xi d\eta =$$
$$\frac{|[J]| f_s^1 f_s^2}{6}\Big(6T_1 - 6T_{sol} + 2T_1 {f_s^2}^2 - 2T_3 {f_s^2}^2 - 3T_1 f_s^1 - 6T_1 f_s^2 + 3T_2 f_s^1 + 3T_3 f_s^1 +$$
$$3T_{sol} f_s^2 + 3T_1 f_s^1 f_s^2 - 3T_2 f_s^1 f_s^2 - T_1 f_s^1 (f_s^2)^2 + T_2 f_s^1 (f_s^2)^2\Big) \tag{7—55}$$

and

$$\int_{\Omega_e} g_l \big(T - T_{liq}\big) \, dV \approx \int_0^1 \int_0^{1-\eta} (N_1 T_1 + N_2 T_2 + N_3 T_3) |[J]| \, d\xi d\eta - \int_0^{f_s^1} \int_0^{f_s^2 (1-\eta)} (N_1 T_1 +$$
$$N_2 T_2 + N_3 T_3 - T_{sol}) |[J]| \, d\xi d\eta = \frac{|[J]|}{6}(T_1 + T_2 + T_3) - \int_{\Omega_e} g_s \, (T - T_{sol}) dV \tag{7—56}$$

7.3.3 The advection and the non-physical source

In chapter 6, results of numerical experiment show that, there is an incompatibility issue between the variable non-physical capacitance and the upwind Petrov-Galerkin method. Nevertheless, numerical instability arises from the advection and thus requires a stability technique such as upwind method. The new non-physical variable method removes the discontinuity from the advection term, and the discontinuity related to the advection is now accounted for by the non-physical source $\hat{Q}$. The evaluation of non-physical source $\hat{Q}$ requires the analytical evaluation for the physical advection.

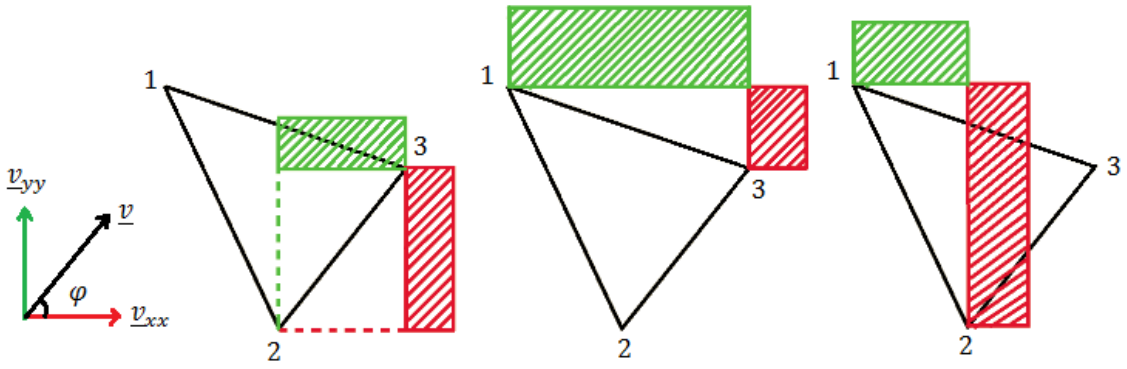

Figure 7.5: Areas swept by the elemental boundaries with velocity $\underline{v}$

Figure 7.5 shows the area swept by each surface of the element due to material motion, and the angle of the velocity is denoted as φ. Different colours are used to distinguish the components of $\underline{v}$ on x-direction and y-direction. The areas are marked with the same colour as their related components. The shape of swept area is rectangle. As a consequence, different shape functions have to be used to evaluate the enthalpy change due to advection in the solidification problem. The shape functions are

$$\{\widetilde{N}\} = \left\{\frac{(1-\xi)(1-\eta)}{4} \quad \frac{(1+\xi)(1-\eta)}{4} \quad \frac{(1+\xi)(1+\eta)}{4} \quad \frac{(1-\xi)(1+\eta)}{4}\right\} \tag{7—57}$$

In a rectangular CV, the interface of solid and liquid may exist in three different situations. The sketches of these situations are presented in Figure 7.6. The shaded area is the solid region and the blank area is the liquid region. The evaluation of the solid/volume fraction in the swept area can be conducted through the calculation of the shaded triangle or the trapezium. Their lengths of sides are approximated by the temperature, which is similar to the triangular element as mentioned in section 7.3.1.

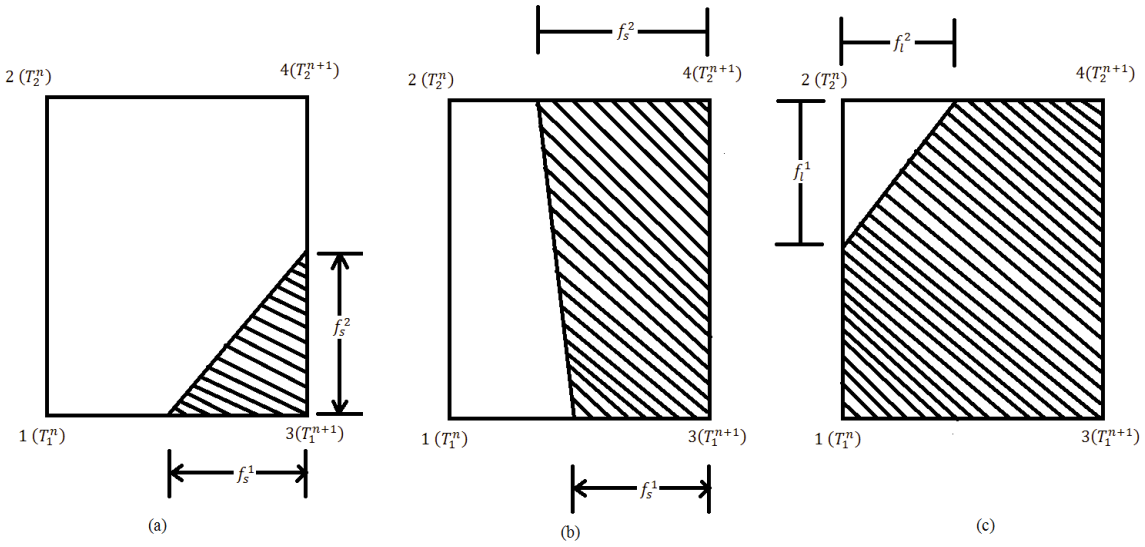

Figure 7.6: Solid volume fraction in the swept area

Thus, the enthalpy in the swept region Ω_f can be calculated as

$$\int_{\Omega_f} \rho h \, dV = \int_{-1}^{1}\int_{-1}^{1} g_s^f \rho_s h_{sol} + g_s^f \rho_s c_s(\tilde{T}_f - T_{sol}) + g_l^f \rho_l h_{sol} + g_l \rho_l l + g_l \rho_l c_l(\tilde{T}_f - T_{liq})\left|[\tilde{J}]\right| d\xi d\eta \tag{7—58}$$

where

$$\tilde{T}_f = \tilde{N}_1 T_1^n + \tilde{N}_2 T_2^n + \tilde{N}_3 T_1^{n+1} + \tilde{N}_4 T_2^{n+1} \tag{7—59}$$

and $[\tilde{J}]$ is the Jacobian matrix for the rectangle, which is expressed as

$$[\tilde{J}] = \begin{bmatrix} \frac{(x_2 - x_2^f)(1+\eta)}{4} + \frac{(x_1 - x_1^f)*(1-\eta)}{4} & \frac{(y_2 - y_2^f)(1+\eta)}{4} + \frac{(y_1 - y_1^f)*(1-\eta)}{4} \\ \frac{(x_2 - x_1)(1+\xi)}{4} + \frac{(x_2^f - x_1^f)(1-\xi)}{4} & \frac{(y_2 - y_1)(1+\xi)}{4} + \frac{(y_2^f - y_1^f)(1-\xi)}{4} \end{bmatrix} \tag{7—60}$$

It should be noticed that the rectangular swept areas do not really exist in the finite element meshes. They are created just to evaluate analytically the enthalpy change for the triangular element according to advection. As a matter of fact, the co-ordinates (x_1^f, y_1^f) and (x_2^f, y_2^f) do not exist as well. They are related to the real co-ordinates (x_1, y_1), (x_2, y_2), the velocity and the time increment. Moreover, the situations of the interface as shown in Figure 7.6 and equations from the (7—55) to (7—57) are examples according to surface 3. In practice,

according to the cooling rate and the direction of heat flow, the order of nodes may change. Thus, there are more combinations, but the evaluations follow the same approach as mentioned.

7.4 The numerical experiments

7.4.1 Updating procedure

Simulation of isothermal solidification using non-physical variable method in 2D requires an update procedure. Assuming that the temperature of the present time $\{T^n\}$ step is known, with given material properties, boundary conditions and initial conditions, the steps below are generally followed.

(1) Obtain the predicted temperature of the future time step, which is denoted as $\{T_p^{n+1}\}$. The approach can be the techniques such as explicit method, the predictor-corrector method, etc.;
(2) Obtain element liquid fraction Υ_l or element solid fraction Υ_s as described in section 7.3.1;
(3) Evaluate each term appearing in equations (7—33) with the temperature $\{T^n\}$, $\{T_p^{n+1}\}$ and element solid fraction Υ_s as described in section 7.3.2;
(4) Evaluate the non-physical vector $\{\tilde{Q}\}$ as described in sections 7.2.4 and 7.3.3;
(5) Construct coefficient matrices and loading vectors via section 7.2.2;
(6) Solve the system of equations in equation (7—33) and obtain $\{T^{n+1}\}$;
(7) If $\{T^{n+1}\}$ satisfies the error criteria, go to the next time step, i.e. $\{T^{n+1}\} \rightarrow \{T^n\}$; if not $\{T^{n+1}\} \rightarrow \{T_p^{n+1}\}$, go through (1) to (7) again at the current time step.

In order to examine the feasibility of non-physical variable method in 2D, three groups of numerical experiments are provided. The geometries of the modelling are different. In the first group, the model is a long and thin tube. The boundary conditions are set identical to the one dimensional study illustrated in chapter 6. This makes it comparable with the analytical solution and the existing numerical method. In the second group, the geometry is modelled as a square, and it is used to examine the performance of method with off-axis material velocity. In the third group, the geometry is a rectangle and more practical BCs are applied. Details of the numerical experiments are described as follows.

7.4.2 The numerical experiments, results and comments

Although different geometries and BCs are designed for the three groups of tests, some settings are commonly applied to all the three groups. For example, thermal dynamic properties of pure zinc are adopted in the modelling; the solidus temperature and liquidus temperature are equal to each other, i.e. $T_{sol} = T_{liq} = 400℃$; and the solidification is isothermal. In addition, the initial temperature T_{init} is 405 ℃ and the ambient temperature T_{amb} is 25 ℃.

7.4.2.1 Numerical experiment 1

In the first numerical experiment, the geometry is modelled as shown in Figure 7.7. The BCs are applied identically to the 1D numerical experiment in chapter 6. This setting makes it comparable with the existing numerical method such as the CVCM [66]. The material velocity is considered as the most important aspect of the project, thus different magnitudes of material velocity are set in the experiment. Detailed settings can be seen in Table 7.1. Moreover, with the modelling of advection, both solid and liquid move. It is assumed here that the difference between the velocity of solid $\underline{v}_s$ and the velocity of liquid $\underline{v}_l$ are relatively small, i.e. $\underline{v}_s = \underline{v}_l$.

Magnitude	Direction
$\|\underline{v}\| = 0.0001\ m/s$	$\varphi = 180°$
$\|\underline{v}\| = 0.0005\ m/s$	$\varphi = 180°$
$\|\underline{v}\| = 0.001\ m/s$	$\varphi = 180°$

Table 7.1: Material velocities for TEST 1

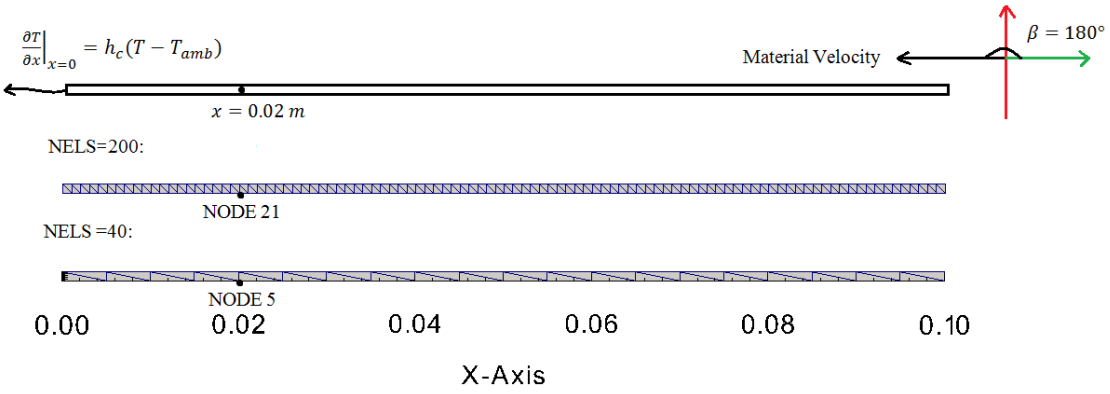

Figure 7.7: Sketch of solidifying model for experiment 1

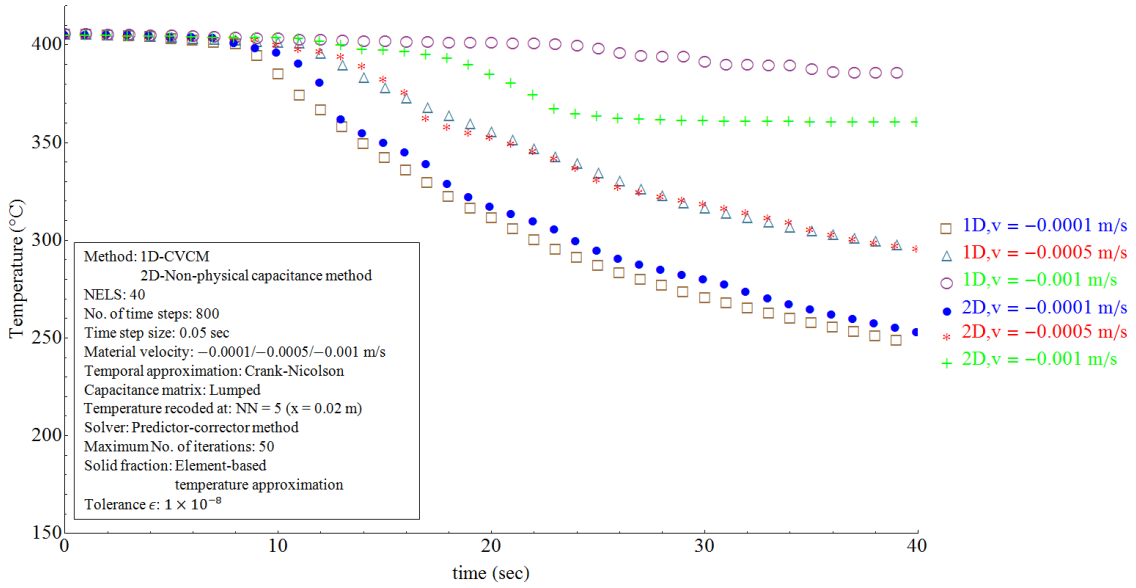

Figure 7.8: Nodal temperature provided by the non-physical capacitance method

Figure 7.8 illustrates the change of nodal temperature of node 5 which is provided by the non-physical capacitance method. Recall the concepts of the non-physical enthalpy and the non-physical source term as displayed in Figure 7.10, which is shown in Figure 7.8 again for convenience. The non-physical capacitance belongs to the concept (a) in Figure 7.9, in which the discontinuities exist on the boundary of element. In the experiment with 40 triangular elements, result shows that when the material velocity is low, e.g. $\|\underline{v}\| = 0.0001\ m/s$ and $\|\underline{v}\| = 0.0005\ m/s$, the results in 2D agree well with the results in 1D. However, when the material velocity is high, e.g. $\|\underline{v}\| = 0.001\ m/s$, inaccuracy arises. The reason is believed as the incompatibility between the rapid changing non-physical capacitance and the advection term.

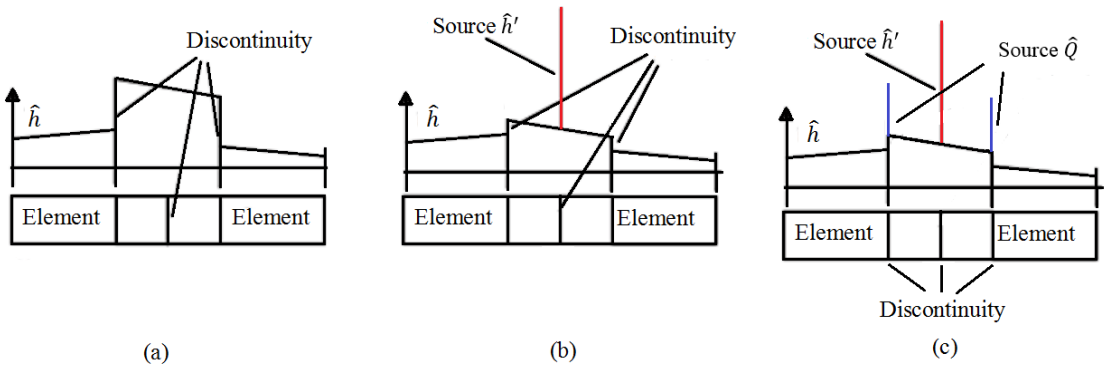

Figure 7.9: Concepts of non-physical enthalpy and source

It is known that the construction of Petrov-Galerkin weighting equations requires the element Pecl ̀et number, and is further dependent on the capacitance. In the non-physical capacitance method, the significant change of capacitance of the element under phase change results in a different level of upwind than the continuous elements, this may provide inaccurate results, e.g. the history of temperature when $v = -0.001\ m/s$ in Figure 7.8. The new non-physical variable method provided in chapter 5 was confirmed by numerical experiments that it effectively solves the incompatibility issue. However, the two-dimensional modelling is more complicated than the one-dimensional modelling. For example, the nodes of one-dimensional element are also the boundary of the element, so the analytical advection is evaluated from the boundary assigned to the node. This feature of one-dimensional elements allows the consistency to be satisfied with analytical advection. Nevertheless, Figure 7.2 shows that the node and face are different, and the inconsistency may arise from the assignment of analytical advection from elemental face to the elemental node.

Figure 7.10 shows the results provided by the new non-physical variable method, in which the concept (c) is applied. In other words, the removal of discontinuity procedure makes the non-physical capacitance for advective term to be almost continuous, and it is now compatible with the Petrov-Galerkin method. In Figure 7.10, the results agree well with the CVCM and it is also stable for high material velocity, i.e. $\|\underline{v}\| = 0.001\ m/s$.

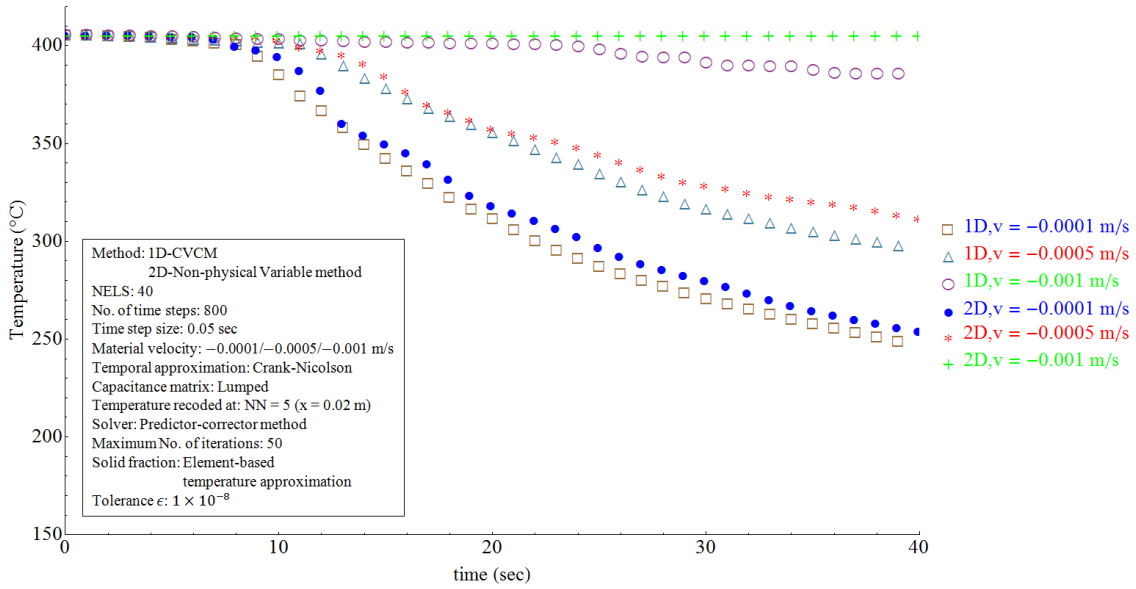

Figure 7.10: Nodal temperature provided by the new non-physical variable method, NELS=40

Moreover, it also can be seen that undulation exists in the change of nodal temperature from both figures. However, the author believes it arises from the rapid change of non-physical capacitance in the temporal term. And this can be removed by refining the mesh. One example can be seen in Figure 7.11 that, when the number of elements is increased from 40 to 200, the undulation disappears.

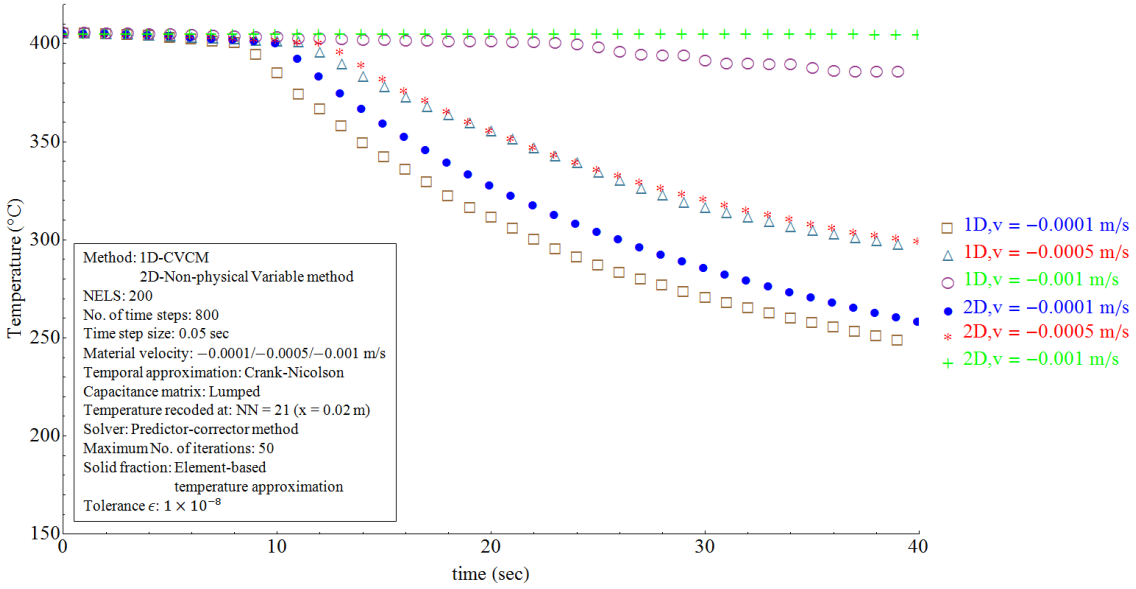

Figure 7.11: Nodal temperature provided by the new non-physical variable method, NELS=200

The numerical experiments also show that the increase of mesh density cannot be applied for the non-physical capacitance method (i.e. concept (a)) because the incompatibility between the non-physical capacitance and the advection term becomes more severe when the mesh density is increased. As to the non-physical variable method (i.e. concepts (c)), a relaxation factor $R \in [0, 1]$ is required to prevent the inconsistency and temperature overflow. Normally, greater mesh density requires higher relaxation factor. In the two simulations, the factor $R = 0.7$.

7.4.2.2 Numerical experiment 2

In this experiment, a $0.1\ m \times 0.1\ m$ square plate is modelled. The thermodynamic material properties of the plate are exactly the same as those applied in the previous experiments, which can be seen in Table 4.9. The initial temperature is $405\ ℃$ and the ambient temperature is $25\ ℃$. The Robin boundary condition is applied on the bottom and left boundaries of the plate, and the other two boundaries are isolated. The off-axis material velocity is assigned in this experiment, magnitude of which is $0.001\ m/s$ and angle is $210°$.

This configuration of material property gives the component of velocity on x-direction $v_{xx} = -0.00086\ m/s$ and the component of velocity on y-direction $v_{yy} = -0.0005\ m/s$. The purposes of conducting this experiment are, firstly, to exam the feasibility and stability of non-physical variable methods when complex boundary conditions and off-axis material velocity are applied; secondly, to see the effect of the off-axis material velocity on the cooling rate in different directions of the model; and thirdly, to display the ability of front tracking by temperature in 2D. A sketch of a model is drawn in Figure 7.12. The model is discretised into 5000 linear triangular elements, which generate 2601 nodes. The mesh is plotted in Figure 7.13, which also displays the example node numbers chosen for results collection.

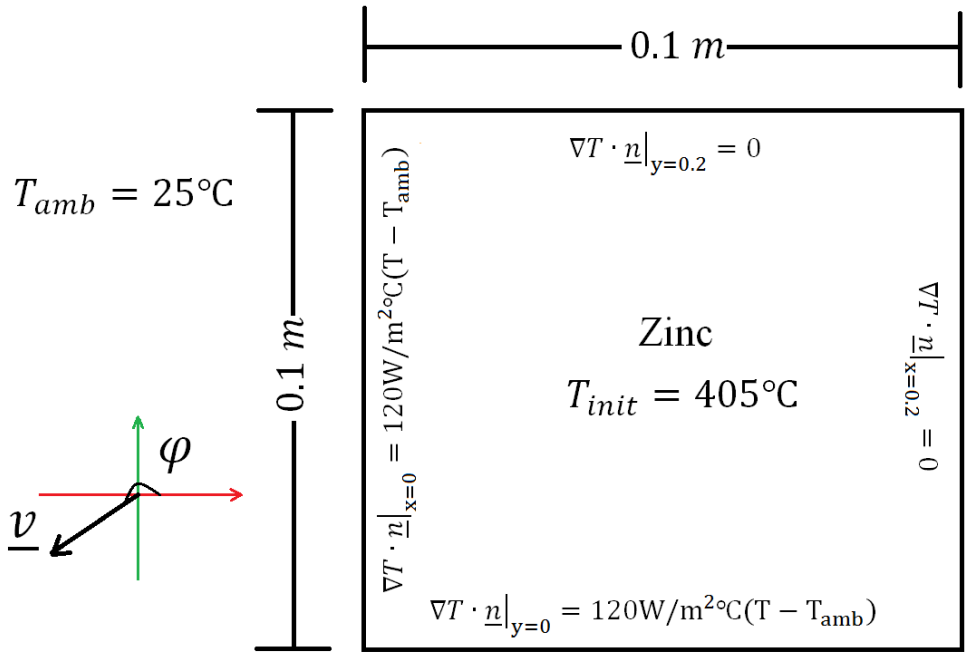

Figure 7.12: Sketch of solidifying model for TEST 2

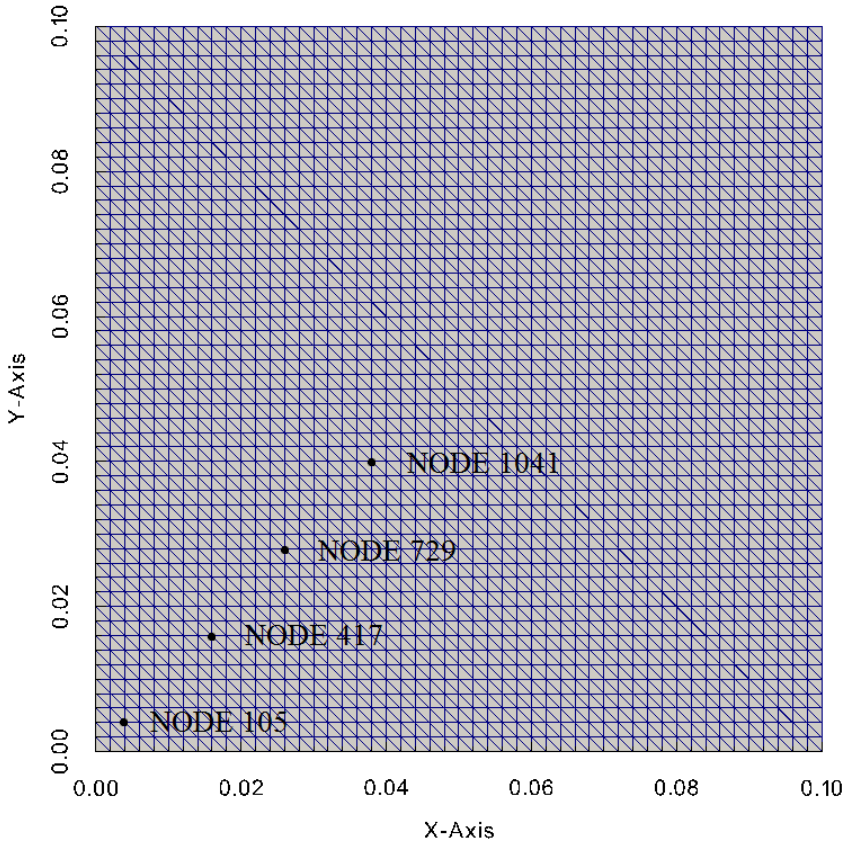

Figure 7.13: Mesh of square plate

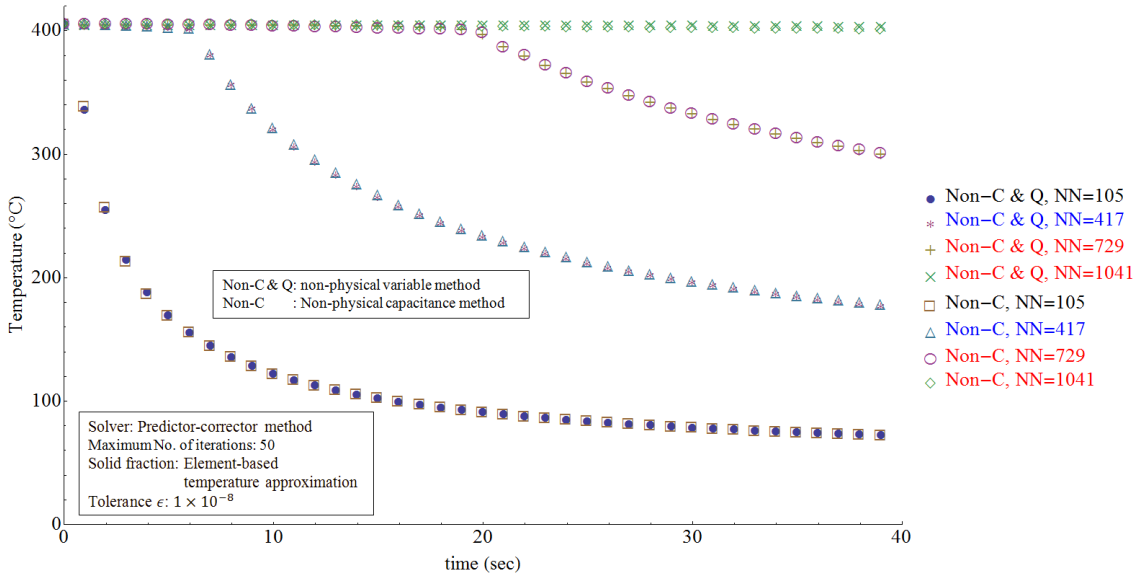

Figure 7.14: Comparison of temperature profile between the non-physical capacitance method and the non-physical variable method

Figure 7.14 illustrates results from the non-physical capacitance method. The results are compared against the results from the non-physical variable method. It can be seen in Figure 7.14 that, results returned from both strategies agree well for all picked example nodes.

However, this good agreement relies on the relaxation factor applied on the non-physical source. In the simulation, the relaxation factor is set as $R = 0.5$.

Figure 7.15 presents the phase front position which is visualised by the software ParaView. It can read files in the Visualisation Tool Kit (VTK) format, which are directly created by the self-made programme. The examples are captured at time 7.44 seconds, 14.94 seconds, 22.44 seconds and 29.94 seconds respectively. The phase front is plotted with the assumption that the temperature of the interface is the solidus temperature, e.g. 400 ℃. In Figure 7.15, the contour plotted by the combination strategy is smoother than the non-physical capacitance method.

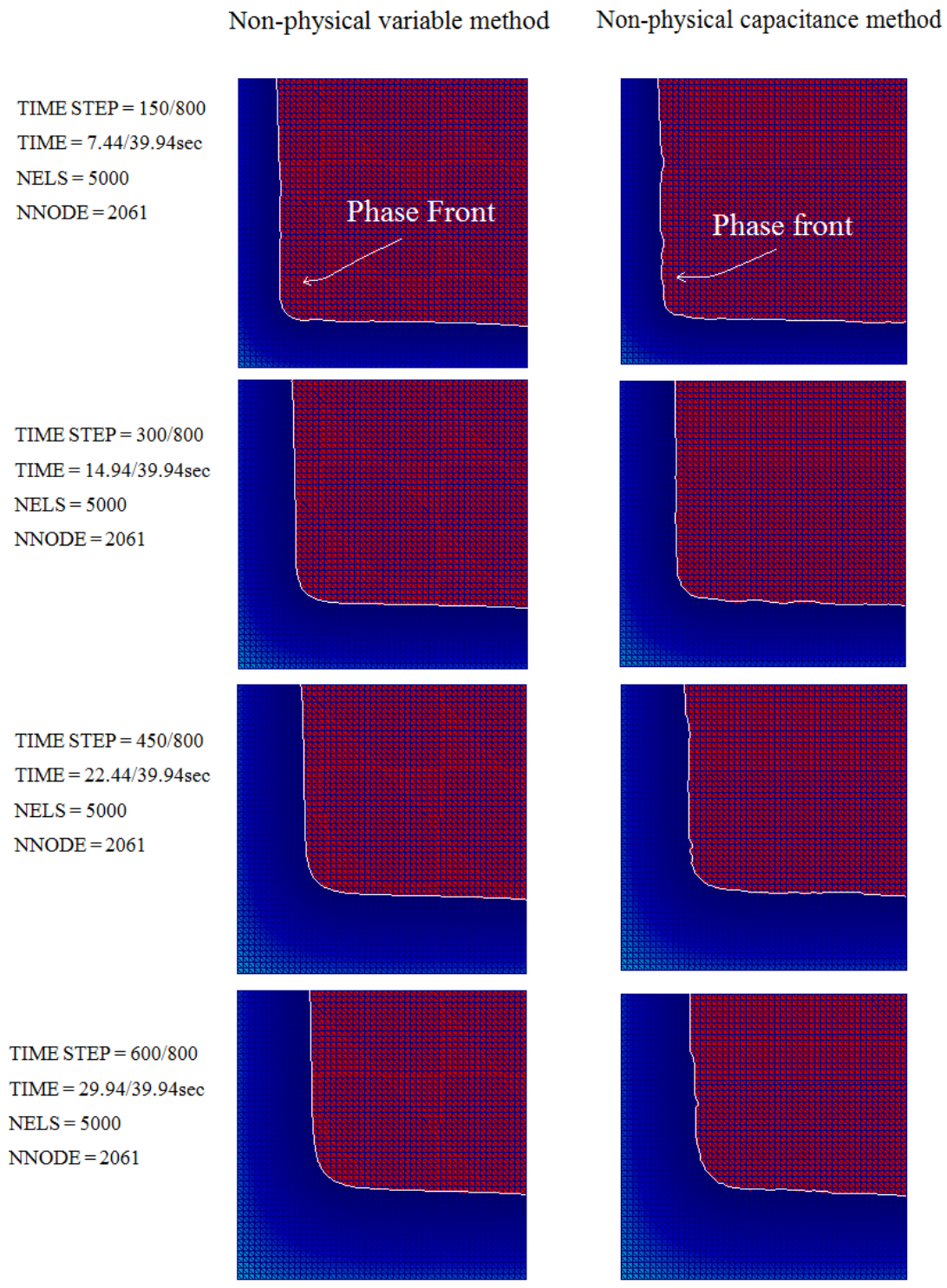

Figure 7.15: Phase front tracked by temperature

7.4.2.3 Numerical experiment 3

In the third numerical experiment, a more practical simulation is considered, which refers to continuous casting. A sketch of a continuous casting is presented as Figure 7.16.

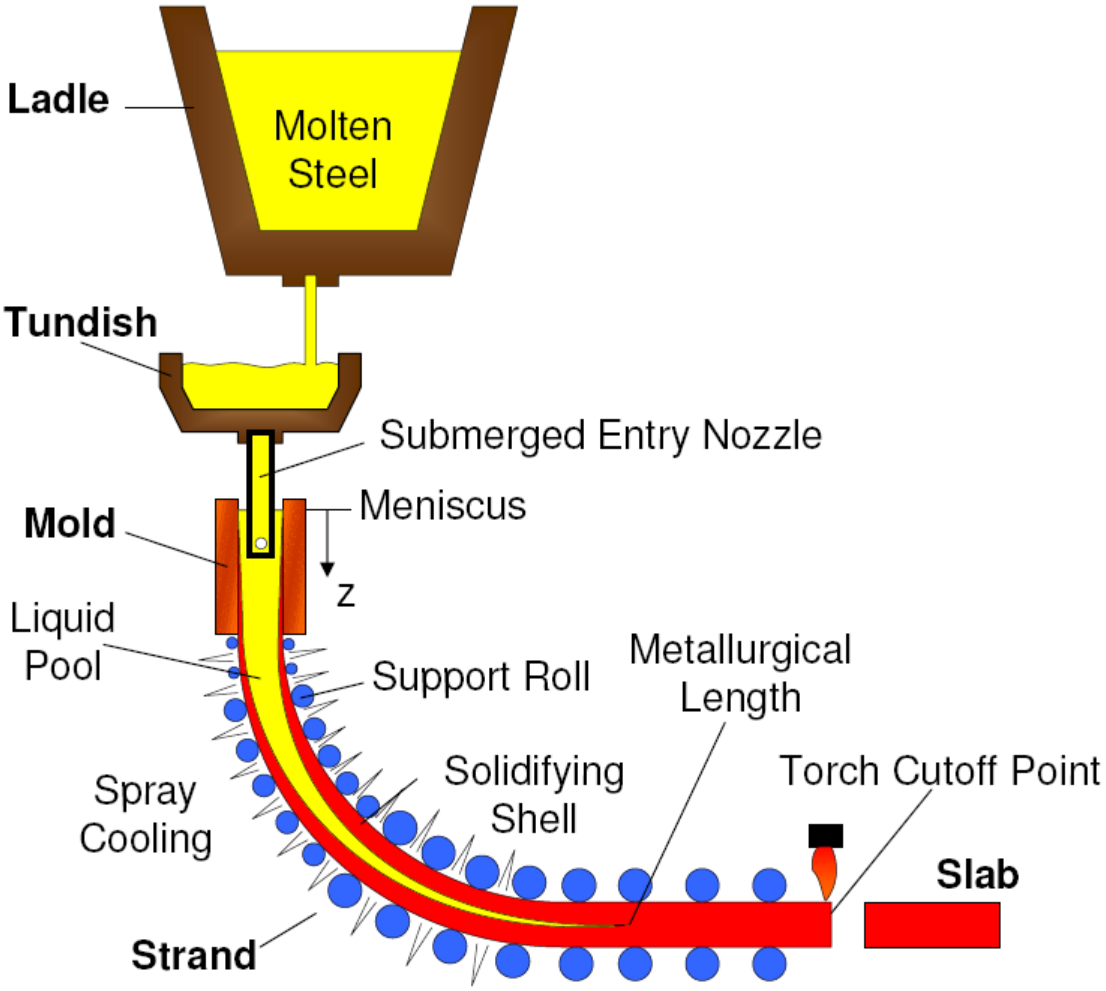

Figure 7.16: The Continuous casting machine [140]

In the simulation, the model is simplified as two components, the entry nozzle and the mould. The geometry of the model is a 0.1 m by 0.05 m rectangle. The area marked in red is assumed as the nozzle, and the area marked in blue is the mould as shown in Figure 7.16. It is assumed that the model is only in thermal contact with the environment on the surface of the mould, thus these are the places where the Robin BCs apply. The nozzle is assumed thermal isolated. The molten material (i.e. Zinc) flows in from the left surface of the rectangle and the material is then flowing out from the right end of the model. It is also assumed that, the model is filled with molten material initially. Although this model is simple, it shows the ability to deal with the isothermal solidification with advection-diffusion.

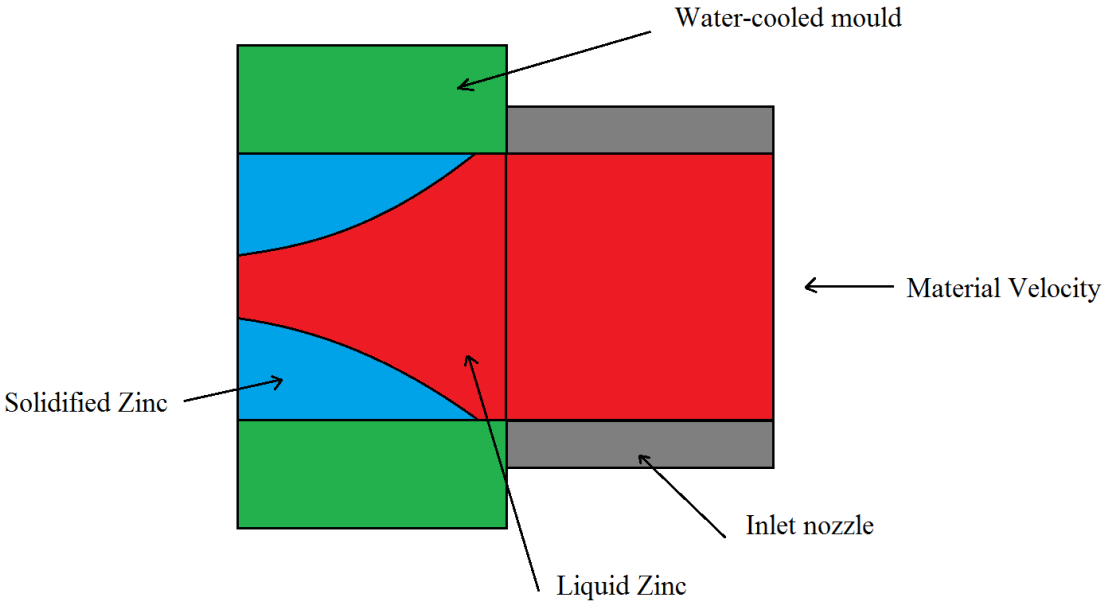

Figure 7.17: The simplified model

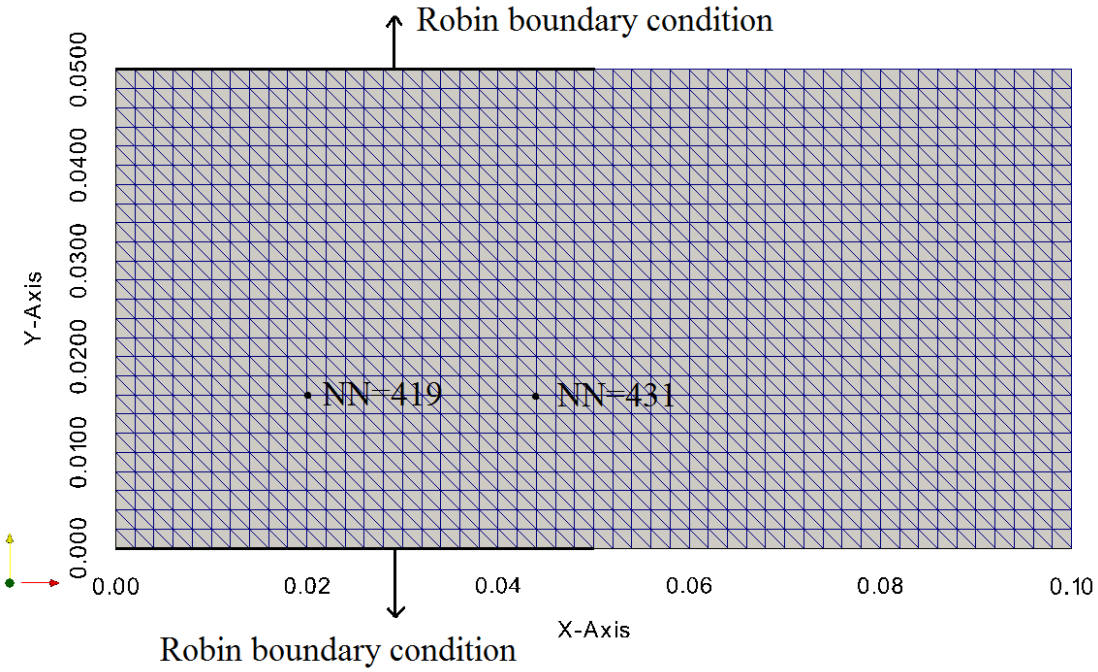

Figure 7.18: Mesh of simplified model

The geometry of the simplified model is shown in Figure 7.18. It is meshed with 2500 linear triangular elements. The total time for the cooling process is 40 seconds, with 0.05 seconds time step and 800 time steps. The Robin boundary condition with forced convective term $h_c = 4800\ W/m^2$℃ is applied to the surfaces which is highlighted with thick lines. The material velocity in the simulations is set to be $\|\underline{v}\| = 0.001\ m/s$ and $\|\underline{v}\| = 0.0001\ m/s$ respectively. And the angle of velocity φ is always 180°.

Figure 7.19 is the history of temperature recorded at the co-ordinate (0.02 m, 0.018m). It can be seen that increasing of material velocity reduces the cooling time for the material in the mould. Consequently, the energy state of the numerical model is higher. This phenomenon is already confirmed in the one-dimensional simulation, which can be used to control the cooling rate in the continuous casting, and the temperature of the leaving solidified material.

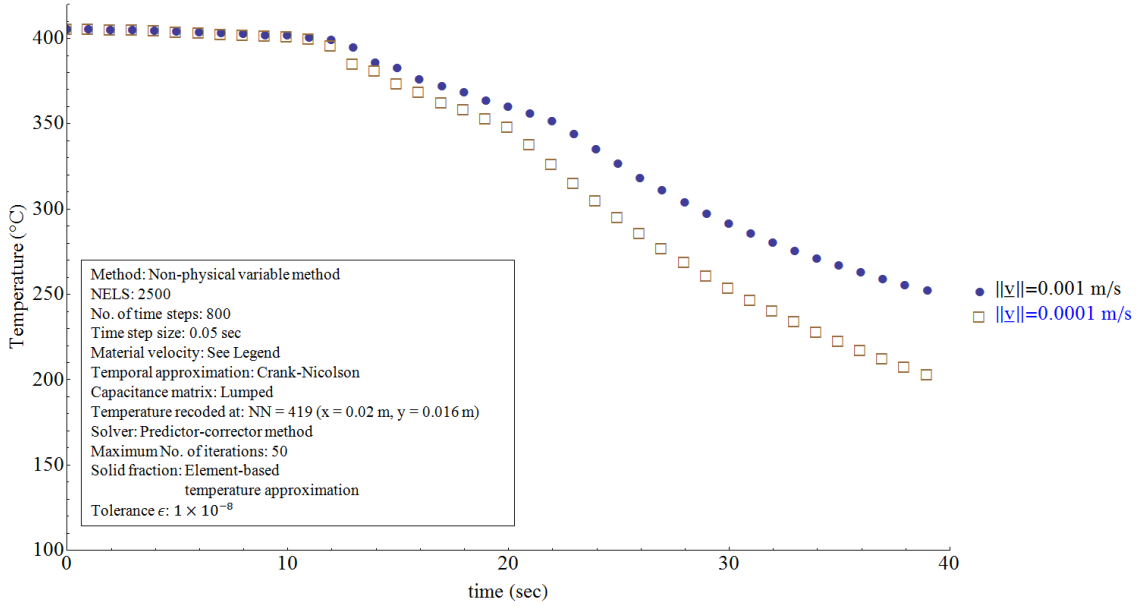

Figure 7.19: History of temperature, node number = 419

Figure 7.20 is the history of temperature recorded at the co-ordinate (0.044 m, 0.018 m), which is 0.024 m away from the first example node in the x direction. This example temperature profile shows that the influence of material velocity in the continuous casting simulation is consistent for all points of the model, showing evidence of stability.

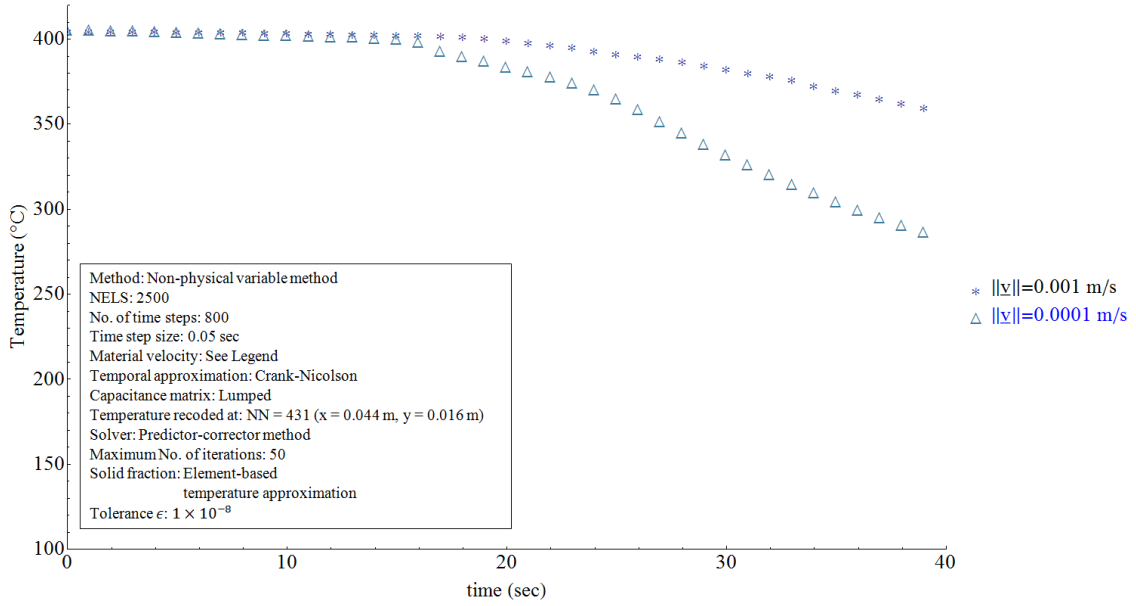

Figure 7.20: History of temperature, node number = 431

In Figure 7.21, some features of continuous casting can be seen, i.e. the solidifying shell, the liquid pool and the metallurgic length. The size of the model is very small if compared with a real continuous casting mould, i.e. this model is only 0.05 metres long while the length of a real casting mould is between 0.5 metres to 1.2 metres. It makes the material in the mould solidify fast and it results in a "cold shut" (the solidified material blocks the nozzle) when the material velocity is $0.0001\ m/s$ and the forced convective coefficient is 4800 W/m^2℃. It means that the cooling rate is too high for this model. Reference [136] introduces several factors that have effects on the cooling rate of continuous casting mould, including the flow-rate of cooling water, the type of mould lubricant, the material composition and the casting speed. In this numerical simulation, the flow-rate of cooling water is reflected by the forced convective term, the casting speed is considered identical to the material velocity. When the material velocity is increased to $0.001\ m/s$, but the forced convective coefficient stays at 4800 W/m^2℃, the status of continuous casting for time 7.44 sec, 14.94 sec, 22.44 sec and 39.94 sec are shown on the left of Figure 7.21. It can be seen that increasing the velocity alone is not sufficient enough to prevent the "cold shut". Thus, on the right side of Figure 7.21, the new simulation reduces the forced convective coefficient to $1000\ W/m^2$℃ (this operation can be achieved by adjusting the flow rate of cooling water in practice). It shows that the metallurgical length is long enough for material to flow out of the mould.

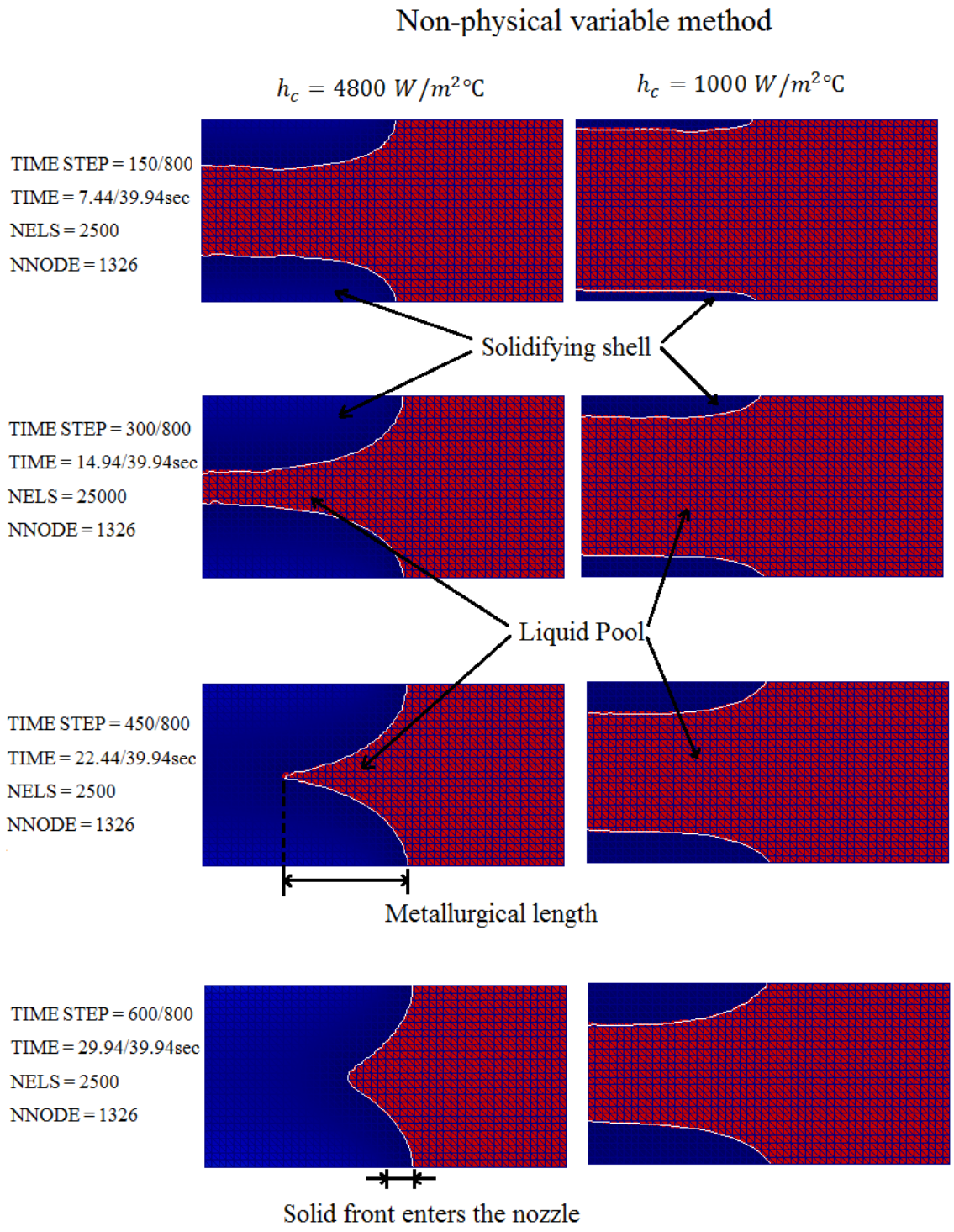

Figure 7.21: Simulation of a continuous casting mould by Non-physical variable method

7.4.2.4 Execution time

The Execution time of programme is dependent on four factors, which are the specification of the computer, the number of elements/nodes, the number of time steps and the number of iterations. Table 7.2 presents three computers on which, the programme is executed. In the numerical experiments, the total number of time steps is always 800, and the total number

of iterations is constantly 50, thus, comparisons can be conducted through different mesh densities, which are shown in Table 7.3.

Hardware	Low specification	Medium specification	High Specification
CPU	Intel(R) Core(TM) i5 1.60 ~ 2.26GHz	Intel(R) Core(TM) i7 1st Generation 2.80GHz	Intel(R) Core(TM) i7 2nd Generation 3.50GHz
RAM	DDR3 1600MHz 4GB	DDR3 1333MHz 4GB	DDR3 1600MHz 8GB
Hard drive	SSD 256 GB	SATA HHD 500 GB 7200 rpm	SSD 256 GB
Operating System	Microsoft Windows 8.1 64-bit	Microsoft Windows 7 Enterprise SP1-64 bit	Microsoft Windows 8.1 64-bit

Table 7.2: Specifications of test computer

SPEC.	Low			Medium			High		
NELS	200	2500	5000	200	2500	5000	200	2500	5000
Time (HH:MM:SS)	00:02:59	02:40:26	15:34:55	00:03:56	02:13:39	10:49:55	00:01:49	01:24:12	07:16:36
CPU (%)	~51.1	~47.0	~45.8	~48	~41	~35	~57.1	~51.3	~42.2
RAM (MB)	~18.4	~138	~378.7	~21.0	~144.2	~445.6	~18.8	~138.9	~381.8

Table 7.3: Execution time, CPU and memory usages

7.5 Summary

In summary, the chapter 7 extends the application of non-physical variable method into two-dimension. However, in this process, there are three major difficulties including:

(1) The implementation of Petrov-Galerkin finite element method into two-dimensional linear triangular element;

(2) The evaluation of enthalpy and solid volume fraction on the base triangular element;

(3) The analytical evaluation of advective term.

The first difficulty is overcome by equations (7—28a) and (7—28b), which makes the Petrov-Galerkin element applicable for all elements as long as the shape functions are known. The second difficulty is overcome by the element-based temperature approximations, which evaluates the solid volume fraction and further evaluate the specific enthalpy. For the last difficulty, the physical advection is analytically evaluated by the addition volume swept by the element surface with material velocity. The additional volumes are generated with respect to the components with material velocity in the x and y directions. This strategy promises that the addition volume generated is always a square in geometry, and it makes the simulation simpler as fewer situations are required to be considered.

This chapter also provides three groups of tests. In the first group, the geometry of the model is a long and thin slab, which makes the results comparable with one-dimensional simulation. Though an exact solution with advection and transient phase change is difficult to obtain, the results returned in this group of tests are compared with the classic CVCM [66]. The second group of tests, the off-axis material velocity is applied. The simulation is conducted on the base of a square. The comparison between the non-physical capacitance method and the non-physical variable method shows good agreement in results. However, it also shows that relaxation is required if the non-physical source is involved. In the final group, a continuous caster is simplified. The simulations present many features of the continuous casting process, such as solidifying shell, liquid pool and metallurgical length. Moreover, based on the theory of continuous casting [136], the “cold shut” is solved by increasing the material velocity and reducing the forced convective coefficient.

Chapter 8 Conclusion and Future Work

8.1 General

This project aims to establish an effective numerical methodology for phase change problem. The concept underpinning this project is to define several non-physical variables through weak forms of transport equations, which helps to adjust the distributions of discontinuities in the governing transport equations. This concept can in principle be applied to various discontinuous problems, such as shock propagation and fluid flow through porous medium. Particularly, this project focuses on the isothermal solidification, which is a typical Stefan problem.

In chapter 2, a literature review is conducted to better understand the theory related to the project, such as the establishment of a mathematical model for solidification, which includes the governing equation of energy, the initial condition, the boundary conditions and the Stefan condition. A review of an enrichment scheme for solidification modelling is provided. This enrichment scheme is a representative front-tracking method, which uses XFEM but is limited to one-dimension. This project is founded on the recently discovered non-physical enthalpy method. Following the review of references [62-63], it is shown in Chapter 2 how the non-physical method can be further extended by considering the following aspects. First of all, the possibility that the weighting functions may vary with movement of the control volume. Secondly, the application of a non-physical source as a source term in the finite element method. Thirdly, to situations where advection is involved, i.e. when the material velocity is non-zero.

In chapters 3 and 4, a series of studies, which followed the control volume capacitance method (CVCM) [66] and the weak non-physical enthalpy method [62-63, 139], was provided to solve the problem of isothermal solidification. These two chapters provided alternative solution methods to the existing CVCM and non-physical enthalpy method. The study in chapter 3 indicates that information about the liquid volume fraction is essential to the non-physical enthalpy method, especially when the non-physical source term is adopted

to capture the discontinuity, as different approximations of liquid volume fraction that control the behaviour of non-physical variables can be seen in this chapter. It is also indicated in chapter 4 that when advection is involved in the evaluation of non-physical capacitance, it may result in an instability problem because negative capacitance may be generated. In order to solve this problem, a new definition of non-physical enthalpy was defined through energy conservation equation in chapter 5. The advective term is isolated from the temporal term, which helps to prevent the negative capacitance. Chapter 6 provided three concepts which illustrated how the discontinuities distribute in the non-physical capacitance and non-physical source. In the three concepts, concept (a) account the discontinuities in the change of enthalpy of an element, e.g. the non-physical capacitance method; concept (b) is that the discontinuities are completely annihilated in the enthalpy and re-applied to the system as a source, e.g. the non-physical enthalpy method; concept (c) is the new definition of non-physical variables, in which the non-physical jump $\hat{h}'$ is established to facilitate the removal of discontinuity from the volumetric domain, while the non-physical source $\hat{Q}$ is designed to account for the discontinuity related to advection. The one-dimensional study in chapter 6 was then extended into two-dimensional study in chapter 7, and the stability and feasibility of non-physical variable method were verified.

8.2 Contributions

This project provides the new definition of non-physical variable method, and studies the distribution of discontinuities within the non-physical variables. Application of non-physical variable method together with the upwind Petrov-Galerkin method breaks the limitation of the CVCM and non-physical enthalpy method to the advection-diffusion problem. It also illustrates the implementation of non-physical variable method into the finite element method in detail, which includes:

(1) The temporal and spatial discretization of governing equation, which involves the non-physical variables. The Galerkin weighted residual method is applied for one-dimensional and two dimensional studies, the advection is discretised by the Petrov-Galerkin method if required;
(2) The evaluation of solid/liquid volume fraction via element-based temperature fraction. The effects of solid/liquid volume fraction to the non-physical variables are studied;

(3)

(4) The evaluations of non-physical variables and the influence of approximation and updating procedure on the performance of non-physical variable method.

(5) Most importantly, it describes how the non-physical source is applied to maintain the energy conservation, which is not very clear in reference [62-63, 139].

Both the non-physical capacitance method and non-physical source method are applied to the stationary (material velocity $\|\underline{v}\| = 0\ m/s$) isothermal solidification. Different configuration of mesh density, matrix format and temporal approximation are examined by the numerical experiments. For the example node positioned at $x = 0.03\ m$, the non-physical capacitance method achieves its most accurate simulation with maximum percentage error only 1.16 %, and the classic non-physical enthalpy method achieves its most accurate simulation with maximum percentage error of only 0.79%. In chapters 6 and 7, the numerical experiments show that, the new non-physical variable method performs well with material velocity in different magnitudes and in different directions. This stable performance also persists in two-dimensional simulation. The non-physical variable method is now able to solve the solidification problem with advection-diffusion. In the two-dimensional simulation, it also shows the possibility of tracking the phase front via temperature approximation.

8.3 Limitations

The study of non-physical variable method requires the knowledge of solidification, heat transfer, numerical method and advanced mathematics. Restricted by the author's knowledge, this study has some limitations.

First of all, the exact solution of solidification problem with advection-diffusion cannot be established, which makes the accuracy of non-physical variable method cannot be examined. Though the results provided by the non-physical variable method is compared with the CVCM, however, it only confirms the stability of the new method and it is hard to determine which method is more accurate.

Secondly, this study evaluates the non-physical source analytically. The element-based temperature approximation may not be precise enough for the evaluation of the non-physical source. Moreover, the assignment of non-physical source to the FEM is not well considered.

For example, once the non-physical source is evaluated on the base of an element, its assignment is only conducted by the average approach. This may give rise to the numerical temperature "overflow" (nodal temperature may be greater than the initial temperature, which is wrong for a cooling process), thus the author had to use a relaxation factor to prevent it. But there is no clear mathematical formulation for the evaluation of relaxation factor, and it is only measured through experiments.

Thirdly, this study offers three updating methods, the predictor-corrector method, the secant method and the homotopy method, to calculate future time-step temperature and update the material properties. It also offers three solution methods, the successive under-relaxation method, the Gauss-Jordan elimination method and the LU decomposition method to solve the linear system of equations. However, due to the time constraints, there is not enough time to refine the program to improve the time efficiency and accuracy.

Finally, the study is conducted based on some assumptions. For example, the thermodynamic material properties of each phase are assumed constant; the material velocity of solid and the material velocity of liquid are assumed equal, i.e. $\|\underline{v}_s\| = \|\underline{v}_l\|$; And the solidification is isothermal. However, these assumptions may not be met in the alloy solidification. The non-physical variable method is only able to simulate macro-solidification, since only one governing equation (i.e. the energy conservation equation) is involved. Thus, caution should be taken when using these methods.

8.4 Possible further research

The research described in this thesis breaks the limitation of the CVCM due to the generation of negative capacitance. It also refines the concept of non-physical enthalpy method and provides a new definition for it. Although this thesis has these advantages, this research give rise to more questions that needs further exploration.

First of all, in the non-physical variable method, the removal of the discontinuities from the governing equation will absolutely generate a non-physical source term. The averaging technique adopted in this research arises overflow issues, and it requires relaxation. Thus the distribution of non-physical source to each node of an element requires further study. A point-based approximation of solid/liquid volume fraction may solve this problem, but its implementation to the FEM needs to be developed.

As to the solid/liquid volume fraction, this research utilises the temperature approximation, which leads to a cumulative solid volume fraction. When implemented with the non-physical variable method, it generates a significant peak in the change of non-physical capacitance and non-physical source. This peak increases the possibility that the instability occurs. In the comparison with analytical solutions, the author found that the evaluation of solid/liquid fraction through the position of phase front gives almost constant increasing rate of solid volume fraction. And this prevents the generation of the peak. In the author's point of view, the non-physical variable method can be developed as a fixed grid front tracking method, which may fulfil the potential of non-physical variable method.

Secondly, the research is based on isothermal solidification, which is the pure material solidification in practice. Alloy solidification requires the study on the mushy zone solidification, which has multiple phase fronts. The ground theory can be easily developed from this thesis. However, the implementation of it to the FEM is more challenging.

Thirdly, this research provides the governing equation with respect to the jump $\hat{h}'$. This term is not directly applied to the solution procedure. A simultaneous solution of the non-physical governing equation, the linkage equation and the source equation may avoid the troublesome updating process for solid/liquid fraction.

Moreover, this research solves the governing equation of energy conservation alone. However, the non-physical concept can be applied to all mass conservation equation, the momentum conservation equation and the concentration conservation equation as well. The application of non-physical variable method to these equations and solve them simultaneously may provide greater insight.

In the end, the accuracy of results provided by the non-physical variable method is required to be determined, especially when advection is involved and it is in two dimensions.

8.5 Implications for further research

This thesis presents detailed derivations of non-physical variables in mathematics, which helps to understand how this new methodology is established. The complicated equations may be hard to comprehend, thus the author uses the prescribed temperature profile from the exact solution to illustrate how these non-physical variables behave in the numerical method. This analysis provided in chapter 3 also highlights the crucial relationship between the

liquid/solid volume fraction and the non-physical variables, which may be an important direction in the further study.

Examples of application of non-physical variable method to both one-dimensional modelling and two-dimensional modelling are illustrated. The programme is updated to the latest format in Fortran. It provides alternative updating techniques, such as predictor corrector method, the secant method and the homotopy method, and also provides multiple solution methods as seen in Chapter 4. Rather than an unknown "black box", the programme has better data input and output. Through input file, the researcher can change mesh density, time step information, material properties, etc., which helps to comprehensively examine the method. The output function includes the use of CSV file format, which is readable for Microsoft Excel and Wolfram Mathematica. Data such as temperature, enthalpy, non-physical capacitance and non-physical source can be output and documented in the CSV, which helps the user to check and identify the problem. It also enables visualisation through VTK file formats; both static picture and dynamic animation can be created for two-dimensional modelling.

It is believed that this thesis provides a good grounding study on the non-physical variable method. The derivations of non-physical variables and the studies of their behaviour provide new insights for researchers to better develop this theory and implement it into practical application. The programme is well constructed which allow researchers to modify and verify their ideas. Therefore, the theory and the programmes illustrated in this thesis can be adopted for further study.

References

[1] W.W. Mullins and M. C. Shaw, *Metal Transformations*, Gordon and Breach, Science Publishers, New York, 1966.

[2] J. P. LaRue, *Basic Metal Casting*, American Foundrymen's Society, Des Plaines, 1989.

[3] U.S. Environmental Protection Agency, Profile of the Metal Casting Industry, Washington, DC, 1998.

[4] D. M. Stefanescu, *Science and Engineering of Casting Solidification*, Kluwer Academic/Plenum Publishers, New York, 2002.

[5] R. Bonnerot and P. Jamet, *A Conservative Finite Element method for One-Dimensional Stefan Problems with Appearing and Disappearing Phases*, Journal of Computational Physics 1981, **41**, 357-388.

[6] R. Bonnerot and P. Jamet , *A Third Order Accurate Discontinuous Finite Element Method for the One-Dimensional Stefan Problem*, Journal of Computational Physics 1979; **32**, 145-167.

[7] C. H. Li, *A Finite-element Front-Tracking Enthalpy method for Stefan Problems*, Journal of Numerical Analysis 1983; **3**, 87-107.

[8] J. Chessa, P. Smlinski and T. Belytschko, *The Extended Finite Element Method (XFEM) for Solidification Problems*, International Journal for Numerical Methods in Engineering 2002; **53**, 1959-1977.

[9] T. Belytschko, N. Moës, S. Usui and C. Parimi, *Arbitrary Discontinuities in Finite Elements*, International Journal for Numerical Methods in Engineering 2001; **50**, 993-1013.

[10] T.P. Fries and T. Belytschko, *The Extended/Generalized Finite Element Method: An Overview of the Method and Its Applications*, International Journal for Numerical Methods in Engineering 2010; **84**, 253-304.

[11] P. Duysinx, L. V. Miegroet, T. Jacobs and C. Fleury, *Generalized Shape Optimization Using X-FEM and Level Set Methods*, IUTAM Symposium on Topological Design Optimization of Structures, Machines and Materials Solid Mechanics and Its Applications Volume, 2006; **137**, 23-32.

[12] R. Merle and J. Dolbow, *Solving Thermal and Phase Change Problems with the eXtended Finite Element Method*, Computational Mechanics 2002; **28**, 339-350.

[13] H. Sauerland and T.P. Fries, *The Stable XFEM for Two-Phase Flows*, Computers and Fluids 2013; 87: 41-49.

[14] H. Ji, D. Chopp and J. E. Dolbow, *A Hybrid Extended Finite Element/Level-set Method for Modeling Phase Transformations*, International Journal for Numerical Methods in Engineering 2002; **54** 1209-1233.

[15] M. Farsad, F. J. Vernerey and H. S. Park, *An Extend Finite Element/Level-Set Method to Study Surface Effects on the Mechanical Behavior and Properties of nanomaterials*, International Journal for Numerical Methods in Engineering 2010; **84**, 1466-1489.

[16] D. Juric and G. Tryggvason, *A Front-Tracking Method for Dendritic Solidification*, Journal of Computational Physics 1996; **123**, 127-148.

[17] L. Tan and N. Zabaras, *A Level Set Simulation of Dendritic Solidification of Multi-component Alloys*, Journal of Computational Physics 2007; **221**, 9-40.

[18] D. Peng, B. Merriman, S. Osher, H. Zhao and M. Kang, *A PDE-Based Fast Local Level Set Method*, Journal of Computational Physics 1999; **155**, 410-438.

[19] S. Chen, B. Merriman, S. Osher, P. Smereka, *A Simple Level Set Method for Solving Stefan Problems*, Journal of Computational Physics 1997; **135**, 8-29.

[20] B. Engquist, A.K. Tornberg and R. Tsai, *Discretization of Dirac Delta Functions in Level Set Methods*, Journal of Computational Physics 2005; **207**, 28-51.

[21] N. P. Dijk, M. Langelaar and F. Keulen, *Explicit Level-set-based Topology Optimization Using an Exact Heaviside Function and Consistent Sensitivity Analysis*, International Journal for Numerical Methods in Engineering 2012; **91**, 67-97.

[22] S. Oscher and R. P. Fedkiw, *Level Set Methods: An Overview and Some Recent Results*, Journal of Computational Physics 2001; **169**, 463-502.

[23] A. B. Crowley, *Numerical Solution of Stefan Problems*, International Journal of Heat and Mass Transfer 1978; **21**, 215-219.

[24] K. Tacke, *Discretization of the Explicit Enthalpy method For Planar Phase Change*, International Journal of Numerical Methods in Engineering 1985; **21**, 543-554.

[25] V. Voller and M. Cross, *Accurate Solution of Moving Boundary Problems Using The enthalpy method*, International Journal of Heat and Mass Transfer 1981; **24**, 545-556.

[26] G. H. Meyer, *Multidimensional Stefan Problems*, Journal of Numerical Analysis 1973; **10**, 522-538.

[27] D. R. Atthey, *A Finite Difference Scheme for Melting Problems*, Journal of the Institute of Mathematics and its Applications 1974;

[28] V. Voller and M. Cross, *An Explicit Numerical Method to Track a Moving Phase Change Front*, International Journal of Heat and Mass Transfer 1983; **26**, 147-150.

[29] V. R. Voller, *An Implicit Enthalpy Solution for Phase Change Problems: with Application to A Binary Alloy Solidification*, Applied Mathematical modelling 1987; **11**, 110-116.

[30] M. Salcudean and Z. Abdulah, *On the Numerical Modelling of Heat Transfer During Solidification Processes*, International Journal For Numerical Methods in Engineering 1988; **25**, 445-473.

[31] G. Comini, S. DelGiudice, R. W. Lewis and O. C. Zienkiewicz, *Finite Element Solution of Nonlinear Heat Conduction Problems with Special Reference to Phase Change*, International Journal For Numerical Methods in Engineering 1974; **8**, 613-624.

[32] E. Laitinen and P. Neittaanmäki, *On Numerical Simulation of the Continuous Casting Process*, Journal of Engineering Mathematics 1988; **22**, 335-354.

[33] V. R. Voller, *Development and Application of a Heat Balance Integral Method for Analysis of Metallurgical Solidification*, Applied Mathematical Modelling 1989; **13**, 3-11.

[34] C. Prakash and V. Voller, *On the Numerical Solution of Continuum Mixture Model Equations Describing Binary Solid-Liquid Phase Change*, *Numerical Heat Transfer*, Part B: Fundamentals: An International Journal of Computation and Methodology 1989; **15**, 171-189.

[35] P. Chow and M. Cross, *An Enthalpy Control-Volume-Unstructured-Mesh (CV-CM) Algorithm For Solidification By Conduction Only*, International Journal For Numerical Methods In Engineering 1992; **35**, 1849-1870.

[36] Y. Rabin and E. Korin, *An efficient Numerical Solution for the Multidimensional Solidification (or Melting) Problems Using a Microcomputer*, International Journal of Heat and Mass Transfer 1993; **36**, 673-683.

[37] C. R. Swaminathan and V. R. Voller, *On the Enthalpy Method*, International Journal of Numerical Methods for Heat and Fluid Flow 1993, **3**, 233-244.

[38] M. Lees, *A Linear Three-Level Difference Scheme for Quasilinear Parabolic Equations*, Mathematics of Computation 1966; **20**, 516-622.

[39] S. Bounds, K. Davey and S. Hinduja, *A modified Effective Capacitance Method For Solidification Modelling Using Linear Tetrahedral Finite Elements*, International Journal for Numerical Methods In Engineering 1996; **39**, 3195-3215.

[40] R. W. Lewis and P. M. Roberts, *Finite Element Simulation of Solidification Problems*, Applied Scientific Research 1987; **44**, 61-92.

[41] K. Davey and S. Bounds, *Modelling the Pressure Die Casting Process using Boundary and Finite Element Methods*, Journal of Materials Processing Technology 1997; **63**, 696-700.

[42] M. Salcudean and Z. Abdulah, *On the Numerical Modelling of Heat Transfer During Solidification Processes*, International Journal For Numerical Methods in Engineering 1988; **25**, 445-473.

[43] L. Clavier, E. Arquis and J. P. Caltagirone, *A Fixed Grid Method for the Numerical Solution of Phase Change Problems*, International Journal for Numerical Methods in Engineering 1994; **37**, 4247-4261.

[44] V. R. Voller, *Fast Implicit Finite-Difference Method For the analysis of Phase Change Problems, Numerical Heat Transfer*, Part B 1990, **17**, 155-169.

[45] M. Lacroix and V. R. Voller, *Finite Difference Solutions of Solidification Phase Change Problems: Transformed Versus Fixed Grids, Numerical Heat Transfer*, Part B: Fundamentals: An International Journal of Computation and Methodology.

[46] V. R. Voller and C. R. Swaminathan, *General Source-Based Method For Solidification Phase Change*, Numerical Heat Transfer, Part B: Fundamentals: An International Journal of Computation and Methodology 1991; **19:2**, 175-189.

[47] W. D. Rolph and K. J. Bathe, *An Efficient Algorithm for Analysis of Nonlinear Heat Transfer with Phase Changes*, International Journal for Numerical Methods in Engineering 1982; **18**, 119-134.

[48] J. Roose and O. Storrer, *Modelization of Phase Changes by Fictitious Heat Flow*, International Journal for Numerical Methods in Engineering 1984; **20**, 217-225.

[49] V. R. Voller, *A Fixed Grid Numerical Modelling Methodology for Convection-Diffusion Mushy Region Phase-Change Problems*, International Journal of Heat and Mass Transfer 1987; **30**, 1709-1719.

[50] M. Lacroix, *Numerical Simulation of melting and Resolidification of a Phase Change Material Around Two Cylindrical Heat Exchangers*, Numerical Heat Transfer, Part A: Applications: An International Journal of Computation and Methodology 1993; **24**, 143-160.

[51] E. Majchrzak and A. Piasecka, *The Numerical Micro/Macro Model of Solidification Process*, Journal of Materials Processing Technology 1997; **64**, 267-276.

[52] E. Majchrzak, B. Mochnacki and J. S. Suchy, *Numerical Model of Macro-Segregation During Directional Crystallization Process*, Journal of Materials Processing Technology 1998; **78**, 122-127.

[53] I.T. Im, W.S. Kim and K.S. Lee, *A Unified Analysis of Filling and Solidification in Casting With Natural Convection*, International Journal of Heat and Mass Transfer 2001; **44**, 1507-1515.

[54] B. Moussa, J. E. Simpson and S. V. Garimella, *Concentration fields in the Solidification Processing of Material Matrix Composites*, International Journal of Heat and Mass Transfer 2002; **45**, 4251-4266.

[55] J. H. Brusche, A. Segal and C. Vuik, *An Efficient Numerical Method for Solid-Liquid Transitions in Optical Rewritable Recording*, International Journal For Numerical Methods in Engineering 2009; **77**, 702-718.

[56] S. McFadden and D.J. Browne, *A Front-Tracking Model to Predict Solidification Macrostructures and Columnar to Equiaxed Transitions in Alloy Castings*, Applied Mathematical Modelling 2009; **33**, 1397-1416.

[57] T. V. Vu, G. Tryggvason, S.Homma, J. C. Wells, And H. Takakura, *A Front-Tracking Method for Three-Phase Computations of Solidification with Volume Change*, Journal of Chemical Engineering of Japan 2013, **46**, 726-731.

[58] M. Ulvrova, S. Labrosse, N. Coltice P. Raback and P. J. Tackley, *Numerical Modelling of Convection Interfacing with a Melting and Solidification Front: Application to the Thermal Evolution of the Basal Magma Ocean*, Physics of the Earth and Planetary Interiors 2012; **206-207**, 51-56.

[59] R. W. Lewis, E. W. Postek, Z. Han and D. T. Gethin, *A Finite Element Model of the Squeeze Casting Process*, International Journal of Numerical methods for Heat & Fluid Flow 2006, **16**, 539-572.

[60] A. Joulin, Z. Younsi, L. Zalewski, S. Lassue, D. Rousse and J.P. Cavrot, *Experimental and Numerical Investigation of a Phase Change Material: Thermal-energy Storage and Release*, Applied Energy 2011; **88**, 2454-2462.

[61] D. Sun, S. V. Garimella, S. Singh and N. Naik, *Numerical and Experimental Investigation of the Melt Casting of Explosives, Propellants, Explosives*, Pyrotechnics 2005; **5**, 369-380.

[62] K. Davey and R. Mondragon, *A Non-physical Enthalpy Method for the Numerical Solution of Isothermal Solidification*, International Journal for Numerical Methods in Engineering 2010; **84**, 214-252.

[63] R. Mondragon, K. Davey, *Weak Discontinuity Annihilation in Solidification modelling*, Computers & Structures 2011; **89**, 681-701.

[64] A. Cosimo, V. Fachinott and A. Cardona, An Enrichment Scheme for Solidification Problems, Computational Mechanics 2013; **52**, 17-35.

[65] M. Salcudean and Z. Abdullah, *On the numerical modelling of heat transfer during solidification processes*, International Journal for Numerical methods in Engineering 1988; Vol. **25**, 445-473.

[66] K. Davey and N. J. Rodriguez, *A control volume capacitance method for solidification modelling with mass transport*, International Journal for Numerical methods in Engineering 2002;

[67] H. S. Carslaw, J. C. Jaeger, *Conduction of Heat in Solids*, Clarendon Press, Oxford, 1959.

[68] P. J. Schneider, *Conduction Heat Transfer*, Addison-Wesley, Xenia, 1955.

[69] A.H. Coppola-Owen and R. Codina, Improving Eulerian Two-phase Flow Finite Element Approximation with Discontinuous Gradient Pressure for Phase-change Problem, International Journal of Numerical Method in Eginnering 2005; **49**, 1287-1304.

[70] V. S. Rao, T. J. R. Hughes and K. Garikipati, *On the Modeling Thermal Oxidation of Silicon II: Numerical Aspects*, International Journal for Numerical Methods in Engineerging 2000; **47**, 359-377.

[71] T. Coratekin, J. Keuk and J Ballmann, *Performance of Upwind Schemes and Turbulence Models in Hypersonic Flows*, AIAA Journal 2004; **42:5**, 945-957.

[72] Z.X. Gong and A. S. Mujumdar, *A Finite Element Model for Convection-Dominated Melting and Solidification Problems*, International Journal of Numerical Methods for Heat & Fluid Flow 1998; **8**-4, 393-408.

[73] A. N. Brooks and T. J. R. Hughes, *Streamline upwind/Petrov-Galerkin Formulations for Convection Dominated Flows with Particular Emphasis on the incompressible Navier-Stokes Equations*, Computer Methods in Applied Mechanics and Engineering 1982; **32, 1-3**, 199-159.

[74] J. Argyris, *Petrov-Galerkin Finite Element Approach to Coupled Heat and Fluid Flow*, Computer Methods in Applied Mechanics and Engineering 1992; **94-2**, 181-200.

[75] B. A. Finlayson, *The Method of Weighted Residuals and Variational Principles*: With Application in Fluid Mechanics, Heat and Mass Transfer, Academic Press, INC., London, 1972.

[76] D. V. Hutton, *Fundamentals of finite element analysis*, McGraw-Hill, New York, 2004.

[77] J. A. Sethian and J. Strain, *Crystal Growth and Dendritic Solidification*, Journal of Computational Physics 1992; **98**, 231-253.

[78] M. E. Glicksman, *Principles of Solidification: An Introduction to Modern Casting and Crystal Growth Concepts*, Springer, New York, 2011.

[79] D. Gobin, Natural Convection at a Solid-Liquid Phase Change Interface, in *Phase Change with Convection: Modteelling and Validation*, Edited by T. A. Kowalewski, D. Gobin, Springer, Springer-Verlag Wien New York, New York, 2004.

[80] F. Stella and M. Gingi, Modelling Methodologies for Convection-Diffusion Phase-Change Problems, in *Phase Change with Convection: Modteelling and Validation*, Edited by T. A. Kowalewski, D. Gobin, Springer, Springer-Verlag Wien New York, New York, 2004.

[81] G. Amberg, Solidification Microstructure, Dendrites and Convection, in *Phase Change with Convection: Modteelling and Validation*, Edited by T. A. Kowalewski, D. Gobin, Springer, Springer-Verlag Wien New York, New York, 2004.

[82] D. M. Stefanescu, *Science and Engineering of Casting Solidification*, Springer, New York, 2009.

[83] M. Mbaye and E. Bilgen, *Phase Change Process by Natural Convection-diffusion in Rectangular Enclosures*, Heat and Mass Transfer 2001, **37**, 35-42.

[84] C. A. Brebbia, W. G. Gray and G. F. Pinder, *Finite elements in Water Resources*, Proceedings of the Second International Conference on Finite Elements in Water Resources held on Imperial Collage, London, 1978.

[85] B. A. Finlayson, *Numerical Methods for Problems with Moving Front*, Ravenna Park Publishing, Seattle, 1992.

[86] R. E. Ewing and H. Wang, A Summary of Numerical Methods for Time-dependent Advection-dominated Partial Differential Equations, Journal of Computational and Applied Mathematics 2001;**128**, 423-445.

[87] R. Courant, E. Isaacson, M. Rees, *On the Solution of Nonlinear Hyperbolic Differential Equations by Finite Differences*, Communications on Pure And Applied Mathematics 1952; **V**, 243-25.

[88] A. J. Ghajar and Y. H. Zurigat, *Numerical Study of The Effect of Inlet Geometry on Stratification in Thermal Energy Storage, Numerical Heat Transfer, Part A: Applications*: An International Journal of Computation and Methodology 1991; **19**, 65-83.

[89] T. Coratekin, J. Keuk and J Ballmann, *Performance of Upwind Schemes and Turbulence Models in Hypersonic Flows*, AIAA Journal 2004; **42:5**, 945-957.

[90] Z.X. Gong and A. S. Mujumdar, *A Finite Element Model for Convection-Dominated Melting and Solidification Problems*, International Journal of Numerical Methods for Heat & Fluid Flow 1998; **8**-4, 393-408.

[91] A. N. Brooks and T. J. R. Hughes, *Streamline upwind/Petrov-Galerkin Formulations for Convection Dominated Flows with Particular Emphasis on the incompressible Navier-Stokes Equations*, Computer Methods in Applied Mechanics and Engineering 1982; **32, 1-3**, 199-159.

[92] J. Argyris, *Petrov-Galerkin Finite Element Approach to Coupled Heat and Fluid Flow*, Computer Methods in Applied Mechanics and Engineering 1992; **94-2**, 181-200.

[93] J.F. Hetu, F. Ilinca, *A Finite Element Method For Casting Simulations, Numerical Heat Transfer Part A: Applications*: An International Journal of Computation and Methodology 1999; **36:7**, 657-679.

[94] P. M. Steffler, *Upwind Basis Finite Elements for Convection-Dominated Problems*, International Journal for Numerical Methods in Fluids 1989; **9**, 385-403.

[95] P. J. Harley and A. R. Mitchell, *A Finite Element Collocation Method for the Exact Control of a Parabolic Problem*, International Journal for Numerical Methods in Engineering 1977; **11**, 345-353.

[96] Z. P. Bazant and H. Ohtsubo, *Geothermal Heat Extraction by Water Circulation Through A Large Crack in Dry Hot Rock Mass*, International Journal for Numerical and Analytical Methods in Geomechanics 1978; **2**, 317-327.

[97] D. Stromeyer, *Downward Continuation of Heat Flow Data by Means of the Least Squares Method*, Tectonophysics 1984, 103, 55-66.

[98] S. Frey, M. L. Martins-Costa and R. M. Saldanha da Gama, *Stabilized Finite Element Approximations for Heat Conduction in a 3-D Plate with Dominant Thermal Source*, Computational Mechanics 1999; **24**, 118-126.

[99] I. Harari, S. Frey and L. P. Franca, *A Note on a Recent Study of Stabilized Finite Element Computations for Heat Conduction*, Computational Mechanics 2002; **28**, 63-65.

[100] F. Ilinca and J.F. Hétu, *Galerkin Gradient Least-squares Formulations for Transient Conduction Heat Transfer*, Computer Methods in Applied Mechanics and Engineering 2002; **191**, 3073-3097.

[101] J. Donea, *Recent Advances in Computational Methods for Steady and Transient Transport Problems*, Nuclear Engineering and Design 1984; **80-2**, 141-162.

[102] B. N. Jiang, *Least-Squares Finite Element Method for Fluid Dynamics*, Computer Methods in Applied Mechanics and Engineering 1990; **81-1**, 13-37.

[103] L. L. Thompson and P. M. Pinsky, *A Galerkin Least-Squares Finite Element Method for the Two-Dimensional Helmholtz Equation*, International Journal for Numerical Methods in Engineering 1995; **38**, 371-397.

[104] R. Lin, *A Robust Finite Element Method for Singularly Perturbed Convection-Diffusion Problems*, Discrete and Continuous Dynamical Systems 2008; 496-505.

[105] V.R. Voller and C. R. Swaminathan, *Fixed grid techniques for phase change problems: a review*, International Journal for Numerical Methods in Engineering 1990; Vol. **30**, 875-898.

[106] I. D. Chivers and . Sleightholme, Introduction to Programming with Fortran, SpringerLink, Online, 2006.

[107] D. Adalsteinsson and J. A. Sethian, *The Fast Construction of Extension Velocities in Level Set methods*, Journal of Computational Physics 1999; **148**, 2-22.

[108] O. C. Zienkiewicz, R. L. Taylor and J. Z. Zhu, *The finite method: Its basis and fundamentals*, Elsevier Butterworth-Heinemann, Oxford, 2005.

[109] J. N. Reddy and D. K. Garkling, *The Finite Element Method in Heat Transfer and Fluid Dynamics*, CRC Press, Taylor & Francis Group, Boca Raton, 2010.

[110] C. A. J. Fletcher, *Computational Galerkin methods*, Springer-Verlag, California, 1984.

[111] B. A. Finlayson, *The Method of Weighted Residuals and Variational Principles*: With Application in Fluid Mechanics, Heat and Mass Transfer, Academic Press, INC., London, 1972.

[112] D. V. Hutton, *Fundamentals of finite element analysis*, McGraw-Hill, New York, 2004.

[113] K. Yamamura, T. Sekiguchi and Y. Inoue, *A Fixed-Point Homotopy Method for solving Modified Nodal Equations*, IEEE Transactions on Circuits and Systems—I: Fundamental theory and Applications 1999; **46**, No. 6.

[114] T. W. Clyne and W. Kurz, *Solute Redistribution during Solidification with Rapid Solid State Diffusion*, Metallurgical Transactions A 1981; **12-6**, 965-971.

[115] I. B. Jacques, *Predictor-Corrector Methods for parabolic Partial Differential Equations*, International Journal of Numerical Methods in Engineering 1983; **19**, 451-465.

[116] P. J. Houwen, B. P. Sommeijer and H. B. Vries, *Generalized Predictor-Corrector Methods of High Order for the Time Integration of Parabolic Differential Equations*, ZAMM Journal of Applied Mathematics and Mechanics 1986; **12**, 595-605.

[117] P. J. Houwen and B. P. Sommeijer, *Improving the Stability of Predictor-Corrector Methods by Residue Smoothing*, IMA Journal of Numerical analysis 1990; **9**, 361-378.

[118] R. Codina and A. Folch, *A Stabilized Finite Element Predictor-Corrector Scheme for the Incompressible Navier-Stokes Equations Using a Nodal-Based Implementation*, International Journal for Numerical Methods in Fluids 2004; **44**, 483-503.

[119] P. M. Gresho, R. L. Lee, S. T. Chan and R. L. Sani, *Solution of The Time-Dependent Incompressible Navier-Stokes and Boussinesq Equations Using the Galerkin Finite Element Method*, Lecture Notes in Mathematics 1980; **771**, 203-222.

[120] S. J. Liao, *The proposed homotopy analysis technique for the solution of nonlinear problems*, PhD thesis, Shanghai Jiao Tong University, Shanghai, 1992.

[121] Y. Jong and W. Kim, *A Newton-Fixed Point Homotopy Algorithm For Nonlinear Complementarity Problems With Generalized Monotonicity*, *arXiv preprint arXiv:1207.1145*, 2012.

[122] T. M. Wu, *A Study of Convergence on the Newton-Homotopy Continuation Method*, Applied Mathematics and Computation 2005; **168**, 1169-1174.

[123] N. H. A. Rahman, A. IbraHim and M. I. Jayes, *Newton Homotopy Solution for Nonlinear Equations Using Maple 14*, Journal of Science and Technology 2011; **3,** No. 2, 69-75.

[124] B. Zivkovic and I. Fujii, *An Analysis of Isothermal Phase Change of Phase Change Material Within Rectangular and Cylindrical Containers*, Solar Energy 2001; **70**, No. 1, 51-61.

[125] R. W. Lewis, K. Morgan, H. R. Thomas and K. N. Seetharamu, *The Finite Element Method in Heat Transfer Analysis*, John Wiley & Sons, Chichester, 1996.

[126] O. C. Zienkiewicz, R. L. Taylor, *The Finite Element Method, Volume 2: Solid Mechanics*, Butterworth-Heinemann, Oxford, 2000.

[127] NAG Fortran library, Mark 22, The Numerical Algorithms Group Limited, 2009.

[128] V. Voller and M. Cross, *Accurate Solution of Moving Boundary Problems Using The enthalpy method*, International Journal of Heat and Mass Transfer 1981; **24**, 545-556.

[129] M. Cross, S. Johnson and P. Chow, Mapping Enthalpy-Based Solidification Algorithm onto Vector and Parallel Architecture, Applied Mechanics and Materials 1989; **13**, 702-709.

[130] K. Davey, Private Communication, 2014.

[131] J. Donea, *Taylor-Galerkin method for convective transport problems*, International Journal of Numerical Methods in Engineering, 1984; **20**, 101-119.

[132] A. Berman, R. J. Plemmons, Nonnegative Matrices in the Mathematical Sciences, Siam, Philadelphia, 1994.

[133] A. Hadjidimos, Successive Overrelaxation (SOR) and Related Methods, Journal of Computational and Applied Mathematics 2000; **123**, 177-199.

[134] G. R. Liu and S. S. Quek, The Finite Element Method: a Practical Course, Butterworth-Heinemann, Oxford, 2003.

[135] K. Salari, P. Knup, *Code Verification by the Method of Manufactured Solutions*, Sandia Report, Sandia National Laboratories, 2000.

[136] W. R. Irving, *Continuous casting of steel*, The Institute of Materials, London, 1993.

[137] O. C. Zienkiewicz, R. L. Taylor and P. Nithiarasu, *The Finite Element Method for Fluid Dynamics Sixth Edition*, Elsevier Butterworth-Heinemann, Oxford, 2005.

[138] A. Malatip, N. Wansophark and P. Dechaumphai, *A Second-Order Time-Accurate Finite Element Method for Analysis of Conjugate Heat Transfer Between Solid and Unsteady Viscous Flow*, Journal of Machanical Science and Technology, 2009; 23, 775-789.

[139] R. Mondragon, *Non-physical Enthalpy Method For Phase Change Modelling in The Solidification Process*, University of Manchester, Manchester, 2010.

[140] https://wiki.engr.illinois.edu/download/attachments/118358041/cc.PNG.

Appendix I

(a) The analytical solution (2—7)

Considering a one-dimensional semi-infinite slab, $0 \leq x < \infty$. The material is initially all liquid with a constant temperature $T_{init} > T_{sol}$, where T_{sol} is the solidus temperature. At $x = 0$, Newton's Law of cooling is applied, i.e. $k_s \partial T/\partial x = h_c(T - T_{amb})$, where h_c is the forced convective heat transfer coefficient, T is the surface temperature, and T_{amb} is the ambient temperature. The density of the model is assumed to be constant. The parameters c and k denote the capacitance and thermal conductivity respectively, and the sub-script s and l refer to the solid phase and liquid phase respectively.

The problem is governed by the first law of thermodynamics. The governing equation is a parabolic PDE which is applied in different phases as

$$\frac{\partial T}{\partial t} = \alpha_s \frac{\partial^2 T}{\partial x^2} \qquad if \quad 0 \leq x < X_i(t) \tag{I—1}$$

for the solid phase,

$$\frac{\partial T}{\partial t} = \alpha_l \frac{\partial^2 T}{\partial x^2} \qquad if \quad x > X_i(t) \tag{I—2}$$

for the liquid phase, where $\alpha_s = k_s/(\rho_s c_s)$ and $\alpha_l = k_l/(\rho_l c_l)$ are the thermal diffusivity of solid phase and liquid phase, respectively.

The solution of equations (I—1) and (I—2) requires the boundary conditions, for which, Robin boundary conditions is applied as

$$k_s \frac{\partial T}{\partial x}\Big|_{x=0} = h_c(T(0,t) - T_{amb}) \quad when \;\; x = 0, \; t > 0 \tag{I—3a}$$

This is a phase change problem. The moving front is governed by the Stefan condition, which is

$$L \frac{dX_i(t)}{dt} = -k_s \frac{\partial T(X_i(t),t)}{\partial x} + k_l \frac{\partial T(X_i(t),t)}{\partial x} \tag{I—3b}$$

where L is the latent heat of fusion, and $X_i(t)$ is the phase interface position.

Its relative boundary condition of the phase interface is

$$T((X_i(t),t) = T_{sol} \qquad when \quad x = X_i(t), t > 0 \tag{I—3c}$$

Moreover, since this is a transient state problem, the initial condition as shown in equation (3—5d) is needed to initiate the problem.

$$T(x,t) = T_{init} \qquad when \quad x > 0, t = 0 \tag{I—3d}$$

In equations (I—1) and (I—2), it can be observed that the solution T has two dependent variables, space x and time t. One approach that in sometimes useful is the substitution method which applied to the equations. Consider then the new variable $\zeta = x/\sqrt{t}$ which is chosen, so that the solution becomes $F(\xi)$ instead of $T(x,t)$. Applying chain rule to each term in equation (I—1) gives

$$\frac{\partial T}{\partial t} = \frac{\partial F}{\partial \zeta}\frac{\partial \zeta}{\partial t} = -\frac{1}{2}\frac{x}{t^{\frac{3}{2}}}\frac{dF}{d\zeta} \tag{I—4}$$

and

$$\frac{\partial^2 T}{\partial x^2} = \frac{\partial F}{\partial \zeta}\frac{\partial^2 \zeta}{\partial x^2} + \frac{\partial^2 F}{\partial \zeta^2}\left(\frac{\partial \zeta}{\partial x}\right)^2 = \frac{1}{t}\frac{d^2F}{d\zeta^2} \tag{I—5}$$

Substitution of equations (I—4) and (I—5) transforms equation (I—1) from a parabolic PDE to a second order ordinary differential equation (ODE). After simplification, it gives

$$-\frac{1}{2}\zeta\frac{dF}{d\zeta} = \alpha_s\frac{d^2F}{d\zeta^2} \tag{I—6}$$

which is evidently dependent on the single variable ζ.

The substitution method is applied again by letting $\theta = \frac{dF}{d\zeta}$, then equation (I—6) becomes a 1st order ODE, which is

$$-\frac{1}{2}\zeta\theta = \alpha_s\frac{d\theta}{d\zeta} \tag{I—7}$$

Integration of equation (I—7) with respect to ζ gives

$$\frac{dF}{d\zeta} = \theta = e^{C_1}e^{-\frac{1\zeta^2}{4\alpha_s}} = Be^{-\frac{1\zeta^2}{4\alpha_s}} \tag{I—8}$$

Integration of equation (I—8) with respect to ζ again gives the general solution $F(\zeta)$, which is

$$F(\zeta) = B\int^{\zeta} e^{-\frac{1\zeta^2}{4\alpha_s}} d\zeta + C = B\sqrt{\pi\alpha_s}\,\boldsymbol{erf}\left(\frac{\zeta}{2\sqrt{\alpha_s}}\right) + C \qquad \text{(I—9)}$$

where B and C are constant values, and $\boldsymbol{erf}(x) = \left(2/\sqrt{\pi}\right)\int^{x} e^{-\tau^2} d\tau$ is the error function. Applying boundary condition (I—3a) to equation (I—9), the exact solution for $F(\zeta)$ is calculated as

$$F(\zeta) = \left(\frac{T_{sol}-T_{amb}}{1+h_c\sqrt{\pi\alpha_s t}\,\boldsymbol{erf}\left(\frac{X_i(t)}{2\sqrt{\alpha_s t}}\right)}\right)\sqrt{\pi\alpha_s t}\,\boldsymbol{erf}\left(\frac{\zeta}{2\sqrt{\alpha_s}}\right) + \frac{T_{sol}+T_{amb}h_c\sqrt{\pi\alpha_s t}\boldsymbol{erf}(\frac{X_i(t)}{2\sqrt{\alpha_s t}})}{1+h_c\sqrt{\pi\alpha_s t}\boldsymbol{erf}(\frac{X_i(t)}{2\sqrt{\alpha_s t}})} \qquad \text{(I—10)}$$

Substituting the replacement $\zeta = x/\sqrt{t}$ back to equation (I—10), the exact solution of the temperature in the solid phase is

$$T(x,t) = \left(\frac{T_{sol}-T_{amb}}{\frac{1}{h_c\sqrt{\pi\alpha_s t}}+\boldsymbol{erf}(\frac{X_i(t)}{2\sqrt{\alpha_s t}})}\right)\boldsymbol{erf}\left(\frac{x}{2\sqrt{\alpha_s t}}\right) + \frac{T_{sol}+T_{amb}h_c\sqrt{\pi\alpha_s t}\boldsymbol{erf}(\frac{X_i(t)}{2\sqrt{\alpha_s t}})}{1+h_c\sqrt{\pi\alpha_s t}\boldsymbol{erf}(\frac{X_i(t)}{2\sqrt{\alpha_s t}})} \qquad \text{(I—11)}$$

For the liquid region, the exact solution as shown in equation (I—11) can be found in a similar way. Thus, the solution of the phase change problem with Robin boundary condition can be written as

$$T(x,t) = \begin{cases} \left(\frac{T_{sol}-T_{amb}}{\frac{1}{h_c\sqrt{\pi\alpha_s t}}+\mathrm{erf}(\frac{X_i(t)}{2\sqrt{\alpha_s t}})}\right)\boldsymbol{erf}\left(\frac{x}{2\sqrt{\alpha_s t}}\right) + \frac{T_{sol}+T_{amb}h_c\sqrt{\pi\alpha_s t}\boldsymbol{erf}(\frac{X_i(t)}{2\sqrt{\alpha_s t}})}{1+h_c\sqrt{\pi\alpha_s t}\boldsymbol{erf}(\frac{X_i(t)}{2\sqrt{\alpha_s t}})} & (0 \le x < X_i(t)) \\ T_{init} + (T_{sol}-T_{init})\dfrac{\boldsymbol{erfc}\left(\frac{x}{2\sqrt{\alpha_l t}}\right)}{\boldsymbol{erfc}(\lambda\sqrt{\frac{\alpha_s}{\alpha_l}})} & (x > X_i(t)) \end{cases}$$

(I—12)

It can be seen in equation (I—12) that the exact solution requires the evaluation of the phase interface position which is changing with time. In order to evaluate the phase interface position, a variable $\lambda = X_i(t)/(2\sqrt{\alpha_s t})$ is introduced. The value of λ can be computed via a transcendental equation, which is established by substituting equation (I—12) into the Stefan condition. After simplification, it is written as

$$\sqrt{\pi}\lambda = -\frac{St_s}{e^{\lambda^2}\left(\frac{1}{h_c\sqrt{\pi\alpha_s t}}+\mathrm{erf}(\lambda)\right)} + \frac{St_l}{ve^{(v\lambda)^2}erfc(v\lambda)} \qquad \text{(I—13)}$$

where $St_s = c_s(T_{sol} - T_2)/L$ and $St_l = c_l(T_1 - T_{sol}/L$ are the Stefan numbers, and $v = \sqrt{\alpha_s/\alpha_l}$.

The computation of λ in the [67-68] was conducted with approximations. But the direct solution of equation (I—13) can be conducted through a good root finding method, such as the Newton's method, which is used in this project.

(b) The equation (3—5)

Equation (3—5) is obtained from equation (3—4) under standard assumed conditions of differentiation and integration. For example, the CV Ω is compact and its CS Γ is piecewise smooth. The field variables and vector fields are continuously differentiable. Equation (3—4) is repeated here for convenience and it is of the form

$$\frac{D^*}{D^*t}\int_\Omega \hat{h}\, dV = \frac{D^*}{D^*t}\int_\Omega \rho h\, dV + \int_\Gamma \rho h\left(\underline{v} - \underline{v}^*\right)\cdot \underline{n} d\Gamma = -\int_\Gamma \underline{q}\cdot \underline{n} d\Gamma + \int_\Omega \rho Q\, dV \quad \text{(I—14)}$$

Recall that the CV Ω is a time dependent region, and its motion is governed by the velocity $\underline{v}^*$. Thus, application of Reynolds transport theorem to the LHS term of equation (3—4) and the first term in the middle of equation (3—4) gives

$$\frac{D^*}{D^*t}\int_\Omega \hat{h}\, dV = \int_\Omega \left(\frac{D^*}{D^*t}\hat{h} + \hat{h}\nabla\cdot \underline{v}^*\right) dV \quad \text{(I—15)}$$

And similarly

$$\frac{D^*}{D^*t}\int_\Omega \rho h\, dV = \int_\Omega \left(\frac{D^*}{D^*t}\rho h + \rho h\nabla\cdot \underline{v}^*\right) dV \quad \text{(I—16)}$$

Then applying the divergence theorem to the boundary terms $\int_\Gamma \rho h\left(\underline{v} - \underline{v}^*\right)\cdot \underline{n} d\Gamma$ and $-\int_\Gamma \underline{q}\cdot \underline{n} d\Gamma$ gives

$$\int_\Gamma \rho h\left(\underline{v} - \underline{v}^*\right)\cdot \underline{n} d\Gamma = \int_\Omega \nabla\cdot\left(\rho h\left(\underline{v} - \underline{v}^*\right)\right) dV \quad \text{(I—17)}$$

and

$$-\int_\Gamma \underline{q}\cdot \underline{n} d\Gamma = -\int_\Omega \nabla\cdot \underline{q}\, dV \quad \text{(I—18)}$$

The substitution of equations (I—15), (I—16), (I—17) and (I—18) into the equation (I—14), which is equation (3—4) in the chapter 3, gives

$$\int_\Omega \frac{D^*}{D^*t}\hat{h} + \hat{h}\nabla\cdot \underline{v}^* dV = \int_\Omega \frac{D^*}{D^*t}\rho h + \rho h\nabla\cdot \underline{v}^*\, dV + \int_\Omega \nabla\cdot\left(\rho h\left(\underline{v} - \underline{v}^*\right)\right) dV = -\int_\Omega \nabla\cdot \underline{q}\, dV + \int_\Omega \rho Q\, dV \quad \text{(I—19)}$$

Since the CV Ω is essentially arbitrary in shape it can be shrunk to a point to give the strong form of the equation (I—14), which is

$$\frac{D^*}{D^*t}\hat{h} + \hat{h}\nabla\cdot\underline{v}^* = \frac{D^*}{D^*t}\rho h + \rho h\nabla\cdot\underline{v}^* + \nabla\cdot\left(\rho h\left(\underline{v}-\underline{v}^*\right)\right) = -\nabla\cdot\underline{q} + \rho Q \qquad \text{(I—20)}$$

In the view of the identity $D^*/D^*t = \partial/\partial t + \underline{v}^*\cdot\nabla$, the LHS of equation (I—20) reduces to

$$\frac{D^*}{D^*t}\hat{h} + \hat{h}\nabla\cdot\underline{v}^* = \frac{\partial}{\partial t}\hat{h} + \underline{v}^*\cdot\nabla\hat{h} + \hat{h}\nabla\cdot\underline{v}^* = \frac{\partial}{\partial t}\hat{h} + \nabla\cdot\left(\hat{h}\underline{v}^*\right) \qquad \text{(I—21)}$$

The application of the product rule to the middle terms of equation (I—21) gives

$$\rho\frac{D^*h}{D^*t} + h\frac{D^*\rho}{D^*t} + \rho h\nabla\cdot\underline{v}^* + h\nabla\cdot\left(\rho\left(\underline{v}-\underline{v}^*\right)\right) + \rho\left(\underline{v}-\underline{v}^*\right)\nabla h = -\nabla\cdot\left(\underline{q}\right) + \rho Q \qquad \text{(I—22)}$$

Rearranging equation (I—22) gives

$$\frac{D^*h}{D^*t} + \rho\left(\underline{v}-\underline{v}^*\right)\nabla h + h\left(\frac{D^*\rho}{D^*t} + \rho\nabla\cdot\underline{v}^* + \nabla\cdot\left(\rho\left(\underline{v}-\underline{v}^*\right)\right)\right) = -\nabla\cdot\left(\underline{q}\right) + \rho Q \qquad \text{(I—23)}$$

In the equation (I—23), the analysis of the terms $\frac{D^*\rho}{D^*t} + \rho\nabla\cdot\underline{v}^* + \nabla\cdot\left(\rho\left(\underline{v}-\underline{v}^*\right)\right)$ can be conducted through the governing equation of the mass conservation, which is

$$\frac{D^*}{D^*t}\int_\Omega \rho dV + \int_\Gamma \rho\left(\underline{v}-\underline{v}^*\right)\cdot\underline{n}d\Gamma = 0 \qquad \text{(I—24)}$$

Similar to equation (I—14), the strong form of equation (I—24) is obtained by applying the Reynold transport theorem and the divergence theorem, which is

$$\frac{D^*\rho}{D^*t} + \rho\nabla\cdot\underline{v}^* + \nabla\cdot\left[\rho\left(\underline{v}-\underline{v}^*\right)\right] = 0 \qquad \text{(I—25)}$$

Consequently, equation (I—24) reduces to

$$\frac{D^*h}{D^*t} + \rho\left(\underline{v}-\underline{v}^*\right)\nabla h = -\nabla\cdot\left(\underline{q}\right) + \rho Q \qquad \text{(I—26)}$$

And the definition of non-physical enthalpy in the strong form is obtained by the equation of (I—21) and (I—26), which gives

$$\frac{D^*}{D^*t}\hat{h} + \hat{h}\nabla\cdot\underline{v}^* = \frac{D^*h}{D^*t} + \rho\left(\underline{v}-\underline{v}^*\right)\nabla h = -\nabla\cdot\left(\underline{q}\right) + \rho Q \qquad \text{(I—27)}$$

The equation (I—27) is the equation (3—5) in chapter 3.

(c) The weighted residual method

Many discrete methods has been developed to obtain the approximate solution of continuous problems, such as the direct continuum elements, the variational methods and the weighted residual method. From the weighted residual method, is developed the computational Galerkin methods which contains the modern finite element method [108, 110]. The weighted residual method is preferred because it is easy to apply to a great many PDEs with different boundary conditions and initial conditions, but other methods such as the variational method requires more mathematical operation but it does not apply to all problems [111]. This project uses the Galerkin weighted residual method, which fundamental theory has been described by Finlayson [111], and its examples application can be found in the books [108, 111-112].

In Chapter 3, the equation required to be solved by the Galerkin weighted residual method is

$$\frac{D^*}{D^*t}\int_\Omega \hat{h}\,dV = -\int_\Gamma \underline{q}\cdot\underline{n}d\Gamma + \int_\Omega \rho Q\,dV \qquad \text{(I—28)}$$

Assuming that the trial solution of equation (I—28) is

$$\tilde{h} = \sum_{j=1}^{NN} C_j f_j \qquad \text{(I—29)}$$

where the accent ■̃ signifies the solution is an approximation, the upper case letters NN is the number of nodes, C_j $(j = 1,2,3 \ldots NN)$ are the unknown constants and $f_j (j = 1,2,3 \ldots NN)$ are the trial solutions.

It is obvious that the trial solution $\tilde{h}$ is only approximated, and if substituting the solution $\tilde{h}$ back to (I—28), the equation (I—28) will not be satisfied, and it will generate an error or residual. And the residual R is defined as

$$\int_\Omega R(\tilde{h})\,dV = \frac{D^*}{D^*t}\int_\Omega \tilde{h}\,dV + \int_\Gamma \underline{q}(\tilde{h})\cdot\underline{n}d\Gamma - \int_\Omega \rho Q(\tilde{h})\,dV \qquad \text{(I—30)}$$

where the flux $\underline{q}(\tilde{h})$ and the specific heat source $Q(\tilde{h})$ may be indirectly dependent on $\tilde{h}$ through temperature.

Observing equation (I—30), it is sensible that once the residual $R(\tilde{h}) \equiv 0$, the trial solution approaches the exact solution of equation (I—29). To achieve this, the inner product of the residual $R(\tilde{h})$ and the weighting functions W has to be zero, say

$$\int_\Omega WR(\tilde{h})\,dV = 0 \qquad \text{(I—31)}$$

The expansion of equation (I—31) gives

$$\int_\Omega WR(\tilde{h})dV = \frac{D^*}{D^*t}\int_\Omega W\tilde{h}\,dV + \int_\Gamma W\underline{q}\cdot\underline{n}d\Gamma - \int_\Omega \underline{q}\cdot\nabla W dV - \int_\Omega W\rho Q\,dV = 0 \qquad \text{(I—32)}$$

which is equation (3—30) in chapter 3. Both the terms $\int_\Gamma W\underline{q}\cdot\underline{n}d\Gamma$ and $\int_\Omega \underline{q}\cdot\nabla W dV$ are come from $-\int_\Gamma \underline{q}\cdot\underline{n}dA$ by the product rule of differentiation and the divergence therom, i.e. $\int_\Gamma W\underline{q}\cdot\underline{n}d\Gamma = \int_\Omega W\nabla\cdot\underline{q}dV + \int_\Omega \underline{q}\cdot\nabla W dV$.

The set of W and the $R(\tilde{h})$ is required to be orthogonal so that the residual can approaches to zero in the mean. The weighting functions and the trial functions can be different through different approaches. In the Galerkin weighted residual method, both the test functions and the weighting functions are set as the shape functions, thus the trial solution is

$$\tilde{h}_e = \sum_{\varsigma=1}^{NN} N_\varsigma \hat{h}_\varsigma \qquad \text{(I—33)}$$

where $\tilde{h}_e$ refers to the trial solution with respect to the element, and the upper-case letters NN refers to the local node number of the element.

And the weighting functions are

$$W_\vartheta = N_\vartheta \tag{I—34}$$

(d) The analytical evaluation of advective term (3—38)

In the numerical simulation of advection-diffusion problem, the material flowing through the element boundary can be regarded as an additional volume attached on the boundary of element. For example the volume swept by the elemental boundary with material velocity in one-dimension can be seen in Figure I.1. The swept volume is not real, but the advective term can be evaluated analytically through this volume.

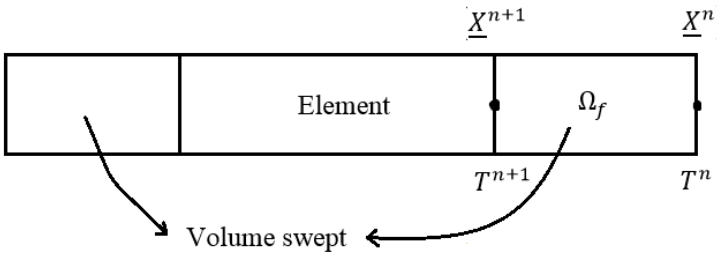

Figure I.1: The virtual CV swept by elemental CS with material velocity

Recall the equation (3—38) in Chapter 3, which is

$$\int_{t^n}^{t^{n+1}} \int_{\Gamma_e} \rho h \underline{v} \cdot \underline{n} d\Gamma \, dt = \int_{\Gamma_e} \rho h \left(\underline{X}^{n+1} - \underline{X}^{n}\right) \cdot \underline{n} \, d\Gamma \tag{I—35}$$

With the concept of swept volume, it can be approximated as

$$\int_{t^n}^{t^{n+1}} \int_{\Gamma_e} \rho h \underline{v} \cdot \underline{n} d\Gamma \, dt \approx \int_{\Omega_f} \rho h dV \tag{I—36}$$

where the volume of swept CV can be evaluated as $vol(\Omega_f) \approx A_e(X^{n+1} - X^n)$.

Assuming then the swept CV is also a one-dimensional element, whose nodal position is X^{n+1} and X^n respectively, and its nodal temperatures are T^{n+1} and T^n respectively. Then the same approach for equation (3—46) can be adopted for equation (I—36).

(e) The evaluation of jump term Equation (3—41)

The jump appeared in equation (3—41) is

$$\int_{t^n}^{t^{n+1}} \int_{\Gamma_{ie}} \rho h(\underline{v} - \underline{v}^{\times}) \cdot (-\underline{n}) d\Gamma\, dt = \int_{t^n}^{t^{n+1}} \int_{\Gamma_i^e} \rho_s h_s (\underline{v}_s - \underline{v}^{\times}) \cdot \underline{n}_l - \rho_l h_l (\underline{v}_l - \underline{v}^{\times}) \cdot \underline{n}_l d\Gamma\, dt \quad \text{(I—37)}$$

The equation (I—37) is written according to equations (3—11a) and (3—12) in section 3.2. Then, breaking the brackets in the integral gives

$$\int_{t^n}^{t^{n+1}} \int_{\Gamma_i^e} \rho_s h_s (\underline{v}_s - \underline{v}^{\times}) \cdot \underline{n}_l - \rho_l h_l (\underline{v}_l - \underline{v}^{\times}) \cdot \underline{n}_l d\Gamma\, dt = \int_{t^n}^{t^{n+1}} \int_{\Gamma_i^e} \rho_s h_s \underline{v}_s \cdot \underline{n}_l - \rho_s h_s \underline{v}^{\times} \cdot \underline{n}_l - \rho_l h_l \underline{v}_l \cdot \underline{n}_l + \rho_l h_l \underline{v}^{\times} \cdot \underline{n}_l d\Gamma\, dt \quad \text{(I—38)}$$

Furthermore, rearranging equation (I—38) and the application of linear combination gives

$$\int_{t^n}^{t^{n+1}} \int_{\Gamma_i^e} \rho_s h_s \underline{v}_s \cdot \underline{n}_l - \rho_s h_s \underline{v}^{\times} \cdot \underline{n}_l - \rho_l h_l \underline{v}_l \cdot \underline{n}_l + \rho_l h_l \underline{v}^{\times} \cdot \underline{n}_l d\Gamma\, dt = \int_{t^n}^{t^{n+1}} \int_{\Gamma_i^e} \rho_s h_s \underline{v}_s \cdot \underline{n}_l - \rho_l h_l \underline{v}_l \cdot \underline{n}_l d\Gamma\, dt + \int_{t^n}^{t^{n+1}} \int_{\Gamma_i^e} \rho_l h_l \underline{v}^{\times} \cdot \underline{n}_l - \rho_s h_s \underline{v}^{\times} \cdot \underline{n}_l d\Gamma\, dt \quad \text{(I—39)}$$

Rearranging equation (I—39) gives

$$\int_{t^n}^{t^{n+1}} \int_{\Gamma_i^e} \rho_s h_s \underline{v}_s \cdot \underline{n}_l - \rho_l h_l \underline{v}_l \cdot \underline{n}_l d\Gamma\, dt + \int_{t^n}^{t^{n+1}} \int_{\Gamma_i^e} \rho_l h_l \underline{v}^{\times} \cdot \underline{n}_l - \rho_s h_s \underline{v}^{\times} \cdot \underline{n}_l d\Gamma\, dt = \int_{t^n}^{t^{n+1}} \int_{\Gamma_i^e} (\rho_s h_s \underline{v}_s - \rho_l h_l \underline{v}_l) \cdot \underline{n}_l d\Gamma\, dt + \int_{t^n}^{t^{n+1}} \int_{\Gamma_i^e} (\rho_l h_l - \rho_s h_s) \underline{v}^{\times} \cdot \underline{n}_l d\Gamma\, dt \quad \text{(I—40)}$$

From equation (I—37) to equation (I—40) are applicable based on the assumption that the integral is Riemann integrable on the surface Γ_i^e. Assuming that $\rho_s \underline{v}_s = \rho_l \underline{v}_l$ as the amount of liquid swept by the surface Γ_i^e becomes the same amount of solid in mass. Thus, the first term on the RHS of equation (I—40) gives

$$\int_{t^n}^{t^{n+1}} \int_{\Gamma_i^e} (\rho_s h_s \underline{v}_s - \rho_l h_l \underline{v}_l) \cdot \underline{n}_l d\Gamma\, dt = \int_{t^n}^{t^{n+1}} \int_{\Gamma_i^e} \rho_l (h_s - h_l) \underline{v}_l \cdot \underline{n}_l d\Gamma\, dt \quad \text{(I—41)}$$

(f) The analytical evaluation of equation (3—51)

The evaluation of enthalpy in an element is conducted via equation (3—46), which is

$$\int_{\Omega_e} \rho^n h^n\, dV = \int_{\Omega_e} \Upsilon_s{}^n \rho_s h_{sol}\, dV + \int_{\Omega_e} \Upsilon_s{}^n \rho_s \int_{T_{sol}}^{T^n} c_s(T') dT'\, dV + \int_{\Omega_e} \Upsilon_l{}^n \rho_l h_{sol} dV + \int_{\Omega_e} \Upsilon_l{}^n \rho_l l\, dV + \int_{\Omega_e} \Upsilon_l{}^n \rho_l \int_{T_{liq}}^{T^n} c_l(T') dT' \quad \text{(I—42)}$$

It can be divided into two equations, which are

$$\int_{\Omega_s^e} \rho^n h^n \, dV = \int_{\Omega_e} {\Upsilon_s}^n \rho_s h_{sol} \, dV + \int_{\Omega_e} {\Upsilon_s}^n \rho_s \int_{T_{sol}}^{T^n} c_s(T') dT' \, dV \quad \text{(I—43a)}$$

and

$$\int_{\Omega_l^e} \rho^n h^n \, dV = \int_{\Omega_e} {\Upsilon_l}^n \rho_l h_{sol} dV + \int_{\Omega_e} {\Upsilon_l}^n \rho_l l \, dV + \int_{\Omega_e} {\Upsilon_l}^n \rho_l \int_{T_{liq}}^{T^n} c_l(T') dT' \quad \text{(I—43b)}$$

respectively.

Equation (I—43a) evaluates the enthalpy of solid in the element, and equation (I—43b) evaluates the enthalpy of liquid in the same element.

Assuming that the thermoproperties of material (i.e. ρ_s, ρ_l, c_s, c_l and L) are constants, the first term on the RHS of equation (I—43a) gives

$$\int_{\Omega_e} {\Upsilon_s}^n \rho_s h_{sol} \, dV = \int_{\Omega_s^e} \rho_s h_{sol} \, dV \approx \rho_s V_s^n h_{sol} = M_s^n h_{sol} \quad \text{(I—44)}$$

where M_s^n is the mass of solid in the element. The volume of solid $V_s^n = \Upsilon_s^n V_e$, and the volume of element is the product of cross-sectional area A_e and the length of one-dimensional element L_e, i.e. $V_e = A_e L_e$. The phase change enthalpy $h_{sol} = c_s T_{sol}$ is constant.

The temperature T appearing in the second term on the RHS of equation (I—43a) requires integration. Since all material properties are constant, it gives

$$\int_{\Omega_e} {\Upsilon_s}^n \rho_s \int_{T_{sol}}^{T^n} c_s(T') dT' \, dV = \int_{\Omega_s^e} \rho_s c_s (T^n - T_{sol}) \, dV \quad \text{(I—45)}$$

Substitution of $T^n = \frac{1-\xi}{2} {T_1}^n + \frac{1+\xi}{2} {T_2}^n$ into equation (I—45) gives

$$\int_{\Omega_s^e} \rho_s c_s (T^n - T_{sol}) \, dV = \int_{\Omega_s^e} \rho_s c_s \left(\frac{1-\xi}{2} {T_1}^n + \frac{1+\xi}{2} {T_2}^n - T_{sol}\right) dV \quad \text{(I—46)}$$

In Figure 3.6, it can be seen that, for the solid elemental domain Ω_s^e, the integration through ξ is only conducted from -1 to $2 \times {\Upsilon_s}^n - 1$, thus

$$\int_{\Omega_s^e} \rho_s c_s \left(\frac{1-\xi}{2} {T_1}^n + \frac{1+\xi}{2} {T_2}^n - T_{sol}\right) dV \approx \rho_s c_s \frac{A_e L_e}{2} \int_{-1}^{2\times {\Upsilon_s}^n - 1} \frac{1-\xi}{2} {T_1}^n + \frac{1+\xi}{2} {T_2}^n - T_{sol} d\xi =$$

$$\rho_s c_s \frac{A_e L_e}{2} \left(\frac{\xi - \frac{\xi^2}{2}}{2} {T_1}^n + \frac{\xi + \frac{\xi^2}{2}}{2} {T_2}^n - \xi T_{sol} \right) \Bigg|_{-1}^{2\times {g_s}^n - 1} = \rho_s c_s \frac{A_e L_e}{2} {\Upsilon_s}^n [2{T_1}^n - 2T_{sol} +$$

$${\Upsilon_s}^n ({T_2}^n - {T_1}^n)] \quad \text{(I—47)}$$

Furthermore, the evaluation of equation (I—43b) follows the same approach adopted for equation (I—43a). For the first term on the RHS of equation (I—43b)

$$\int_{\Omega_e} \Upsilon_l^{\,n} \rho_l h_{sol}\, dV = \int_{\Omega_l^e} \rho_l h_{sol}\, dV \approx \rho_l V_l^n h_{sol} = M_l^n h_{sol} \tag{I—48}$$

where M_l^n is the mass of liquid in the element. The volume of solid $V_l^n = \Upsilon_l^n V_e$.

Similarly, the second term on RHS of equation (I—43b) is

$$\int_{\Omega_e} \Upsilon_l^{\,n} \rho_l L\, dV = \int_{\Omega_l^e} \rho_l L\, dV \approx \rho_l V_l^n L = M_l^n L \tag{I—49}$$

Substitution of $T^n = \frac{1-\xi}{2} T_1^{\,n} + \frac{1+\xi}{2} T_2^{\,n}$ into the third term on the RHS of equation (I—43b) gives

$$\int_{\Omega_e} \Upsilon_l^{\,n} \rho_l \int_{T_{liq}}^{T^n} c_l(T')dT' = \int_{\Omega_l^e} \rho_l c_l \left(\frac{1-\xi}{2} T_1^{\,n} + \frac{1+\xi}{2} T_2^{\,n} - T_{liq}\right) dV \tag{I—50}$$

With the identity $\Upsilon_s + \Upsilon_l = 1$ for isothermal solidification, the integration for liquid domain through ξ is only conducted from $2 \times \Upsilon_s^n - 1$ to 1, consequently

$$\int_{\Omega_l^e} \rho_l c_l \left(\frac{1-\xi}{2} T_1^{\,n} + \frac{1+\xi}{2} T_2^{\,n} - T_{liq}\right) dV \approx \rho_l c_l \frac{A_e L_e}{2} \int_{2\times\Upsilon_s^{\,n}-1}^{1} \frac{1-\xi}{2} T_1^{\,n} + \frac{1+\xi}{2} T_2^{\,n} - T_{liq} d\xi =$$
$$\rho_l c_l \frac{A_e L_e}{2} (1 - \Upsilon_s^{\,n})[T_1^{\,n} + T_2^{\,n} - 2T_{sol} + \Upsilon_s^{\,n}(T_2^{\,n} - T_1^{\,n})] \tag{I—51}$$

For isothermal solidification, $T_{liq} = T_{sol}$, and total mass of element $M_e^n = M_s^n + M_l^n$. Substitution of equations (I—44), (I—47), (I—48), (I—49) and (I—51) into equation (I—42) gives

$$\int_{\Omega_e} \rho^n h^n\, dV \approx M_e^n h_{sol} + \rho_s c_s \frac{A_e L_e}{2} \Upsilon_s^{\,n} [2T_1^{\,n} - 2T_{sol} + \Upsilon_s^{\,n}(T_2^{\,n} - T_1^{\,n})] + M_l^n L +$$
$$\rho_l c_l \frac{A_e L_e}{2} (1 - \Upsilon_s^{\,n})[T_1^{\,n} + T_2^{\,n} - 2T_{sol} + \Upsilon_s^{\,n}(T_2^{\,n} - T_1^{\,n})] \tag{I—52}$$

Finally, the equation (3—51) is obtained.

(g) Equation (5—12)

Equation (5—12) is obtained from equation (5—11). Suppose that the term $\hat{h}'$, the vector field $\underline{v}^+$ are continuously differentiable on CS Γ_i. Also, the jump terms $\left]\rho h\left(\underline{v} - \underline{v}^+\right) \cdot \underline{n}\right[$, $\left]\hat{h}\left(\underline{v} - \underline{v}^+\right) \cdot \underline{n}\right[$ and $\left]\underline{q} \cdot \underline{n}\right[$ are assumed to be constant on CS Γ_i. Equation (5—11) is repeated here for convenience and is of the form

$$\frac{D^+}{D^+t}\int_{\Gamma_i}\hat{h}'d\Gamma+\int_{\Sigma_i}\hat{h}'(\underline{v}^*-\underline{v}^+)\cdot\underline{t}\underline{n}d\Sigma-\int_{\Gamma_i}]\hat{h}\underline{v}\cdot\underline{n}[d\Gamma+\int_{\Gamma_i}\hat{Q}'dA=-\int_{\Gamma_i}]\rho h(\underline{v}-\underline{v}^+)\cdot$$

$$\underline{n}[d\Gamma=\int_{\Gamma_i}]\underline{q}\cdot\underline{n}[\,d\Gamma \qquad \text{(I—53)}$$

Thus, application of Reynolds transport theorem to the LHS term of equation (I—53) gives

$$\frac{D^+}{D^+t}\int_{\Gamma_i}\hat{h}'d\Gamma=\int_{\Gamma_i}\left(\frac{D^+}{D^+t}\hat{h}'+\hat{h}'\nabla\cdot\underline{v}^+\right)dV \qquad \text{(I—54)}$$

Then applying the divergence theorem to the boundary term $\int_{\Sigma_i}\hat{h}'(\underline{v}^*-\underline{v}^+)\cdot\underline{t}\underline{n}d\Sigma$ gives

$$\int_{\Sigma_i}\hat{h}'(\underline{v}^*-\underline{v}^+)\cdot\underline{t}\underline{n}d\Sigma=\int_{\Gamma_i}\left(\nabla_{\Gamma_i}\cdot\left(\hat{h}'(\underline{v}^*-\underline{v}^+)_T\right)\right)d\Gamma \qquad \text{(I—55)}$$

where the subscript Γ_i of divergence ∇_{Γ_i} refers to the tangent plane of Γ_i, and the $\underline{v}_T{}^+$ indicates that the CS Γ_i expands or shrinks in the tangent direction.

The substitution of equations (I—32) and (I—33) into the equation (I—31) gives

$$\int_{\Gamma_i}\left(\frac{D^+}{D^+t}\hat{h}'+\hat{h}'\nabla\cdot\underline{v}^+\right)d\Gamma-\int_{\Gamma_i}\left(\nabla_{\Gamma_i}\cdot\left(\hat{h}'(\underline{v}^*-\underline{v}^+)_T\right)\right)d\Gamma-\int_{\Gamma_i}]\hat{h}\underline{v}\cdot\underline{n}[d\Gamma+\int_{\Gamma_i}\hat{Q}'d\Gamma=$$

$$-\int_{\Gamma_i}]\rho h(\underline{v}-\underline{v}^+)\cdot\underline{n}[d\Gamma=\int_{\Gamma_i}]\underline{q}\cdot\underline{n}[\,d\Gamma \qquad \text{(I—56)}$$

Since the CS Γ_i is essentially arbitrary in shape it can be shrunk to a point to give the strong form of the equation (I—31), which is

$$\frac{D^+}{D^+t}\hat{h}'+\hat{h}'\nabla\cdot\underline{v}^+\nabla_{\Gamma_i}\cdot\left(\hat{h}'(\underline{v}^*-\underline{v}^+)_T\right)-]\hat{h}\underline{v}\cdot\underline{n}[+\hat{Q}'=-]\rho h(\underline{v}-\underline{v}^+)\cdot\underline{n}[=]\underline{q}\cdot\underline{n}[$$

(I—57)

Equation (I—57) is equation (5—12) in chapter 5.

(h) Consideration on the term $\lim_{vol(\Omega_i)\to 0}\int_{\Omega_i}\underline{q}\cdot\nabla W\,dV$

The extended divergence theorem is of the form

$$\int_{\Omega\setminus\Gamma_i}\nabla\cdot\left(W\cdot\underline{q}\right)dV=\int_{\Gamma}\ W\underline{q}\cdot\underline{n}d\Gamma-\int_{\Gamma_i}]W\underline{q}\cdot\underline{n}[\,d\Gamma \qquad \text{(I—58)}$$

which provides an extended Green's first theorem

$$\int_{\Omega\setminus\Gamma_i}\nabla\mathrm{W}\cdot\underline{q}dV=\int_{\Gamma}\ W\underline{q}\cdot\underline{n}d\Gamma-\int_{\Gamma_i}]W\underline{q}\cdot\underline{n}[\,d\Gamma-\int_{\Omega\setminus\Gamma_i}\mathrm{W}\nabla\cdot\underline{q}dV \qquad \text{(I—59)}$$

Moreover it is a simple matter to show with $\nabla\cdot\underline{q}$ taking the form of a distribution at Γ_i that

$$\int_{\Omega}\ \mathrm{W}\nabla\cdot\underline{q}dV=\int_{\Omega\setminus\Gamma_i}\mathrm{W}\nabla\cdot\underline{q}dV+\int_{\Gamma_i}]W\underline{q}\cdot\underline{n}[\,d\Gamma \qquad \text{(I—60)}$$

which on substitution into equation (I—59) gives

$$\int_{\Omega\setminus\Gamma_i} \nabla \mathrm{W}\cdot \underline{q} dV = \int_{\Gamma}\ W\underline{q}\cdot\underline{n} d\Gamma - \int_{\Omega}\ \mathrm{W}\nabla\cdot\underline{q} dV \qquad \text{(I—61)}$$

It is of interest to observe that Γ_i is excluded from the left hand side of equation (I—61) but not from the right hand side. It is apparent from the non-physical theory and equation (5—26) that $\lim_{vol(\Omega_i)\to 0}\int_{\Omega_i}\underline{q}\cdot\nabla W\, dV$ takes on a finite value which suggests that (I—61) takes the form

$$\int_{\Omega}\ \nabla \mathrm{W}\cdot\underline{q}\, dV - \lim_{vol(\Omega_i)\to 0}\int_{\Omega_i}\underline{q}\cdot\nabla W\, dV = \int_{\Gamma}\ W\underline{q}\cdot\underline{n} d\Gamma - \int_{\Omega}\ \mathrm{W}\nabla\cdot\underline{q} dV \qquad \text{(I—62)}$$

or equivalently

$$-\int_{\Gamma}\ W\underline{q}\cdot\underline{n} d\Gamma + \int_{\Omega}\ \mathrm{W}\nabla\cdot\underline{q} dV = \lim_{vol(\Omega_i)\to 0}\int_{\Omega_i}\underline{q}\cdot\nabla W\, dV - \int_{\Omega\setminus\Gamma_i}\mathrm{W}\nabla\cdot\underline{q} dV - \int_{\Gamma_i}\left]W\underline{q}\cdot\underline{n}\right[d\Gamma \qquad \text{(I—63)}$$

It is evident that the weighting of transport equation (5—1) to arrive at equation (5—19) has some unintended consequences since $-\int_{\Gamma}\ W\underline{q}\cdot\underline{n} d\Gamma + \int_{\Omega}\ \underline{q}\cdot\nabla W dV$ does not equal $-\int_{\Omega\setminus\Gamma_i}\nabla \mathrm{W}\cdot\underline{q} dV$ but in fact gives rise to two additional terms, i.e. a source term $\lim_{vol(\Omega_i)\to 0}\int_{\Omega_i}\underline{q}\cdot\nabla W\, dV$ and a jump term $\int_{\Gamma_i}\left]W\underline{q}\cdot\underline{n}\right[d\Gamma$.

(i) Derivation of equation (5—32)

The CV Ω is time dependent and is transported with the velocity $\underline{v}^*$, application of Reynold transport theorem to the weighted term $(D^*/D^*t)\int_{\Omega}\ W\hat{h} dV$ gives

$$\frac{D^*}{D^*t}\int_{\Omega}\ W\hat{h} dV = \int_{\Omega}\ \frac{D^*}{D^*t}W\hat{h} + W\hat{h}\nabla\cdot\underline{v}^* dV \qquad \text{(I—64)}$$

According to the theorem of product rule on differentiation, equation (I—64) can be expanded as

$$\frac{D^*}{D^*t}\int_{\Omega}\ W\hat{h} dV = \int_{\Omega}\ W\frac{D^*}{D^*t}\hat{h} + \hat{h}\frac{D^*}{D^*t}W + W\hat{h}\nabla\cdot\underline{v}^* dV \qquad \text{(I—65)}$$

Assuming that, the CV Ω is compact and its CS Γ is piecewise smooth. Application of Divergence theorem to the RHS of equation (I—65) gives

$$\frac{D^*}{D^*t}\int_{\Omega}\ W\hat{h} dV = \int_{\Omega}\ W\frac{\partial}{\partial t}\hat{h} + W\underline{v}^*\cdot\nabla\hat{h} + \hat{h}\frac{D^*}{D^*t}W + W\hat{h}\nabla\cdot\underline{v}^* dV \qquad \text{(I—66)}$$

Re-arrangement of equation (I—66) gives

$$\frac{D^*}{D^*t}\int_\Omega W\hat{h}dV = \int_\Omega W\frac{\partial}{\partial t}\hat{h}\,dV + \int_\Omega \left(\frac{D^*W}{D^*t}\right)\hat{h}dV + \int_\Omega W\nabla\cdot\left(\hat{h}\underline{v}^*\right)dV \quad \text{(I—67)}$$

According to the theorem of product rule on differentiation and the divergence theorem again, equation (I—67) becomes

$$\frac{D^*}{D^*t}\int_\Omega W\hat{h}dV = \int_\Omega W\frac{\partial}{\partial t}\hat{h}\,dV + \int_\Omega \left(\frac{D^*W}{D^*t}\right)\hat{h}dV + \int_\Gamma W\hat{h}\underline{v}^*\cdot\underline{n}dV - \int_\Omega \hat{h}\underline{v}^*\nabla\cdot W dV \quad \text{(I—68)}$$

Similarly, for the CV Ω^+, the term $(D^+/D^+t)\int_{\Omega^+} W\hat{h}dV$ can be expanded as

$$\frac{D^+}{D^+t}\int_{\Omega^+} W\hat{h}dV = \int_{\Omega^+} W\frac{\partial}{\partial t}\hat{h}\,dV + \int_{\Omega^+}\left(\frac{D^+W}{D^+t}\right)\hat{h}dV + \int_{\Gamma^+} W\hat{h}\underline{v}^+\cdot\underline{n}dV - \int_{\Omega^+}\hat{h}\underline{v}^+\nabla\cdot W dV \quad \text{(I—69)}$$

Despite the transport of two domains, the following identity is always true, which is

$$\int_\Omega W\frac{\partial}{\partial t}\hat{h}\,dV = \int_{\Omega^+} W\frac{\partial}{\partial t}\hat{h}\,dV \quad \text{(I—70)}$$

Substitution of equations (I—68) and (I—69) into equation (I—70) returns

$$\frac{D^*}{D^*t}\int_\Omega W\hat{h}dV - \int_\Omega\left(\frac{D^*W}{D^*t}\right)\hat{h}dV - \int_\Gamma W\hat{h}\underline{v}^*\cdot\underline{n}dV + \int_\Omega \hat{h}\underline{v}^*\nabla\cdot W dV = \frac{D^+}{D^+t}\int_{\Omega^+} W\hat{h}dV - \int_{\Omega^+}\left(\frac{D^+W}{D^+t}\right)\hat{h}dV - \int_{\Gamma^+} W\hat{h}\underline{v}^+\cdot\underline{n}dV + \int_{\Omega^+}\hat{h}\underline{v}^+\nabla\cdot W dV \quad \text{(I—71)}$$

Thus, equation (5—32) in Chapter 5 is obtained, which is the same as equation (I—71).

(j) The Taylor Galerkin method

The Taylor-series expansion can be expressed as

$$T^{n+1} \approx T^n + \frac{\Delta t}{1!}\frac{\partial T^n}{\partial t} + \frac{\Delta t^2}{2!}\frac{\partial^2 T^n}{\partial t^2} \quad \text{(I—72)}$$

Thus

$$\frac{T^{n+1}-T^n}{\Delta t} \approx \frac{\partial T^n}{\partial t} + \frac{\Delta t}{2}\frac{\partial^2 T^n}{\partial t^2} \quad \text{(I—73)}$$

From the strong form of the transport equation,

$$\hat{c}\frac{\partial T^n}{\partial t} = -\hat{c}v\frac{\partial T^n}{\partial x} + k\frac{\partial^2 T^n}{\partial x^2} + \hat{Q}(T^n) \quad \text{(I—74)}$$

where v is a scalar value and $v = \underline{v} \cdot \underline{n}$.

Similarly,

$$\hat{c}\frac{\partial^2 T^n}{\partial t^2} = -\hat{c}v\frac{\partial}{\partial x}\frac{\partial T^n}{\partial t} + k\frac{\partial^2}{\partial x^2}\frac{\partial T^n}{\partial t} + \hat{Q}\left(\frac{\partial T^n}{\partial t}\right) \quad \text{(I—75)}$$

Substitution of equations (I—74) and (I—75) back to equation (I—73) gives

$$\hat{c}\frac{T^{n+1}-T^n}{\Delta t} = -\hat{c}v\frac{\partial T^n}{\partial x} + k\frac{\partial^2 T^n}{\partial x^2} + \hat{Q}(T^n) + \frac{\Delta t}{2}\left(-\hat{c}v\frac{\partial}{\partial x}\frac{\partial T^n}{\partial t} + k\frac{\partial^2}{\partial x^2}\frac{\partial T^n}{\partial t} + \hat{Q}\left(\frac{\partial T^n}{\partial t}\right)\right) \quad \text{(I—76)}$$

Then, application of forward Euler method to the temporal derivative, i.e. $\partial T^n/\partial t \approx (T^{n+1} - T^n)/\Delta t$, equation (I—54) gives

$$\hat{c}\frac{T^{n+1}-T^n}{\Delta t} = -\hat{c}v\frac{\partial T^n}{\partial x} + k\frac{\partial^2 T^n}{\partial x^2} + \hat{Q}(T^n) - \frac{\Delta t}{2}\left(-\frac{\hat{c}v}{\Delta t}\frac{\partial}{\partial x}(T^{n+1} - T^n) + \frac{k}{\Delta t}\frac{\partial^2}{\partial x^2}(T^{n+1} - T^n) + \frac{\hat{Q}(T^{n+1})-\hat{Q}(T^n)}{\Delta t}\right) \quad \text{(I—77)}$$

Rearrangement of equation (I—77) gives

$$\left(\hat{c} + \frac{\Delta t}{2}\hat{c}v\frac{\partial}{\partial x} - \frac{\Delta t}{2}k\frac{\partial^2}{\partial x^2}\right)T^{n+1} = \left(\hat{c} - \frac{\Delta t}{2}\hat{c}v\frac{\partial}{\partial x} + \frac{\Delta t}{2}k\frac{\partial^2}{\partial x^2}\right)T^n + \frac{\Delta t}{2}\hat{Q}(T^{n+1}) + \frac{\Delta t}{2}\hat{Q}(T^n) \quad \text{(I—78)}$$

Application of standard Galerkin Finite Element method to equation (I—78) gives a system of equations which are exactly the same as equation (6—2) with $\theta = \frac{1}{2}$.

(k) The matrix of advection $[K_v]_e$

In chapter 7, the matrix for advection can be constructed as

$$[K_v]_e = \hat{c}\int_0^1\int_0^{1-\eta}\{W\}:[v]([J]^T)^{-1}[D]|[J]|d\xi d\eta \quad \text{(I—79)}$$

For a two-dimensional triangular element, the Jacobian matrix can be established as

$$[J] = \begin{bmatrix} \frac{\partial((1-\xi-\eta)x_1+\xi x_2+\eta x_3)}{\partial \xi} & \frac{\partial((1-\xi-\eta)x_1+\xi x_2+\eta x_3)}{\partial} \\ \frac{\partial((1-\xi-\eta)y_1+\xi y_2+\eta y_3)}{\partial \xi} & \frac{\partial((1-\xi-\eta)y_1+\xi y_2+\eta y_3)}{\partial \eta} \end{bmatrix} = \begin{bmatrix} x_2 - x_1 & x_3 - x_1 \\ y_2 - y_1 & y_3 - y_1 \end{bmatrix} \quad \text{(I—80)}$$

Consequently, the inverse matrix of the transposed Jacobian matrix is

$$([J]^T)^{-1} = \frac{1}{|[J]^T|}\begin{bmatrix} y_3 - y_1 & y_1 - y_2 \\ x_1 - x_3 & x_2 - x_1 \end{bmatrix} \tag{I—81}$$

According to equation (7—22) in chapter 7, it is known that

$$[D] = \begin{bmatrix} \frac{\partial N_1}{\partial \xi} & \frac{\partial N_2}{\partial \xi} & \frac{\partial N_3}{\partial \xi} \\ \frac{\partial N_1}{\partial \eta} & \frac{\partial N_2}{\partial \eta} & \frac{\partial N_3}{\partial \eta} \end{bmatrix} = \begin{bmatrix} -1 & 1 & 0 \\ -1 & 0 & 1 \end{bmatrix} \tag{I—82}$$

Thus, inside the integral in equation (I—79), the terms can be evaluated as

$$[v]([J]^T)^{-1}[D]|[J]| = \begin{bmatrix} v_{xx} & 0 \\ 0 & v_{yy} \end{bmatrix}\frac{1}{|[J]^T|}\begin{bmatrix} y_3 - y_1 & y_1 - y_2 \\ x_1 - x_3 & x_2 - x_1 \end{bmatrix}\begin{bmatrix} -1 & 1 & 0 \\ -1 & 0 & 1 \end{bmatrix}|[J]| =$$

$$\begin{bmatrix} v_{xx} & 0 \\ 0 & v_{yy} \end{bmatrix}\begin{bmatrix} y_3 - y_1 & y_1 - y_2 \\ x_1 - x_3 & x_2 - x_1 \end{bmatrix}\begin{bmatrix} -1 & 1 & 0 \\ -1 & 0 & 1 \end{bmatrix} =$$

$$\begin{bmatrix} v_{xx}(y_2 - y_3) & v_{xx}(y_3 - y_1) & v_{xx}(y_1 - y_2) \\ v_{yy}(x_3 - x_2) & v_{yy}(x_1 - x_3) & v_{yy}(x_2 - x_3) \end{bmatrix} \tag{I—83}$$

Substitution of equation (I—83) into equation (I—79) gives

$$[K_v]_e = \hat{c}\int_0^1\int_0^{1-\eta}\begin{Bmatrix} 1-\xi-\eta \\ \xi \\ \eta \end{Bmatrix} : \begin{bmatrix} v_{xx}(y_2 - y_3) & v_{xx}(y_3 - y_1) & v_{xx}(y_1 - y_2) \\ v_{yy}(x_3 - x_2) & v_{yy}(x_1 - x_3) & v_{yy}(x_2 - x_3) \end{bmatrix} d\xi d\eta \tag{I—84}$$

According to the Frobenius inner product of a vector and matrix,

$$[K_v]_e =$$

$$\hat{c}v_{xx}\int_0^1\int_0^{1-\eta}\begin{bmatrix} (1-\xi-\eta)(y_2 - y_3) & (1-\xi-\eta)(y_3 - y_1) & (1-\xi-\eta)(y_1 - y_2) \\ \xi(y_2 - y_3) & \xi(y_3 - y_1) & \xi(y_1 - y_2) \\ \eta(y_2 - y_3) & \eta(y_3 - y_1) & \eta(y_3 - y_1) \end{bmatrix} d\xi d\eta +$$

$$\hat{c}v_{yy}\int_0^1\int_0^{1-\eta}\begin{bmatrix} (1-\xi-\eta)(x_3 - x_2) & (1-\xi-\eta)(x_1 - x_3) & (1-\xi-\eta)(x_2 - x_3) \\ \xi(x_3 - x_2) & \xi(x_1 - x_3) & \xi(x_2 - x_3) \\ \eta(x_3 - x_2) & \eta(x_1 - x_3) & \eta(x_2 - x_3) \end{bmatrix} d\xi d\eta =$$

$$\frac{\hat{c}v_{xx}}{6}\begin{bmatrix} y_2 - y_3 & y_3 - y_1 & y_1 - y_2 \\ y_2 - y_3 & y_3 - y_1 & y_1 - y_2 \\ y_2 - y_3 & y_3 - y_1 & y_1 - y_2 \end{bmatrix} + \frac{\hat{c}v_{yy}}{6}\begin{bmatrix} x_3 - x_2 & x_1 - x_3 & x_2 - x_1 \\ x_3 - x_2 & x_1 - x_3 & x_2 - x_1 \\ x_3 - x_2 & x_1 - x_3 & x_2 - x_1 \end{bmatrix} \tag{I—85}$$

Finally, the matrix for advection can be written as

$$[K_v]_e = [Kv]_{xx} + [Kv]_{yy} \tag{I—86}$$

(l) The evaluation of solid volume fraction for triangular element

In equations (7—47) and (7—48), the length of each face of element is required to be evaluated first, and it can be simply conducted as

$$L_1 = \sqrt{(x_3 - x_2)^2 + (y_3 - y_2)^2} \quad \text{(I—87a)}$$

$$L_2 = \sqrt{(x_3 - x_1)^2 + (y_3 - y_1)^2} \quad \text{(I—87b)}$$

$$L_3 = \sqrt{(x_2 - x_1)^2 + (y_2 - y_1)^2} \quad \text{(I—87c)}$$

the relationship between the node number and face number can be seen in Figure I.2.

Once the lengths are calculated, the angles can be evaluated as

$$\boldsymbol{sin}(\beta_1) = \sqrt{\frac{1-(L_2^2+L_3^2-L_1^2)}{(2L_2L_3)^2}} \quad \text{(I—88a)}$$

$$\boldsymbol{sin}(\beta_2) = \sqrt{\frac{1-(L_1^2+L_3^2-L_2^2)}{(2L_1L_3)^2}} \quad \text{(I—88b)}$$

$$\boldsymbol{sin}(\beta_3) = \sqrt{\frac{1-(L_1^2+L_2^2-L_3^2)}{(2L_1L_2)^2}} \quad \text{(I—88c)}$$

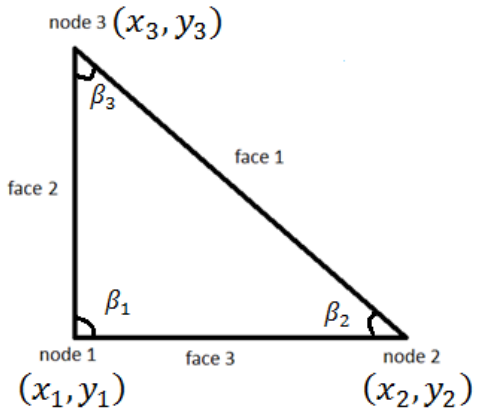

Figure I.2: the numbering of triangular element

At last, the semi-parameter of the triangle is evaluated as

$$P = \frac{1}{3}(L_1 + L_2 + L_3) \quad \text{(I—89)}$$

Appendix II The user Manual for 1D programme

II.1 The programme for one-dimensional simulation

II.1.1 end user manual

The programme for one-dimensional study is under the folder named as “Solidification_V20”. And “Solidification_V20.exe” is the executable file. In order to run this program, the file “SIM_DATA.dat” must be contained in the same folder of “Solidification_V20”. Because the file “SIM_DATA.dat” is used to give the material properties, mesh and time step to the programme. This file can be opened and edited by the Notepad in Windows operating system. The corresponding arguments in the programme, together with respect to values in the file “SIM_DATA.dat”, are displayed in the box.

!---------------------------------Format-of-SIM_DATA.dat---

cap_liq cap_sol con_liq con_sol den_liq den_sol lat_heat t_sol t_liq

total_length

NELS

no_steps

tinit

hc

material_velocity

heat_source

be_control

dtime_in

mat_form

dis_form

l_solver

t_solver

jout, cout

snode, tpri, npri

no_convergence

sigma

Pbeta

relax

!----------

where

cap_liq: specific thermal capacitance of liquid c_l $(J/kg℃)$;

cap_sol: specific thermal capacitance of solid c_s $(J/kg℃$;

con_liq: thermal conductivity of liquid k_l $(W/m℃)$;

con_sol: thermal conductivity of solid k_s $(W/m℃)$;

den_liq: density of liquid ρ_l (kg/m^3);

den_sol: density of solid ρ_s (kg/m^3);

lat_heat: Latent heat (J/kg);

t_sol: solidus temperature (℃);

t_liq: liquidus temperature (℃);

total_length: total length of the one-dimensional slab;

NELS: total number of elements;

T_init: initial temperature (℃);

T_amb: ambient temperature (℃);

h_c: forced convective coefficient (W/m^2℃);

material_velocity: material velocity (m/s);

heat_source: external heat source (J);

be_control: 1.0D0 = Neumann's boundary condition, 0.0D0 = isolation;

dtime_in: time step size (sec);

no_steps: total number of time steps;

THETA: $\theta = 1$ for implicit scheme, $\theta = 0.5$ for Crank-Nicolson scheme and $\theta = 0$ for explicit scheme;

mat_form: LUMPED/lumped = lumped capacitance, CONSIST/consist = consistent matrix;

dis_form: FUPWIND/fupwind = full upwind, PUPWIND/pupwind = Perov-Garkin method, CENTRAL/central = central difference);

SOLVER: ANATST/anatst = analytical method, SECANT/ secant = secant method, HOMOTO/homoto = homotopy method, LINEAR/linear = predictor-corrector method;

Non_Physical: CVCMO/cvcmo: the non-physical capacitance method,
CVCMV/cvcmv: the control volume capacitance method,
CVCMX/cvcmx: the weak annihilation method,
CVCMU/cvcmu: non-physical capacitance + continuous advection + non-physical source method,
CVCMQ/cvcmq: non-physical source method;

JOUT: data of time step JOUT is recorded in the file "TEST.res" for debug;

COUT: data of convergence step COUT is recorded in the file "TEST.res" for debug;

SNODE: results of node number "SNODE" is displayed on screen, also documented in the file "ERROR.csv".

TPRI: result is collected every "TPRI" time step;

NPRI: result is collected every “NPRI” node;

No_convergence: Maximum number of convergence loop is set to prevent infinite loop;

relax: relaxation factor for non-physical source method.

Note: All floats in the programme are double precision, thus the value should be given as 500.0D0, where “D0” informs the program this value is in double precision. For string argument such as “Non_Physical”, the string should be all in uppercase or in lowercase.

Other files contained in the folder “Solidification_V20” are

ALL_RESULTS.csv: this file saves the nodal temperatures with respect to time;

BETA.csv: this file saves the upwind factor β for exam;

CAPACITANCE.csv: this file saves the non-physical capacitance of element with respect to time;

CONDUCTIVITY.csv: this file saves the conductivity of element with respect to time;

ENTHALPY.csv: this file saves the nodal enthalpy with respect to time;

NON_PHYSICAL_SOURCE_TERM.csv: this file saves the non-physical source with respect to time;

TEST.res: this file saves the matrices, loading vectors, temperatures, etc. for debug.

Note: the format “*.csv” is

!----------

VALUE,VALUE, VALUE, VALUE,…

VALUE,VALUE, VALUE, VALUE,…

VALUE,VALUE, VALUE, VALUE,…

!----------

This format is readable by the package “Microsoft Excel for a quick check. It is also readable by the package “Wolfram Mathematics”, which can be used for plotting. All files have a storage limitation (1228800 bite). However, users can set “TPRI” and “NPRI” to prevent the

data overflow. The file "TEST.res" can be used to examine the assembled matrices and loading vectors, but the number of element NELS<=10 is necessary.

The execution of program "Solidification_V20.exe" requires user to specify the file name to save the example nodal profile as shown in Figure II.1. The user can give any name to it, but the string has to be no more than 10 characters long including the file extension name ".csv". This file saves the corresponding analytical solution of node "SNODE", the numerical solution of node "SNODE" and the numerical solution of node "$(\mathrm{SNODE}-1)/3*2+1$". This file helps for post-process such as plotting by Mathematica.

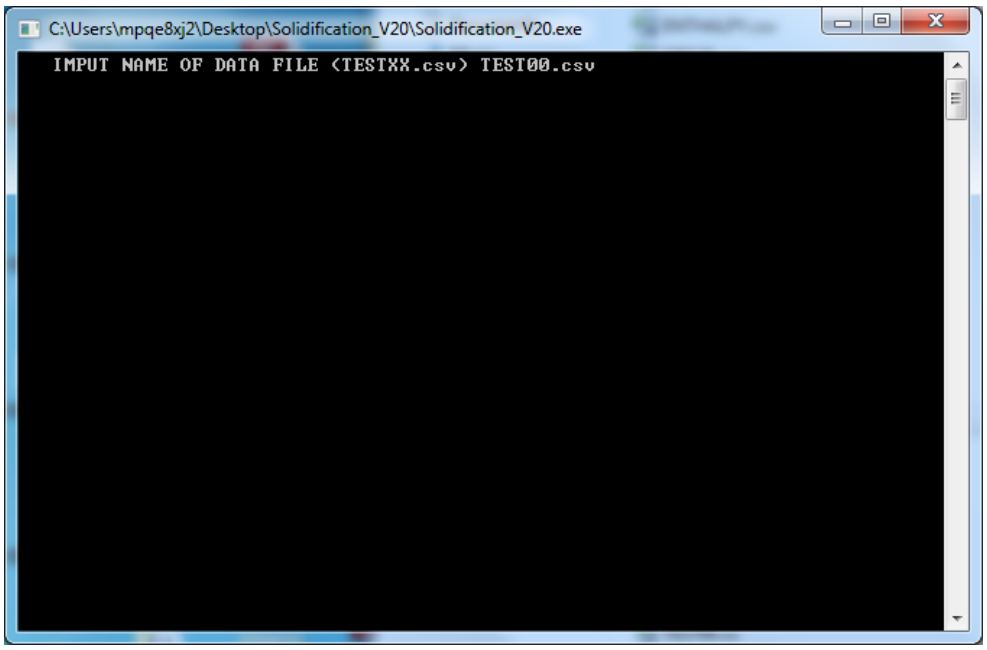

Figure II.1: The input of file name for result output

Then, the program contains several statements "PAUSE". At first "PAUSE", which is displayed in Figure II.2, users can check whether the data (i.e. material properties, mesh information and selected method etc.) is correctly assigned or not. By pressing the key "ENTER", execution continues. As program continues, Figure II.3 will display. The "TIME STEP J PASS" means that the time step "J" is successfully computed. Then the result of example node 16 (SNODE) is displayed. The information includes the numerical solution as "NUMERICAL SOLN", the corresponding analytical solution as "ANALYTICAL SOLN", the maximum error is "ERR", and the maximum percentage error is "% ERR". The argument "MAX_ERR" refers to the tolerances $|\mathrm{F}(\mathrm{T}_{k+1}^{n+1})|$ for secant method and $|\mathrm{H}(\mathrm{T}_{k+1}^{n+1},\lambda)|$ for homotopy method. Detailed information can be seen in section 5.4 of chapter 5 and section 7.4.1 of chapter 7. For predictor-corrector method, please ignore this display.

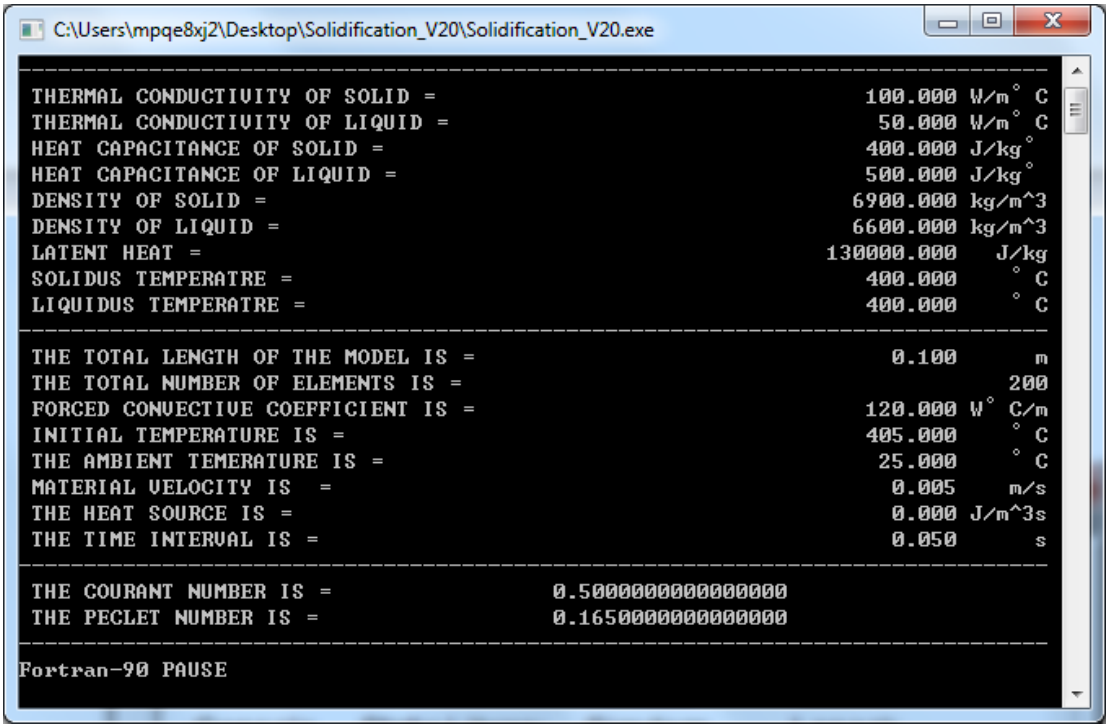

Figure II.2: Display the assigned data

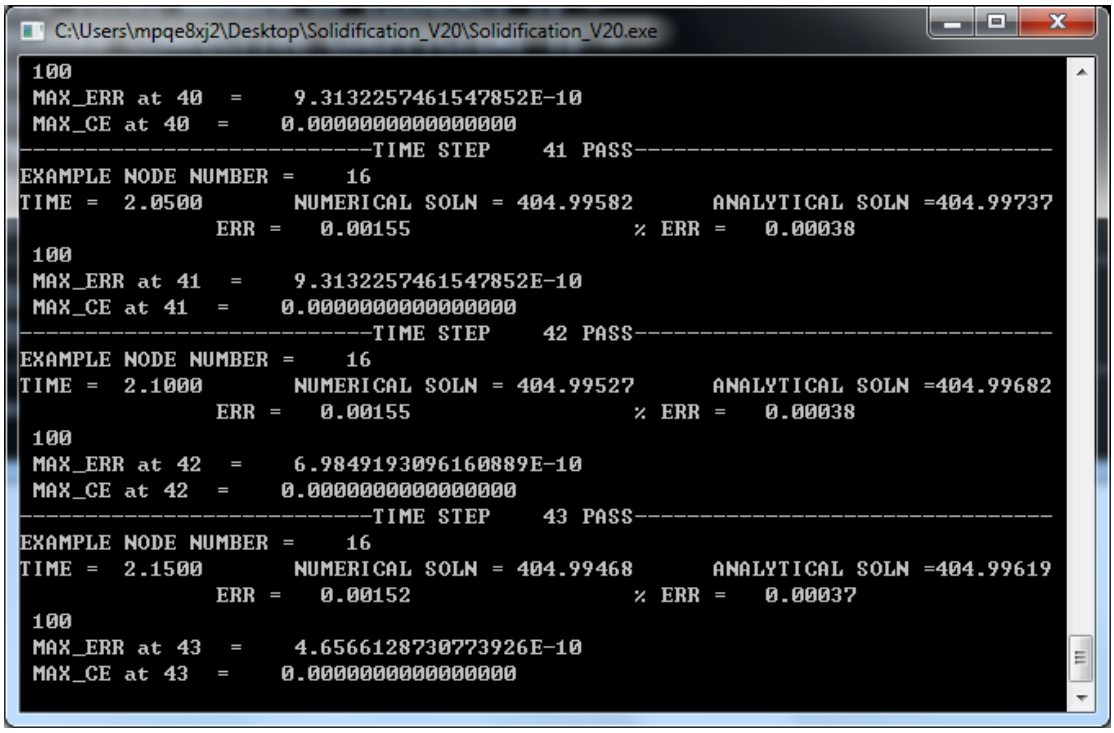

Figure II.3: Display during the solution

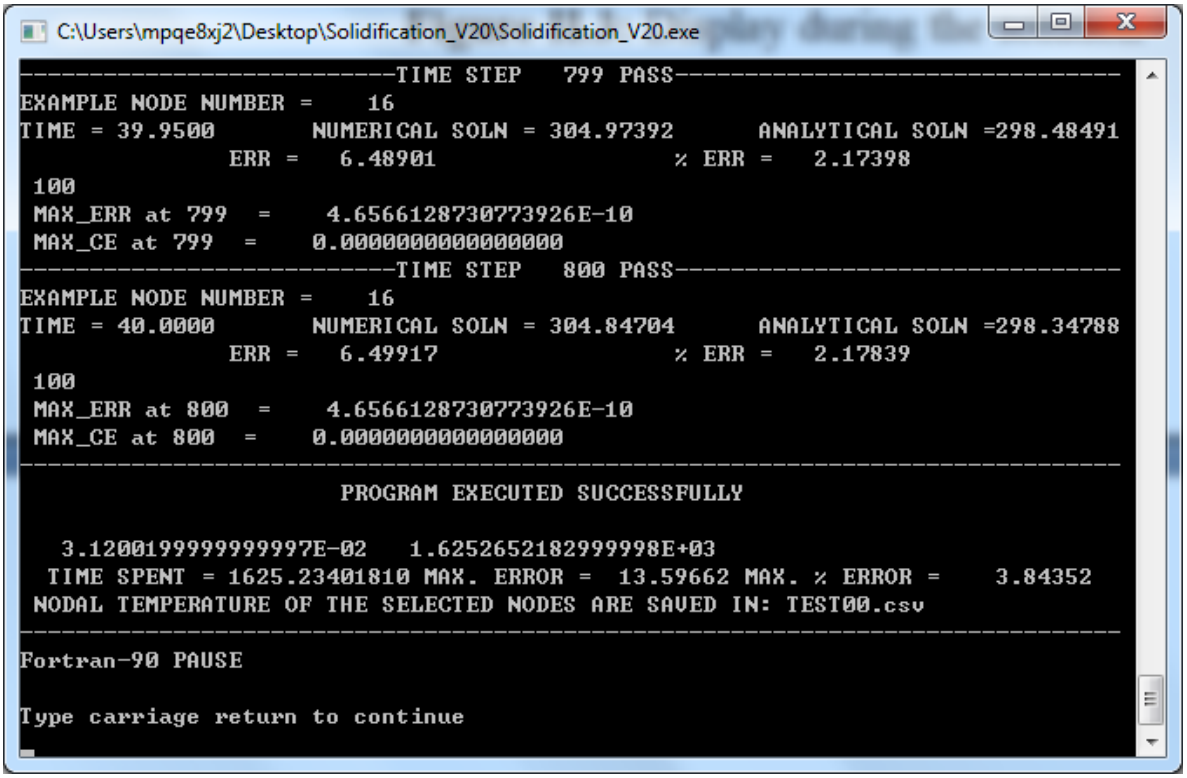

Figure II.4: The display when the program executed successfully

When the program finishes the computation, it displays information as shown in Figure II.4. The argument "TIME SPENT" provides the time for execution with respect to CPU time. The argument "MAX. ERROR" provides the maximum error of the example node after the comparison through the results of all time steps. The argument "% ERROR" provides the maximum percentage error of the example node after the comparison through the results of all time steps.

It has to be mentioned that the built-in analytical solution is calculated in the absence of material velocity, which derivation can be seen in chapter 3. Thus, when the advection-diffusion is involved in the numerical simulation, please ignore the result comparison with the analytical solution.

II.2.2 developer's manual

The programme is originally coded with the compiler NAG Fortran Builder 5.2, and it is compatible for the version 5.3. The programme is created as a project, which can be seen in Figure II.5. It has to be noticed that the NAG Library Application is selected, because the programme calls some routines from NAG Fortran Library Mark 22. For that reason, the NAG Fortran Library Mark 22 is required to be installed in the computer. If user doesn't

have the library, the subroutines such as “DGESV” have to be deleted by hand, then the secant method and the homotopy method will not be available, and only the Gauss-Jordan elimination method is available as a solver. The project can be directly opened by double clicking the file “Solidification_V20.fbp” in the folder “Solidification_V20”. And the project only contains one source file which is “Solidification_V20.f95”.

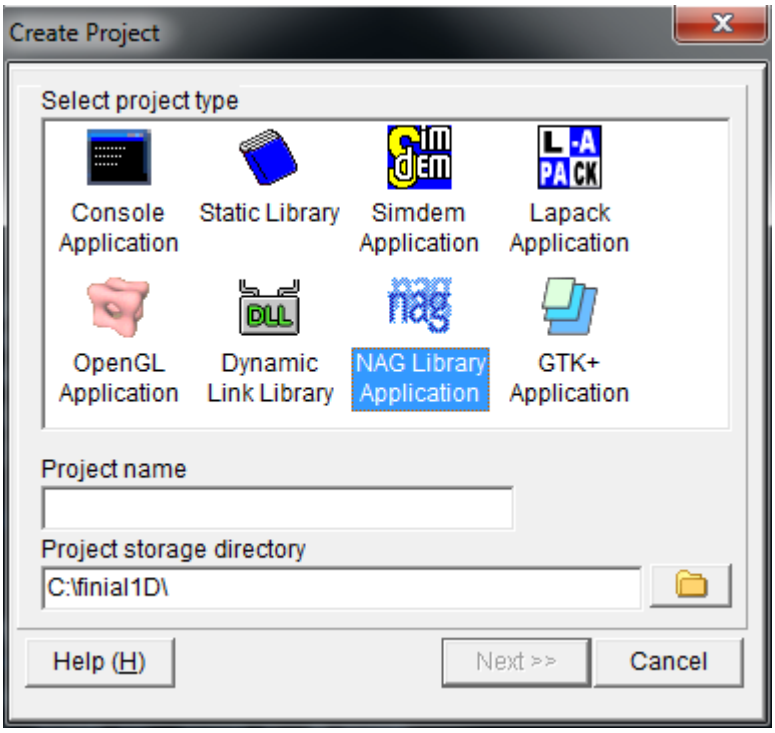

Figure II.5: The Fortran project

The Main structure of the programme is shown as below.

!----------Declare-the-arguments----------

PROGRAM Solidification_V20

Define arguments;

Input data such as material properties, mesh density, time step, solution methods, etc;

Allocate arrays for coefficient matrices and loading vectors;

Prepare the files for output.

!----------Main-Program----------

```
timestep_loop1 : DO  J = 1, Time_steps
  SolverSelection : IF(SOLVER == 'ANATST' .OR. SOLVER == 'anatst') THEN
     Execute the module for analytical method
  ELSEIF(SOLVER == 'SECANT' .OR. SOLVER == 'secant') THEN
     Execute the module for secant method
 ELSEIF(SOLVER == 'HOMOTO' .OR. SOLVER == 'homoto') THEN
     Execute the module for homoto method
 ELSEIF(SOLVER == 'LINEAR' .OR. SOLVER == 'linear') THEN
     Execute the module for predictor corrector method
 END IF
 Output data returned for time step J.
END DO
!-----------------------------------------------------------------------------------------------------
CONTAINS
Subroutines ready to be called by the main programme.
END PROGRAM Solidification_V20
!-----------------------------------------------------------------------------------------------------
```

Above describes the fundamental structure of the program. The program involves thousands of lines of statements and explanation of the whole program requires a great many pages. Fortunately, the program is “modularized”, and the modules are programmed with similar procedure and logic. Thus, this manual only explains one module as an example, which includes the functions of statement and their relation to the theory. The module explained here is the module for the non-physical capacitance method, in which the non-physical capacitance is applied for both temporal term and the advective term. This is illustrated as

the non-physical capacitance method in chapter 6. And this part of code is for the first time step and first convergence loop for predictor corrector method.

For each time step and each iteration, it is important that some arrays (i.e. the coefficient matrices and the loading vectors) are required to be initiated. Especially for the assembled matrices, the algorithm of assembly is incrementation, thus clearing the data from the previous iteration is very important. The subroutine "ZERO" assigns the value 0 to arrays.

```
!-----------------------------------------------------------------------------------------------------------

CALL ZERO(C_matn, K_matn, Kv_matn, C_matn1, K_matn1, Kv_matn1, GC_matn,     &
GK_matn, GKv_matn, GC_matn1, GK_matn1, GKv_matn1, LHS_MAT, RHS_MAT,     &
gs_n, gs_n1, q_n, q_n1, Enthalpy_s, Jacob_F, Inv_JF, nonQ_n1, nonQ_n, nonQ_n1,     &
G_nonQ, BETA, Jacob_T, Inv_JT)

!-----------------------------------------------------------------------------------------------------------
```

For the first time step of predictor corrector method, the explicit time approximation is adopted. Thus, the blending factor θ is set to be 0.0D0. The related theory can be seen in section 4.2 in chapter 4 and section 6.3 in chapter 6.

```
!-----------------------------------------------------------------------------------------------------------

   THETA = 0. 0D0

!-----------------------------------------------------------------------------------------------------------
```

Then, the sensible enthalpy is calculated by the following loop. The calculation follows the identity that

$$H_{NN} = \begin{cases} \rho_l c_l T_{NN} & T_{sol} \leq T_{NN} \\ \rho_s c_s T_{NN} & T_{NN} < T_{sol} \end{cases} \qquad \text{(II—1)}$$

where NN is the node number, and NNODE is the total number of nodes.

```
!-----------------------------------------------------------------------------------------------------------

    Node_Loops_03 : DO NN = 1, NNODE

     IF (GTp_n1(NN) > T_liq) THEN

       Enthalpy_n1(NN) = (GTp_n1(NN) * den_liq * cap_liq)
```

```
      ELSEIF (GTp_n1(NN) <= T_liq) THEN
        Enthalpy_n1(NN) = (GTp_n1(NN) * den_sol * cap_sol)
      END IF
    END DO Node_Loops_03
```

!----------

Once the argument “Non_physical” is assigned as “CVCMO” or “cvcmo”, it means that the non-physical capacitance method is selected.

!----------

```
IF(Non_physical == 'CVCMO' .OR. Non_physical == 'cvcmo') THEN
```

!----------

Then, the following loop evaluates the coefficients such as solid volume fraction, non-physical capacitance and conductivity for the element with the number “IEL”. The array “NUM” records the node number of element “IEL”. After the evaluations of coefficients, the matrices are established and directly being assembled to the global coefficient matrices.

!----------

```
  ElementLoop_03 : DO IEL = 1, NELS
      NUM = (/IEL, IEL + 1/)
```

!----------

The subroutine “Sol_Fraction” evaluates the solid volume fraction via the element based temperature approximation. The theory can be seen in chapter 3 as equation (3—49) and in chapter 6 as equation (6—7).

!----------

```
      CALL Sol_Fraction(GT_n(NUM(1)), GT_n(NUM(2)), T_liq, gs_n(IEL), Pbeta)
      CALL Sol_Fraction(GTp_n1(NUM(1)), GTp_n1(NUM(2)), T_liq, gs_n1(IEL),  &
                        Pbeta)
```

```
!-----------------------------------------------------------------------------------------------------
```

The subroutine “nonc” evaluates the non-physical capacitance, according to equations (3—55) and (6—53). This related to the concept (a), which is described in chapter 6.

```
!-----------------------------------------------------------------------------------------------------

      CALL nonc(GT_n(NUM(1)), GT_n(NUM(2)), GTp_n1(NUM(1)),                    &
                GTp_n1(NUM(2)), gs_n(IEL), gs_n1(IEL), lat_heat, h_sol, den_liq,  &
                den_sol, cap_liq, cap_sol, t_liq, capacitance_n(IEL),          &
                capacitance_n1(IEL), Senthalpy_n(IEL), Senthalpy_n1(IEL), 1.0D0,
                e_length(iel), J, CLOOP, IEL)

!-----------------------------------------------------------------------------------------------------
```

The subroutine “nonk1” evaluates the conductivity for different time steps. It is known that the discontinuity embodied in the flux term is annihilated, thus, a mixture conductivity is applied. The annihilation procedure can be seen in section 3.4 in chapter 3, and section 5.4.1 in chapter 5. The mixture conductivity can be seen in equation (3—53).

```
!-----------------------------------------------------------------------------------------------------

      CALL nonk1(con_liq, con_sol, gs_n(iel), conductivity_n(iel))

      CALL nonk1(con_liq, con_sol, gs_n1(iel), conductivity_n1(iel))

!-----------------------------------------------------------------------------------------------------
```

Once the non-physical capacitance and conductivity are evaluated, they are substituted into the elemental matrices. The subroutine “rod_cm” constructs elemental matrices for non-physical capacitance. The lumped form and the consistent form can be selected by setting the argument “mat_form”. The subroutine “rod_km” constructs the conductivity matrix.

The subroutine “beta_get” calculates the parameter β for Patrov-Galerkin method. It is then substituted into subroutine “rod_kvm” to construct matrix for advective term.

The theory related to the construction of each matrix is described in section 4.2 in chapter 4 and section 6.3 in chapter 6.

The subroutine “matrix_assembly” assembles the matrices.

```
!-------------------------------------------------------------------------------------------------------

      CALL rod_cm(C_matn, E_length(IEL), mat_form, capacitance_n1(IEL))

      CALL rod_cm(C_matn1, E_length(IEL), mat_form, capacitance_n1(IEL))

      CALL rod_km(K_matn, conductivity_n(IEL), E_length(IEL))

      CALL rod_km(K_matn1, conductivity_n1(IEL), E_length(IEL))

      CALL beta_get(BETA(IEL), material_velocity, conductivity_n1(IEL), &
                    capacitance_n1(IEL), e_length(iel), dis_form)

      CALL rod_kvm(kv_matn, capacitance_n1(IEL), material_velocity, BETA(IEL))

      CALL rod_kvm(kv_matn1, capacitance_n1(IEL), material_velocity, BETA(IEL))

      CALL matrix_assembly(GC_matn, C_matn, NUM(1), NUM(2))

      CALL matrix_assembly(GK_matn, K_matn, NUM(1), NUM(2))

      CALL matrix_assembly(GKv_matn, kv_matn, NUM(1), NUM(2))

      CALL matrix_assembly(GC_matn1, C_matn1, NUM(1), NUM(2))

      CALL matrix_assembly(GK_matn1, K_matn1, NUM(1), NUM(2))

      CALL matrix_assembly(GKv_matn1, kv_matn1, NUM(1), NUM(2))

!-------------------------------------------------------------------------------------------------------

    END DO ElementLoop_03

  ELSEIF …

!-------------------------------------------------------------------------------------------------------
```

This program includes the method “CVCMO/cvcmo” (non-physical capacitance method) as well as other methods, e.g.

Non_Physical: CVCMO/cvcmo: the non-physical capacitance method,
CVCMV/cvcmv: the control volume capacitance method,
CVCMX/cvcmx: the weak annihilation method,

CVCMC/cvcmc: non-physical capacitance + continuous advection + non-physical source method,

CVCMQ/cvcmq: non-physical source method;

They are programmed similarly, thus they are omitted in this manual.

Once the coefficient matrices are created, the next step is to construct loading vectors for boundary conditions (BCs). The array "BC_ACTIVE" controls the boundary where BCs are applied. For example, "BC_ACTIVE = (/1.0D0, 0.0D0/)" means that the BC is applied on the left of the one-dimensional model and the right boundary is isolated.

As described in chapter 4, "two adjacent elements share the same boundary node, which will make the numerical flux q_ς cancel for any node ς shared by two elements after assembly. The cancellation of numerical flux is because that, at node ς, the flux leaving the present element and the flux entering the next element are equal in quantities, but they are in opposite directions and have opposite signs in equations." Thus only the first node and last node are required to be evaluated.

```
!-------------------------------------------------------------------------------------------------------

h_c = BC_ACTIVE(1) * hc_in * conductivity_n1(1) + BC_ACTIVE(2) * hc_in *          &
      conductivity_n1(NELS)

q_n(1) = BC_ACTIVE(1) * D_time * (1.0D0 - THETA) * h_c * T_amb

q_n1(1) = BC_ACTIVE(1) * D_time * THETA * h_c * T_amb

 q_n(NNODE) = BC_ACTIVE(2) * D_time * (1.0D0 - THETA) * h_c * T_amb

 q_n1(NNODE) = BC_ACTIVE(2) * D_time * THETA * h_c * T_amb

!-------------------------------------------------------------------------------------------------------
```

As described in section 6.2, the system of equation appears in the form as equation (6—5). According to that, the arrays

$$\text{LHS\_MAT}=\left[\hat{C}^{n+1}\right]+\theta\Delta t\left[{K_v}^{n+1}\right]+\theta\Delta t[K^{n+1}] \quad \text{(II—2)}$$

and

$$\text{RHS\_MAT}=\left[\hat{C}^{n}\right]-(1-\theta)\Delta t[{K_v}^{n}]-(1-\theta)\Delta t[K^{n}] \quad \text{(II—3)}$$

respectively.

```
!-------------------------------------------------------------------------------------------------------

 LHS_MAT = GC_matn1 +  D_time * THETA * GK_matn1 + D_time * THETA *        &
           GKv_matn1

 RHS_MAT = GC_matn - D_time * (1.0D0 - THETA) * GK_matn - D_time *         &
           (1.0D0 - THETA) * GKv_matn

!-------------------------------------------------------------------------------------------------------
```

Since, the Newton's law of cooling is applied as BCs, the unknown temperature requires the forced convective coefficient h_c to be updated into the coefficient matrices. Thus the following procedure is adopted.

```
!-------------------------------------------------------------------------------------------------------

 LHS_MAT(1, 1) = LHS_MAT(1, 1) + BC_ACTIVE(1) * THETA * D_time * h_c

 LHS_MAT(NNODE, NNODE) = LHS_MAT(nnode, nnode) + BC_ACTIVE(2) *          &
                         THETA * D_time * h_c

 RHS_MAT(1, 1) = RHS_MAT(1, 1) - BC_ACTIVE(1) * (1.0D0 - THETA) *        &
                 D_time * h_c

 RHS_MAT(NNODE, NNODE) = RHS_MAT(nnode, nnode) - BC_ACTIVE(2) *          &
                         (1.0D0 - THETA) * D_time * h_c

!-------------------------------------------------------------------------------------------------------
```

From now on, the coefficient matrices and the loading vectors are ready. The system of equations can be solved by the following statements. The string "GJE/gje" refers to the Gauss Jordan elimination method, which is independent of NAG Fortran library; the string "NAG/nag" is the LU composition method which is call from NAG Fortran library.

```
!-------------------------------------------------------------------------------------------------------

GT_s = MATMUL(RHS_MAT,GT_n) + q_n1 + q_n1 - G_nonQ

IF (lesolver == 'GJE' .OR. lesolver == 'gje') THEN

  CALL gaussj(LHS_MAT, tps_n1, GT_s, NNODE)
```

```
ELSEIF (lesolver == 'NAG' .OR. lesolver == 'nag') THEN

  GTp_n1 = GT_s

   CALL DGESV(W,1,LHS_MAT,LDA,IPIV,GTp_n1,LDB,INFO)

END IF

!-----------------------------------------------------------------------------------------------------------
```

The following algorithm is an over-shooting/under-shooting technique, similar to the technique that is applied for liquid fraction in references [37, 46]. It follows the fact that, the temperature of future time step should always be less than or equal to the temperature of present time step in a cooling process.

```
!-----------------------------------------------------------------------------------------------------------

     DO NN = 1, NNODE

      IF(GTp_n1(NN) > GT_n(NN) .AND. T_init >=T_sol) THEN

        GTp_n1(NN) = GT_n(NN)

      ELSEIF(GTp_n1(NN) < GT_n(NN) .AND. T_init <T_sol) THEN

        GTp_n1(NN) = GT_n(NN)

      END IF

     END DO

!-----------------------------------------------------------------------------------------------------------
```

Then, the nodal temperature of future time step is computed as “GTp_n1”. The argument “GTp_n1” is used rather than “GT_n1” means that this future time step temperature requires to be checked. If it doesn’t meet the specified criterion, it goes back to the next convergence loop.

```
!-----------------------------------------------------------------------------------------------------------
```

The following example is a subroutine that calculates the non-physical capacitance. For convenience, all subroutines are put into the same source file as “Solidification_V20.f95”, which are under the statement “CONTAINS”.

```
!-----------------------------------------------------------------------------------------------------

SUBROUTINE nonc(T1_n, T2_n, T1_n1, T2_n1, gs, gs1, lat, h_sol, den_l, den_s, cap_l, &
cap_s, T_liq, cap_n, cap_n1, h_n, h_n1, area, elength, J, CLOOP, IEL)

DOUBLE PRECISION, INTENT(IN) :: T1_n, T2_n, T1_n1, T2_n1, gs, gs1, lat, h_sol,    &
den_l, den_s, cap_l, cap_s, t_liq, area, elength

INTEGER, INTENT(IN) :: J, CLOOP, IEL

DOUBLE PRECISION, INTENT(INOUT) :: cap_n, cap_n1

DOUBLE PRECISION, INTENT(OUT) :: h_n, h_n1

DOUBLE PRECISION :: T11_n, T22_n, T11_n1, T22_n1

DOUBLE PRECISION :: ms_n, ms_n1, ml_n, ml_n1, mt_n, mt_n1, e_vol, hn_d

DOUBLE PRECISION :: non_h, tn_vol, tn1_vol

non_h = 0.0D0

cap_n1 = 0.0D0

!-----------------------------------------------------------------------------------------------------
```

The following conditional execution statements do not have any physical meaning. These are applied to mathematically minimise the effect of any oscillations during computation. Since they only affect the subroutine, which evaluates the non-physical capacitance, they have no influence on the main programme and the numerical results.

```
!-----------------------------------------------------------------------------------------------------

IF (T1_n < T2_n) THEN

  T11_n = T1_n

  T22_n = T2_n
```

```
ELSE
  T11_n = T2_n
  T22_n = T1_n
END IF

IF (T1_n1 < T2_n1) THEN
  T11_n1 = T1_n1
  T22_n1 = T2_n1
ELSE
  T11_n1 = T2_n1
  T22_n1 = T1_n1
END IF
!-----------------------------------------------------------------------------------------------------
e_vol = area * elength
h_n = 0.0D0
h_n1 = 0.0D0
hn_d = 0.0D0
non_h = 0.0D0
!-----------------------------------------------------------------------------------------------------
```

The following statements calculate the mass of solid, the mass of liquid and the total mass of an element.

```
!-----------------------------------------------------------------------------------------------------
ms_n = gs * den_s * e_vol
```

```
ms_n1 = gs1 * den_s * e_vol

ml_n = (1.0D0 - gs) * den_l * e_vol

ml_n1 = (1.0D0 - gs1) * den_l * e_vol

mt_n = ms_n + ml_n

mt_n1 = ms_n1 + ml_n1

!-----------------------------------------------------------------------------------------------------
```

Then, the following statements calculate the values of terms $\int_{\Omega_e} \rho^{n+1} \mathrm{h}^{n+1} dV$ and $\int_{\Omega_e} \rho^{n} \mathrm{h}^{n} dV$, which appear in equations (3—46) and (3—51) in chapter 3 and in equation (6—8) in chapter 6. For an element, three conditions arise, i.e. the element is completely in liquid state ($\Upsilon_s = 0$); the element is partially in liquid state and partially in solid state ($0 < \Upsilon_s < 1$); and the element is completely in solid state ($\Upsilon_s = 1$). The conditional execution statements are coded with respect to the element-based temperature approximation of solid volume fraction to inform the program in which condition the enthalpy is evaluated. The evaluation of terms $\int_{\Omega_e} \rho^{n+1} \mathrm{h}^{n+1} dV$ and $\int_{\Omega_e} \rho^{n} \mathrm{h}^{n} dV$ are conducted via equation (3—51) or (6—8).

```
!-----------------------------------------------------------------------------------------------------

IF(gs == 0.0D0) THEN

  h_n = den_l * e_vol * h_sol + e_vol * den_l * lat + (e_vol / 2.0D0) * den_l * cap_l * &
        (T11_n + T22_n - 2.0D0 * T_liq)

ELSEIF(gs > 0.0D0 .AND. gs < 1.0D0) THEN

  h_n = mt_n * h_sol + ml_n * lat + (e_vol * gs / 2.0D0) * (2.0D0 * T11_n - 2.0D0 * &
        T_liq + gs * (T22_n - T11_n)) * den_s * cap_s + (e_vol * (1.0D0 - gs) /    & 2.0D0)
        * (T11_n + T22_n - 2.0D0 * T_liq + gs * (T22_n - T11_n)) * den_l * & cap_l

ELSE

  h_n = den_s * e_vol * h_sol + den_s * cap_s * (e_vol / 2.0D0) * (T11_n + T22_n - &
        2.0D0 * T_liq)
```

```
END IF


IF(gs1 == 0.0D0) THEN

  h_n1 = den_l * e_vol * h_sol + e_vol * den_l * lat + (e_vol / 2.0D0) * den_l *       & cap_l
         * (T11_n1 + T22_n1 - 2.0D0 * T_liq)

ELSEIF(gs1 > 0.0D0 .AND. gs1 < 1.0D0) THEN

  h_n1 = mt_n1 * h_sol + ml_n1 * lat + (e_vol * gs1 / 2.0D0) * (2.0D0 * T11_n1 - & 2.0D0
* T_liq + gs1 * (T22_n1 - T11_n1))* den_s * cap_s + (e_vol * (1.0D0 - gs1) / & 2.0D0) *
(T11_n1 + T22_n1 - 2.0D0 * T_liq + gs1 * (T22_n1 - T11_n1)) * den_l * cap_l

ELSE

  h_n1 = den_s * e_vol * h_sol + den_s * cap_s * (e_vol / 2.0D0) * (T11_n1 + T22_n1 - &
2.0D0 * t_liq)

END IF

!-----------------------------------------------------------------------------------------------------
```

The following statements calculate the volumetric temperatures appeared as denominator in equation (3—52).

```
!-----------------------------------------------------------------------------------------------------

tn_vol = (area * elength / 2.0D0) * (T11_n + T22_n)

tn1_vol = (area * elength / 2.0D0) * (T11_n1 + T22_n1)

!-----------------------------------------------------------------------------------------------------
```

The evaluation of volumetric temperatures has one problem. It is highly possible that $\mathrm{tn\_vol} - \mathrm{tn1\_vol} = 0$. The denominator returned as 0 definitely gives rise to error. Thus, the conditional execution statements are programmed to prevent this error. Despite the situation that the element is complete solid or liquid, the following equation can be applied to prevent the 0 denominator, which is

$$\hat{c}^{n+1} = \frac{\int_{\Omega_e} \rho^{n+1} h^{n+1} dV - \int_{\Omega_e} \rho^n h^n dV + \hat{c}^n \int_{\Omega_e} T^n dV}{\int_{\Omega_e} T^{n+1} dV} \quad \text{(II—3)}$$

However, equation (II—3) is no longer an averaged approach as described in chapter 3. Thus, the following equation is required, which is

$$\hat{c} = \frac{\hat{c}^{n+1} + \hat{c}^n}{2} \quad \text{(II—4)}$$

```
!-----------------------------------------------------------------------------------------------------------

IF(T11_n >= t_liq .AND. T22_n >= t_liq .AND. T11_n1 >= t_liq .AND. T22_n1 >= t_liq) THEN

  cap_n1 = cap_l * den_l

ELSEIF (T11_n < t_liq .AND. T22_n < t_liq .AND. T11_n1 < t_liq .AND. T22_n1 < t_liq) THEN

  cap_n1 = cap_s * den_s

ELSE

!  non_h = (gs - gs1) * (den_l * (cap_s * T_liq - cap_l * T_liq) + den_l * lat) * elength * & area

!-----------------------------------------------------------------------------------------------------------

  IF (ABS(tn_vol - tn1_vol) <= 1.E-10) THEN

    cap_n1 = cap_n * tn_vol / tn1_vol + (h_n1 - h_n - non_h) / tn1_vol

    cap_n1 = (cap_n + cap_n1) / 2.0D0

  ELSE

    cap_n1 =(h_n1 - h_n - non_h) / (tn1_vol - tn_vol)

  END IF

END IF

!-----------------------------------------------------------------------------------------------------------
```

```
IF(IEL == 1 .AND. J == 1) THEN

  cap_n1 = gs1 * den_s * cap_s + (1 - gs1) * den_l * cap_l

END IF

!---------------------------------------------------------------------------------------------------

END SUBROUTINE nonc

!---------------------------------------------------------------------------------------------------
```

Now the subroutine “nonc” calculates the non-physical capacitance and returns the value to the main program “Solidification_V20”. As the program contains a lot of subroutines, they can be decompiled in a similar approach as this example.

Appendix III The user Manual for 2D Programme

III.1 The programme for two-dimensional simulation

III.1.1 end user manual

The program for two-dimensional simulation is coded in a similar manner as one-dimensional simulation. However, the mesh in two-dimension is more complicated than the mesh in one-dimension. It has influence not only on the matrix assembly, but also on the data output and post-processing. Figure III.1 is a sketch of a rectangle meshed in this program. The simple model is meshed by 32 elements, which generates 25 nodes. Their order of number is shown in Figure III.1. The circled numbers ①, ② and ③ are the local node number of an element, the Roman number refers to the number of element, and the Arabic number refers to the global node number. With these numbers, the program can assemble the coefficient matrices, calculate non-physical variables with respect to element and organise data output.

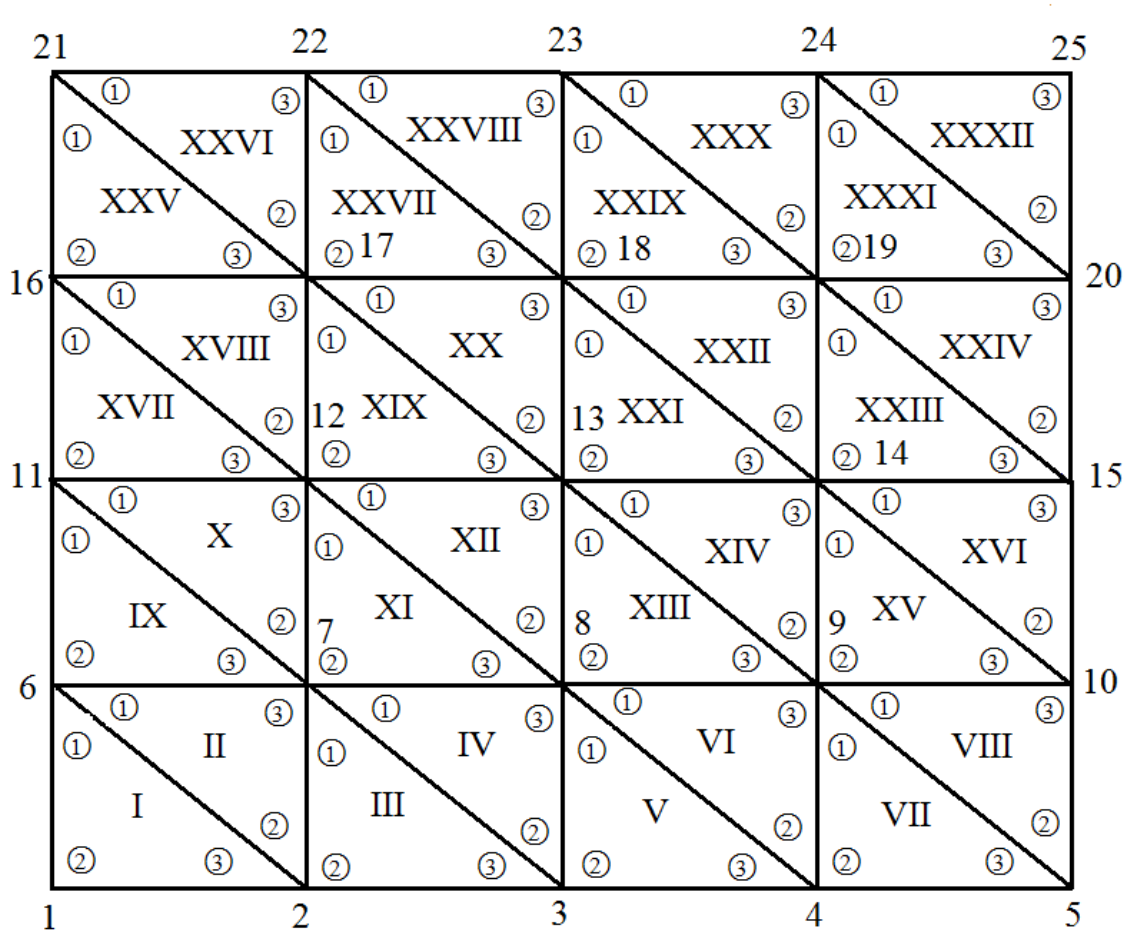

Figure III.1: The numbering of mesh

The two-dimensional program also contains a "SIM_DATA.dat" file which stores the important data such as the material properties, the mesh and time step information and the selected solution methods. It is editable by the Notepad in Windows operating system, and it must be stored in the main folder of the program, which is "Sldfctn2D_V3". The statements corresponding to the format of the file "SIM_DATA.dat" in the program is shown below.

!----------READ-MATERIAL-PROPERTIES----------

READ(91, *) cap_liq, cap_sol, den_liq, den_sol, lat_heat, t_sol, t_liq

READ(91, *) xcon_liq, ycon_liq, xcon_sol, ycon_sol

!----------

The number "91" refers to the file "SIM_DATA.dat". These two lines collect the material properties from file "SIM_DATE.dat" to the main program. The arguments are defined as double precision, and their meanings are listed as below,

cap_liq: specific thermal capacitance of liquid c_l $(J/kg℃)$;

cap_sol: specific thermal capacitance of solid c_s $(J/kg℃)$;

con_liq: thermal conductivity of liquid k_l $(W/m℃)$;

con_sol: thermal conductivity of solid k_s $(W/m℃)$;

den_liq: density of liquid ρ_l (kg/m^3);

den_sol: density of solid ρ_s (kg/m^3);

lat_heat: Latent heat (J/kg);

t_sol: solidus temperature (℃);

t_liq: liquidus temperature (℃);

xcon_liq: principal thermal conductivity of liquid $k_{l_{xx}}$ in x direction $(W/m℃)$;

ycon_liq: principal thermal conductivity of liquid $k_{l_{yy}}$ in y direction $(W/m℃)$;

xcon_sol: principal thermal conductivity of solid $k_{s_{xx}}$ in x direction $(W/m℃)$;

ycon_sol: principal thermal conductivity of solid $k_{s_{yy}}$ in y direction $(W/m℃)$.

It is slightly different from one-dimensional simulation that, the conductivity is input as principal thermal conductivity in case that nonhomogeneous conductivity is preferred. Detailed discussion about the theory can be seen in section 7.2.2 in Chapter 7.

The next two lines provide the geometry of the model and the mesh. The statement "geometry" is a 1 by 2 array, which records the length and height of a rectangle. The argument "c_partition" is an integer which is the number of partitions along the horizontal edge. The argument "r_partition" is an integer which is the number of partitions along the vertical edge. For example, in the mesh as shown in Figure II.6, the array "geometry = (/0.10D0, 0.080D0)", the arguments "c_partition = 4" and "r_partition = 4".

!----------READ-MODEL-AND-MESH-IN----------

READ(91, *) geometry

READ(91, *) c_partition, r_partition

!----------

Once the material properties are defined, the mesh information is provided. The following four lines provide the boundary conditions, which are

t_init: initial temperature (℃);

t_amb: ambient temperature (℃);

hc_top: the forced convective coefficient applied on the top surface of model (W/m^2℃);

hc_btm: the forced convective coefficient applied on the bottom surface of model (W/m^2℃);

hc_lft: the forced convective coefficient applied on the left surface of model (W/m^2℃);

hc_rgt: the forced convective coefficient applied on the right surface of model (W/m^2℃);

material_velocity: magnitude of material velocity $\|\underline{v}\|$ (m/s);

v_angle: angle of material velocity φ in arcdgree.

!----------READ-BOUNDARY-CONDITION-IN----------

READ(91, *) t_init

READ(91, *) t_amb

!----------

READ(91, *) hc_top, hc_btm, hc_lft, hc_rgt

READ(91, *) material_velocity, v_angle

!----------

The following statements specify the time step, the matrix format and the solution method applied. At the end of this part of the code is the configuration for the data output. The meanings of arguments are

dtime_in: time step size (sec);

Time_steps: total number of time steps;

mat_form: LUMPED/lumped = lumped capacitance, CONSIST/consist = consistent matrix;

dis_form: FUPWIND/fupwind = full upwind, PUPWIND/pupwind = Perov-Garkin method,
CENTRAL/central = central difference);

l_solver: NAG/nag = LU composition mehod, GJE/gle = Gauss Jordan Elimination method;

Non_Physical: CVCMO/cvcmo: the non-physical capacitance method,
CVCOQ/cvcmq: new non-physical variable method;

JOUT: data of time step JOUT is recorded in the file "TEST.res" for debug;

COUT: data of convergence step COUT is recorded in the file "TEST.res" for debug;

SNODE: results of node number "SNODE" is displayed on screen, also documented in the file "ERROR.csv".

Opnode : number of first node for the results output to the file "ALL_RESULTS.csv";

tpri: result is collected every "tpri" time step;

vtk_pri: VTK file is constructed every "vtk_pri" time steps for visualization;

relax: relaxation factor for non-physical source method;

No_convergence: Maximum number of convergence loop is set to prevent infinite loop;

file_path: the location where the VTK files are saved for visualization.

```
!-----------------------------------------------------------------------------------------------------
READ(91, *) dtime_in

READ(91, *) Time_steps

READ(91, *) mat_form

READ(91, *) dis_form

READ(91, *) l_solver
```

READ(91, *) Non_physical

READ(91, *) jout, cout

READ(91, *) snode, opnode

READ(91, *) tpri, vtk_pri

READ(91, *) no_convergence

READ(91, *) relax

READ(91, *) file_path

!----------

An example VTK file which relates to the model shown in Figure III.1 is displayed as below. The VTK file can be divided into four parts. In the first part, it records the co-ordinates for the nodes; in the second part, it saves the global node number for each element with respect to its local node number; in the third part, it saves the shape of the element, and the number "5" refers to the triangle; in the last part, it saves the nodal values.

!----------

vtk DataFile Version 3.1

This is a temperature distribution at a time step

ASCII

DATASET UNSTRUCTURED_GRID

POINTS 25 FLOAT

0.000000 0.000000 0.000000

0.025000 0.000000 0.000000

0.050000 0.000000 0.000000

0.075000 0.000000 0.000000

0.100000 0.000000 0.000000

0.000000 0.020000 0.000000

0.025000 0.020000 0.000000

0.050000 0.020000 0.000000

0.075000 0.020000 0.000000

0.100000 0.020000 0.000000

0.000000 0.040000 0.000000

0.025000 0.040000 0.000000

0.050000 0.040000 0.000000

0.075000 0.040000 0.000000

0.100000 0.040000 0.000000

0.000000 0.060000 0.000000

0.025000 0.060000 0.000000

0.050000 0.060000 0.000000

0.075000 0.060000 0.000000

0.100000 0.060000 0.000000

0.000000 0.080000 0.000000

0.025000 0.080000 0.000000

0.050000 0.080000 0.000000

0.075000 0.080000 0.000000

0.100000 0.080000 0.000000

CELLS 32 128

3 0 1 5

3 5 1 6

3 1 2 6

3 6 2 7

3 2 3 7

3 7 3 8

3 3 4 8

3 8 4 9

3 5 6 10

3 10 6 11

3 6 7 11

3 11 7 12

3 7 8 12

3 12 8 13

3 8 9 13

3 13 9 14

3 10 11 15

3 15 11 16

3 11 12 16

3 16 12 17

3 12 13 17

3 17 13 18

3 13 14 18

3 18 14 19

3 15 16 20

3 20 16 21

3 16 17 21

3 21 17 22

3 17 18 22

3 22 18 23

3 18 19 23

3 23 19 24

CELL_TYPES 32

5 5 5 5 5 5 5 5 5 5 5 5 5 5 5 5 5 5 5 5 5 5 5 5 5 5 5 5 5 5 5 5

POINT_DATA 25

SCALARS Temperature float

LOOKUP_TABLE default

403.7609

405.0000

405.0000

405.0000

405.0000

404.2692

405.0000

405.0000

405.0000

405.0000

404.3091

405.0000

405.0000

405.0000

405.0000

404.3091

405.0000

405.0000

405.0000

405.0000

405.0000

404.4818

405.0000

405.0000

405.0000

405.0000

405.0000

!----------

The VTK file can be constructed by the program automatically. However, users need to define a location for the VTK files and it is recommended to create a folder named as “VTK” under the folder “Sldfctn2D_V3”. If the folder “Sldfctn2D_V3” is located directly under C drive, then the location for the VTK files should be specified as “file_path = C:\Sldfctn2D_V3\VTK”.

Once the “SIM_DATA.dat” is correctly set up, the execution of two-dimensional program can be achieved by simply double-clicking the file “Sldfctn2D_V3.exe” under the folder “Sldfctn2D_V3”. The on-screen display is similar to the one-dimensional program which is shown in Figure III.2.

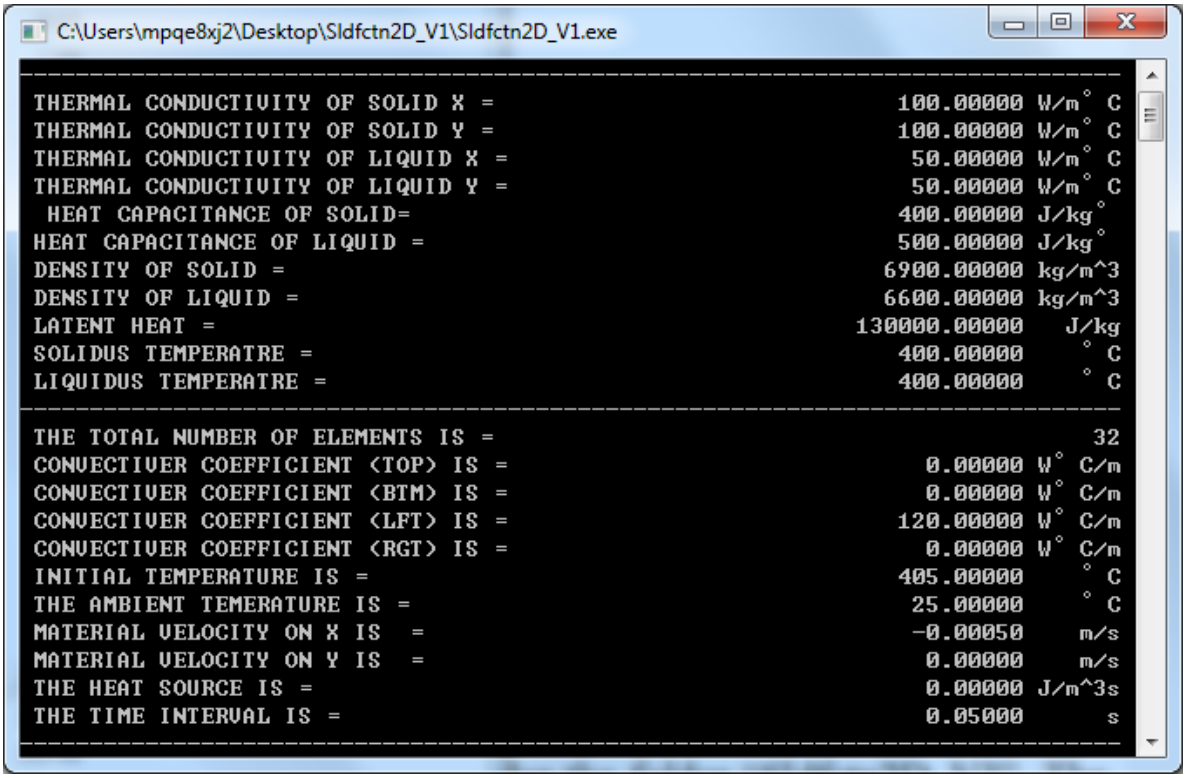

Figure III.2: On-screen display of two-dimensional program

The programme is originally coded with the compiler NAG Fortran Builder 5.3. It is created as a project, which can be seen in Figure II.5. It has to be noticed that the NAG Library Application is selected, because the programme calls some routines from NAG Fortran Library Mark 22. For that reason, the NAG Fortran Library Mark 22 is required to be installed in the computer. If user doesn’t have the library, the subroutines such as “DGESV” have to be deleted by hand, and only the Gauss-Jordan elimination method is then available as a solver. The project can be directly opened by double-clicking the file “Sldfctn2D_V3.fbp” in the folder “Sldfctn2D_V3_V20”. And the project only contains one source file which is “Sldfctn2D_V3.f95”.

The Main structure of the programme is shown as below.

!----------Declare-the-arguments----------

```
PROGRAM Sldfctn2D_V3

Define arguments;

Input data such as material properties, mesh density, time step, solution methods, etc;

Allocate arrays for coefficient matrices and loading vectors;

Prepare the files for output;

Specify the boundary nodes and calculate the nodal-co-ordinates.

!----------------------------------------Main-Program----------------------------------------------

timestep_loop1 : DO  J = 1, Time_steps

  Construct VTK file for time step J

  IF(Non_physical == 'CVCMO' .OR. Non_physical == 'cvcmo') THEN

     Execute the module for non-physical capacitance method

  ELSEIF(Non_physical == 'CVCOQ' .OR. Non_physical == 'cvcoq') THEN

     Execute the module for non-physical capacitance + continuous advection + non-
     physical source method

 END IF

  Write nodal temperatures to VTK file

 Output data returned for time step J.

END DO

!-------------------------------------------------------------------------------------------------------

CONTAINS

Subroutines ready to be called by the main programme.

END PROGRAM Sldfctn2D_V3

!-------------------------------------------------------------------------------------------------------
```

Similar to one-dimensional program, the two-dimensional program is constructed by several modules. In the developer's manual for one-dimensional program, the module for non-physical capacitance method is selected as an example to describe the development of the program. In this manual for two-dimensional program, the non-physical source method, which removes discontinuity from advective term and be re-applied as non-physical source, is illustrated. This method is described as the non-physical variable method in chapter 4. In order to use this method, the string argument "Non_physical" has to be defined as "CVCOQ" or "cvcoq" through the file "SIM_DATA.dat".

```
!-------------------------------------------------------------------------------------------------------

…

IF…

ELSEIF(Non_physical == 'CVCOQ' .OR. Non_physical == 'cvcoq') THEN

!-------------------------------------------------------------------------------------------------------
```

This module runs element by element. First of all, the 1 by 3 array "num" road the global node number of element "iel". For example, in Figure III.1, if the element number "iel = IX", the array "num = (/7, 8, 12/)".

```
!-------------------------------------------------------------------------------------------------------

    element_loopOQL1:  DO iel = 1, nels

     num = el_nodes(1:3,iel)

!-------------------------------------------------------------------------------------------------------
```

The subroutine "sol_fraction" calculates the solid volume fraction for triangular element. This calculation is achieved by the element-based temperature approximation, and the relative theory can be seen in section 7.3.1 in chapter 7.

```
!-------------------------------------------------------------------------------------------------------

      CALL sol_fraction(gs(iel), gt_n(num(1)), gt_n(num(2)), gt_n(num(3)), t_liq,  &
           n_coordinate(1:2, num(1)), n_coordinate(1:2, num(2)),                   &
           n_coordinate(1:2, num(3)))
```

```
      CALL sol_fraction(gs1(iel), gtp_n1(num(1)), gtp_n1(num(2)), gtp_n1(num(3)), &
           t_liq, n_coordinate(1:2, num(1)), n_coordinate(1:2, num(2)),          &
           n_coordinate(1:2, num(3)))

!-------------------------------------------------------------------------------------------------------
```

Once the solid volume fraction is evaluated, the next step is to evaluate the non-physical capacitance and the thermal conductivity. The subroutine "cvcm" calculates the non-physical capacitance. The approximation of each term in the equations is described in section 7.3.2 in chapter 7. The subroutine "nonk" evaluates the conductivity with the mixture technique.

```
!-------------------------------------------------------------------------------------------------------

      CALL cvcm(capacitance_n1(iel), capacitance_n(iel), gt_n(num(1)), gt_n(num(2)), &
           gt_n(num(3))， gtp_n1(num(1)), gtp_n1(num(2)), gtp_n1(num(3)),          &
           t_liq, gs(iel), gs1(iel), den_sol, den_liq, cap_sol, cap_liq, h_sol, lat_heat, &
           n_coordinate(1:2, num(1)), n_coordinate(1:2, num(2)),                   &
           n_coordinate(1:2, num(3)), IEL)

      CALL nonk(conductivity_n1(1:2,iel), gs(iel), gs1(iel), xcon_sol, xcon_liq, & ycon_sol,
           ycon_liq, theta)

!-------------------------------------------------------------------------------------------------------
```

The subroutine "triangle_cm1" constructs the capacitance matrix for an element. The subroutine "triangle_km" constructs the conductivity matrix for the element. The lumped capacitance matrix is adopted for the subroutine. Their relative theory can be seen in section 7.2.2 in chapter 7.

```
!-------------------------------------------------------------------------------------------------------

      CALL triangle_cm1(c_mat, n_coordinate(1:2, num(1)), n_coordinate(1:2, num(2)), &
           n_coordinate(1:2, num(3)), capacitance_n1(iel))

      CALL triangle_km(k_mat, n_coordinate(1:2, num(1)), n_coordinate(1:2, num(2)), &
           n_coordinate(1:2, num(3)),conductivity_n1(1,iel), conductivity_n1(2,iel))

!-------------------------------------------------------------------------------------------------------
```

The capacitance in the advective term is forced continuous in chapter 5. Thus, the subroutine "mixc" calculates the mixture capacitance only for the advective term. Then, the subroutine "triangle_kvm" constructs the matrix for advection, the theory of which can be seen in section 7.2.2 in chapter 7. The factor β offers the possibility to switch between the central difference method, the full upwind method and the Petrov-Galerkin method. The subroutine "beta_get" provides the factor β for Petrov-Galerkin method. And the subroutine "triangle_kup" constructs the artificial conductive matrix is the full upwind method or the Petrov-Galerkin method is selected.

```
!-------------------------------------------------------------------------------------------------------

      CALL mixc(gs(IEL), gs1(IEL), den_liq, den_sol, cap_liq, cap_sol,                &
           capacitance_nx(IEL), capacitance_n1x(IEL))

      CALL triangle_kvm(kvx_mat, kvy_mat, den_liq * cap_liq,                          &
           n_coordinate(1:2, num(1)), n_coordinate(1:2, num(2)),                      &
           n_coordinate(1:2, num(3)), velocity_xx, velocity_yy)

      CALL beta_get(beta(iel), material_velocity, den_liq * cap_liq, capacitance_n1(iel), &
           n_coordinate(1:2, num(1)), n_coordinate(1:2, num(2)),                      &
           n_coordinate(1:2, num(3)), dis_form)

      CALL triangle_kup(kup_mat, n_coordinate(1:2, num(1)),                           &
           n_coordinate(1:2, num(2)), n_coordinate(1:2, num(3)),                      &
           material_velocity, velocity_xx, velocity_yy, beta(iel))

!-------------------------------------------------------------------------------------------------------
```

The subroutine "non_source" calculates the non-physical source, which is the discontinuity in the advective term. Details will be discussed later in the example of subroutines.

```
!-------------------------------------------------------------------------------------------------------

      CALL non_source(G_nonQ, gt_n(num(1)), gt_n(num(2)), gt_n(num(3)),               &
           gtp_n1(num(1)), gtp_n1(num(2)), gtp_n1(num(3)), den_sol, den_liq,          &
           cap_sol, cap_liq, h_sol, lat_heat, t_liq, velocity_xx, velocity_yy, dtime(j), &
           n_coordinate(1:2, num(1)), n_coordinate(1:2, num(2)), & n_coordinate(1:2,
           num(3)), kvx_mat, kvy_mat, kup_mat, THETA, NUM)
```

```
!-------------------------------------------------------------------------------------------------------
```

The subroutine “matrix_assembly” assembles the element coefficient matrix into the global coefficient matrix.

```
!-------------------------------------------------------------------------------------------------------

      CALL matrix_assembly(gc_mat, c_mat, num)

      CALL matrix_assembly(gk_mat, k_mat, num)

      CALL matrix_assembly(gkvx_mat, kvx_mat, num)

      CALL matrix_assembly(gkvy_mat, kvy_mat, num)

      CALL matrix_assembly(gkup_mat, kup_mat, num)

    END DO element_loopOQL1

!-------------------------------------------------------------------------------------------------------

  END IF

!-------------------------------------------------------------------------------------------------------
```

The subroutine “boundary_condition” loads boundary conditions to the system according to equation (7—39). The boundary nodes are already specified automatically by the program and saved as arrays “hbc_nodes” and “vbc_nodes”. The boundary conditions are applied based on the boundary nodes. Since the Robin boundary condition is applied, this subroutine also updates the information of coefficient matrices.

```
!-------------------------------------------------------------------------------------------------------

   CALL  boundary_condition(q_n, gk_mat, hc_top, hc_btm, hc_lft, hc_rgt, t_amb, & nnode,
              cnode, rnode, hbc_nodes, vbc_nodes, n_coordinate,          & conductivity_n1,
              bc_iel)

!-------------------------------------------------------------------------------------------------------
```

According to the equation (7—33) in chapter 7, the two-dimensional arrays “lhs_mat” and “rhs_mat” are evaluated as

lhs_mat = $\left[\hat{C}\right] + \Delta t\theta[K^{n+1}] + \Delta t\theta[Kv_{xx}^{n+1}] + \Delta t\theta\left[Kv_{yy}^{n+1}\right] + \Delta t\theta\left[K_{up}^{n+1}\right]$ (II—5)

and

rhs_mat = $\left[\hat{C}\right] - \Delta t\theta[K^{n}] - \Delta t\theta[Kv_{xx}^{n}] - \Delta t\theta\left[Kv_{yy}^{n}\right] - \Delta t\theta\left[K_{up}^{n}\right]$ (II—6)

```
!-----------------------------------------------------------------------------------------------------------

   lhs_mat = gc_mat + dtime(j) * theta * gk_mat + dtime(j) * theta * gkvx_mat +        &
             dtime(j) * theta * gkvy_mat +   dtime(j) * theta * gkup_mat

   rhs_mat = gc_mat - dtime(j) * (1.0D0 - theta) * gk_mat - dtime(j) * (1.0D0 - theta) * &
             gkvx_mat - dtime(j) * (1.0D0 - theta) * gkvy_mat - dtime(j) * (1.0D0 - & theta)
             * gkup_mat

!-----------------------------------------------------------------------------------------------------------
```

Then, the coefficient matrices and the loading vectors are ready to be solved by the solvers as system of equations. The subroutine “gaussj” refers to the Gauss Jordan elimination method. The subroutine “DGESV” is a solver from the commercial NAG Fortran Library.

```
!-----------------------------------------------------------------------------------------------------------

   gt_s = MATMUL(rhs_mat, gt_n) + dtime(j) * q_n + G_nonQ

   IF (l_solver == 'GJE' .OR. l_solver == 'gje') THEN

     CALL gaussj(lhs_mat, gtp_n1, gt_s, nnode)

   ELSEIF (l_solver == 'NAG' .OR. l_solver == 'nag') THEN

     CALL DGESV(W,1,lhs_mat,LDA,IPIV,gt_s,LDB,INFO)

     gtp_n1 = gt_s

   END IF

!-----------------------------------------------------------------------------------------------------------
```

The following example is a subroutine that calculates the non-physical source, which is under the statement “CONTAINS”. In chapter 5 and chapter 7, it is described that the non-physical source can be regarded as the difference between the physical advection and the continuous numerical advection. The subroutine “non_source” calculates the non-physical source term $\int_{\Omega} \tilde{Q}\, dV$ which is returned as an array “G_nonQ”.

```
!-----------------------------------------------------------------------------------------------------

SUBROUTINE non_source(G_nonQ, TN_1, TN_2, TN_3, TN_n1, TN_n2, TN_n3, &
den_s, den_l, cap_s, cap_l, h_sol, lat, T_sol, v_xx, v_yy, d_time, coord_i1, coord_j2, &
coord_k3, kvm_xx, kvm_yy, kvupm, THETA, NUM)

IMPLICIT NONE

DOUBLE PRECISION, DIMENSION(:), INTENT(INOUT) :: G_nonQ

DOUBLE PRECISION, INTENT(IN) :: TN_1, TN_2, TN_3, TN_n1, TN_n2, TN_n3

DOUBLE PRECISION, INTENT(IN) :: den_s, den_l, cap_s, cap_l, h_sol, lat, T_sol, & v_xx,
                                v_yy, d_time

DOUBLE PRECISION, DIMENSION(1:2), INTENT(IN) :: coord_i1, coord_j2, coord_k3

DOUBLE PRECISION, DIMENSION(1:3,1:3), INTENT(IN) :: kvm_xx, kvm_yy, kvupm

DOUBLE PRECISION, INTENT(IN) :: THETA

INTEGER, DIMENSION(1:3), INTENT(IN) :: NUM

DOUBLE PRECISION :: Hv1_xx, Hv1_yy, Hv2_xx, Hv2_yy, Hv3_xx, Hv3_yy, &
                    areaf1_xx, areaf1_yy, areaf2_xx, areaf2_yy, areaf3_xx, &
                    areaf3_yy

DOUBLE PRECISION :: gs1_xx, gs1_yy, gs2_xx, gs2_yy, gs3_xx, gs3_yy, Hv_xx, &
                    Hv_yy, Hvn_xx, Hvn_yy

DOUBLE PRECISION :: SIGN1_XX, SIGN1_YY, SIGN2_XX, SIGN2_YY, &
                    SIGN3_XX, SIGN3_YY

DOUBLE PRECISION :: nonQ_xx, nonQ_yy
```

```
DOUBLE PRECISION, DIMENSION(1:3) :: Te_n, Te_n1, Hv_xn, Hv_yn

!-----------------------------------------------------------------------------------------------------------
```

After the declaration of all arguments and arrays for this subroutine, the elemental nodal temperatures are assigned to the arrays “Te_n” and “Te_n1” with respect to time-steps n and $n+1$ by the following two statements.

```
!-----------------------------------------------------------------------------------------------------------

Te_n(1:3) = (/TN_1, TN_2, TN_3/)

Te_n1(1:3) = (/TN_n1, TN_n2, TN_n3/)

!-----------------------------------------------------------------------------------------------------------
```

In chapter 7, it is described that the physical advection can be evaluated analytically. The analysis involves the evolution of the area of material that is swept by the boundary surface of an element. Detailed discussion can be seen in section 7.3.3. The following six statements calculate the areas swept by the three boundary surfaces of a triangular element. The areas are evaluated as projections on the x-direction and y-direction respectively for each boundary surface.

```
!-----------------------------------------------------------------------------------------------------------

areaf1_xx = ABS(v_xx) * d_time * ABS(coord_j2(2) - coord_k3(2))

areaf1_yy = ABS(v_yy) * d_time * ABS(coord_j2(1) - coord_k3(1))


areaf2_xx = ABS(v_xx) * d_time * ABS(coord_i1(2) - coord_k3(2))

areaf2_yy = ABS(v_yy) * d_time * ABS(coord_i1(1) - coord_k3(1))


areaf3_xx = ABS(v_xx) * d_time * ABS(coord_i1(2) - coord_j2(2))

areaf3_yy = ABS(v_yy) * d_time * ABS(coord_i1(1) - coord_j2(1))

!-----------------------------------------------------------------------------------------------------------
```

It is possible that in a times step, the phase interface may pass through the boundary surfaces to get into the element. This phenomenon is evaluated as the change of solid volume fraction on the base of the additional areas calculated before. The theory is described in section 7.3.3 and Figure 7.6 specifies all the possibilities that an additional area may experience. The subroutine "vel_fraction" evaluates the solid volume fraction for the additional area via the element-based temperature approximation, which is denoted as Υ_s^f in chapter 7.

```
!-----------------------------------------------------------------------------------------------------

CALL vel_fraction(gs1_xx, TN_2, TN_3, TN_n2, TN_n3, v_xx, areaf1_xx, coord_j2(1), &
        coord_k3(1), d_time)

CALL vel_fraction(gs1_yy, TN_2, TN_3, TN_n2, TN_n3, v_yy, areaf1_yy, coord_j2(2), &
        coord_k3(2), d_time)



CALL vel_fraction(gs2_xx, TN_1, TN_3, TN_n1, TN_n3, v_xx, areaf2_xx, coord_i1(1), &
        coord_k3(1), d_time)

CALL vel_fraction(gs2_yy, TN_1, TN_3, TN_n1, TN_n3, v_yy, areaf2_yy, coord_i1(2), &
        coord_k3(2), d_time)



CALL vel_fraction(gs3_xx, TN_1, TN_2, TN_n1, TN_n2, v_xx, areaf1_xx, coord_i1(1), &
       coord_j2(1), d_time)

CALL vel_fraction(gs3_yy, TN_1, TN_2, TN_n1, TN_n2, v_yy, areaf1_yy, coord_i1(2), &
        coord_j2(2), d_time)

!-----------------------------------------------------------------------------------------------------
```

Following the evaluation of solid volume fraction for the additional volumes swept by the element boundaries, the magnitude of enthalpy that passes through the element boundary is computed by the subroutine "enthalpy_Hv". The corresponding equation in chapter 7 is (7—58).

```
!-----------------------------------------------------------------------------------------------------
```

```
CALL enthalpy_Hv(Hv1_xx, den_s, den_l, cap_s, cap_l, lat, h_sol, T_sol, areaf1_xx, &
     TN_2, TN_3, TN_n2, TN_n3, gs1_xx)

CALL enthalpy_Hv(Hv1_yy, den_s, den_l, cap_s, cap_l, lat, h_sol, T_sol, areaf1_yy, &
     TN_2, TN_3, TN_n2, TN_n3, gs1_yy)


CALL enthalpy_Hv(Hv2_xx, den_s, den_l, cap_s, cap_l, lat, h_sol, T_sol, areaf2_xx, &
     TN_1, TN_3, TN_n1, TN_n3, gs2_xx)

CALL enthalpy_Hv(Hv2_yy, den_s, den_l, cap_s, cap_l, lat, h_sol, T_sol, areaf2_yy, &
     TN_1, TN_3, TN_n1, TN_n3, gs2_yy)


CALL enthalpy_Hv(Hv3_xx, den_s, den_l, cap_s, cap_l, lat, h_sol, T_sol, areaf3_xx, &
     TN_1, TN_2, TN_n1, TN_n2, gs3_xx)

CALL enthalpy_Hv(Hv3_yy, den_s, den_l, cap_s, cap_l, lat, h_sol, T_sol, areaf3_yy, &
     TN_1, TN_2, TN_n1, TN_n2, gs3_yy)

!-------------------------------------------------------------------------------------------------------
```

The enthalpy computed by the subroutine (enthalpy_Hv) is only a magnitude. The following operations will assign the signs "+/−" to the enthalpies. The sign of enthalpy is dependent on the direction of material flow. For example, if the material is flowing in through an element surface, then the sign for the enthalpy corresponding to this element surface is given as "+"; on the contrary, it the material is flowing out of the element through this surface, then the sign for the enthalpy corresponding to this surface is given as "−".

```
!-------------------------------------------------------------------------------------------------------

IF(v_xx > 0.0D0) THEN

  IF(coord_k3(2) - coord_j2(2) < 0.0D0) THEN

    SIGN1_XX = 1.0D0

  ELSEIF(coord_k3(2) - coord_j2(2) > 0.0D0) THEN
```

```
    SIGN1_XX = -1.0D0
   ELSE
    SIGN1_XX = 0.0D0
   END IF

   IF(coord_i1(2) - coord_k3(2) < 0.0D0) THEN
    SIGN2_XX = 1.0D0
   ELSEIF(coord_i1(2) - coord_k3(2) > 0.0D0) THEN
    SIGN2_XX = -1.0D0
   ELSE
    SIGN2_XX = 0.0D0
   END IF

   IF(coord_j2(2) - coord_i1(2) < 0.0D0) THEN
    SIGN3_XX = 1.0D0
   ELSEIF(coord_j2(2) - coord_i1(2) > 0.0D0) THEN
    SIGN3_XX = -1.0D0
   ELSE
    SIGN3_XX = 0.0D0
   END IF
  ELSEIF(v_xx < 0.0D0) THEN
   IF(coord_k3(2) - coord_j2(2) < 0.0D0) THEN
    SIGN1_XX = -1.0D0
```

```
 ELSEIF(coord_k3(2) - coord_j2(2) > 0.0D0) THEN
   SIGN1_XX = 1.0D0
 ELSE
   SIGN1_XX = 0.0D0
 END IF


 IF(coord_i1(2) - coord_k3(2) < 0.0D0) THEN
   SIGN2_XX = -1.0D0
 ELSEIF(coord_i1(2) - coord_k3(2) > 0.0D0) THEN
   SIGN2_XX = 1.0D0
 ELSE
   SIGN2_XX = 0.0D0
 END IF


 IF(coord_j2(2) - coord_i1(2) < 0.0D0) THEN
   SIGN3_XX = -1.0D0
 ELSEIF(coord_j2(2) - coord_i1(2) > 0.0D0) THEN
   SIGN3_XX = 1.0D0
 ELSE
   SIGN3_XX = 0.0D0
 END IF
ELSEIF(v_xx == 0.0D0) THEN
 SIGN1_XX = 0.0D0
```

```
  SIGN2_XX = 0.0D0

  SIGN3_XX = 0.0D0

END IF

!-----------------------------------------------------------------------------------------------------------

IF(v_yy > 0.0D0) THEN

  IF(-(coord_k3(1) - coord_j2(1)) < 0.0D0) THEN

    SIGN1_YY = 1.0D0

  ELSEIF(-(coord_k3(1) - coord_j2(1)) > 0.0D0) THEN

    SIGN1_YY = -1.0D0

  ELSE

    SIGN1_YY = 0.0D0

  END IF


  IF(-(coord_i1(1) - coord_k3(1)) < 0.0D0) THEN

    SIGN2_YY = 1.0D0

  ELSEIF(-(coord_i1(1) - coord_k3(1)) > 0.0D0) THEN

    SIGN2_YY = -1.0D0

  ELSE

    SIGN2_YY = 0.0D0

  END IF


  IF(-(coord_j2(1) - coord_i1(1)) < 0.0D0) THEN

    SIGN3_YY = 1.0D0
```

```
  ELSEIF(-(coord_j2(1) - coord_i1(1)) > 0.0D0) THEN
    SIGN3_YY = -1.0D0
  ELSE
    SIGN3_YY = 0.0D0
  END IF
 ELSEIF(v_yy < 0.0D0) THEN
  IF(-(coord_k3(1) - coord_j2(1)) < 0.0D0) THEN
    SIGN1_YY = -1.0D0
  ELSEIF(-(coord_k3(1) - coord_j2(1)) > 0.0D0) THEN
    SIGN1_YY = 1.0D0
  ELSE
    SIGN1_YY = 0.0D0
  END IF

  IF(-(coord_i1(1) - coord_k3(1)) < 0.0D0) THEN
    SIGN2_YY = -1.0D0
  ELSEIF(-(coord_i1(1) - coord_k3(1)) > 0.0D0) THEN
    SIGN2_YY = 1.0D0
  ELSE
    SIGN2_YY = 0.0D0
  END IF

  IF(-(coord_j2(1) - coord_i1(1)) < 0.0D0) THEN
```

```
    SIGN3_YY = -1.0D0
  ELSEIF(-(coord_j2(1) - coord_i1(1)) > 0.0D0) THEN
    SIGN3_YY = 1.0D0
  ELSE
    SIGN3_YY = 0.0D0
  END IF
ELSEIF(v_yy == 0.0D0) THEN
  SIGN1_YY = 0.0D0
  SIGN2_YY = 0.0D0
  SIGN3_YY = 0.0D0
END IF
!-----------------------------------------------------------------------------------------------------
Hv1_xx = SIGN1_XX * Hv1_xx
Hv1_yy = SIGN1_YY * Hv1_yy

Hv2_xx = SIGN2_XX * Hv2_xx
Hv2_yy = SIGN2_YY * Hv2_yy

Hv3_xx = SIGN3_XX * Hv3_xx
Hv3_yy = SIGN3_YY * Hv3_yy
!-----------------------------------------------------------------------------------------------------
```

The following summation statements provide the total enthalpy changes due to advection in one time step. The summation is conducted with respect to the changes in x-direction and in y direction respectively.

```
!-----------------------------------------------------------------------------------------------------------

Hv_xx = Hv1_xx + Hv2_xx + Hv3_xx

Hv_yy = Hv1_yy + Hv2_yy + Hv3_yy

!-----------------------------------------------------------------------------------------------------------
```

The above analytical evaluation of advection includes both the continuity and the discontinuity. However, the continuous advection is already evaluated by the numerical method, so it has to be extracted from analytical evaluation.

```
!-----------------------------------------------------------------------------------------------------------

Hv_xn = d_time * (1.0D0 - THETA) * MATMUL(kvm_xx, Te_n) + D_time *     & THETA
        * MATMUL(kvm_xx, Te_n1) + d_time * (1.0D0 - THETA) *          &
        MATMUL(kvupm, Te_n) + D_time * THETA * MATMUL(kvupm, Te_n1)

Hv_yn = d_time * (1.0D0 - THETA) * MATMUL(kvm_yy, Te_n) + D_time *     & THETA
        *  MATMUL(kvm_yy, Te_n1)

Hvn_xx = Hv_xn(1) + Hv_xn(2) + Hv_xn(3)

Hvn_yy = Hv_yn(1) + Hv_yn(2) + Hv_yn(3)

nonQ_xx = Hv_xx + Hvn_xx

nonQ_yy = Hv_yy + Hvn_yy

!-----------------------------------------------------------------------------------------------------------
```

The arguments “nonQ_xx” and “nonQ_yy” are the non-physical sources for an element. These two arguments have to be assembled to the global loading vector “G_nonQ” through the following statements. The number “0.50D0” is a relaxation factor to prevent the temperature overflow. It is not necessary for crude mesh, but for a refine mesh, it is recommended.

```
!-------------------------------------------------------------------------------------------------------

G_nonQ(NUM(1)) = G_nonQ(NUM(1)) + 0.50D0 * (1.0D0 / 3.0D0) * (nonQ_xx + &
                 nonQ_yy)

G_nonQ(NUM(2)) = G_nonQ(NUM(2)) + 0.50D0 * (1.0D0 / 3.0D0) * (nonQ_xx + &
                 nonQ_yy)

G_nonQ(NUM(3)) = G_nonQ(NUM(3)) + 0.50D0 * (1.0D0 / 3.0D0) * (nonQ_xx + &
                 nonQ_yy)

END SUBROUTINE non_source

!-------------------------------------------------------------------------------------------------------
```

Now, the subroutine “non_source” finishes its execution and returns the non-physical source to the main program. It has to be mentioned that the array “G_nonQ” requires the return-to-zero operation for every iteration step, just the same as all the other arrays with incrementation algorithm for system assembly.

Appendix IV Parametric Study

VI.1 General

VI.1 General

The non-physical variable method generates a transport equation, which can be solved by the finite element method. The idea underpinning the finite element method is the discretisation of a continuous problem domain into smaller, simpler finite domains, which can be assembled and solved numerically by computers. This process is termed discretization. The finite domain is termed a finite element. The finite element method is an approximation method, so the size of the finite elements or the mesh density is essential to the accuracy of the approximation. Mesh density is usually associated with spatial discretization only. For transient problems, temporal discretization is important and also influences the accuracy of the method. This gives rise to concern on the time step size. One example that illustrates the importance of the time step size can be seen in chapter 4. The time step size is required to satisfy equation (4—9) for an explicit method, otherwise complex eigenvalues are generated and the problem is divergent. Another important parameter that is important to the non-physical variable method is the blending factor ϑ, which is introduced via equation (4—41) in chapter 4. This parameter is required to counter the possible absence of latent heat in the predictor step. In fact, the predicted nodal value (i.e. temperature) may be lower than the true value. This blending technique artificially brings the predicted value back closer to the true value. The blending parameter $\vartheta \in [0,1]$ and when the parameter $\vartheta = 0$, the predicted temperature is at the current iteration, and when the parameter $\vartheta = 1$, the predicted temperature is at the previous iteration. However, a major disadvantage of introducing this parameter is that, there is no clear definitive mathematical identification for the optimum value. The parameter can be determined analytically with the assistance of exact solution as shown in equation (2—7) but this approach is seldom available in practice. In this section, a parametric study is conducted in order to better understand the influences of mesh density and time step size on the accuracy of non-physical variable method. Also, the influence of the blending parameter ϑ is examined for various different mesh densities and time step sizes. In this parametric study, there are three variants, the total number of elements (NELS), the total number of time steps (N_STEPS) and the blending factor (ϑ). The study is based on a

thin slab, which can be seen in Figure 4.4. It is 0.1 metres long. Consequently, the element size L_e can be determined as

$$L_e = \frac{L_{total}}{NELS} \quad \text{(IV—1)}$$

where L_{total} is the total length of the model.

Moreover, the total cooling time of the simulations are set as 40 seconds and consequently the time step size $\triangle t$ can be calculated as

$$\triangle t = \frac{t_{total}}{N\_STEPS} \quad \text{(IV—2)}$$

where t_{total} is the total cooling time.

Since temperature profile is not important in the parametric study, this section focuses on the percentage error defined as

$$Er = \frac{|numerical\ results - exact\ results|}{exact\ results} \times 100\% \quad \text{(IV—3)}$$

where Er is the percentage error.

The problem is transient, so the percentage error can change with time, e.g. there are 800 percentage errors for a sample node, in a simulation with 800 time-steps. As a consequence, the average percentage error and the maximum error are provided to sufficiently reflect the influence of the parameters, i.e.

$$Er_{ave} = \frac{\sum_{j=1}^{N\_STEPS} Er_j}{N\_STEPS} \quad \text{(IV—4)}$$

where Er_{ave} is the average percentage error.

$$Er_{max} = MAX(Er_1, Er_2, \dots, Er_{N\_STEPS}) \quad \text{(IV—5)}$$

where Er_{max} is the maximum percentage error, and $MAX(\blacksquare)$ signifies a maximum.

This parametric study contains 8 groups of numerical experiments and each group has 9 simulations. The results and comments are shown as follows.

IV.2 The time step size and the blending factor

In this section, the parametric study focuses on the relationship between the time step size $\triangle t$ and the blending factor ϑ. The total number of elements is set constant, i.e. NELS = 100 and $L_e = 0.001\ m$. The samples of total number of time steps are set as, N_STEPS = 40, 80, 400 and 800, respectively, so the time step size are 1.0 seconds, 0.5 seconds 0.1 seconds and

0.05 seconds, respectively. As for the blending factor, simulation is executed every 0.1 from 0.1 to 0.9.

The average percentage error and the maximum percentage error versus the blending factor are depicted from Figure IV.1 to Figure IV.8. It can be seen from these figures that, both the average percentage error and the maximum percentage error perform a U-shape with the blending factor ϑ increases. The peaks of errors occur at $\vartheta = 0.1$ for all the simulations of different time step size. With greater time step size, the peak is even larger, e.g. $Er_{ave} = 33.7\%$ (see Figure IV.1) and $Er_{max} = 69.2\%$ (see Figure IV.2) when $\vartheta = 0.1$ and $\Delta t = 1\ seconds$. The peak is reduced when the time step size is smaller, e.g. $Er_{ave} = 10.08\%$ (see Figure IV.7) and $Er_{max} = 13.65\%$ (see Figure IV.8) when $\vartheta = 0.1$ and $\Delta t = 0.05\ seconds$. If considering 5% as the upper bound of tolerance error, it can be seen that when the blending factor is between 0.5 to 0.7, the tolerance is satisfied in most situations (except $Er_{max} = 6.15\%$ (see Figure IV.4) when $\vartheta = 0.7$ and $\Delta t = 0.5\ seconds$). When the time step size is less than 0.1 seconds, the minimum values of average percentage error and maximum percentage error occur at $\vartheta = 0.5$. And when the time step size is greater than 0.1 seconds, they occur at $\vartheta = 0.6$.

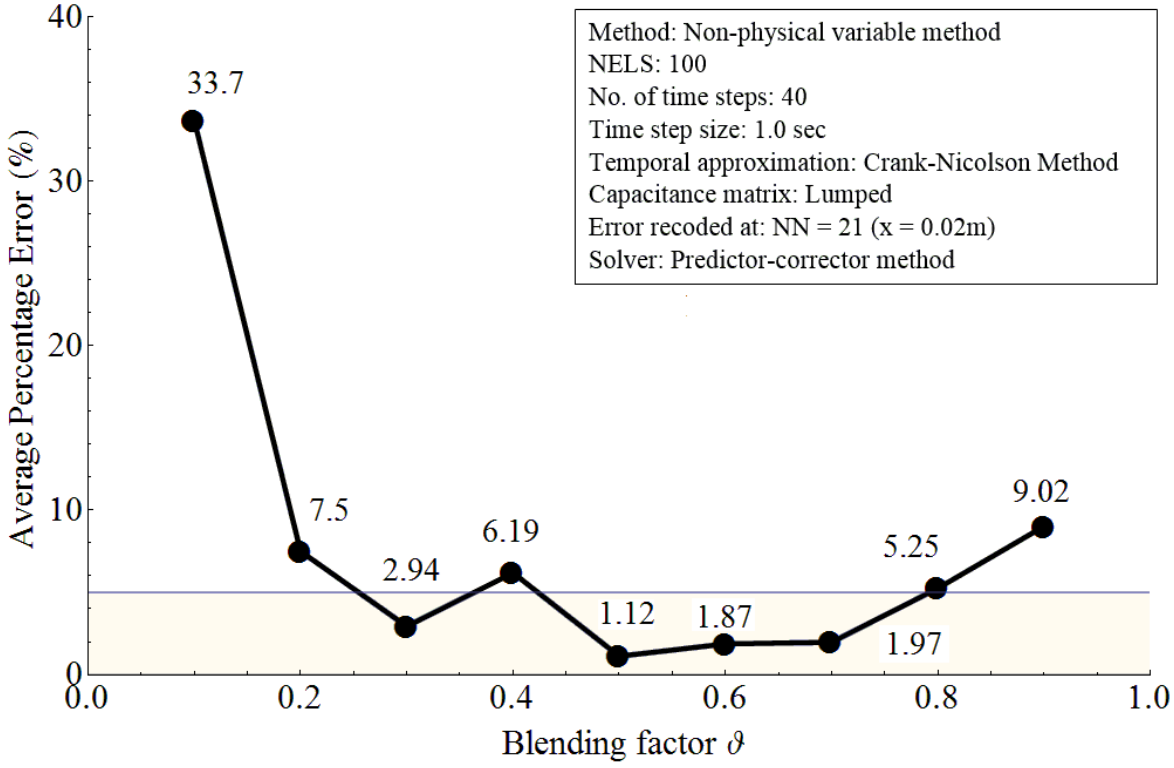

Figure IV.1: Average percentage error vs. blending factor, when $l_e = 0.001\ m$ and $\Delta t = 1\ s$

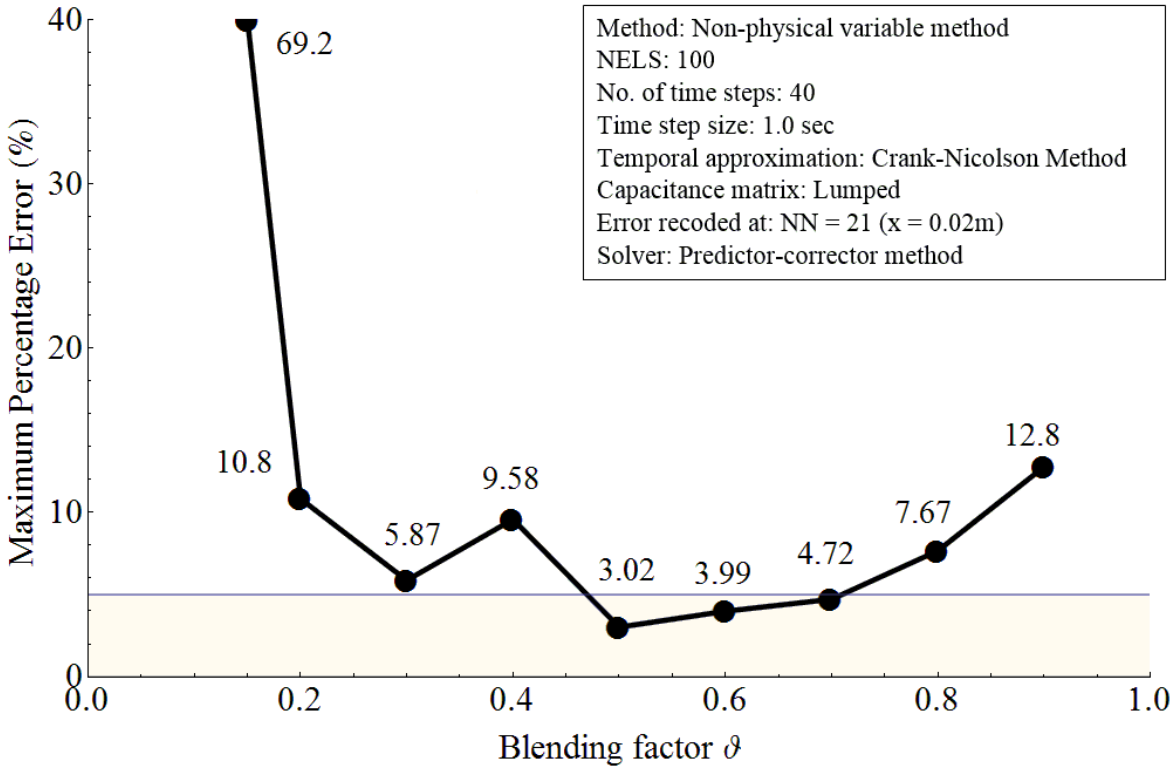

Figure IV.2: Maximum percentage error vs. blending factor, when $l_e = 0.001\ m$ and $\Delta t = 1\ s$

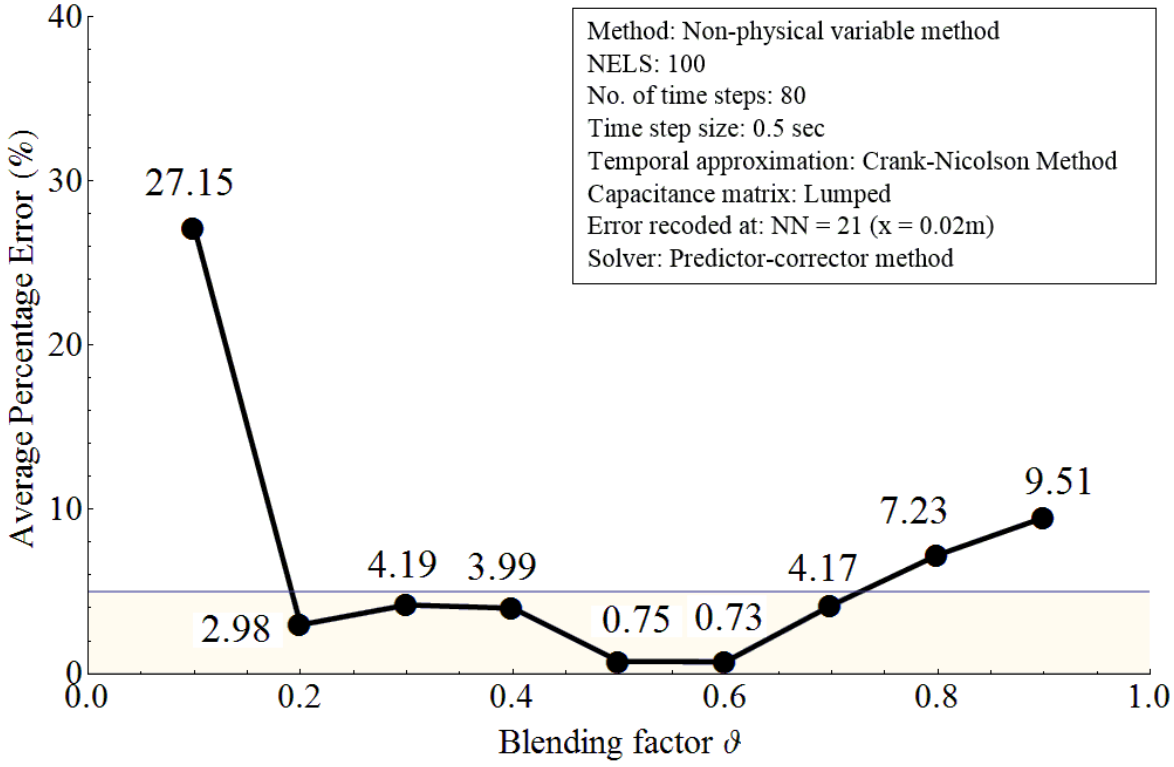

Figure IV.3: Average percentage error vs. blending factor, when $l_e = 0.001\ m$ and $\Delta t = 0.5\ s$

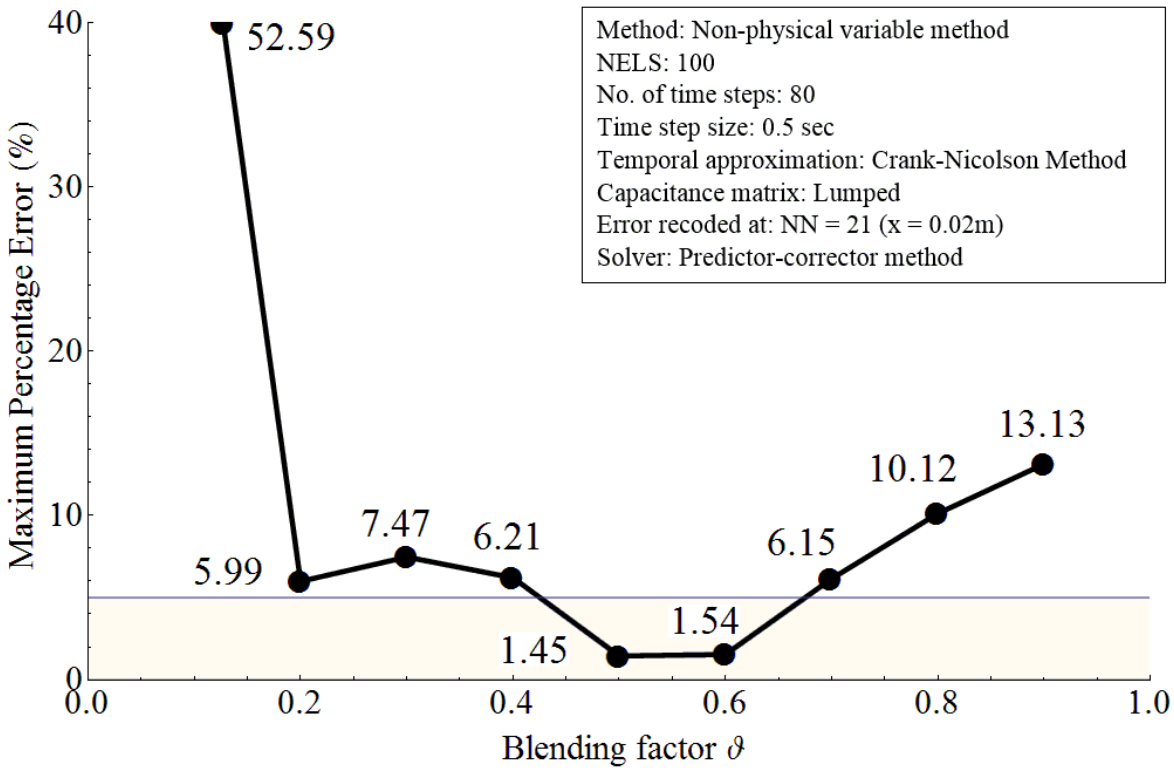

Figure IV.4: Maximum percentage error vs. blending factor, when $l_e = 0.001\ m$ and $\Delta t = 0.5\ s$

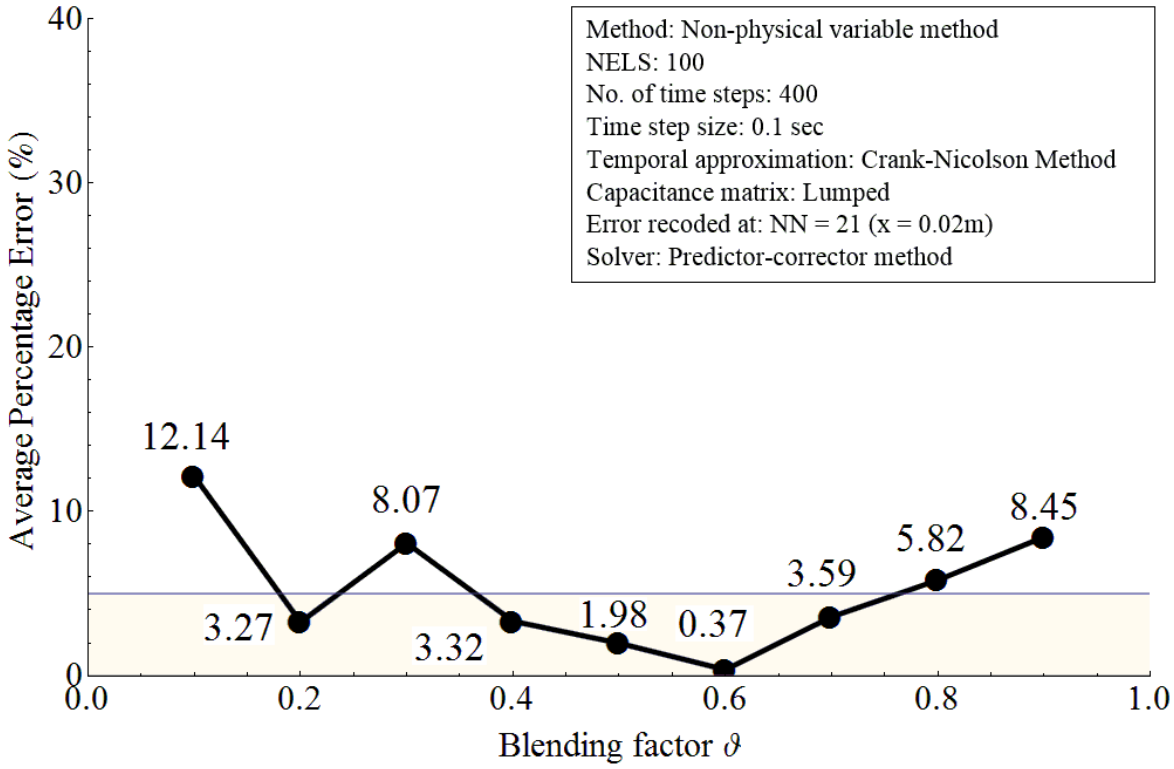

Figure IV.5: Average percentage error vs. blending factor, when $l_e = 0.001\ m$ and $\Delta t = 0.1\ s$

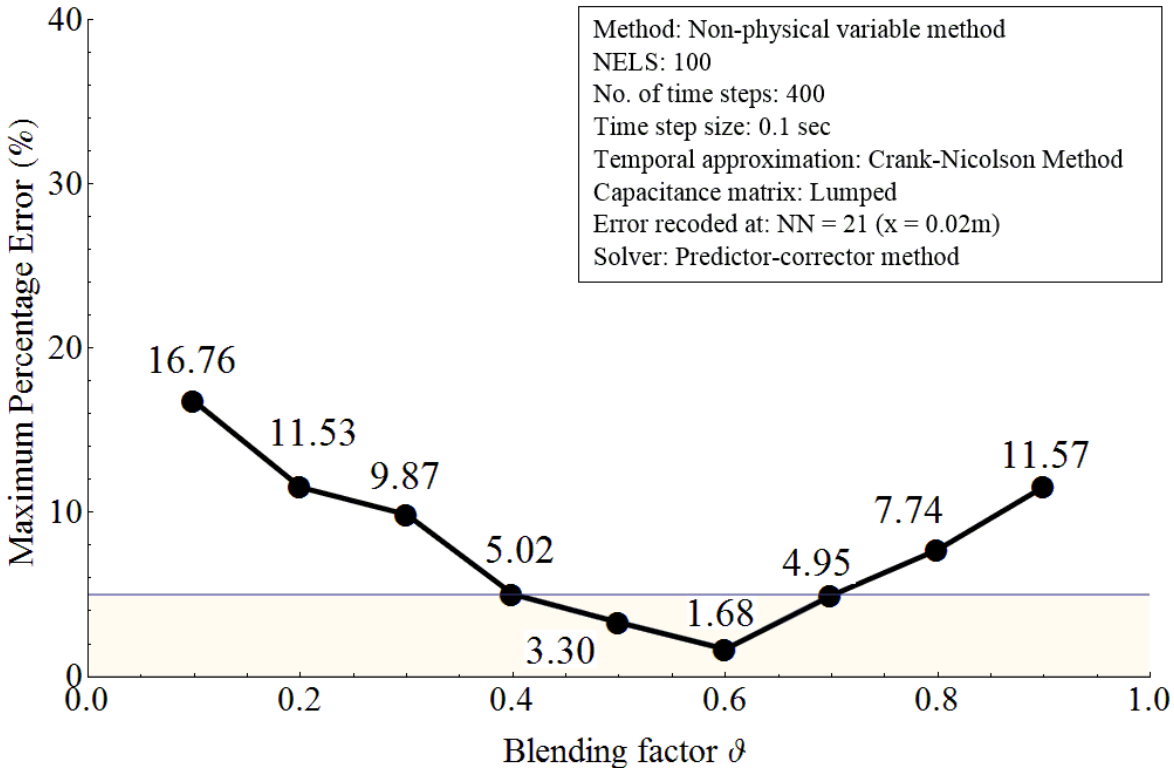

Figure IV.6: Maximum percentage error vs. blending factor, when $l_e = 0.001\ m$ and $\Delta t = 0.1\ s$

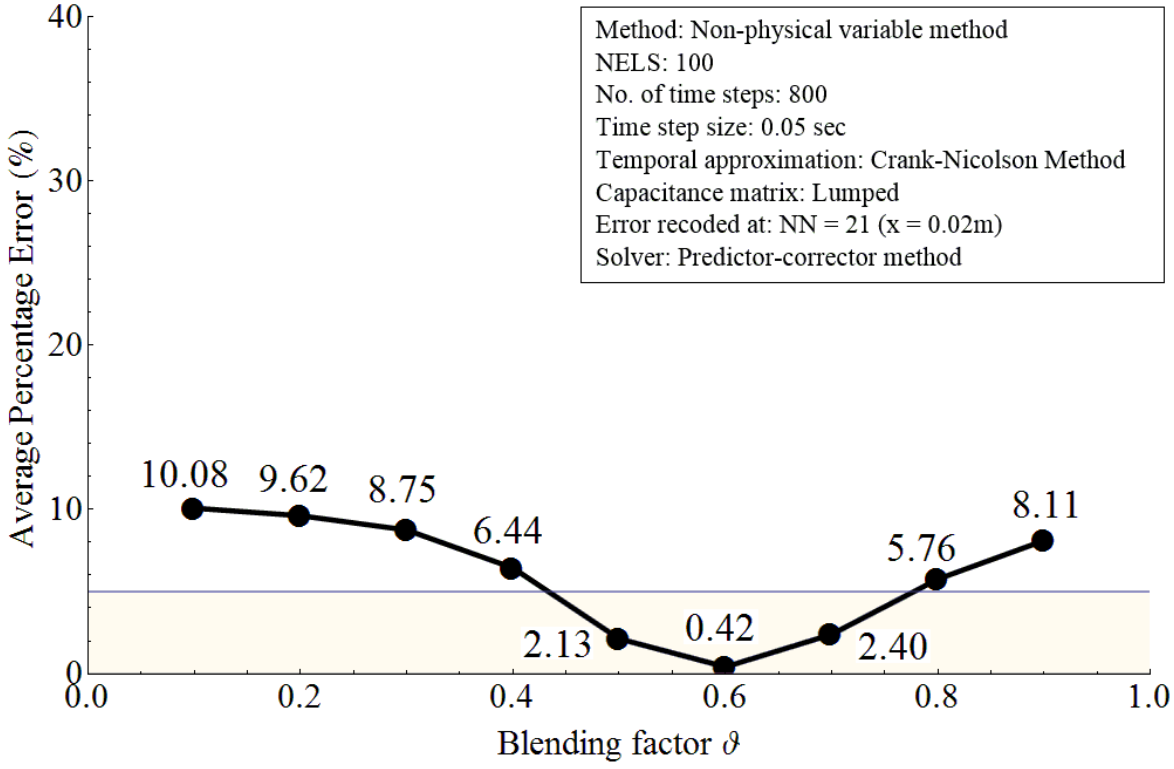

Figure IV.7: Average percentage error vs. blending factor, when $l_e = 0.001\ m$ and $\Delta t = 0.05\ s$

Figure IV.7:

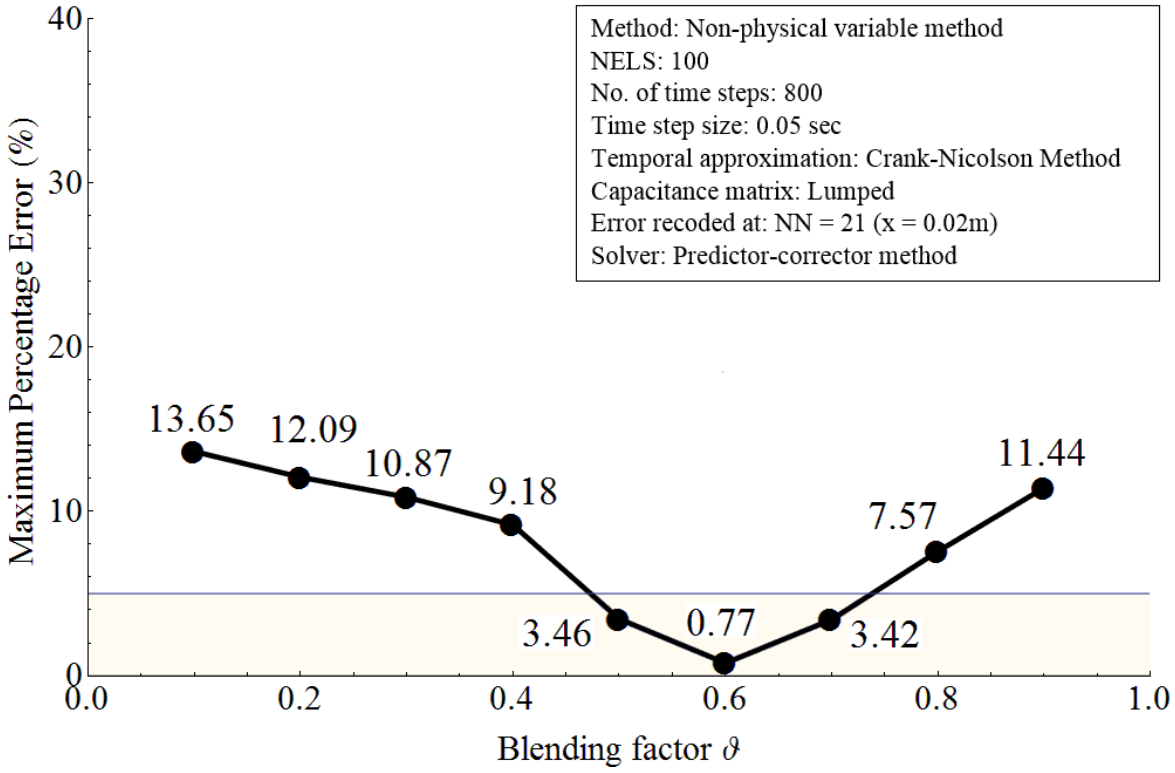

Figure IV.8: Maximum percentage error vs. blending factor, when $l_e = 0.001\ m$ and $\Delta t = 0.05\ s$

IV.3 The mesh density and the blending factor

In this section, the parametric study focuses on the relationship between the mesh density (element size L_e) and the blending factor ϑ. The total number of time steps is set constant, i.e. N_STEPS = 800 and $\Delta t = 0.05\ s$. The model is meshed with 50 elements, 200 elements, 400 elements and 800 elements, respectively. Together with the 100-element mesh in section IV.2, the size of the element is set as 0.002 m, 0.001 m, 0.0005 m, 0.00025 m and 0.000125 m, respectively. As for the blending factor, simulation is also executed every 0.1 from 0.1 to 0.9.

The average percentage error and the maximum percentage error versus the blending factor are depicted from Figure IV.9 to Figure IV.16. Similar to the results in section IV.2, both the average percentage error and the maximum percentage error perform a U-shape with the blending factor ϑ increases. However, it can be seen in Figures IV.9, IV.13 and IV.15 that, the peak of the average percentage error is not attained at $\vartheta = 0.1$ if the total number of elements is not 100 or 200. Instead, the peak occurs at $\vartheta = 0.2$ in these Figures. Despite the 50-element mesh (as can be seen in Figure IV.10, the maximum percentage error is 8.45%

when $\vartheta = 0.1$, but it is 13.1% when $\vartheta = 0.2$), the peak of maximum percentage error still occurs at $\vartheta = 0.1$. The percentage error can be lowered below the 5% tolerance if the blending factor ϑ is 0.6 and 0.7. The minimum values of average percentage error and maximum percentage error occur at $\vartheta = 0.6$ when the total number of mesh 50 or 100 (see Figures from IV.7 to IV.10) and they occur at $\vartheta = 0.7$ when the total number of elements is 200, 400 or 800 (see Figures from IV.11 to IV.16).

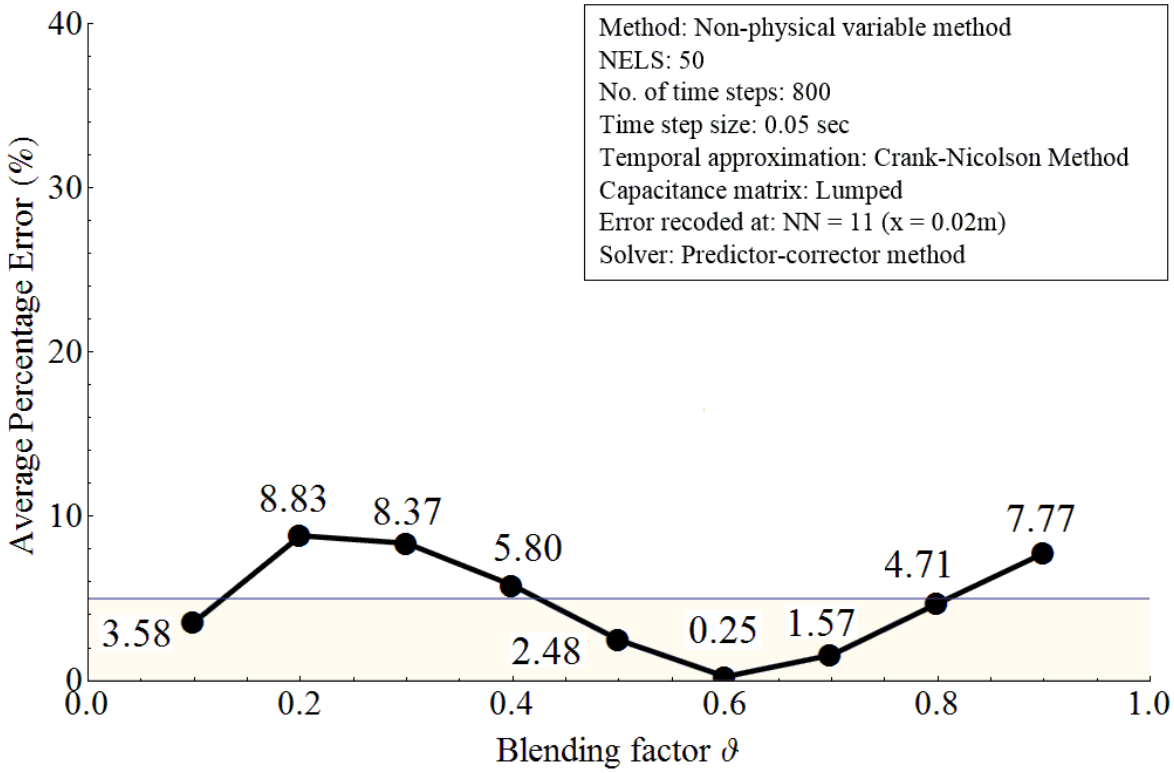

Figure IV.9: Average percentage error vs. blending factor, when $l_e = 0.002m$ and $\Delta t = 0.05\ s$

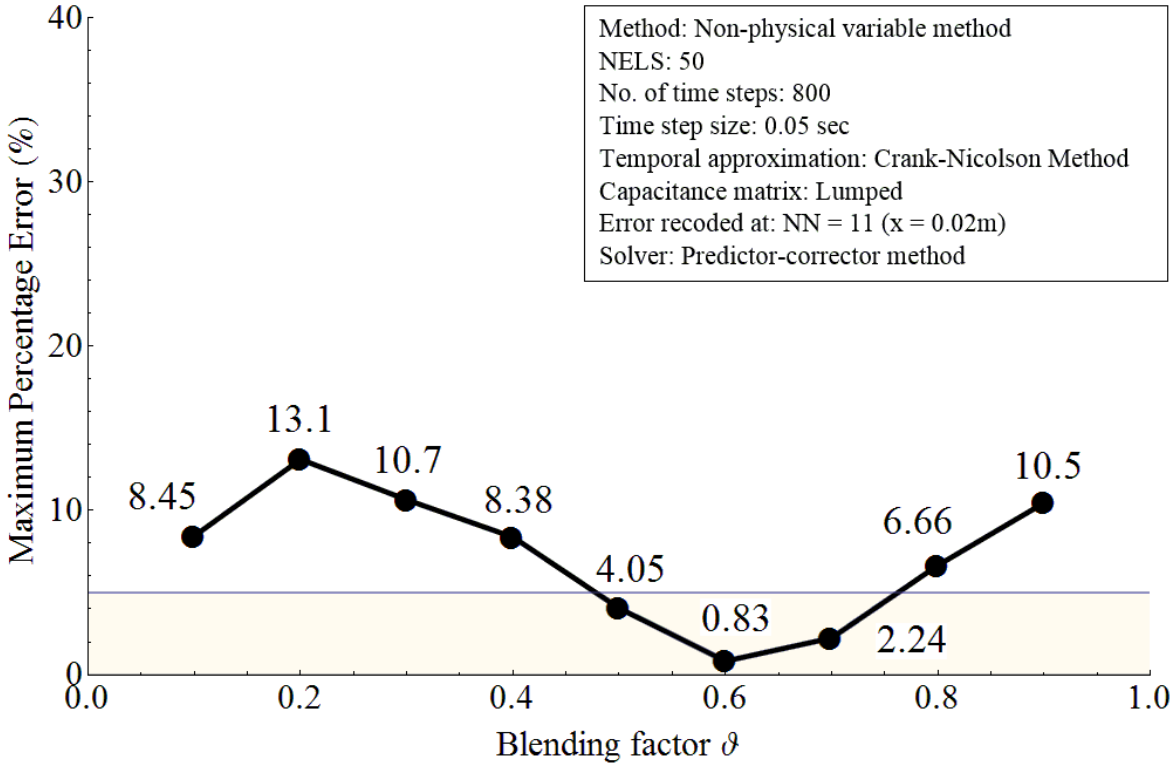

Figure IV.10: Maximum percentage error vs. blending factor, when $l_e = 0.002m$ and $\Delta t = 0.05\ s$

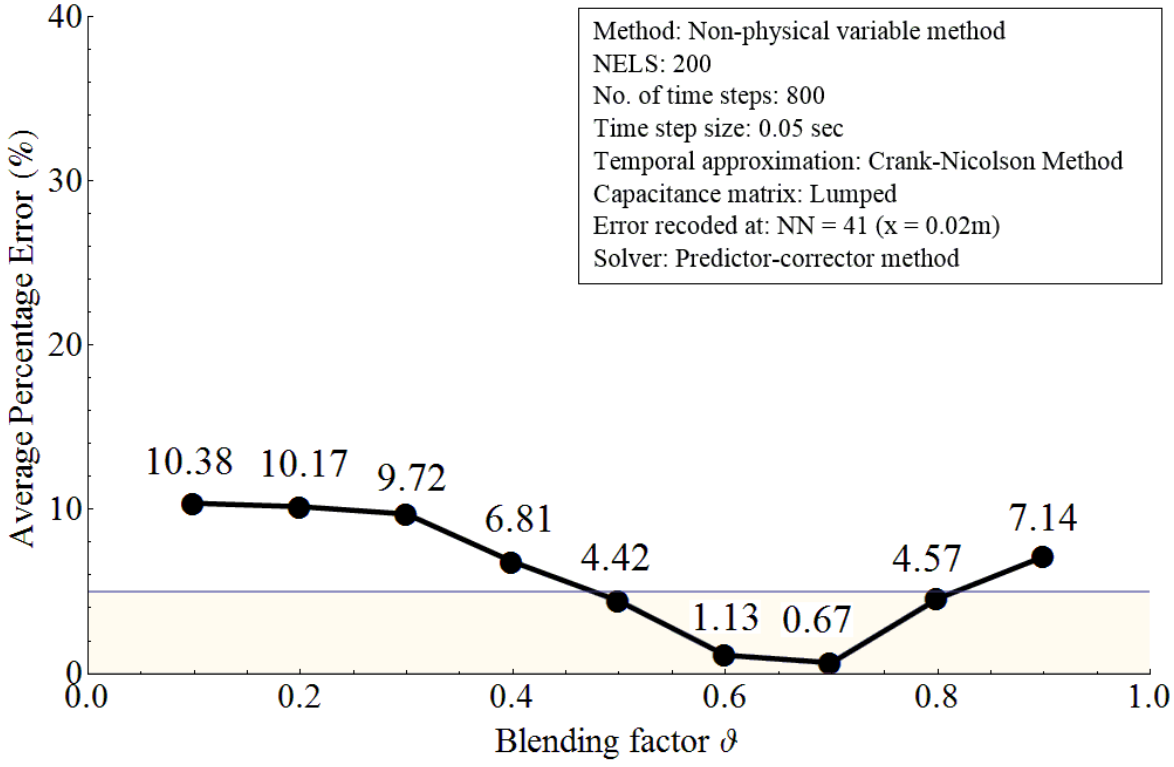

Figure IV.11: Average percentage error vs. blending factor, when $l_e = 0.0005m$ and $\Delta t = 0.05\ s$

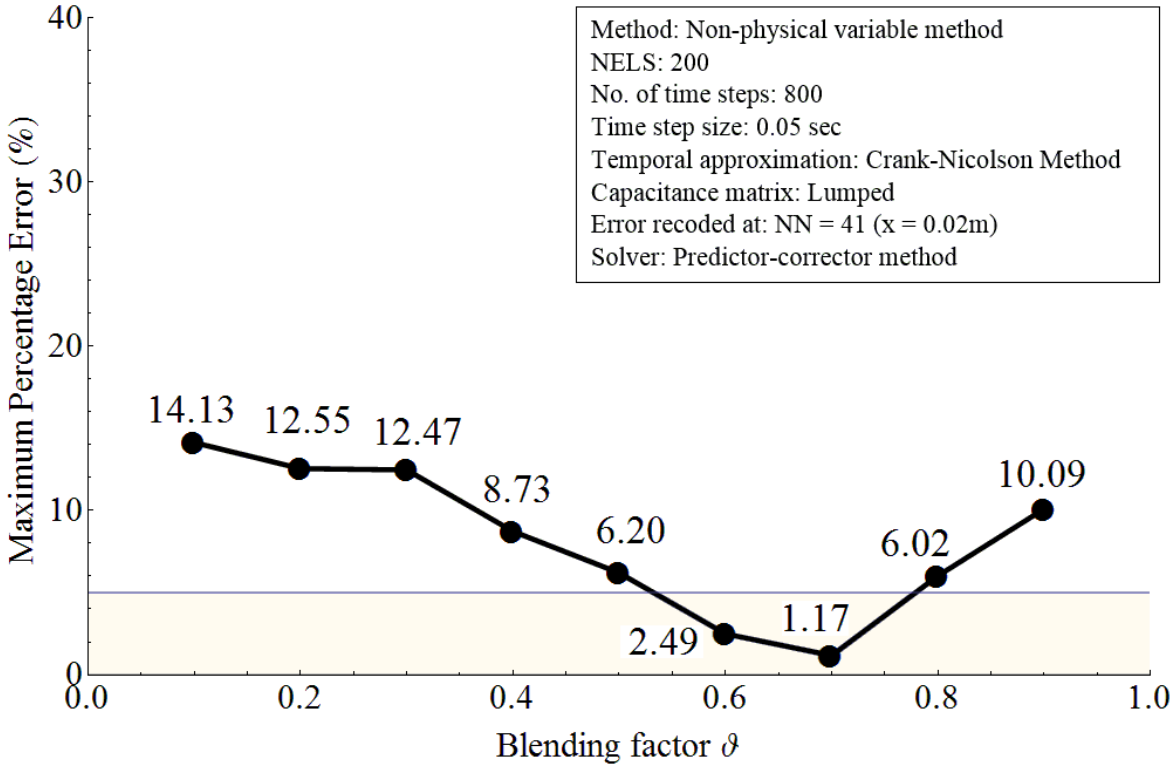

Figure IV.12: Maximum percentage error vs. blending factor, when $l_e = 0.0005m$ and $\Delta t = 0.05\ s$

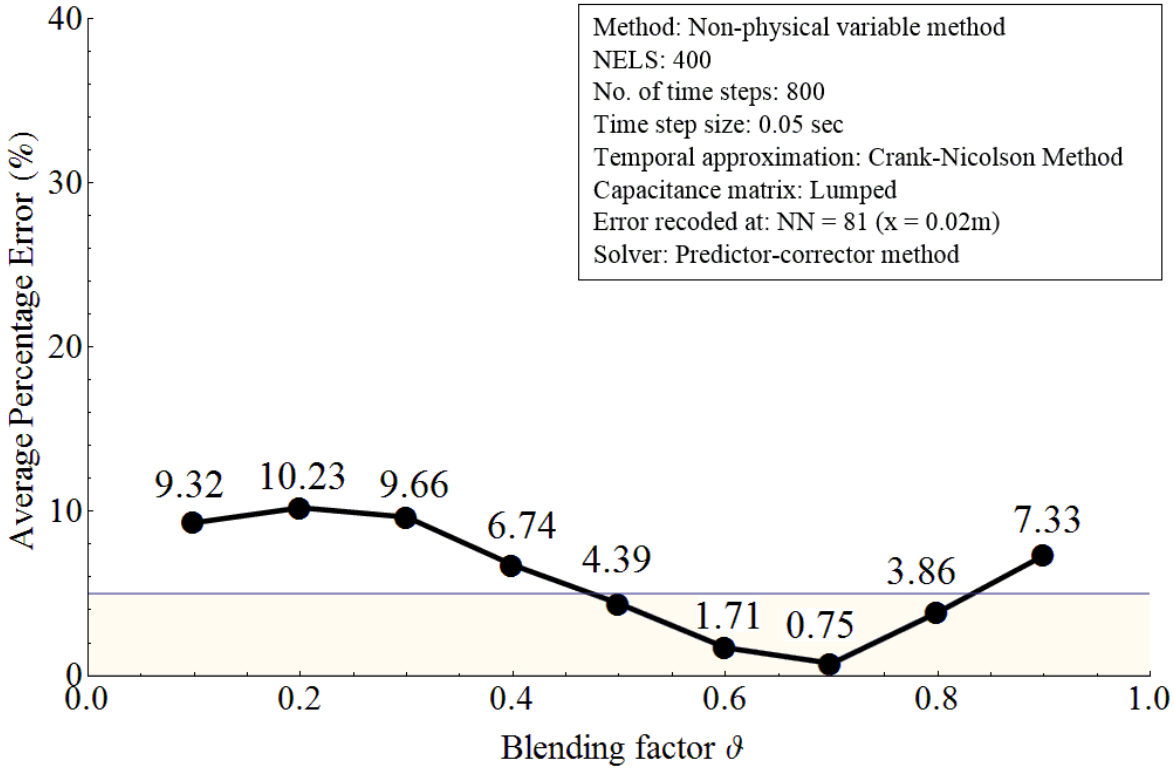

Figure IV.13: Average percentage error vs. blending factor, when $l_e = 0.00025m$ and $\Delta t = 0.05\ s$

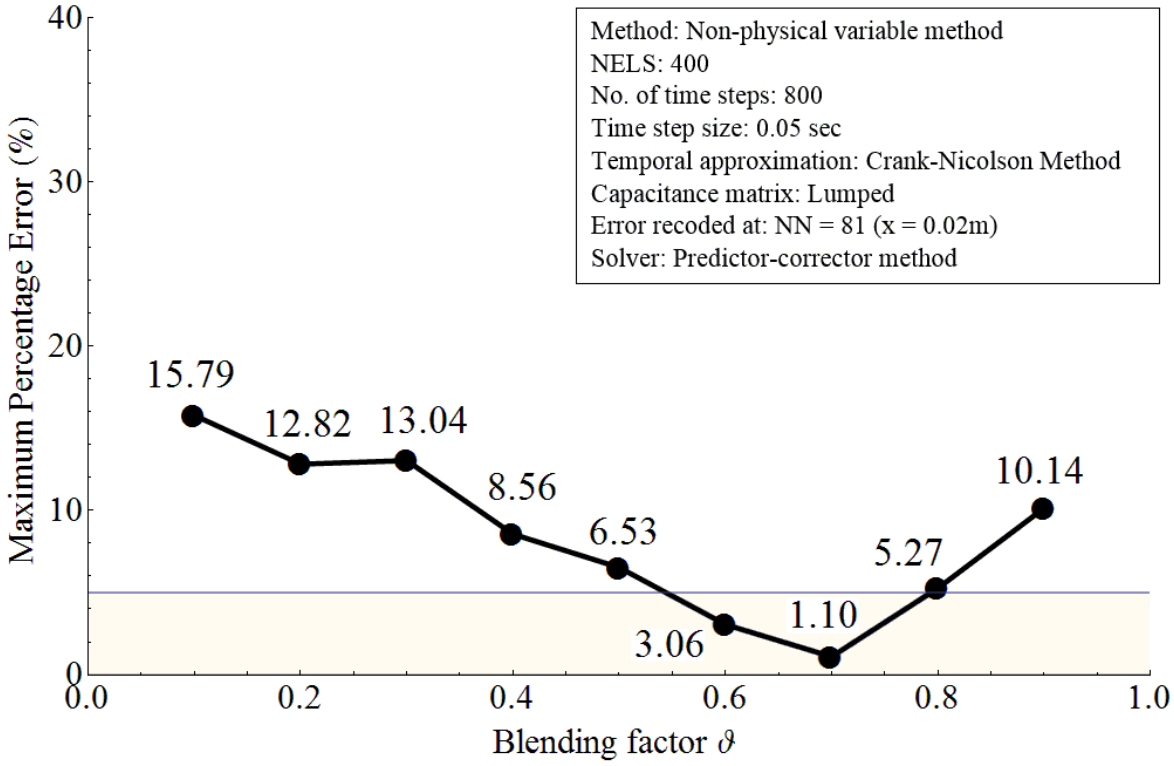

Figure IV.14: Maximum percentage error vs. blending factor, when $l_e = 0.00025m$ and $\Delta t = 0.05\ s$

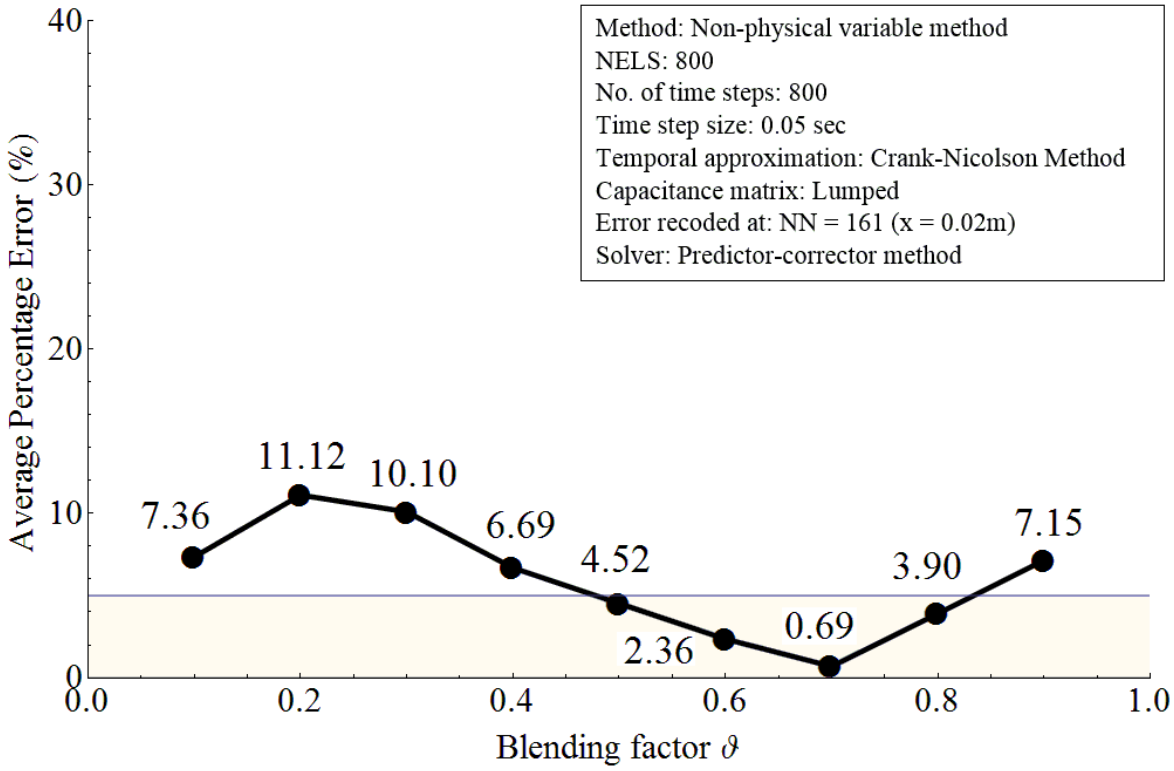

Figure IV.15: Average percentage error vs. blending factor, when $l_e = 0.000125m$ and $\Delta t = 0.05\ s$

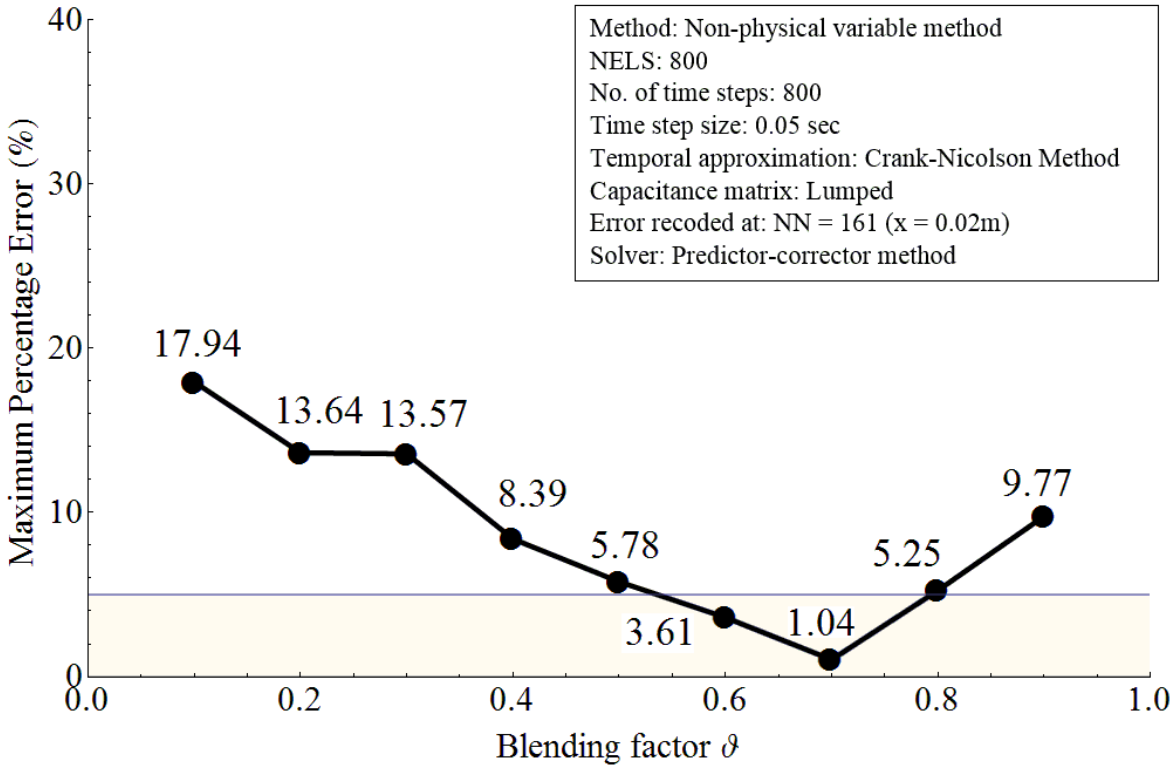

Figure IV.16: Maximum percentage error vs. blending factor, when $l_e = 0.000125m$ and $\Delta t = 0.05\ s$

IV.4 Summary

In summary, this appendix shows the relationship between the accuracy of the non-physical variable method and the parameters of finite element method, such as mesh density, time step size and the blending factor ϑ. Although there is not a definitive mathematical definition for the blending factor ϑ, in the parametric study, the relationship between accuracy and the blending factor performs consistently with different mesh densities and different time-step sizes. The study shows that, higher accuracy can be achieved by setting the blending factor ϑ between 0.6 and 0.7 depending on the mesh density and the time step size.